



HAL
open science

Nonlinear Ultrafast Optics in Multipass Cells

Nour Daher

► **To cite this version:**

Nour Daher. Nonlinear Ultrafast Optics in Multipass Cells. Optics [physics.optics]. Université Paris-Saclay, 2021. English. NNT: 2021UPASP127 . tel-03610245

HAL Id: tel-03610245

<https://pastel.hal.science/tel-03610245>

Submitted on 16 Mar 2022

HAL is a multi-disciplinary open access archive for the deposit and dissemination of scientific research documents, whether they are published or not. The documents may come from teaching and research institutions in France or abroad, or from public or private research centers.

L'archive ouverte pluridisciplinaire **HAL**, est destinée au dépôt et à la diffusion de documents scientifiques de niveau recherche, publiés ou non, émanant des établissements d'enseignement et de recherche français ou étrangers, des laboratoires publics ou privés.

Nonlinear Ultrafast Optics in Multipass Cells

*Optique non-linéaire ultra-brève dans des cellules
multipassages*

Thèse de doctorat de l'université Paris-Saclay

École doctorale n° 572, Ondes et matière (EDOM)

Spécialité de doctorat : Physique

Graduate School : Physique, Référent : Institut d'Optique

Thèse préparée dans l'unité de recherche LCF (Université Paris-Saclay, Institut d'Optique Graduate School, CNRS), sous la direction de Marc HANNA, directeur de recherche, le co-encadrement de Xavier DÉLEN, maître de conférence

Thèse soutenue à Paris-Saclay, le 14 décembre 2021, par

Nour DAHER

Composition du jury

Sophie KAZAMIAS Professeure des universités, Université Paris-Saclay	Présidente
Aurélié JULLIEN Directrice de recherche, Université Côte d'Azur	Rapporteuse
Thibaut SYLVESTRE Directeur de recherche, Université de Franche-Comté	Rapporteur
Clara SARACENO Professeure, Université de Bochum	Examinatrice
Marc HANNA Directeur de recherche, Université Paris-Saclay	Directeur de thèse
Xavier DÉLEN Maître de conférence, Université Paris-Saclay	Co-encadrant de thèse

Remerciements

Ce manuscrit ne serait jamais complet sans avoir remercié les personnes avec qui j'ai pu partager ces trois années et qui ont fait de cette thèse une expérience assez exceptionnelle et mémorable.

Je tiens tout d'abord à remercier l'ensemble des membres de mon jury, à commencer par Sophie Kazamias pour avoir accepté de présider ce jury de thèse. Je remercie également Aurélie Jullien et Thibaut Sylvestre, rapporteurs de ce travail, pour leur lecture attentive de ce manuscrit et pour leurs commentaires constructifs. Merci finalement à Clara Saraceno d'avoir examiné le travail de cette thèse.

Je souhaite remercier profondément Marc, mon directeur de thèse, de m'avoir adoptée en tant que thésarde et de m'avoir fait confiance dès le début. Toujours très calme et d'une efficacité incroyable, il a toujours réussi à trouver un moment soit pour m'expliquer, d'une manière super pédagogique, un phénomène physique, pour analyser et résoudre des problèmes expérimentaux ou théoriques, pour discuter d'une nouvelle idée, ou bien même pour aborder des sujets non scientifiques. Je garderai un excellent souvenir de tes passages réguliers en salle de manip (en mode surprise), de nos petites discussions en attendant devant le pc pour que le scan (parfois très long) de la mesure FROG se termine, et de nos petites conversations musicales. Je te remercie beaucoup pour ta patience pendant ces quelques années. J'ai beaucoup appris en travaillant à tes côtés. Merci pour tout !

Je tiens à remercier également Xavier, mon co-encadrant de thèse, qui en mars 2018, m'a accueillie en stage de fin d'étude sur le sujet des cellules multipassages et qui finalement a abouti à cette thèse. Grâce à sa bonne humeur et son enthousiasme communicatif, il a toujours réussi à garder ma motivation inchangée. Ses conseils et ses remarques étaient toujours pertinents et constructifs. Durant ces quelques années, j'ai beaucoup apprécié ton investissement dans les différents projets et j'étais impressionnée par ta manière de gérer les choses que ce soit en enseignement ou en recherche. Merci de m'avoir encouragée à faire du monitorat. Merci beaucoup pour ton aide précieuse. C'était un très grand plaisir de travailler avec toi.

Je souhaite aussi remercier Patrick, de m'avoir accueillie au sein du Laboratoire Charles Fabry. Nous avons la chance d'avoir un directeur de labo et un responsable de groupe comme toi. Toujours de bonne humeur et une véritable source d'énergie positive. Merci d'avoir gardé une très belle ambiance de travail au sein de l'équipe, même pendant le confinement. Je n'oublierai jamais nos petits séminaires du groupe et nos petites pauses café que tu organisais sur Zoom. C'est toujours un grand plaisir de te voir passer à nos bureaux dès que tu le pouvais. Grand merci !

Durant cette thèse j'ai eu l'opportunité de travailler en collaboration étroite avec les différents membres du laboratoire commun d'Amplitude. Je tiens tout d'abord à remercier sincèrement Yoann pour ses conseils pertinents tout au long de ma thèse et ses supers idées de manip. Un grand merci à Florent, qui malgré son emploi du temps surchargé, a toujours trouvé le temps pour me débloquer en salle d'expérience, surtout quand le laser n'était pas en forme. Merci pour ton aide régulière et pour toutes les astuces d'alignement que tu m'as transmises. Parmi les membres du labo commun il y a aussi Michele, qui est toujours prêt à donner un coup de main en manip. Merci pour le temps que tu consacres à t'occuper de la machine à café. Tu as gâté l'équipe avec la nourriture italienne ! Je remercie également Alexandre pour sa bonne humeur et les nombreuses conversations intéressantes. Je remercie aussi Aura, pour sa bienveillance et pour son soutien régulier (Quieres una cerveza mi amiga ?).

Je remercie tous les membres du groupe Lasers du laboratoire Charles Fabry. Un groupe très vivant avec sa propre histoire et ses nombreuses pratiques. Je garderai de très beaux souvenirs des événements comme le SAUCEPAN, le PINIOUF et le Chlip. Je tiens à remercier tous les permanents du groupe. Fred, une personne super sympa et avec un grand cœur. Avec sa bonne humeur quotidienne, il a toujours réussi à me faire sourire (parfois à me faire pleurer de rire). Le bureau de Fred est toujours ouvert pour une petite discussion scientifique ou bien pour une petite leçon de grammaire et d'orthographe de la langue française (Hussein peut confirmer). Merci d'avoir pris le temps de passer me voir en salle de manip (j'ai bénéficié de ton expertise dans le monde du femto), et d'assister à ma répétition de soutenance. Tes conseils et tes remarques pertinentes m'ont beaucoup aidé à améliorer la qualité de ma soutenance. François, une personne dynamique et toujours optimiste avec une capacité d'organisation incomparable. C'est un grand plaisir d'avoir encadré des TDs et des TPs avec toi. J'ai pu profiter pas seulement de ta qualité d'enseignant-chercheur mais aussi de ta qualité humaine. Merci pour tout ce que j'ai appris sur les systèmes lasers grâce à toi. Gaëlle, merci pour ta bienveillance. J'apprécie ton dévouement pour l'enseignement et la recherche. Ta culture générale enrichissait toujours les discussions de nos pauses déjeuner et nos pauses café. N'oublions pas Sylvie, qui par sa gentillesse et son organisation du matériel et des optiques a beaucoup facilité le travail au sein de l'équipe.

Je remercie tous les doctorants passés et présents du groupe avec qui j'ai partagé des moments inoubliables au laboratoire et à l'extérieur. Je commence par remercier Loïc, avec qui j'ai passé de nombreux jours, voire semaines, en salle d'expérience pendant mon stage. Merci de m'avoir transmis tes connaissances (théoriques et pratiques) sur les MPCs qui m'ont servies comme base solide pour la thèse. Il y a aussi Tiphaine, une personne d'une capacité incroyable à gérer plusieurs choses en même temps. Je me demandais comme elle faisait ! Depuis mon arrivée à l'IOGS, elle m'a apporté de l'aide de tous les côtés. Tiphaine est une personne dynamique, pleine de vie et toujours prête à donner un coup de main à tout le monde. Je garderai de très forts souvenirs de tous les moments que nous avons passés ensemble au bureau, en salle de manip et en dehors du labo. Je te souhaite tout le meilleur dans ta vie personnelle et professionnelle. Merci également à Thomas (pour nos petites pauses café très tôt le matin), Gaëtan (pour sa super personnalité et pour les bons moments que nous avons passés en salle de manip), Philipp (pour son humour exceptionnel). Parmi les doctorants encore présents,

il y a Hussein, une personne qui donne tout son mieux dans tout ce qu'il fait. Très attentionné et prêt à fournir de l'aide à tout moment. N'hésitez pas à lui demander, il est toujours prêt pour un match de ping-pong. Dans le même bureau qu'Hussein, il y a aussi Maxime, le sportif du groupe, toujours motivé pour courir le midi. Ton insistance régulière m'a finalement encouragée à franchir le pas et à commencer à courir. Je te remercie pour ça. Il y a aussi Lisa, ma dernière voisine du bureau. Ta passion pour les aquariums et les poissons a animé notre bureau en installant notre propre aquarium où s'installe notre cher poisson Flash ! Je te remercie de m'avoir supportée pendant tout ce temps. Je n'oublierai pas nos discussions, nos petites bêtises, nos blagues immortelles et nos partages de sucreries. L'ambiance de notre bureau va me manquer. Merci Hippolyte de prendre soin de tes nouveaux collègues de bureau, Lisa et Flash. Bon courage et bienvenue à cette nouvelle aventure. Merci également à Quentin (qui par sa super bonne humeur a toujours réussi à me faire éclater de rire), Anahita (pour sa tendresse, nos conversations et nos rires), Isabel (pour sa gentillesse absolue), et Lucas (pour ses remarques pertinentes). Bon courage pour la suite de vos thèses. Merci également à notre post-doc, Pierre.

Je remercie également les autres personnes avec qui j'ai pu partager le bureau pendant ces années : Jonas, Timothé et Hector. Bon courage pour la suite de vos thèses. Merci également à tous les doctorants, stagiaires et post-doctorants passés que j'ai pu croiser dans l'équipe : Kevin, Christine (#TeamMPC), Lauren, Philippe, Marie, Anna et Christina.

Durant ces trois années de thèse, j'ai pu découvrir le monde de l'enseignement au sein de l'IOGS. Je tiens à remercier toutes les personnes avec qui j'ai pu partager cette expérience. En particulier, je remercie Franck Delmotte, Fabienne Bernard, Thierry Avignon, Cédric Lejeune, Denis Boiron, Louis Daniault, Sylvain Almonacil, Sylvie Lebrun, Henri Benisty, et la liste continue. Merci également à François, Xavier et Philipp, mes collègues du groupe lasers avec qui j'ai partagé aussi des moments précieux en salle de cours et TP.

Merci également à tous les membres de l'Institut d'Optique et du Laboratoire Charles Fabry qui ont contribué à garder une très bonne ambiance de travail durant ces trois années. Merci à tous les membres de l'atelier d'optique et de mécanique, de la reprographie, de la médiathèque et de l'administration. Merci également aux personnes de l'accueil de l'Institut.

Je souhaite remercier les personnes des autres laboratoires avec qui nous avons collaboré. Merci à Fabien Quéré, Antoine Jeandet et à Spencer W. Jolly du LIDYL, pour le temps qu'ils ont consacré pour venir au LCF et réaliser des mesures INSIGHT et TERMITES. Je remercie tous les membres du groupe Optical-Cycle Physics du LOA, en particulier Rodrigo Lopez-Martens et Louis Daniault ainsi que Jean-François Hergott, Olivier Tcherbakoff et Fabrice Réau et tous les membres du groupe SLIC du LIDYL, pour les efforts qu'ils ont mis en œuvre afin de rendre possible la réalisation de la manip de la compression temporelle d'une source Titane saphir.

Sur un plan plus personnel, je remercie tous mes amis pour leur soutien pendant ces trois années. En particulier, je remercie mes amies à Paris, Ghewa et Shatha. Je suis très heureuse d'avoir partagé avec vous de nombreux moments agréables. Je vous souhaite tout le meilleur

pour la suite de vos carrières futures.

Je souhaite remercier tous les membres de ma famille au Liban et à l'étranger pour leur aide et leur soutien constant. En particulier, je tiens à adresser ma reconnaissance à mon frère Georges et ma sœur Jana, qui m'ont épaulé ces trois dernières années. Georges, merci de m'avoir encouragée à venir continuer mes études supérieures en France et à se lancer dans le monde de la recherche. Ta joie de vivre et ta passion pour la science et la recherche sont pour moi une véritable source de motivation quotidienne. Occupé par ta propre thèse et tes heures d'enseignements, tu as toujours trouvé le temps de m'aider et de me remonter le moral quand il fallait. Merci pour tes conseils pertinents et ton aide précieuse dans ma vie personnelle ainsi que professionnelle. Merci de m'avoir motivée à toujours faire de mon mieux dans tout ce que je fais. Jana, merci d'être toujours à l'écoute et de m'apporter de l'aide quand j'en ai besoin. Je sais que dans les moments difficiles je peux toujours compter sur toi. Nos petites séances musicales étaient pour moi une évasion de la thèse et un moment de joie et de bonheur. Je te souhaite bon courage pour la suite de ta thèse. Merci à tous les deux pour les moments inoubliables que nous avons vécus ensemble ici en France.

Enfin, je remercie profondément mes chers parents, pour leur soutien sans faille tout au long de ma vie et de mon parcours académique. Je ne pourrai jamais vous remercier assez. You are my greatest blessing !

Contents

General Introduction	9
I Nonlinear Optics in Multipass Cells	13
1 Short pulse propagation	15
1.1 Propagation equation	15
1.2 Chromatic dispersion	16
1.3 Third-order nonlinear effects	18
1.4 Combination of SPM and GVD	24
2 Multipass cells	26
2.1 Theory	26
2.2 Solid-state MPCs	28
2.3 Gas-filled MPCs	29
3 Numerical models for pulse propagation	29
3.1 3D model	29
3.2 2D model	30
3.3 1D model	30
4 Nonlinear temporal compression	34
4.1 Principle	34
4.2 Free propagation in bulk	35
4.3 Multiplate	36
4.4 Waveguides	36
4.5 State of the art in MPCs	37
5 Conclusion	39
II Study of Spatio-spectral Couplings at High Nonlinearity in a Multipass Cell	41
1 Introduction	42
1.1 Spatio-temporal couplings in optical pulses	42
1.2 The question of spatial and spatio-temporal degradation in nonlinear MPCs	43
2 Study of a highly nonlinear MPC	46
2.1 Experimental setup	46
2.2 Observation of wave breaking and 1D model validation	49
2.3 Measurement of intensity and phase spatio-spectral profiles	51
3 Conclusion	55
III Spectral Compression in a Multipass Cell	57

1	Introduction	58
2	Concept of SPM-induced spectral compression	60
3	Preliminary results	62
3.1	Spectral compression in 3.8 bar of xenon	62
4	Generation of high energy near FTL picosecond pulses	63
4.1	Experimental setup	63
4.2	Results and discussions	65
4.3	Control of the output spectral shape	67
4.4	Comparison between experimental and numerical simulation results	70
4.5	Spatial and spatio-spectral characterization	72
5	Conclusion	73
IV Raman Conversion in a Multipass cell		75
1	Introduction	76
2	Study of stimulated Raman scattering in a MPC	77
2.1	Influence of the input temporal duration	77
2.2	Spatial filtering action in a MPC	82
2.3	Temporal characterization	90
3	Conclusion	96
General Conclusion		97
Bibliography		102
List of Publications		117
Summary of the thesis in French		155

General Introduction

One of the most important fields of photonics research is nonlinear optics. In 1961, just after the invention of the laser, the scientific breakthrough that revolutionized our daily lives, the first laser-driven nonlinear optical experiment was conducted [Franken 61]. It demonstrated the generation of second harmonic of light by focusing a ruby laser in a quartz crystal. Since then, the field of nonlinear optics started growing rapidly expanding its utility from the fundamental understanding of light-matter interaction to scientific and industrial applications. The necessity to use nonlinear optics in the development of novel ultrafast laser sources is crucial. Few examples of the applications combining nonlinear optics and ultrafast laser sources are temporal or spectral compression by means of self-phase modulation, supercontinuum generation, parametric amplification, XUV and attosecond sources, and the list goes on and on.

The fundamental description of nonlinear optics and first experimental implementations have been done for beams propagating in free space. For example, it was used in the context of nonlinear temporal compression of laser pulses by performing spectral broadening (Kerr effect) through focusing the beam inside a slab of material [Rolland 88]. Although it is easy to implement, the Kerr nonlinearity, in addition to self-phase modulation, introduces spatio-temporal effects such as a spatial variation of the phase that sets a limit on the compression factor that can be attained. In order to increase the compression factor that one wants to achieve, other methods can be employed while limiting the spatio-temporal effects. Such methods includes the use of waveguide structures such as optical fibers and capillaries. These techniques play a major importance in implementing nonlinear optics expanding its domain of applications. Their importance relies on the capability to confine the field in the core over a certain interaction length, opening the door to lower pulse energies and average powers. Moreover, the single transverse mode fiber guiding structure fixes the spatial properties of the beam. Therefore, a large level of nonlinearity can be obtained while avoiding the detrimental effects such as self-focusing and spatio-temporal couplings. In such transverse single mode solid core structures, energy scaling is limited by the highly localized spatial mode.

Many other designs have emerged in order to maintain a certain control on the spatial properties of high energy pulses while propagating and nonlinearly interacting with matter in the waveguide structure. Theses designs include the large mode area fiber, large and hollow gas-filled core fibers with Kagome and antiresonant cladding structures, and standard and stretched gas-filled capillaries.

The beam interaction with nonlinear medium in free space reappeared recently aiming to improve the implementation of nonlinear optical effects. Some methods consist in distributing the nonlinearity in several stages spaced by linear free-space propagation. This limitation of the nonlinearity at each stage keeps the spatio-temporal couplings under control. A succession of numerous slabs of nonlinear material placed around one or more foci of the propagation beam is one example. This strategy is known as the multiplate compression scheme in the context of nonlinear temporal compression.

In 2016, an experimental demonstration conducted by [Schulte 16] showed that the concept of distributing the nonlinearity in multiple stages can be expanded to larger number of stages. This is possible by using a Herriott-type configuration recirculating cell that focuses the beam inside a nonlinear medium (solid or gas), providing therefore an increase in the interaction length. This concept is known by the multipass cell (MPC). The results of experimental implementation using MPCs showed an homogeneous and good spatial properties in the output beam of such setups. Alongside the good spatial properties and the low spatio-spectral couplings observed at the output of MPCs, these setups possess a certain flexibility in terms of:

- Energy scalability by the variety of choices of the nonlinear medium (solid or gas) or even by adapting the waist size inside the MPC by selecting its configuration (distance between the mirrors and the radius of curvatures).
- Operating wavelength by adapting the mirror coatings.
- The propagation regime (normal or anomalous) by using adapted dispersive mirrors.

When this thesis started in 2018, there were only few experimental demonstrations of post-compression using gas-filled MPCs and no studies were provided on the limitations of MPCs in terms of the spatio-temporal couplings at the output of such experimental setups used for nonlinear temporal compression. In addition, the use of nonlinear MPCs was almost exclusively used to perform spectral broadening induced by self-phase modulation of the laser pulses in order to temporally compress the laser pulse with additional dispersion compensation devices. Therefore, the need for more investigation of the robustness of such nonlinear systems to spatio-spectral properties were missing alongside the possibility to use nonlinear multipass cells to perform nonlinear effects other than the Kerr effect.

This manuscript is divided into four chapters describing the different activities and experiments done in the scope of this thesis addressing the two points mentioned just above. In the various studies that we performed, we focused on the manipulation of Ytterbium-doped fiber based laser sources commonly used due to their high energy and high repetition rate:

Chapter 1: Provides a brief reminder of the nonlinear phenomena that are related to the work done in this thesis. The description behind the concept of multipass cells is also provided, along with the numerical models that can be used to simulate the propagation in such setups, starting with a 3D model to a more simplified 1D model.

Chapter 2: Describes the experimental study done in a gas-filled MPC with a high level of nonlinearity with the aim to study the spatio-spectral properties at the output of the MPC. The effect of wave breaking, a nonlinear effect observed in normal dispersion regime presenting high level of nonlinearity, is observed and illustrated. The obtained results are then compared with numerical simulations. Finally, in collaboration with LIDYL (CEA), a 3D characterization technique called INSIGHT is performed for the first time in a multipass cell setup.

Chapter 3: Illustrates the work done to perform spectral compression in a solid-state MPC. This work showed the possibility to generate near Fourier-transform-limited picosecond pulses from a femtosecond Ytterbium-doped fiber chirped pulse amplifier. We also compared the obtained results with numerical simulations.

Chapter 4: Addresses the study of frequency conversion by stimulated Raman scattering in a solid-state material inserted inside a multipass cell for input pulses with a duration of several picoseconds obtained by positively chirping the initial femtosecond pulses. We first investigate the effect of the pulse temporal duration on the conversion efficiency that can be obtained at the output of a solid-state MPC with a Raman medium inserted near the center. We then perform spatial characterizations in order to look into the spatial quality of the converted beams at the MPC output compared to a single pass scheme. Finally, we temporally characterize the pump and Stokes beams at the MPC output.

Chapter I

Nonlinear Optics in Multipass Cells

Objectives

This first chapter is divided into four parts. First, a brief reminder of the ultrashort pulse propagation theory is presented along with the various optical effects affecting the propagation of a short pulse, with an emphasis on nonlinear effects. In the second part, a description of multipass cells schemes is presented. Then, a presentation of numerical models used to describe the propagation into MPCs is provided. Finally, we round-up the theoretical and experimental realizations done so far in the scientific community regarding the use of multipass cells as a nonlinear tool, especially for applications to temporal post-compression.

Contents

1	Short pulse propagation	15
1.1	Propagation equation	15
1.2	Chromatic dispersion	16
1.3	Third-order nonlinear effects	18
1.3.1	Optical Kerr effect	18
1.3.2	Self-steepening	22
1.3.3	Stimulated Raman Scattering	22
1.4	Combination of SPM and GVD	24
1.4.1	Wave breaking	24
1.4.2	Soliton effects	25
2	Multipass cells	26
2.1	Theory	26
2.2	Solid-state MPCs	28
2.3	Gas-filled MPCs	29
3	Numerical models for pulse propagation	29
3.1	3D model	29
3.2	2D model	30
3.3	1D model	30
4	Nonlinear temporal compression	34

4.1 Principle	34
4.2 Free propagation in bulk	35
4.3 Multiplate	36
4.4 Waveguides	36
4.5 State of the art in MPCs	37
5 Conclusion	39

1 Short pulse propagation

The following sections give a quick overview of important nonlinear effects that are later used and studied in a multipass cell as we will see in the following chapters. We start by describing the nonlinear wave equation from which the nonlinear effects derive their origin and the third-order effects are discussed in greater detail.

1.1 Propagation equation

Maxwell's equations [Maxwell 65] developed in 1865 are the basic equations used to describe electromagnetic phenomena, such as optical pulses. A large number of models can be obtained from these basic equations to describe the propagation of ultrashort pulses in dispersive nonlinear media. In this work, we have chosen to use a generalized nonlinear envelope equation (NEE) introduced by Brabec and Krausz [Brabec 97] which is obtained under the slowly evolving wave approximation (SEWA). This NEE is capable of describing light pulse propagation down to the single cycle regime and reads

$$\frac{\partial A}{\partial z} = -\frac{\alpha_0}{2}A + i\hat{D}A + \frac{i}{2\beta_0} \left(1 + \frac{i}{\omega_0} \frac{\partial}{\partial T}\right)^{-1} \nabla_{\perp}^2 A + i \frac{2\pi\beta_0}{n_0^2} \left(1 + \frac{i}{\omega_0} \frac{\partial}{\partial T}\right) P_{NL}, \quad (\text{I.1})$$

where A is the electric field complex envelope, \hat{D} the dispersion operator, α_0 the medium absorption, $T = t - \beta_1 z$ the retarded time frame, $\beta_0 = \text{Re}[k(\omega_0)] = \frac{\omega_0}{c} n_0$, where $k(\omega) = (\frac{\omega}{c}) \sqrt{\varepsilon(\omega)}$ is the complex propagation constant, $\varepsilon(\omega)$ the frequency-dependent dielectric constant, n_0 the refractive index of the medium at the angular frequency ω_0 , and P_{NL} the amplitude of the induced nonlinear polarization.

This NEE provides a powerful description of light pulse propagation by including several effects such as:

- **Linear losses** through the first right-hand term of Eq.(I.1).
- **Dispersion** through the dispersion operator which is given by

$$\hat{D} = \sum_{m=2}^{\infty} \frac{\beta_m}{m!} \left(i \frac{\partial}{\partial t}\right)^m, \quad (\text{I.2})$$

where

$$\beta_m = \text{Re} \left[(\partial^m k / \partial \omega^m)_{\omega_0} \right]. \quad (\text{I.3})$$

- **Diffraction** through the transverse Laplace operator ∇_{\perp}^2 in the third right-hand term of Eq.(I.1).
- **Space-time coupling** notably through the presence of the differential operator of the third right-hand term of Eq.(I.1). The nonlinear polarization can also be a source of space-time coupling.
- **Nonlinear effects** such as self-phase modulation (SPM) and Raman effect through the term of the amplitude induced nonlinear response P_{NL} , that will be further detailed later in the upcoming sections.

- **Self-steepening** through the presence of the differential operator of the fourth right-hand term of the Eq.(I.1).

We will now highlight the effects that are essential to grasp the physics described in later chapters.

1.2 Chromatic dispersion

Origin of the dispersion Chromatic dispersion originates from the fact that the response of a material to an electromagnetic wave depends on the optical frequency ω . In other words, the various optical frequencies propagate with different velocities in the medium. This property is represented by a frequency dependent refractive index $n(\omega)$, which far from the medium resonance, can be well approximated by the Sellmeier equation [Marcuse 82]:

$$n^2(\omega) = 1 + \sum_{j=1}^m \frac{B_j \omega_j^2}{\omega_j^2 - \omega^2}, \quad (\text{I.4})$$

where ω_j is the resonance frequency and B_j is the strength of the j th resonance. The interaction between an electromagnetic wave and the medium is represented by an induced polarisation \mathbf{P} that is related to the electric field as well as the material response as shown below:

$$\mathbf{P} = \varepsilon_0 \chi^{(1)} \cdot \mathbf{E}, \quad (\text{I.5})$$

where ε_0 is the vacuum permittivity and χ the material susceptibility that depends on the optical frequency which describes the material response. The refractive index can be expressed in terms of the susceptibility by the following relation:

$$n(\omega) = 1 + \frac{1}{2} \Re e(\tilde{\chi}^{(1)}(\omega)). \quad (\text{I.6})$$

Mathematically, dispersion can be accounted for by expanding the propagation constant β in Taylor series around the central frequency ω_0 :

$$\beta(\omega) = n(\omega) \frac{\omega}{c} = \beta_0 + (\omega - \omega_0) \beta_1 + \frac{1}{2} (\omega - \omega_0)^2 \beta_2 + \frac{1}{6} (\omega - \omega_0)^3 \beta_3 + \dots, \quad (\text{I.7})$$

where

$\beta_1 = \frac{\partial \beta}{\partial \omega}$ (ps.m⁻¹): inverse of the group velocity v_g of the pulse.

$\beta_2 = \frac{\partial^2 \beta}{\partial \omega^2}$ (ps².m⁻¹): group velocity dispersion (GVD) which is the derivative of β_1 as a function of ω .

$\beta_3 = \frac{\partial^3 \beta}{\partial \omega^3}$ (ps³.m⁻¹): third-order dispersion (TOD).

$\beta_n = \frac{\partial^n \beta}{\partial \omega^n}$ (psⁿ.m⁻¹): n th order dispersion.

Each of the dispersion terms expressed above has a different effect on the pulse propagation, as discussed hereafter.

Impact of the dispersion on the temporal pulse shape In order to understand the effect of dispersion on the optical pulse, only dispersion effects up to the third-order are considered in the NEE equation, so that it becomes:

$$\frac{\partial A}{\partial z} = -\frac{i\beta_2}{2} \frac{\partial^2 A}{\partial t^2} + \frac{i\beta_3}{6} \frac{\partial^3 A}{\partial t^3}. \quad (\text{I.8})$$

Such an equation exhibits the following solution in the spectral domain:

$$\tilde{A}(z, \omega) = \tilde{A}(0, \omega) \exp \left[i \left(\frac{1}{2} \beta_2 \omega^2 + \frac{1}{6} \beta_3 \omega^3 \right) z \right]. \quad (\text{I.9})$$

From this spectral amplitude, we can notice that the spectral profile of the pulse is not modified by the dispersion. However, the spectral phase $\psi(\omega)$ is affected. In order to better understand what is happening, we introduce the group delay $T(\omega)$ that describes the delay of a frequency component with respect to the central frequency ω_0 , after propagation inside a medium. It is obtained by the derivative of the spectral phase acquired during propagation as a function of the angular frequency $T(\omega) = \frac{\partial \psi}{\partial \omega}(\omega, t)$. This gives the following three relations for the first, second, and third-order dispersion terms:

$$\begin{cases} T_1(\omega) = \beta_1 z & (\text{I.10a}) \\ T_2(\omega) = \beta_2 \omega z & (\text{I.10b}) \\ T_3(\omega) = \frac{1}{2} \beta_3 \omega^2 z & (\text{I.10c}) \end{cases}$$

For a quadratic phase, the delay is linear, given by [I.10b](#). To make things more visual, often a time-frequency diagram representation, called spectrogram, is used. On the spectrogram, this linear delay corresponds to a temporal translation of the pulse linearly dependent on the frequency. As a result, the temporal profile of the pulse is modified while the spectral profile of the pulse is unchanged, as shown in [figure I.1 \(b\)](#). For a Fourier transform limited (FTL) pulse propagating in a dispersive medium, this results in a temporal broadening and thus to a reduction of the peak power. Usually when this happens, the pulse is said to be chirped. This process can be reversed by propagating the pulse in a medium introducing the opposite group delay dispersion (GDD). Similarly, the group delay acquired by the pulse with a third-order dispersion is quadratic and is given by [I.10c](#). This delay is symmetric with respect to the central frequency, which means that the frequencies at the spectrum ends are shifted by the same delay. As a consequence, the temporal profile of the pulse is modulated, as shown in [figure I.1 \(c\)](#).

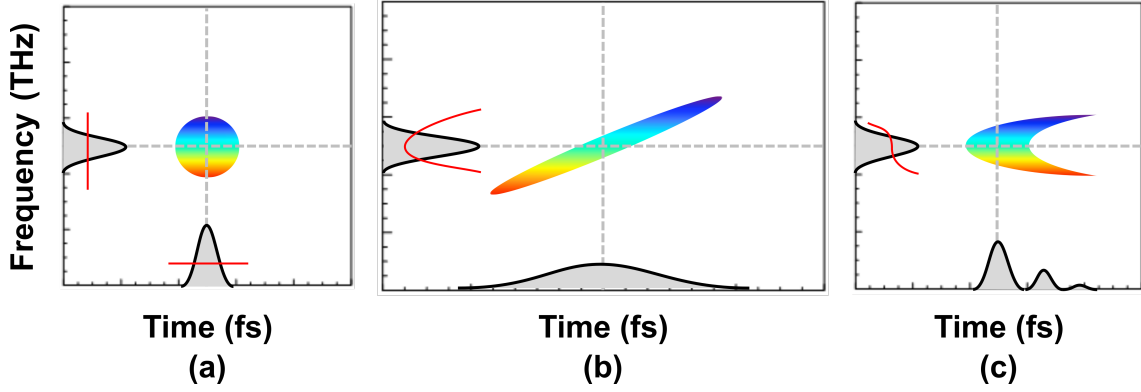


Figure I.1 – (a) Spectrogram of a FTL pulse, (b) Spectrogram of FTL pulse resulting in a dispersed (chirped) pulse after acquiring a quadratic spectral phase, (c) Spectrogram of a FTL pulse after acquiring a cubic spectral phase (or equivalently a quadratic delay) [Morin 10].

1.3 Third-order nonlinear effects

When high intensity femtosecond pulses propagate in a medium, the response of the material becomes non-harmonic and additional terms involving higher order susceptibilities are present in the polarization vector:

$$\mathbf{P} = \varepsilon_0 \chi^{(1)} \cdot \mathbf{E} + \varepsilon_0 \chi^{(2)} : \mathbf{E}\mathbf{E} + \varepsilon_0 \chi^{(3)} : \mathbf{E}\mathbf{E}\mathbf{E} + \dots, \quad (\text{I.11})$$

where $\chi^{(1)}$ represents the linear effects and the $\chi^{(n>1)}$ are higher order tensors representing the nonlinear response of the material.

In centrosymmetric materials, third-order nonlinear effects are dominant due to the absence of second order effects ($\chi^{(2)}$). Therefore, the nonlinear polarization can be expressed as follows:

$$\mathbf{P}_{\text{NL}} = \varepsilon_0 \chi^{(3)} : \mathbf{E}\mathbf{E}\mathbf{E}. \quad (\text{I.12})$$

In the following, we introduce the main consequences of third-order nonlinear effects that will be central to the experiments presented in later chapters.

1.3.1 Optical Kerr effect

One of the well-known third-order nonlinear effect is the so called optical Kerr effect. It originates from the intensity dependence of the refractive index of the material. The dependency of the refractive index n on the intensity of the input field I can be expressed by:

$$n = n_0 + n_2 I, \quad (\text{I.13})$$

with

$$n_2 = \frac{3}{8n_0} \Re(\chi^{(3)}), \quad (\text{I.14})$$

where n_0 is the linear refractive index, and n_2 the nonlinear refractive index.

The order of magnitude of the nonlinear refractive index n_2 is 10^{-20} m²/W in solids and 10^{-23} m²/W in gases at atmospheric pressure [Saleh 19].

Self-phase modulation Self-phase modulation is the nonlinear effect used to shorten the duration of laser pulses by temporal compression. This will be the subject of section 4. It has been observed for the first time in 1967 by [Shimizu 67].

If we only take into account the effect of self-phase modulation in a 1D (z, t) version of Eq.(I.1) through the last right-hand term involving the induced nonlinear polarization, the solution of the slowly varying envelope can be expressed as:

$$A(z, t) = A(0, t) \exp\left(-i \frac{n_2 \omega}{c_0} I(t) z\right). \quad (\text{I.15})$$

After a propagation of $z = L$, an additional nonlinear phase $\Delta\phi_{\max}$ is accumulated at the point of maximum intensity I_{\max} :

$$\Delta\phi_{\max} = \frac{n_2 \omega}{c_0} L I_{\max}. \quad (\text{I.16})$$

The creation of this nonlinear phase is due to the laser field itself, which is why we call this process self-phase modulation. By introducing the nonlinear phase shift into Eq.(I.15), the pulse envelope becomes

$$A_{SPM}(t) = A(t) \exp\left(-i \Delta\phi_{\max} \frac{I(t)}{I_{\max}}\right). \quad (\text{I.17})$$

From Eq.(I.17), one can notice that the effect of SPM only adds a time varying phase and keeps the amplitude of the pulse envelope unchanged. The spectrum of this envelope can be calculated by Fourier transform of $A_{SPM}(t)$. The newly added time varying phase translates into new frequency components added to the spectrum, resulting in spectral broadening. To study the evolution of the spectrum due the presence of SPM, an instantaneous frequency is defined

$$\omega_i(t) = \omega_0 + \frac{\partial\phi}{\partial t}, \quad (\text{I.18})$$

where ϕ is the phase in the time domain of the propagating pulse envelope and ω_0 the central frequency. For a Fourier transform limited pulse that experienced SPM, the instantaneous frequency is

$$\omega_i(t) - \omega_0 = -\frac{\Delta\phi_{\max}}{I_{\max}} \frac{\partial I(t)}{\partial t}. \quad (\text{I.19})$$

As the slope of the pulse envelope changes, the instantaneous frequency shifts and additional spectral components are created. The spectrogram of an initially FTL pulse after being subjected to SPM is represented in figure I.2.

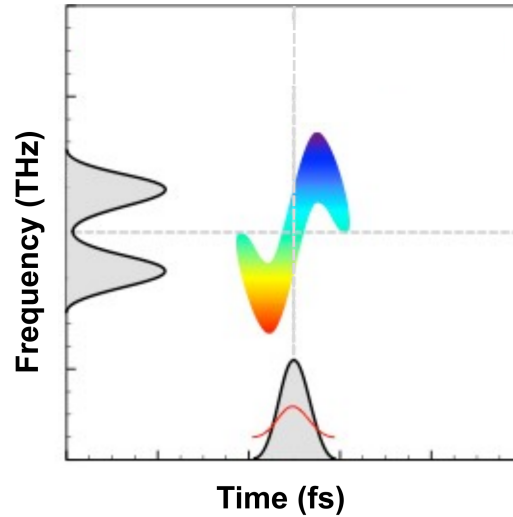


Figure I.2 – Spectrogram of a FTL pulse after acquiring an intensity dependent temporal phase due to SPM [Morin 10].

When a pulse propagates through a nonlinear medium, the accumulated nonlinear phase shift can also be expressed in terms of the so-called B-integral, which is given by:

$$B = \frac{\omega_0}{c} \int_0^L n_2(z) I(z) dz \approx \frac{2\pi n_2}{\lambda} I_0 L_{eff}, \quad (\text{I.20})$$

where $\lambda = 2\pi c/\omega_0$ the central wavelength in vacuum and I_0 the peak intensity of the input pulse, and L_{eff} the effective length of the nonlinear interaction. Spectra broadened by SPM exhibit an interesting feature with oscillating modulations. This is the result of the fact that the change of the instantaneous frequency, in the case of a Gaussian pulse, results in the generation of the same spectral components at different times, leading to spectral interference. This is illustrated in figure I.3, that shows the optical spectrum of an initially unchirped Gaussian pulse after undergoing self-phase modulation with different values of B-integral.

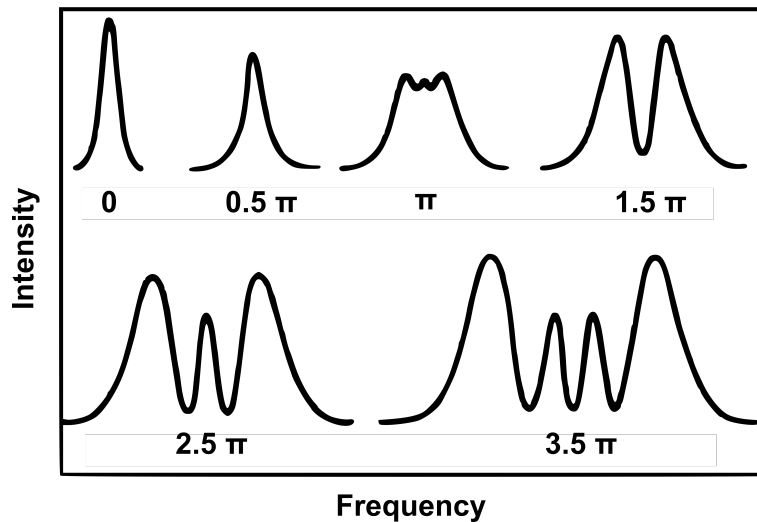


Figure I.3 – SPM-broadened spectra for an unchirped Gaussian pulse for different values of maximum nonlinear phase shift [Agrawal 13].

Self-focusing So far we have seen the impact of the intensity dependent nonlinear refractive index on the pulse spectrum and shape by the fact that it introduces a time-dependent phase shift. Another important aspect of the Kerr effect is the change of the phase over the spatial beam profile, due to a change of the refractive index that depends on the pulse intensity. At the central part of the beam profile, where the intensity is the highest, the Kerr effect is more pronounced and a larger phase shift is introduced. On the other hand, at the outer areas of the beam where the intensity is quite low, the beam experiences a very small nonlinear phase shift. This imparts a concave wavefront distortion that causes the beam to focus (for a positive nonlinear refractive index). For a Gaussian beam, this added spatial phase is nearly parabolic in the vicinity of the beam center, and becomes aberrated on the beam outer region. This effect of beam focusing is called a Kerr lens. Because the Kerr effect is instantaneous, this lens can also be pictured as time-dependent along the pulse temporal profile, which suggests the introduction of space-time couplings in the beam. For a value of the peak power denoted as the critical power, this focusing effect balances the diffraction at the waist of a given Gaussian beam. This power value is independent of the particular waist size considered. When the peak power is higher than this critical value, the beam starts to focus, leading to an increase of the intensity, which itself leads to a smaller Kerr focal length. This effect therefore causes a catastrophic collapse of the beam. It can be shown that this critical power is given by:

$$P_{crit} = \frac{\pi(0.61)^2 \lambda^2}{8n_0 n_2}. \quad (\text{I.21})$$

For example, for amorphous materials, such as fused silica, at a central wavelength of 1030 nm, the critical power is around 4 MW. However, critical powers are of the order of a few GW for gas media at atmospheric pressure. We can notice from Eq.(I.21), that only the power is relevant for this process and not the intensity. Another parameter can be taken into account in order to prevent the beam from collapsing inside a nonlinear medium even if the peak power exceeds the critical power. If the material length L is smaller than the self-focusing distance z_{sf} , the beam exits the medium before its complete collapse. If the output fluence of the beam at the output facet is below the damage threshold, no damage will occur. However, the self-focusing still modifies the geometrical properties of the beam in terms of size and divergence. The Kerr focal length f_{Kerr} and the self-focusing distance z_{sf} are given by the following expressions:

$$\left\{ \begin{array}{l} f_{Kerr} = \frac{\pi w^4}{4n_2 L P_{peak}} \\ z_{sf} = \frac{2n_0 w^2}{\lambda} \frac{1}{\sqrt{\frac{P_{peak}}{P_{crit}} - 1}} \end{array} \right. \quad (\text{I.22a})$$

$$(\text{I.22b})$$

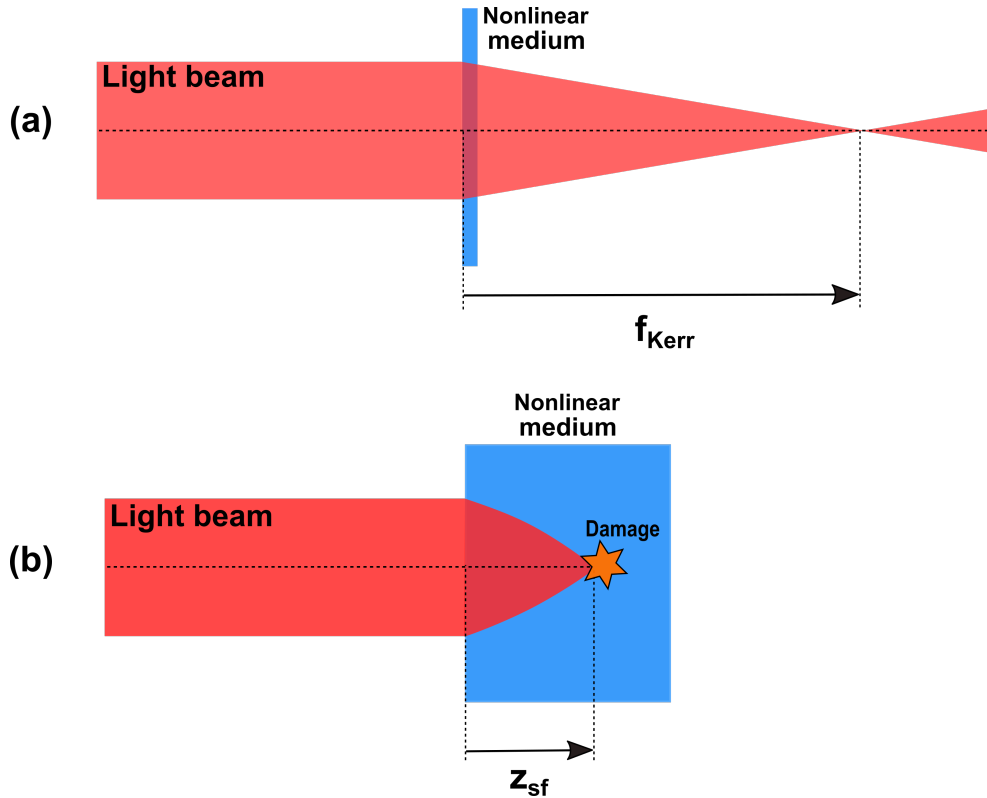


Figure I.4 – (a) Effect of the Kerr focal length, (b) Beam collapse after the self-focusing distance.

1.3.2 Self-steepening

The intensity dependent change of the nonlinear refractive index does not only change the phase velocity according to the pulse intensity, but also affects the group velocity. This is the origin of a third-order nonlinear process called Self-steepening. The high intensity central part of the pulse slows down due to the high refractive index, therefore shifting the peak slowly towards the trailing part of the pulse. The low intensity edges of the pulse, however, are unaffected. This causes a very steep trailing edge and a flattening leading edge. This is translated in the frequency domain by an asymmetrically broadened spectrum with a larger broadening on the short-wavelength side. Self-steepening can be significantly observed when the pulse duration is not much longer than the optical cycle.

1.3.3 Stimulated Raman Scattering

Raman Scattering, firstly reported in 1928 [Raman 28], is another nonlinear effect related to the third-order polarisability. It is a very important nonlinear effect used to create Raman amplifiers or tunable Raman lasers. In the process of stimulated Raman scattering (SRS), a fraction of the energy of the incident pump beam is converted into another beam with a frequency lowered by a quantity determined by the vibrational modes of the medium. It can be seen as an inelastic scattering process. An incident photon (pump) at ω_p is annihilated to create another photon at a lower frequency ω_s (Stokes photon) and a phonon with the corresponding energy.

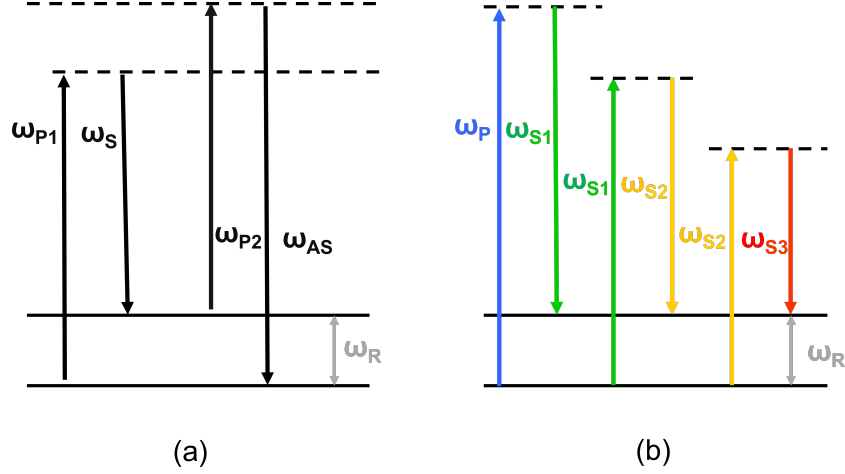


Figure I.5 – (a) Generation mechanism of the Stokes and anti-Stokes signals, (b) Generation of first, second and third Stokes signals (the dotted lines are the virtual levels of energy).

In some cases, the pump photon energy can be transferred to a higher frequency photon ω_{AS} (Anti-Stokes photon) when an adequate phonon is available. These two cases are represented in Figure I.5 (a). The spontaneous Raman scattering process is typically a weak process. However, exposing a material to a high excitation provided by an intense pump laser beam may result in a highly efficient scattering as a result of SRS.

The SRS can be seen as a vibrational contribution of a delayed Raman response, through the nonlinear response function $R(t)$ implemented in the scalar nonlinear polarization, given by

$$P_{NL}(\mathbf{r}, t) = \frac{3\epsilon_0}{4} \chi^{(3)} E(\mathbf{r}, t) \int_{-\infty}^t R(t-t') E^*(\mathbf{r}, t') E(\mathbf{r}, t') dt'. \quad (I.23)$$

The nonlinear response function $R(t)$ is expressed in Eq.(I.24) as the sum of the vibrational contribution of the delayed Raman response through the coefficient f_R , and the instantaneous electronic contribution through the term $(1 - f_R)$:

$$R(t) = (1 - f_R) \delta(t) + f_R h_R(t). \quad (I.24)$$

The response function $h_R(t)$ can be determined by the Raman gain spectrum, and an approximate form is given by:

$$h_R(t) = \frac{\tau_1^2 + \tau_2^2}{\tau_1 \tau_2^2} \exp(-t/\tau_2) \sin(t/\tau_1), \quad (I.25)$$

where τ_1 (inversely proportional to the Raman shift ω_R) and τ_2 (Raman mode dephasing time which is inversely proportional to the Raman gain linewidth) are two adjustable parameters which are chosen to provide a good fit to the actual Raman-gain spectrum of the appropriate material. Table I.1, gives an example of some SRS properties of common used Raman crystals.

Crystal	Frequency shift (cm^{-1})	Raman linewidth (cm^{-1})	Raman gain (cm/GW) @ 1064 nm	Damage threshold (GW/cm^2)
Diamond	1332.9	2.7	16	~ 80
Ba(NO ₃) ₂ (BN)	1048.6	0.4	11	~ 0.4
KGd(WO ₄) ₂ (KGW)	768	5.9	4.4	~ 10
	901	7.8	3.3	
LiIO ₃ (LI)	822	5.0	4.9	~ 0.1
YVO ₄ (YV)	890	3.0	4.5	~ 1

Table I.1 – Properties of SRS for common crystals [Basiev 99, Sabella 11].

1.4 Combination of SPM and GVD

In the previous sections, the effect of GVD and SPM on the pulse propagation were considered separately. For a more realistic description, one should consider both effects combined together. Indeed, propagating in a dispersive medium results in a change of the intensity pulse shape, as presented in section 1.2, which in turn may affect the nonlinear phase shift introduced by self-phase modulation and hence changes the way new frequencies are generated. This combination of SPM and GVD leads to some very rich observations on the evolution of the temporal and spectral shapes of the pulse.

In this context, two length scales, the dispersion length L_D and the nonlinear length L_{NL} are introduced:

$$L_D = \frac{T_0^2}{|\beta_2|} \quad (\text{I.26})$$

$$L_{NL} = \frac{1}{\gamma P_0}, \quad (\text{I.27})$$

where T_0 is the pulse duration at full width at half maximum (FWHM), the nonlinear coefficient $\gamma = n_2 \omega_0 / c A_{eff}$ where $A_{eff} = \pi w^2$ is the effective area of a Gaussian beam with a radius w , and P_0 is the incident peak power. Both lengths are related by a parameter N by:

$$N^2 = \frac{L_D}{L_{NL}} = \frac{\gamma P_0 T_0^2}{|\beta_2|}. \quad (\text{I.28})$$

This parameter N governs the relative importance of the SPM and GVD effects on pulse evolution. Dispersion dominates for $N \ll 1$ while SPM dominates for $N \gg 1$, and for $N \simeq 1$ both effects must be taken into account.

1.4.1 Wave breaking

Even for large values of N , it turns out that the effect of GVD cannot be completely neglected, since the combination of a large amount of SPM-induced frequency chirp imposed on the pulse and the effect of GVD leads to significant pulse shaping, or to the so-called optical wave breaking. It is a nonlinear phenomenon observed in the context of nonlinear fiber optics in the

normal dispersion regime ($\beta_2 > 0$), that involves the interplay between GVD and SPM. The first experimental observation of this effect was done by Tomlinson et al. in 1985 [Tomlinson 85]. This effect of optical wave breaking makes a strong-intensity pulse broaden and change its shape toward an almost rectangular form with a linear frequency chirp variation over most of the pulse. A chirp is imposed by GVD and SPM on the pulse propagating along a fiber. A qualitative understanding of wave breaking can be grasped by considering separately the chirps imparted by GVD and SPM alone. The induced frequency chirp by the GVD of the medium is given by:

$$\delta\omega_{GVD}(T) = -\frac{\partial\phi}{\partial T} = \frac{\text{sgn}(\beta_2)(z/L_D) T}{1 + (z/L_D)^2 T_0^2}. \quad (\text{I.29})$$

This shows that the frequency changes in a perfectly linear fashion across a Gaussian pulse. The chirp depends on the sign of β_2 . On the other hand, the SPM-induced chirp on a Gaussian pulse is given by:

$$\delta\omega_{SPM}(T) = \frac{2}{T_0} \frac{L_{\text{eff}}}{L_{\text{NL}}} \left(\frac{T}{T_0}\right) \exp\left[-\left(\frac{T}{T_0}\right)^2\right] \quad (\text{I.30})$$

This SPM-induced chirp is not strictly linear across the entire pulse. The composite chirp $\delta\omega$ of both chirps contributions has a nonmonotonic behavior across the pulse, meaning that it has a nearly linear behavior at the center part of the pulse, but a very steep transition at the edges as shown in figure I.6 (b). Therefore, the different parts of the pulse propagate at different velocities. In the case of normal GVD ($\beta_2 > 0$), the redshifted light near the leading edge of the pulse travels faster and overtakes the unshifted light in the tail of the pulse, while the opposite takes place at the trailing edge of the pulse. This gives birth to temporal interference oscillations and subsequent generation of new frequency components at the spectrum edge, resulting in an almost rectangular pulse shape [Anderson 92], as shown in figure I.6 (e) and (f). For anomalous GVD ($\beta_2 < 0$), the effect of wave breaking does not occur, since the composite chirp variation has a reversed sign across the central part of the pulse, preventing the red-shifted part of the pulse to take over the fast-moving forward tail. An experimental observation of wave breaking in a multipass cell will be presented in chapter II.

1.4.2 Soliton effects

For pulses propagating in a nonlinear medium with anomalous dispersion regime ($\beta_2 < 0$), soliton dynamics may occur. This is the case for short wave infrared (SWIR) and mid-infrared (MIR) pulses where most of the materials exhibit anomalous dispersion. When combined with the Kerr effect, anomalous dispersion leads to a very rich propagation dynamics that has been particularly studied in optical fibers [Agrawal 13]. During my Master's thesis, I participated in an experiment that used soliton dynamics in an MPC to perform self-compression of pulses in the SWIR [Jargot 18]. However, in the rest of this thesis, this propagation regime will not be relevant.

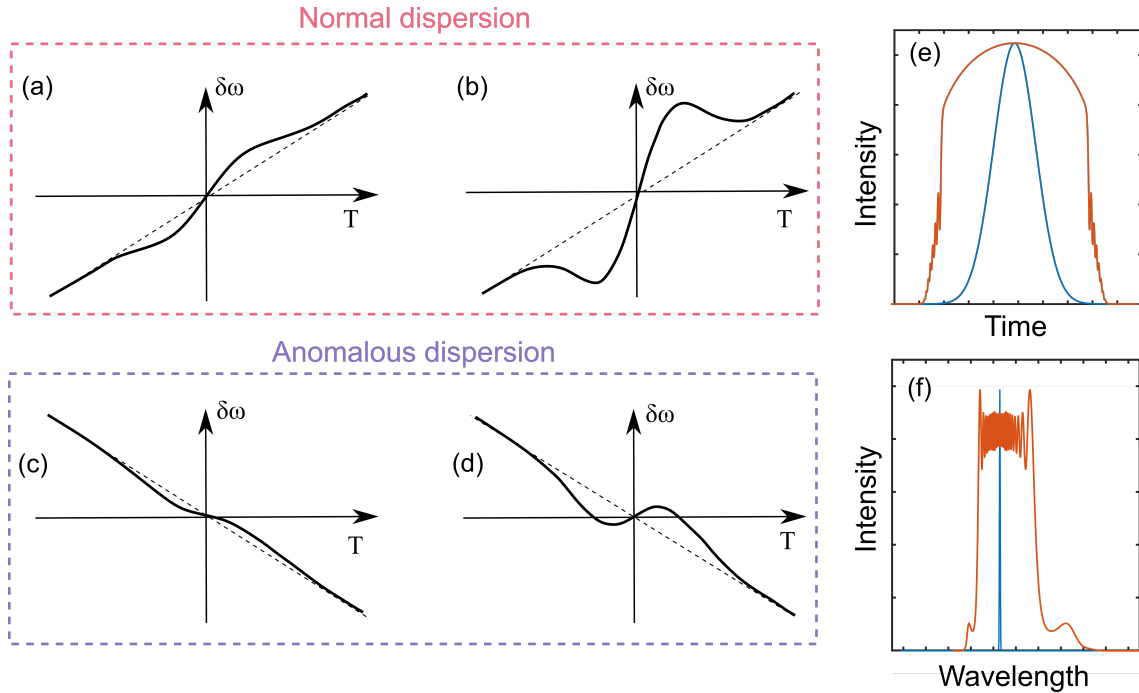


Figure I.6 – Qualitative plot of the chirp inspired by [Anderson 92]: (a) normal dispersion, weak nonlinearity; (b) normal dispersion, strong nonlinearity; (c) anomalous dispersion, weak nonlinear; and (d) anomalous dispersion, strong nonlinearity. Qualitative plot of (e) the pulse temporal profile before (blue) and after (red) wave breaking and (f) the spectral profile before (blue) and after (red) wave breaking in a normal dispersion regime.

2 Multipass cells

In this section we review the basic principles and design rules of a nonlinear multipass cell which is used in the scope of this thesis experiments, discussed in much greater details in the upcoming chapters.

2.1 Theory

A multipass cell consists of two curved mirrors facing each other in a Herriott configuration [Herriott 64], resulting in a back and forth propagation of light in the neighborhood of the optical axis of the stable periodic optical system. In such setup, the distribution of spots on the mirrors forms an elliptical pattern that is dependent on the incoming beam angle and cell geometrical configuration. In most geometries, the radius of curvature R of the mirrors are chosen to be identical and placed at a certain distance $L < 2R$ from one another, as shown in figure I.7 (a). This Herriott-type multipass cell is not a laser resonator because there is no resonance, meaning that it is used in a non-interferometric way. In other words, the rays do not return upon themselves after a certain number of roundtrips. Therefore, the beam must be aligned on a path for which the spot pattern does not overlap, so that it is possible to use small mirrors to perform input and output coupling in the MPC, as shown in figure I.7 (b), without intersecting the beam path inside the cell. For a given MPC geometry with a radius of curvature R and a distance L , there exists a beam size w_0 at the center of the MPC for which

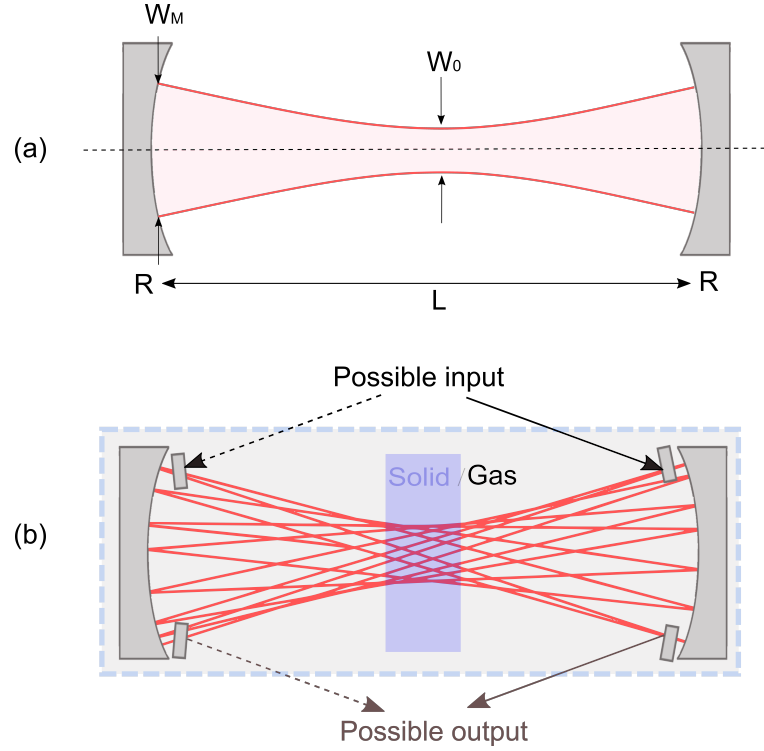


Figure I.7 – MPC symmetric geometry.

the beam size and radius of curvature evolution is periodic over one round trip. For Gaussian beam propagation, the size of the waist radius at the center w_0 and at the MPC mirrors w_M , the radius of curvature R and the distance L separating the two mirrors are related by:

$$\begin{cases} w_0 = \sqrt{\frac{\lambda L}{2\pi}} \sqrt{\frac{2R-L}{L}} & \text{(I.31a)} \\ w_M = w_0 \sqrt{\frac{2R}{2R-L}} & \text{(I.31b)} \end{cases}$$

where λ is the central wavelength.

From the above system of equation, for a fixed radius of curvature, many configurations are possible as depicted in figure I.8. For a given radius of curvature R , the maximum size of w_0 possible is obtained for a confocal configuration (i.e. $L = R$). Its minimal size is reached when the length of cavity L tends to 0 or tends to the stability limit ($L = 2R$).

Nonlinear MPCs are mainly used to increase the interaction length inside a nonlinear medium while distributing the nonlinearity over a large number of passes. Matching the input beam to the stationary beam waist ensures that the nonlinearity accumulates homogeneously over the roundtrips in the MPC, while maintaining a beam size at the mirrors and along the caustic approximately constant. In practical experiments, imperfect initial beam matching and small deviations due to nonlinear refraction can cause some periodic oscillations of the beam diameter.

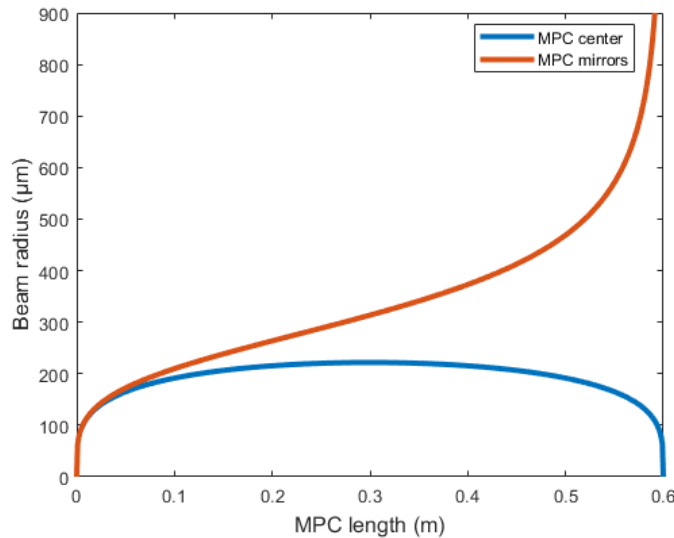


Figure I.8 – Beam radius at the center of the MPC (blue) and at the MPC mirrors (red) as a function of the MPC length for a radius of curvature of 300 mm.

2.2 Solid-state MPCs

One of the possible ways to introduce nonlinearity inside a MPC is to use a solid-state plate placed in air or vacuum chamber. In most cases, the slab of material is placed at the center of the MPC, where the size of the waist is the smallest. However, displacing the slab material from the center can help for additional nonlinearity tuning. The nonlinear medium can also be incorporated in the MPC mirror substrates, as was first demonstrated by [Schulte 16]. Most of the nonlinearity introduced by bulk MPCs originates from the bulk material due to its higher nonlinear refractive index compared to that of air, especially when its length is a few millimeters in a few tens of centimeters long MPC. Therefore, adjusting nonlinearity can be done by adapting the material thickness and the beam size inside. The nonlinearity introduced per pass, in other words the B-integral, must be kept below 1 rad in order to limit the effects of space-time coupling. This limit can be compensated by the multiple passes inside the MPC in order to achieve the necessary total B-integral. A distinct advantage of bulk MPCs is the ability to operate at peak powers beyond the critical power. This is possible by using a plate length much shorter than the self-focusing distance (z_{sf}). In [Schulte 16, Jargot 18], pulses with ten times the critical power of the nonlinear have been successfully used. This is not the case for pulses propagating in an homogeneous medium such as optical fiber.

Carefully optimizing the optical properties of the used optics such as the reflectivity of the cell mirrors and the anti-reflection coatings of the plates can provide an excellent energy throughput as high as 90% [Schulte 16, Weitenberg 17b, Weitenberg 17a]. It is also possible to determine the propagation regime by adjusting the average group-velocity dispersion through the mirror coatings and the choice of the bulk material: normal [Schulte 16, Weitenberg 17b, Weitenberg 17a] or anomalous regime [Jargot 18, Gröbmeyer 20].

For further peak power scaling, typically for femtosecond pulses with energies $> 100 \mu\text{J}$, a gaseous nonlinear medium can be used inside the MPC, as presented in the following section.

2.3 Gas-filled MPCs

Another way to introduce nonlinearity in a MPC is to place it inside a pressurized gas chamber. The propagation is quite different from that of the bulk MPCs, since the beam is always propagating inside the nonlinear medium, so the input peak power must be kept below the critical power of self-focusing, otherwise the beam will collapse. From equation (I.21), the critical power is inversely proportional to the nonlinear index n_2 which itself is proportional to the gas pressure. Therefore, the nature and the pressure of the gas used can be chosen to ensure a behaved propagation of pulses with a specific input duration and energy. The typical operation of gas-filled MPCs is at peak powers between $0.2P_{crit}$ to $0.7P_{crit}$ to ensure large enough B-integral while operating below the critical power.

Most of the gas-filled MPCs use atomic noble gases, such as argon, krypton, xenon, with a purpose at pulse compression while avoiding frequency shifting due to Raman scattering effect present in molecular gases. The design rules of such setups was first described quantitatively by [Hanna 17], and followed by the first experimental demonstration described in [Ueffing 18b]. For a given input peak power, the critical power of self-focusing will limit the pressure of the noble gas in use. Two other limitations are taken into account when designing the MPC geometry: gas ionization and optical damage on the MPC mirrors. These phenomena impose a minimal waist size at the center and at the MPC mirrors, leading in most experiments to the use of cells with near concentric geometries ($L \approx 2R$). In such a geometry, the beam size decreases at the waist and expands rapidly at the MPC mirrors. For a given radius of curvature R , if both limitations cannot be reduced, the radius of curvature R as well as the length L of MPC must be increased. Therefore, MPCs designed for high energy in the 100 mJ range tend to be of the order of 10 m-long as reported in [Kaumanns 21]. Additional discussion of energy scaling can be found in [Kaumanns 20].

Similar to bulk MPCs, dispersion control can be performed. For example, negative dispersion through mirror coatings can be introduced in order to compensate for the excess of positive GVD of noble gases (in the visible and near infrared region), which can limit the spectral broadening, if high pressures are used for moderate pulse energies (100 μ J - 1 mJ).

3 Numerical models for pulse propagation

In order to deeply understand and depict the physics of nonlinear pulse propagation in MPCs, several numerical models can be adapted with a certain computational complexity depending on the problem parameters.

3.1 3D model

A three-dimensional description of the optical field $E(x, y, t)$ propagating along the axis z of the MPC is the most complete numerical simulation of propagation. Two different approaches have been used: the use of generalized envelope equation [Hanna 17], such as Eq.(I.1), and unidirectional pulse propagation equation [Mei 21]. In these models, many physical phenomena can be taken into account, including wavelength-dependent diffraction effects, dispersion to all orders, and nonlinear effects such as SPM, self-focusing, self-steepening, Raman scattering,

ionization, and plasma-related effects. Dispersion as well as the reflectivity of the MPC mirrors can be easily included in these models, since they can affect the dynamic of propagation. However, using a complete 3D model can be quite demanding in terms of computational time, leaving it unpractical to describe simpler cases. For example, for temporally-stretched short pulse or in highly divergent beam configurations (in a near concentric MPC), the temporal and spatial grid size must be adapted and largely expanded. This allows to cover the whole beam size and its divergence in the spatial domain and its initial spectrum and stretched-pulse duration in the temporal domain.

3.2 2D model

A simplified 2D version model can be used, when a radial symmetry is present. This is the case of most beams propagating in a nonlinear MPC. Due to this radial symmetry a full description of the field propagation in 2D $E(r, t)$ is possible. In this model a use of quasi-discrete Hankel transform [Guizar-Sicairos 04] is necessary to tackle and transform the field between the direct and the frequency domain in space, while fast Fourier transform is used in the time domain. An accurate description of spatio-temporal couplings can be obtained by using this approach, and it is necessary for nonlinear propagation affecting the space-time structure of the beam, such as in MPCs where stimulated Raman scattering is performed, as will be discussed in chapter IV.

3.3 1D model

Even a simpler approach, describing the field in the time domain $E(t)$ can be adapted for cases where spatio-temporal couplings can be neglected. This approach is often applied in a similar fashion in optical fiber due to the one-dimensional nature of light propagation. A version of this model is described in [Hanna 20] where it was used to understand and reproduce experimental observations of parasitic nonlinear effects such as four-wave mixing in a MPC. It is based on a split-step method that propagates the field in time using a generalized nonlinear Schrödinger equation and in space using an ABCD matrix model that takes into account Kerr lensing and diffraction. It allows a very rough description of spatial effects, especially when nonlinearity, through Kerr lensing, influences the beam size and radius of curvature upon propagation in the MPC. This model is much faster in terms of computing time compared to the 3D model mentioned earlier. The lower overall nonlinearity level imparted by beam imperfections can be easily taken into account through the use of an M^2 beam quality factor.

Another simplified 1D model can be applied when the nonlinearity is low enough to essentially preserve the beam Gaussian shape and caustic evolution. The nonlinearity can be considered to be constant by averaging the beam size along the beam caustic, thus obtaining an effective area. This can be translated into describing the propagation into MPCs by an equivalent waveguide for the different MPC configurations.

Hereunder, a brief description of the model is presented assuming a Gaussian beam shape and propagation. In the case of MPC including a thin plate of nonlinear medium, as shown in figure I.9 (a), the nonlinearity is considered to be solely introduced by the nonlinear medium, since

the nonlinearity in gas is three order of magnitude lower than that of bulk media. In addition, the beam size inside the material is considered constant if the thickness is much less than the Rayleigh length. Taking both approximations into consideration leads to an equivalent waveguide with an effective area πw_{NL}^2 and a length given by $2N_{rt}z_{NL}$, where w_{NL} the beam waist inside the nonlinear medium, N_{rt} the number of round trips, z_{NL} the thickness of the medium, and n_2 the same nonlinear index as the bulk material. For a gas-filled symmetric two-mirror MPC, with a radius of curvature R , a distance L between the MPC mirrors, a nonlinear index n_2 and a dispersion β_2 of the gas, as shown in figure I.9 (b), the effective area of the equivalent waveguide can be obtained first by expressing the averaged B-integral over the beam profile after one trip in the MPC as

$$B(L) = \frac{4\pi n_2 P_{peak}}{\lambda^2} \operatorname{atan} \left(\sqrt{\frac{L}{2R-L}} \right), \quad (\text{I.32})$$

where P_{peak} the peak power, and M^2 is the beam quality factor of the input beam.

In the case of an equivalent waveguide to a MPC of the same total propagation length, the averaged B-integral over the beam profile for a Gaussian mode can be given by

$$B(z) = \gamma P_{peak} z, \quad (\text{I.33})$$

with $\gamma = \frac{n_2 \omega_0}{c A_{eff}}$.

By identification between (I.32) and (I.33) with $z = L$, we can find that the equivalent effective area can be expressed by

$$A_{eff} = M^2 \frac{\lambda L}{2 \operatorname{atan} \left(\sqrt{\frac{L}{2R-L}} \right)}. \quad (\text{I.34})$$

This equivalent waveguide has the same overall length $2N_{rt}L$, same nonlinear index n_2 and same dispersion β_2 as the initial MPC if the mirror dispersion is added as an additional discrete contribution at each propagation length L .

The last MPC geometry that we consider is that of a $4f$ configuration, shown in figure I.9 and used in [Ueffing 18b]. By using the same approach as in [Hanna 17], the B-integral, averaged over the beam transverse profile, accumulated over one round trip can be given by

$$B = \frac{P_{peak}}{M^2 P_{crit}} \frac{\pi^2}{4}, \quad (\text{I.35})$$

where $P_{crit} = \lambda^2/8n_2$ the critical power for self-focusing in the gas medium. By using the same identification method as the one used to obtain (I.34), the equivalent effective area of a $4f$ configuration is

$$A_{eff} = M^2 \frac{2\lambda L}{\pi}. \quad (\text{I.36})$$

We found interesting to compare numerical results obtained the 1D model with the ones obtained with a full 3D model, to test its validity. The 3D model used is described in [Hanna 17], which is based on an envelope equation [Brabec 97] solved with the split-step approach. In addition to diffraction, dispersion to all orders, and the instantaneous Kerr effect, this model includes self-steepening. The 1D model is a standard split-step algorithm commonly used to

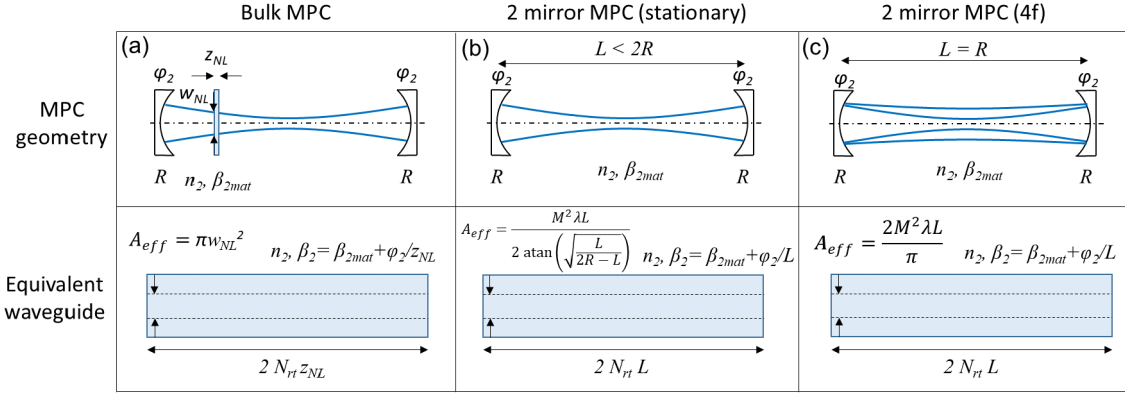


Figure I.9 – Summary of equivalent waveguide parameters for three MPC geometries for three MPC geometries: (a) bulk medium, (b) stationary gas-filled MPC, (c) 4f gas-filled MPC.

represent propagation in single mode fibers except for diffraction. It incorporates all of the same effects as the 3D model. To begin, we compare the 3D and 1D models for a set of parameters that are similar to the experimental setup given in [Lavenu 18]. The MPC presents a near confocal geometry with a radius of curvature of 300 mm, and a cell length of 290 mm filled with 1 bar of xenon, which its nonlinear index is given by $n_2 = 5.2 \times 10^{-23} \text{ m}^2/\text{W}$ [Wahlstrand 12]. The input pulses possess a Gaussian profile in time and space with a 300 fs pulse duration and 150 μJ energy. The beam propagates 35 roundtrips in the MPC. This corresponds to a P_{peak}/P_{crit} ratio of 0.18.

A grid size of $64 \times 64 \times 256$ in the space/time domain with steps $dx = dy = 30 \mu\text{m}$, $dt = 10 \text{ fs}$, and $dz = 12 \text{ mm}$ in the propagation direction. For these parameters, the equivalent effective area of the 1D model is $A_{eff} = 0.19 \text{ mm}^2$. The results obtained are illustrated in figure I.10. We can see that at this level of nonlinearity the 1D model quantitatively reproduces the results of the 3D model at a much reduced computational time. However, there is a slight underestimation of the spectral broadening obtained with the 1D model, which will be explained hereunder.

In a second comparison, the xenon-filled cell is chosen to have a near concentric geometry with a radius of curvature of 300 mm and a cell length 551 mm. The choice of such parameters is made in order to match the experimental parameters of the setup used in chapter II. In this case, 350 fs, 200 μJ input pulses are propagated for 5 roundtrips inside the MPC, with a Gaussian shape in time and space. This low number of roundtrips is chosen in order to facilitate the comparison of the caustic evolution in both models. A pressure of 0.5 bar and 3 bar are considered, corresponding to a ratio of $P_{peak}/P_{crit} = 0.1$ and $P_{peak}/P_{crit} = 0.6$, respectively. This time the 3D model is implemented on a grid size of $128 \times 128 \times 256$ in the space/time domain with steps $dx = dy = 50 \mu\text{m}$, $dt = 10 \text{ fs}$, and $dz = 5.6 \text{ mm}$ in the propagation direction. In the 1D model, this is equivalent to an effective area of $A_{eff} = 0.22 \text{ mm}^2$. From the results obtained in figure I.11, the 1D model follows very closely the 3D model at low nonlinearity. The reason for that behavior is that the caustic evolution during propagation is unmodified by the spatial Kerr effect, as shown in figure I.11 (top). However, at high level of nonlinearity, the Kerr lens modifies the caustic evolution from the stationary case and resulting in an oscillation of the beam size with respect to the unperturbed evolution. In addition, the first pass shows a

beam waist smaller than in the linear case. This results in higher level of nonlinearity than the 1D model predicts, as illustrated in figure I.11 (middle). Thus, the output spectrum is broader for the 3D model than for the 1D model, as shown in figure I.11 (bottom). These observations appear at levels of nonlinearity that are higher than most of the experimental reports, making the 1D model suited for design purposes.

Using the 3D simulation showed no spatio-spectral intensity couplings at 3 bar of xenon, i.e. at high level of nonlinearity, despite the beam size modification by the Kerr effect. The surprisingly low spatio-spectral couplings was also reported experimentally in [Kaumanns 18], where it was revealed by an imaging spectrometer measurement. Despite the rudimentary character of such simplified models compared to real spatio-temporal propagation description, these 1D models are useful design tools to accurately predict the temporal and spectral properties of the output pulse of nearly Gaussian beams. In chapter II, this simplified 1D numerical model is tested and compared with experiment results obtained in a near-concentric MPC at increasing nonlinearity level.

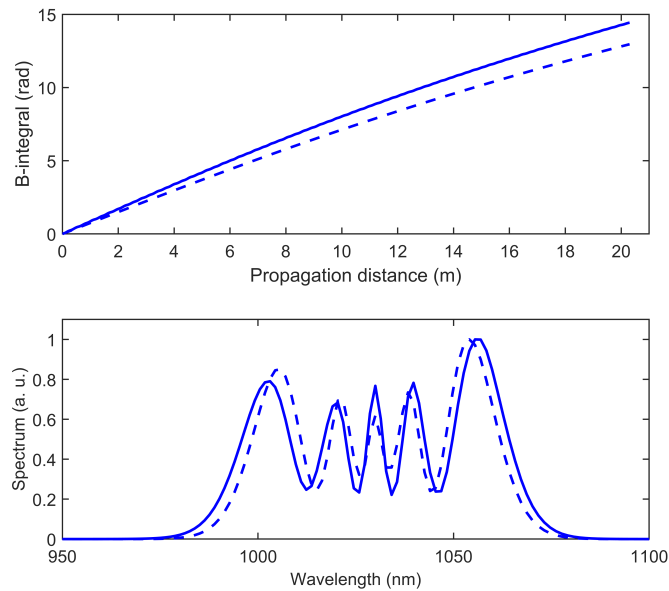


Figure I.10 – Top: B-integral as a function of distance in the near confocal MPC for a xenon pressure of 1 bar. Bottom: Spectrum at the output of the MPC. The solid lines correspond the 3D simulation and the dashed lines to the 1D simulation for $P_{peak}/P_{crit} = 0.18$.

A thing to note here, is that the difference between the 3D model and the 1D model results, observed in figure I.10 and I.11 can be reduced by using the ABCD approach 1D hybrid model mentioned earlier and described in greater details in [Hanna 20]. This hybrid model allows us to include the influence of a non perfect Gaussian beam caustic evolution on the nonlinearity. Compared to the 1D capillary equivalent model, using the hybrid model permits a better description of highly nonlinear propagation in MPCs as long as the beam remains Gaussian with no significantly induced space-time couplings, while negligibly affecting the computational cost. Therefore, the hybrid model enables a more realistic prediction of mirror damage and gas ionization thresholds, since the nonlinear caustic evolution deviates significantly from the

linear stationary beam evolution affecting the maximum fluence at the mirrors or the intensity in the gas.

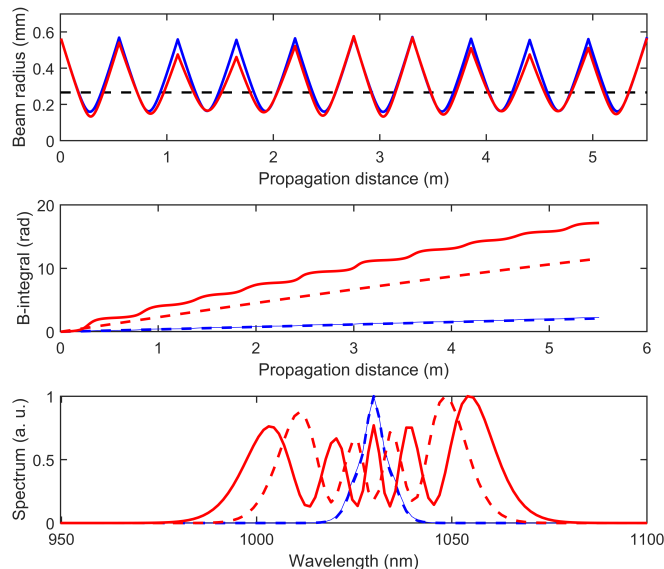


Figure I.11 – Top: beam radius as a function of distance in the near concentric MPC for a xenon pressure of 0.5 bar (blue) and 3 bar (red). The black dashed line corresponds to the equivalent waveguide beam radius. Middle: B-integral as a function of distance in the MPC for a xenon pressure of 0.5 bar (blue) and 3 bar (red). The solid line is the 3D simulation and the dashed line is the 1D simulation. Bottom: Spectrum at the output of the MPC for a xenon pressure of 0.5 bar (blue) and 3 bar (red). The solid line is the 3D simulation and the dashed line is the 1D simulation. The blue curves correspond to the $P_{peak}/P_{crit} = 0.1$ and the red curves to the $P_{peak}/P_{crit} = 0.6$.

4 Nonlinear temporal compression

Nonlinear multipass cells are known for their particular use in the context of temporal compression, rapidly affecting the MPC development theoretically and practically. Therefore, in this section we review the principles behind nonlinear temporal compression, with a reminder of the conventional techniques used, and finishing by the state of the art of the experimental results obtained so far in MPCs.

4.1 Principle

Nonlinear temporal compression, often referred to as post compression, is a technique used in order to temporally compress laser pulses after amplification, to attain down to few-cycle durations. The shortest possible pulse duration that can be obtained is determined by the Fourier-transform relation (I.37), where Δt is the pulse duration at FWHM, $\Delta\omega$ denotes the spectral bandwidth at FWHM, and K a constant where its value depends on the pulse temporal

profile. For a Gaussian pulse $K = 0.441$.

$$\Delta t \cdot \Delta \omega \geq K. \quad (\text{I.37})$$

From this relation, for a given spectrum, the pulse duration has a minimum value when (I.37) becomes equality. Therefore, the generation of few-cycle pulses can be achieved if the spectrum is sufficiently broad and the spectral phase should be nearly constant (flat) across the entire spectrum. Due to the restricted widths of the energy levels of the amplifying medium, the gain bandwidth of most commonly used lasers is narrow, therefore a spectral broadening of their pulses is needed in order to compress them even more. Further spectral broadening can be obtained by interaction of intense light pulses with a nonlinear propagation medium. Such interactions lead to the emergence of new spectral components due to nonlinear phase distortion. In this process, the spectrum broadens but the pulse temporal profile does not change much, resulting in a phase-modulated pulse (chirped) with a much shorter transform-limited duration. A proper chirp management can be applied and brings back all the spectral components in phase, resulting in a constant spectral phase. On that account, most post compression techniques rely on two steps: spectral broadening and subsequent chirp compensation.

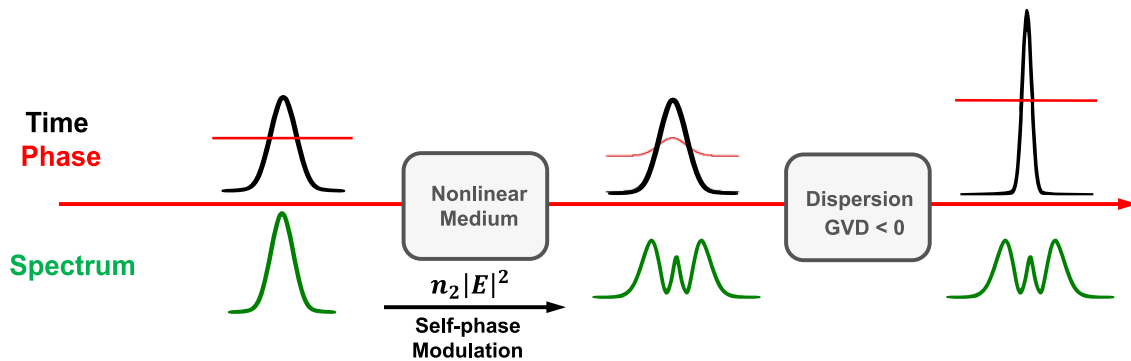


Figure I.12 – The different stages of nonlinear pulse compression.

Spectral broadening is typically achieved by self-phase modulation driven by the optical Kerr-effect, as discussed in section 1.3.1. This spectral broadening approach was first introduced in the context of post compression by [Fisher 69], where a grating pair was used for chirp compensation. The chirp management can be done in several ways depending on the pulse characteristics (duration, spectral bandwidth, and central wavelength). Most post compressors aiming to reach few cycle pulse durations use chirped mirrors with additional wedge pair for continuous tuning of the chirp. Precise chirp management can be achieved by incorporating TOD compensation through a combination of bulk materials with different ratios of the GDD to the TOD. Some post compression setups even include pulse shapers or pulse synthesizers.

4.2 Free propagation in bulk

One of the simplest ways to perform spectral broadening is to propagate in free space in an homogeneous nonlinear medium. The first compression experiment of high-energy fs pulses in a bulk medium was reported by [Rolland 88]. The pulse duration varied between 9 to 24 fs

with 7 to 110 μJ by filtering out the low-intensity wings of the beam. However, this technique is rapidly limited by the amount of nonlinearity that can be achieved in order to minimize the appearance of spatio-spectral inhomogeneity and material damage due to self-focusing. Spatio-spectral inhomogeneity is related to the fact that spectral broadening is proportional to the B-integral which itself depends on the beam intensity profile. If the beam intensity is not uniform across the beam profile, this leads to a variation of the spectral broadening, resulting in a broader spectrum at the center than on the edges in case of a Gaussian beam for example. Furthermore, if the peak power is higher than the critical power then the beam will be subjected to self-focusing. A way to mitigate these two limiting effects, is to distribute the nonlinear propagation into small steps each introducing a moderate amount of B-integral and separated by careful beam filtering.

4.3 Multiplate

In 2000, an idea of using a periodic arrangement of focusing elements and nonlinear media to limit the spatial Kerr effect was proposed [Milosevic 00]. This theoretical concept is at the origin of the experimental results of nonlinear temporal compression first using multiplate setups, then in multipass cells, first reported in 2016 by [Schulte 16]. Based on this concept, the work done in [Lu 14] proposed to use very thin glass plates (0.05-0.5 mm), placed in an intense converging beam ($\sim 2 \text{ TW}/\text{cm}^2$). The peak power in the plate is several hundred times the critical power, the beam starts to self-focus. Since the plates are very thin, the beam exists the material without collapsing and focuses in the air just after exiting the plate. After the beam focus, another plate is placed into the divergent beam which will be subjected again to the effect of self-focusing and focused in the next plate. With such multiple plates arrangement a supercontinuum can be obtained since the B-integral introduced at each plate can reach 4-5 rad [Cheng 16, He 17], as a consequence, very large compression factors down to the single cycle limit can be achieved [Lu 19]. Although such pulse duration compressors can be efficient, stable, robust on a compact footprint, they are limited in energy scalability (sub-mJ regime), as they rely on condensed materials with high nonlinearity, and small amount of remaining spatial chirp in the output beam can be observed [Lu 18].

4.4 Waveguides

Spectral broadening can also be achieved by propagating the pulse in a waveguide structure such as optical fibers and capillaries. Using waveguides as a Kerr medium overcomes the problems of free-propagation mentioned earlier in section 4.2. The spatial beam shape in waveguides is maintained constant during its propagation, resulting in high intensity over a long interaction length. This allows the accumulation of a large B-integral, resulting in a much larger spectral broadening. This accumulation of large nonlinear phase compensates the necessity to operate below the critical power of self-focusing. Depending on the input pulse parameters, in particular the input peak power, the waveguide nature is adapted.

Silica fiber have been successfully used to compress pulses with energies of the order of a few microjoules, for input peak power below the self-focusing threshold in silica (around 4 MW)

[Südmeyer 03, Jocher 12]. Due to the silica nature of the solid core, the nonlinear refractive index is high, making them a good candidates to compress low energetic pulses with a high compression factor. For pulse energies in the 1 to 100 μJ range, large hollow core fibers such as Kagome [Emaury 13, Guichard 15] are used. In such waveguides, gas injected into the core serves as the nonlinear medium with adjustable nonlinearity provided by the choice of the gas and its pressure but mostly requiring a long propagation distance. Recently, in this same energy range, antiresonant cladding designs [Köttig 20] are also employed.

For pulse energies higher than 100 μJ , the use of gas-filled dielectric hollow capillaries is necessary [Nisoli 97, Park 09]. A pulse energy up to 40 mJ is reached after nonlinear temporal compression using a 3 m long gas-filled hollow core fiber, resulting in a record peak power of 1.3 TW for Yb-based laser sources, as demonstrated recently in [Fan 21]. This boost in energy scaling for capillaries was made possible by combining the reduced nonlinear refractive index provided by the gas nature compared to those of silica cores, and a large mode area that is increased by a large factor (typical core diameters of a few hundreds of microns). These structures are not suited for low-energy pulses due to high losses in small diameter capillaries. On the high-energy side, capillaries can be limited by ionization and their length becomes impractically long and very sensitive to bending. To operate very long capillaries, stretched capillaries setup have been developed [Nagy 21].

4.5 State of the art in MPCs

Since its first experimental demonstration in 2016, the use of nonlinear MPCs for post compression purposes increased rapidly. Many experimental demonstrations using MPCs have been performed for input pulse duration in the 200 fs to 10 ps range at a pulse energy ranging from 1 μJ to 100 mJ. The experimental achievements using MPCs to perform nonlinear temporal compression is summarized in figure I.13. In the 1-100 μJ range, MPCs incorporating one or multiple plates are used. Their use is an alternative to gas-filled hollow core fibers, alleviating the drawbacks of poor polarization maintenance, moderate throughput due to confinement losses, and the lack of robustness against the beam pointing instabilities at high power or energy levels often present in hollow core fiber (HCF) systems. In the first experimental demonstration in [Schulte 16] 870 fs pulses were compressed down to 170 fs with a setup power throughput of 91%. The energy of the input pulses is 40 μJ at 10 MHz repetition rate, corresponding to an average power of 400 W. The nonlinear medium is incorporated through the MPC mirror coatings by using at the end of the mirrors substrates an AR coating on the inside and an HR coating on the outside, so that the pulses propagate inside the substrates, serving as the nonlinear medium, upon each reflection. The peak power in this experimental work surpasses ten times the critical power of fused silica. In addition, dispersion control is performed by using adapted engineering HR coatings on the MPC mirrors, in order to compensate for the dispersion introduced by propagation in the nonlinear medium.

A various number of MPCs were used since then in the same concept, compressing low energy (a few μJ) high repetition rate pulses (> 10 MHz) [Weitenberg 17b, Weitenberg 17a, Fisher 69]. In those experimental setups, the nonlinear medium is introduced by adding one or multiple plates near the MPC center. These bulk MPCs are also used to compress the duration of high

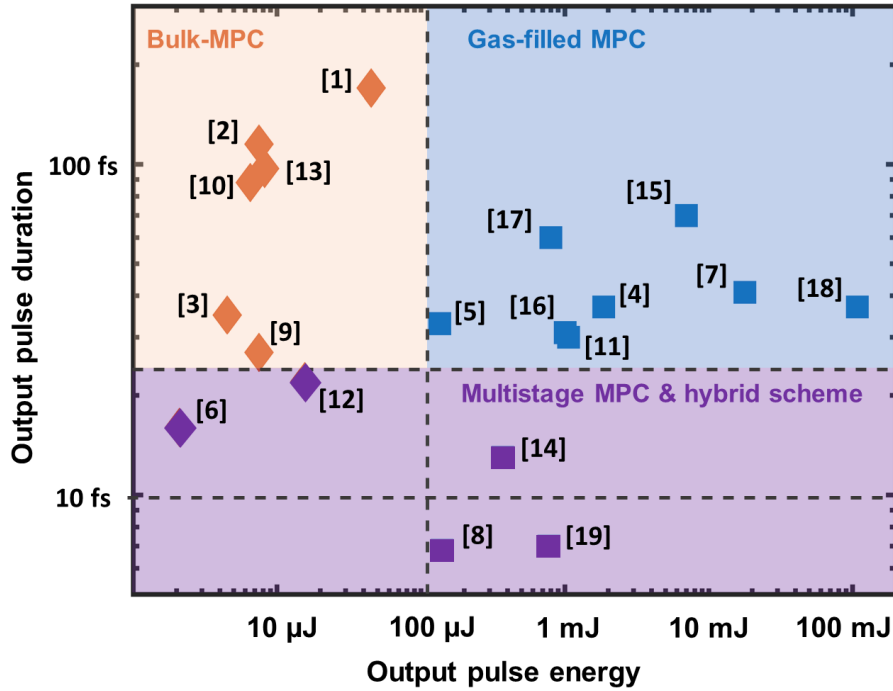


Figure I.13 – A pulse energy-duration diagrams summarizing the experimental results obtained so far: [1]-[Schulte 16]; [2]-[Weitenberg 17b]; [3]-[Weitenberg 17a]; [4]-[Ueffing 18b]; [5]-[Lavenu 18]; [6]-[Fritsch 18]; [7]-[Kaumanns 18]; [8]-[Lavenu 19a]; [9]-[Tsai 19]; [10]-[Meyer 19]; [11]-[Russbuedt 19]; [12]-[Vicentini 20]; [13]-[Meyer 20]; [14]-[Balla 20]; [15]-[Kramer 20]; [16]-[Grebing 20]; [17]-[Viotti 21]; [18]-[Kaumanns 21]; [19]-[Müller 21].

energy thin disk oscillators to reach sub-100 fs pulse durations [Meyer 19, Meyer 20]. All of the mentioned work use a single stage of MPC. However, cascading MPCs is also possible, allowing to reach a compression ratio of 21, compressing the 460 fs pulses down to 22 fs with 15 μJ output pulse energy by using two MPCs, as reported in [Vicentini 20]. It is also possible to cascade three MPCs, since the transmission of each MPC stage is high, compressing 220 fs pulses to 16 fs, while maintaining an overall throughput of 60% [Fritsch 18]. One of the latest experimental demonstration using a bulk MPC reports the compression of 10 ps pulses of a Nd:YVO₄ picosecond amplifier, allowing the generation of 172 fs pulses [Song 21]. Despite the long beam propagation distance provided by the MPC scheme, a bulk MPC was used in a carrier-envelope phase (CEP) stabilized system such as in [Natile 19].

On the high energy side ($> 100 \mu\text{J}$), a number of gas-filled MPCs have been implemented with different geometrical configurations. Most of the experiments were performed with Yb-doped material-based ultrafast laser sources. For input pulses in the 100-300 μJ range, 50 cm-long MPCs are typically used at gas pressures above the atmospheric pressure. One of the first experimental demonstrations compressed a 160 μJ 275 fs Yb-doped fiber chirped pulse amplifier down to 30 fs with a 7 bar argon-filled MPC [Lavenu 18]. For higher pulse energies ($> 1 \text{ mJ}$), larger MPCs are used since the beam size will be larger on the cell mirrors, therefore reducing possible optical damage. A 4f geometry was used in the first experimental demonstration of a gas-filled MPC [Ueffing 18b] at an input average power of 200 W, 200 fs, 2 mJ pulses

originated from an Yb:YAG thin disk laser system. This configuration allows to tune the beam caustic in the MPC in terms of the beam sizes, while maintaining a stationary behavior over one roundtrip. This setup leads to an output pulse duration of 37 fs with an efficiency of 93%.

Several experimental demonstrations illustrated the average power scaling capabilities in MPCs in the 1 to 10 mJ pulse energy range. Output power levels reached 500 W [Russbuedt 19], 700 W [Kramer 20] and 1 kW [Grebing 20] with pulse durations ranging from 30 to 70 fs. Scaling in terms of energy was also demonstrated, at 18 mJ input energy [Kaumanns 18], and at 110 mJ [Kaumanns 21], obtaining 41 fs and 37 fs pulse duration, respectively. It is worth to mention that the second experiment used a 8 m-long cell filled with 0.25 bar of argon.

Typically, nonlinear MPC-based compression experiments compress few hundreds of fs down to a few tens of fs, resulting in compression ratios of ~ 10 . Increasing the compression ratio even further was made possible by using a succession of MPCs. Few-cycle pulses were obtained after compressing 1.2 ps pulses, using 2 m-long MPC filled with Krypton [Balla 20]. However, in this work, the setup suffered from a low overall efficiency of 37%, caused by the use of enhanced metallic mirrors utilised in the second stage to cope with the large bandwidth. A way to improve the overall throughput using a hybrid two-stage architecture was proposed [Lavenu 19a]. The first stage consists of an argon-filled MPC compressing the pulse to few tens of femtosecond, while the second stage uses a gas-filled capillary with reduced losses. Using this setup, generation of few-cycle pulses with an overall setup efficiency of 61% was obtained. MPC-based compressors can also be used as a method to reach few-cycle pulse durations with high efficiency. This is made possible by using a second MPC compression stage comprising dielectrically enhanced silver mirrors with a small number of reflections [Müller 21]. The second MPC stage has a transmission of 82% which is comparable to capillary setups. The MPC is made up of numerous small curved mirrors rather than a single large-diameter mirror, which is a noteworthy characteristic of this work. Despite the non-optimal reflectivity of 98.5% of the metallic enhanced mirrors, each mirror is constructed on a silicon substrate and water-cooled, allowing an output average power of 388 W before the chirped mirrors. The results of this remarkable work show that few-cycle large average power pulses can be efficiently reached using MPC-based setups.

5 Conclusion

In this first chapter, we have introduced the basic notions necessary to understand the physical phenomena involved in the propagation of ultrashort pulses in dispersive nonlinear media. Third-order nonlinear effects such as self-phase modulation, self-focusing and stimulated Raman scattering were described and their effect on the temporal and spectral shape was also discussed. In numerical simulations all these physical phenomena are incorporated in a generalized nonlinear envelope equation.

We also viewed the theoretical description of a MPC in which nonlinearity can be introduced

either by incorporating a solid state plate or by using a gas-filled chamber at specific pressure. Bulk MPC are more adapted for pulse energies below $100 \mu\text{J}$, while providing operation at peak powers above the critical power. However, scaling the energy to higher values reaching the mJ levels, the use of gas-filled MPCs is favored.

We have seen that many numerical models can be used in order to predict the physics in a specific experiment. For a full description of the physics at play, a 3D model must be used. However, it may be unpractical with its high computational time and complexity. In some cases, 2D models can be used while providing an accurate description of spatio-temporal couplings at a reduced computational time. If spatio-temporal couplings can be neglected, simpler 1D model can be applied, for example in predicting results for nonlinear MPCs used for nonlinear temporal compression.

The principle of nonlinear temporal compression was presented with a quick presentation of the techniques used in order to introduce spectral broadening, such as solid-state optical fibers, gas-filled hollow core fibers and capillaries. Finally, an overview of the experimental demonstrations using MPC in postcompression schemes was provided. These versatile results highlight the flexibility and provided by MPCs: choice of the geometrical configuration, the nonlinear medium, and the design of the MPC mirrors. All these degrees of freedom offered by the MPC scheme is accompanied by a high transmission throughput $> 90\%$ for most reported experiments. These various degrees of freedom open the door towards using MPCs to obtain future high peak/ high average power laser sources. In the following chapter, we investigate spatio-temporal couplings inside a highly nonlinear gas-filled MPC.

Chapter II

Study of Spatio-spectral Couplings at High Nonlinearity in a Multipass Cell

Objectives

In this second chapter, we present the experimental work done in a near-concentric gas-filled MPC with the aim to study the limits in terms of spatio-spectral properties of the output beam at high level of nonlinearity. Then the results of the 1D numerical model are compared with the data collected from the experiment, depicting the observation of wave breaking. Finally, we experimentally characterize the spatio-spectral profile at the MPC output using an imaging spectrometer and a complete 3D characterization technique called INSIGHT.

Contents

1 Introduction	42
1.1 Spatio-temporal couplings in optical pulses	42
1.2 The question of spatial and spatio-temporal degradation in nonlinear MPCs	43
2 Study of a highly nonlinear MPC	46
2.1 Experimental setup	46
2.2 Observation of wave breaking and 1D model validation	49
2.3 Measurement of intensity and phase spatio-spectral profiles	51
2.3.1 Spatial and spatio-spectral characterization of the MPC output beam	51
2.3.2 Full 3D characterization of the electric field using INSIGHT	53
3 Conclusion	55

1 Introduction

1.1 Spatio-temporal couplings in optical pulses

Ultrashort laser sources are common scientific tools used in different research areas. Their ability to harness light in time by reducing the pulse duration down to femtoseconds makes them so attractive. Their use is becoming abundant in the investigation of ultrafast phenomena, such as plasma dynamics, chemical reactions and others. Moreover, ultrashort laser sources are essential for laser-matter interactions due to their ability to achieve extraordinary intensity levels in an electric light field.

Ultrashort laser beams are often described by the temporal variation of their power density and frequency (intensity and phase), and by a transverse spatial profile in the (x, y) plane normal to the direction of propagation z . Variation of the temporal/spectral properties of the pulse across this plane are called spatio-temporal/spectral couplings. In other words, spatio-temporal couplings is any property of an ultrashort laser pulse that prevents the ability to describe the spatial and temporal dependence of the electric field as a product of two separated functions. Mathematically, the following statement of the electric field is true in the presence of spatio-temporal/spectral couplings:

$$E(x, y, t) \neq f(x, y) \times g(t) \quad \forall \quad f(x, y), g(t). \quad (\text{II.1})$$

The most common source of such couplings is angular dispersion introduced by prisms or gratings frequently used in pulse compressors and stretchers which take part in every ultrashort-pulsed laser chain. Even the simplest optical elements such as lenses can also be a source of couplings due to difference in the group and phase velocities of the lens material merged with its radially varying thickness, and any other aberrations [Akturk 10].

Properly assessing the impact of spatio-temporal/spectral couplings on the properties of ultrashort lasers requires specific measurement methods that give access to the most complete three-dimensional electric field of an ultrashort laser pulse E in space and time $E(x, y, t)$, or in space and frequency $\tilde{E}(x, y, \omega)$. These two quantities are related to each other by the one dimensional Fourier transform from time to frequency. Developing metrologies to fully determine the spatio-temporal/spectral electric field is crucial because spatio-temporal/spectral couplings can have detrimental effects in some cases. They often have the effect of increasing the pulse duration and reducing the intensity at focus [Akturk 10] which might be critical for applications requiring some advanced performances, such as laser-driven particle acceleration (sensitive to peak intensity at focus), and single attosecond pulse generation (sensitive to pulse duration) [Krausz 09]. Although spatio-temporal/spectral couplings seem undesirable, they can be used as an additional pulse-beam parameter and become quite useful to tailor the pulse-beam properties, thereby achieving advanced control in laser-matter interaction processes [Vincenti 12, Sainte-Marie 17], or enhancing phase matching and nonlinear optical conversion efficiencies by introducing pulse-front tilt [Arisholm 04].

Many variety of elegant purely temporal laser diagnostics have been developed since

the late 90's allowing the measurement of the temporal evolution of the local electric field $E(t)$ of ultrashort pulses [Walmsley 09], such as: frequency-resolved optical gating (FROG) [Kane 93, Trebino 97], spectral phase interferometry for direct electric-field reconstruction (SPIDER) [Iaconis 98], self-referenced spectral interferometry (SRSI, WIZZLER device) [Oksenhendler 10], and D-Scan [Miranda 12, Loriot 13], to list a few examples. Although such temporal diagnostics may suffice to characterize laser pulses in some applications, in many others a more complete characterization is needed. Several techniques have been developed in order to obtain a spatio-temporal/spectral measurement based on different concepts: *spatially-resolved spectral interferometry* such as SEA-TADPOLE [Bowlan 06], RED-SEA-TADPOLE [Gallet 14], STARFISH [Alonso 10] and TERMITES [Pariante 16], *spectrally-resolved spatial interferometry* such as STRIPED-FISH [Gabolde 06], and INSIGHT [Borot 18], or *wavefront sensing* such as HAMSTER [Cousin 12]. Most of these techniques determine the $\tilde{E}(x, y, \omega)$ up to an unknown spatially-homogeneous spectral phase. The access to the spatio-temporal field can be calculated by a Fourier transform with respect to frequency, by performing additional temporal measurement either of a reference beam (e.g. in SEA-TADPOLE, STARFISH or STRIPED FISH) or at any point of the unknown beam (e.g. in TERMITES or HAMSTER). A complete description of the available spatio-temporal characterization of ultrashort laser beams can be found in [Jolly 20].

INSIGHT, one of the above mentioned techniques, happens to be the technique used to characterize the output beam of the experiment described in this chapter where the results are illustrated in section 2.3.2. This technique is a spatio-spectral measurement technique applied for laser sources with a repetition rate higher than 0.1 Hz. It is based on a relatively simple measurement device (figure II.1 (a)), and does not require any reference beam. INSIGHT involves spatially-resolved Fourier-transform interferometry at three positions around the focus. Using a phase retrieval algorithm this allows for reconstruction of the spatio-spectral phase in addition to the spectral amplitude already afforded by the Fourier-transform spectroscopy. Additional temporal measurement at one spatial position of the beam is required in order to reconstruct the E-field in space-time since INSIGHT is insensitive to relative phase between frequencies. This technique is employed successfully on Terawatt [Borot 18] and Petawatt lasers [Jeandet 19]. The principle behind this technique is summarized in figure II.1 and described in greater detail in [Borot 18].

1.2 The question of spatial and spatio-temporal degradation in nonlinear MPCs

As hinted at in chapter I, one of the main advantage of MPCs over single or multi-plate setups is that a large B-integral can be accumulated in the time domain while the spatial and spatio-temporal properties of the output beam remain well-behaved. The question of why this is the case, and up to what level of nonlinearity, triggered the experiment reported in this chapter.

Nonlinear interaction of an optical pulse with a medium is a well-known potential source of spatial and spatio-temporal degradations. For instance, the dependence of nonlinear inter-

action on the pulse's intensity and phase couples the pulse's spatial features to the temporal features [Akturk 10]. It has been known for a long time that the amount of B-integral per pass in a plate (e. g. a vacuum chamber window, or a laser crystal) is limited in ultrafast optics experiments by the tolerable amount of space-time couplings in the output beam to practical values below 1 rad. This is the case when it can be assumed that nonlinearity is imprinted in a single transverse plane, or equivalently over a distance much smaller than the Rayleigh length. For bulk plate-based MPCs, the B-integral per pass in the plate is therefore usually kept below 1 rad.

In gas-filled cells the physical picture is quite different. The fact that nonlinear phase is continuously accumulated while propagating over a distance that is comparable to or larger than the Rayleigh range results in a larger robustness of the beam with respect to space-time couplings than when the B-integral can be considered to be accumulated in a single transverse plane, as is the case for bulk plate-based MPCs. An intuitive picture of this effect is that spatio-temporal components of the beam/pulse are simultaneously modified by the nonlinearity and mixed by diffraction, which homogenizes the spatio-temporal field.

The physical mechanism that prevents the growth of spatial degradation and spatio-temporal couplings when a pulse propagates through its focus in a homogeneous nonlinear medium was described by Milosevic and coauthors [Milosevic 00]. Starting from a fundamental Gaussian beam, they established using coupled-mode theory that, although the pulse couples some of its energy to higher order Laguerre-Gaussian modes when propagating towards its waist due to nonlinearity, the energy flow is reversed after the waist to restore a mostly Gaussian beam after the waist. This can be interpreted in terms of a phase-mismatch due to the difference in accumulation of the Gouy phase between the fundamental and higher-order free-space modes.

Although at the present day, simulations [Ueffing 18a] and experiments [Kramer 20] have established this robustness of MPCs against spatial and spatio-temporal degradations, it was not fully established how far the nonlinearity level can be pushed in MPCs while retaining a spatio-spectral couplings-free output beam, although a clear upper bound is the critical power in the gas medium. To our knowledge there is still no definite quantitative answer, e.g. in terms of B-integral per pass or peak power to critical power ratio.

Therefore, this chapter provides a detailed description of the work published in [Daher 20b], where we implemented a gas-filled MPC with a high level of nonlinearity with a purpose to study the spatio-spectral properties of the output beam. First, we introduce the experimental setup used followed by the validation of the 1D model by comparing the obtained experimental results with the ones obtained in numerical simulation reproducing the observation of optical wave breaking effect. Finally, we represent the obtained spatio-spectral pulse characterization using an imaging spectrometer and an INSIGHT measurement at the output of the MPC for input peak power approaching the critical power.

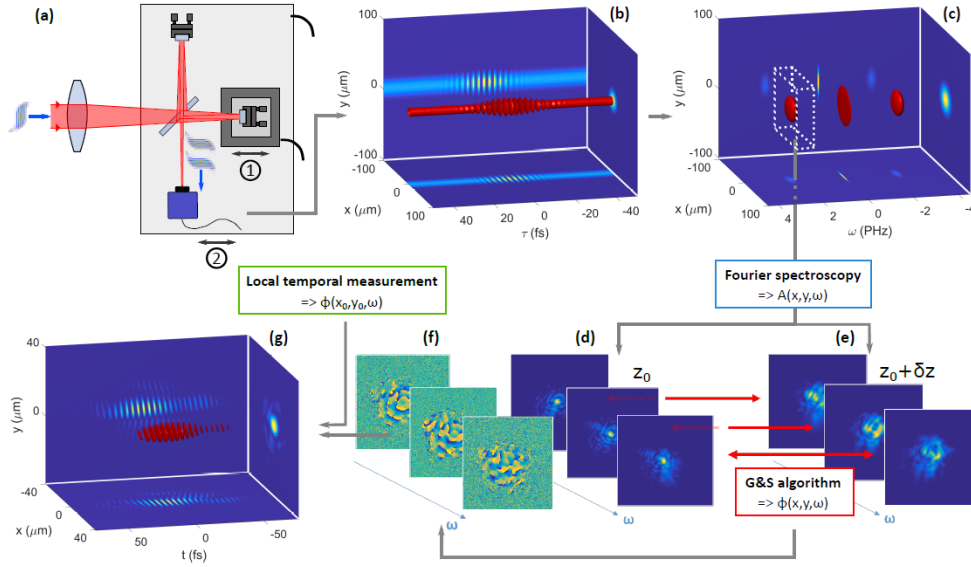


Figure II.1 – Principle and implementation of INSIGHT: (a) The laser beam to be characterized is focused onto a 2D sensor placed at the output of a simple Michelson or Mach-Zehnder interferometer. A piezoelectric stage in one arm (stage 1 in (a)) is used to scan the delay with sub-optical-period accuracy, and thus measure the spatially-resolved linear autocorrelation of the beam at best focus (longitudinal position z_0), shown on (b). The Fourier transform of this signal with respect to delay (c) is then calculated, in order to filter out (white dashed box) the spatially-resolved spectrum $A_{(z_0)}(x, y, \omega)$. This 3D dataset provides the amplitude profiles at each frequency, shown in (d). This process is repeated at two other longitudinal positions near focus $z_0 \pm \delta z$ by shifting the interferometer (stage 2 in (a)), or equivalently the focusing or imaging optics, in the direction of the incoming beam, thus providing the spectrally-resolved spatial amplitudes $A_{(z_0 \pm \delta z)}(x, y, \omega)$ at $z_0 \pm \delta z$. For illustration, panel (e) displays $A_{(z_0 \pm \delta z)}(x, y, \omega)$ only. A Gerchberg Saxton-like phase retrieval algorithm is then applied on each group of amplitudes in order to extract the spatial phase at each frequency, examples of which are shown in (f). INSIGHT provides the spatio-spectral field up to an unknown spatially-homogeneous spectral phase, since the measurement is blind to the evolution of phase with frequency. This unknown can be lifted by an independent measurement of the spectral phase at one position in the beam. Once this is done, a Fourier transformation with respect to ω is performed to obtain the field $E(x, y, t)$ in space-time, the real part of which is shown on (g) [Borot 18].

2 Study of a highly nonlinear MPC

2.1 Experimental setup

Laser system The experimental setup used in this part of study is shown in figure II.2. The laser system used is an Ytterbium-doped fiber amplifier delivering a maximum input pulse of $200 \mu\text{J}$ energy at a central wavelength of 1030 nm at 150 kHz repetition rate. This corresponds to a maximum average power of 30 W. The input pulse sent to the MPC setup is presented in the FROG measurement in figure II.3. Its duration is 300 fs at FWHM with a 7 nm spectral width at FWHM. In order to compare the spectral width with the ones obtained at the output of the MPC, it is better to express the spectral width at -10 dB (i.e. at 10%), since after experiencing self-phase modulation the spectrum will no longer be Gaussian at the output of the MPC. In this case, the spectral width of the laser is 12 nm at -10 dB. The laser has a measured spatial beam quality factor M^2 of 1.2×1.2 along the two orthogonal axes.

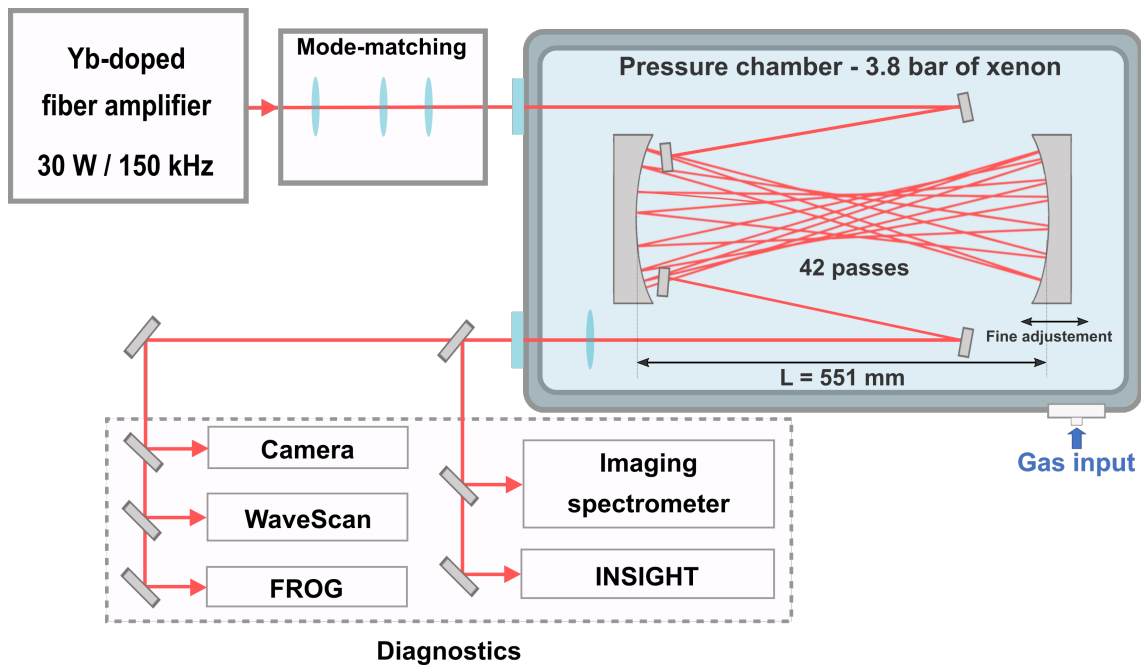


Figure II.2 – Experimental setup used in the study of the spatio-spectral couplings at the output of a xenon-filled MPC.

MPC configuration The implementation of the desired MPC configuration is done in a pressurized chamber designed at the mechanical workshop at the Institute of Optics during a previous thesis. The 3D representation is shown in figure II.4. The total dimension of the chamber is 70 by 25 cm long. The distance between the mirrors can be adjusted from 15 to 60 cm. This chamber is designed to handle a maximum pressure of 10 bar. This maximum pressure resistance is mainly limited by the plexiglass cover, since it is less stiff than aluminium. Two fused silica windows allow the beam to enter and exist the chamber and gas filling is possible through two specific connectors.

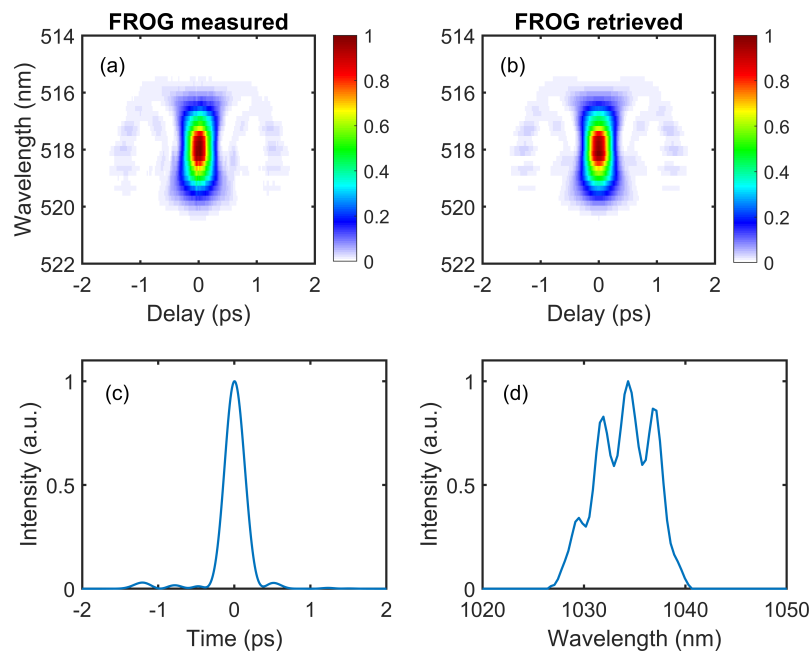


Figure II.3 – FROG measurement for the pulse at the output of the laser system. The measurement is done on a grid of 256×256 points. (a) Measured FROG trace; (b) Retrieved FROG trace with an error of 0.0024, plotted in linear scale; (c) FROG-retrieved temporal intensity; (d) FROG-retrieved spectral intensity profile.

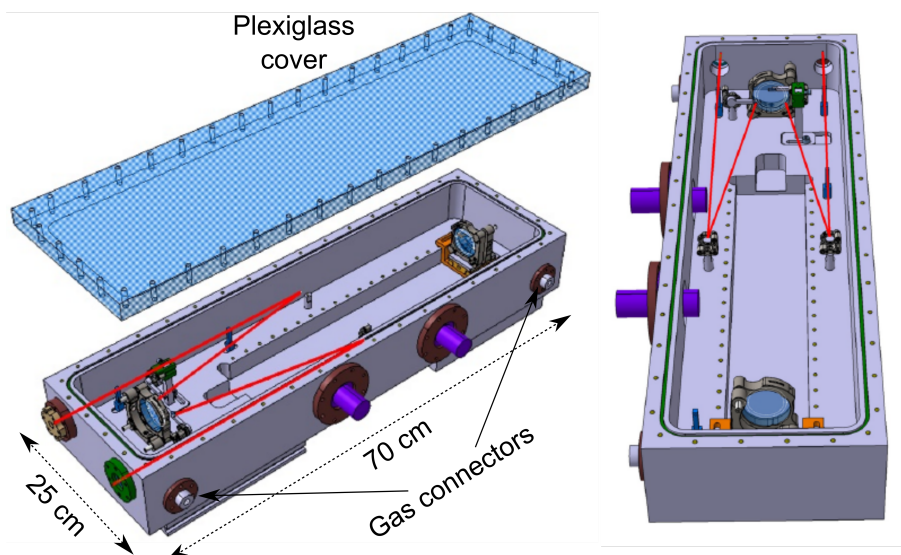


Figure II.4 – MPC pressurized chamber whose plans were made in the mechanical workshop of the Institute of Optics [Lavenu 19b].

As shown in figure II.2, the laser output beam is sent to the gas-filled MPC, passing through an optical zoom composed of three lenses that allow to focus the beam to the desired stationary beam at the center of the MPC. The choice of the focal lengths of the lenses and the distance between them depends on the waist size as well as the distance between the last lens and the center of the MPC. The mirrors of the MPC used in the experiment are two 50 mm diameter

concave mirrors with a radius of curvature of 300 mm. They are chosen to present a high reflection coefficient ($> 99.9\%$) on a 980-1080 nm bandwidth and are coated with a dispersive HR coating with $GDD = -25 \pm 10 \text{ fs}^2$ to partially compensate the normal dispersion induced by the nonlinear gas medium. The distance between the MPC mirrors is chosen to be 551 mm, approaching a concentric geometrical configuration. We used two rectangular $3 \times 10 \text{ mm}^2$ mirrors located in front of one of the MPC mirrors for laser beam coupling. With this configuration we obtain 21 roundtrips resulting in a total propagation length of 24.5 m including the path before and after the MPC in the gas-filled enclosure.

The gas chamber is filled with 3.8 bar of xenon. This noble gas possesses a high nonlinear index among nobles gases, which makes it a good choice as a nonlinear medium for experiments where high nonlinearity is needed while staying below the ionization threshold. At our operating gas pressure of 3.8 bar the nonlinear index is $n_2 = 2.0 \times 10^{-22} \text{ m}^2/\text{W}$, corresponding to a critical power for self-focusing of 0.67 GW. At this pressure the xenon introduces a group velocity dispersion of $296 \text{ fs}^2/\text{m}$. The maximum input peak power that can be reached by our laser source of $P_{peak} = 0.59 \text{ GW}$, is lower yet very close to the critical power in our case, allowing us to investigate highly nonlinear regimes in this MPC configuration.

With this MPC configuration, the beam waist radius is $154 \mu\text{m}$ at the center of the cell expanding to $624 \mu\text{m}$ on the MPC mirrors. This kind of near concentric MPC geometry is advantageous, as mentioned earlier, for inducing spectral broadening at relatively high input pulse energy while mitigating any damage of the MPC mirrors since the beam size becomes large on the mirrors allowing to maintain a fluence on the mirrors well below the damage threshold. However, with a relatively small waist at the center of the cell, one should pay attention to gas ionization. In our case, the maximum intensity at the center of the MPC is $7.9 \times 10^{11} \text{ W}/\text{cm}^2$, well below the ionization threshold for xenon which corresponds to $8.7 \times 10^{13} \text{ W}/\text{cm}^2$ [Faure 01]. The power transmission of the experimental setup is 86%, including the mode matching optics. This reduced value compared to previous reports might be due to aging of the optical coatings. The beam exiting the MPC is collimated with a 700 mm focal length lens and sent to be characterized.

Spectral broadening at the MPC output The first thing to check at the output of the MPC is the spectral broadening of the input initial spectrum due to SPM. Figure II.5 displays the measured spectral profiles at the output of the MPC for increasing values of input energy, i.e., for increasing nonlinearity. The measurements are performed using waveScan spectrometer from A.P.E, presenting a 500-1600 nm wavelength range at 0.2 nm resolution. We can see that significant broadening is obtained at high input energy. The spectral width at -10 dB increased from 15 nm at $6.6 \mu\text{J}$ input energy to 92 nm at $186 \mu\text{J}$ input energy. This spectrum corresponds to a FTL pulse duration of 18 fs.

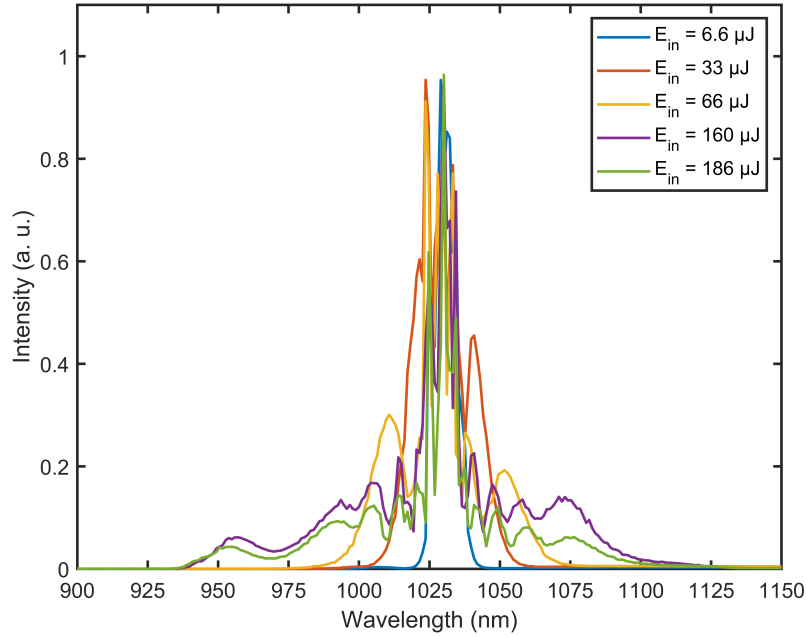


Figure II.5 – Spectra measured at the output of the 3.8 bar xenon-filled MPC for increasing values of input energy, corresponding to P_{peak}/P_{crit} of 0.02 ($6.6 \mu\text{J}$), 0.14 ($33 \mu\text{J}$), 0.29 ($66 \mu\text{J}$), 0.73 ($160 \mu\text{J}$), and 0.81 ($186 \mu\text{J}$).

2.2 Observation of wave breaking and 1D model validation

A temporal characterization of the output pulse is made by means of a home-built Second Harmonic Generation Frequency Resolved Optical Gating (SHG-FROG) allowing the confirmation of the occurrence of wave breaking at the output of the MPC for different values of input energies. The principle behind this nonlinear effect is described in chapter I section 1.4.1, and is observed in 2018 in a MPC [Ueffing 18b]. The observation of the wave breaking requires a high level of nonlinearity, thereby providing an appropriate physical testbed for the 1D numerical model described in chapter I section 3.3. Therefore, we compared the experimental data collected using the FROG measurement at the MPC output with the results obtained by the 1D numerical model. Figure II.6 shows the MPC output pulse temporal and spectral profile measured at different level of input energy (in red) compared with the ones obtained with the 1D numerical model (in blue), taking into account the measured spectrum and spectral phase of the input pulse. As the energy is increased, the temporal profile changes from a Gaussian-shaped pulse to a rectangular-shaped pulse, with oscillations emerging on both temporal edges of the pulse. On the pulse spectrum, these oscillations are accompanied by the appearance of large sidelobes.

In our case, wave breaking is experimentally observed at input energies $> 60 \mu\text{J}$. At this level of energy, the estimated B-integral at which wave breaking occurs is 11.2 rad [Anderson 92], and the accumulated B-integral obtained from the 1D model corresponding to the experimental parameters is 12 rad, which are in quantitative agreement. Even at $160 \mu\text{J}$ pulse energy there is a good agreement between the experimental results and the model which corresponds to P_{peak}/P_{crit} ratios up to 0.73. We believe that this validity of the 1D model at such high level

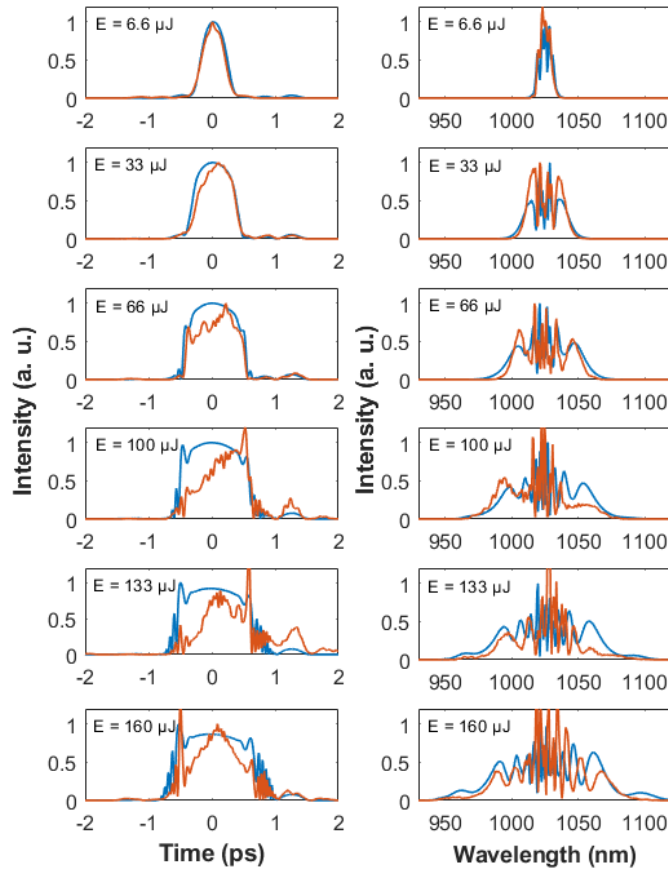


Figure II.6 – Left column, FROG-retrieved temporal intensity profile (red) compared to numerically simulated temporal intensity profile (blue) obtained for different levels of input energy at the output of the MPC filled with 3.8 bar of xenon. Right column, measured spectrum (red) compared to spectrum obtained by simulation (blue).

of nonlinearity is due to the fact that it is straightforward to account for an imperfect beam through the M^2 value, as we have seen in chapter I section 3.3. In 3D models, it might be more difficult to take into account the beam imperfections since an exact shape of intensity and phase imperfections must be assumed or measured.

In figure II.7, a close-up on the pulse shape at input energy of 160 μJ is presented as well as the corresponding spectrograms. We can see clearly that the input pulse is temporally broadened from 300 fs to about 1 ps after propagation in the MPC, and the linearly increased chirp is well observed in the spectrograms obtained numerically and experimentally. From figure II.7 (a) and (b), it is clear that the chirp is mostly linear across the center part of the pulse, but presenting a step transition regions at the leading and the trailing edges of the pulse.

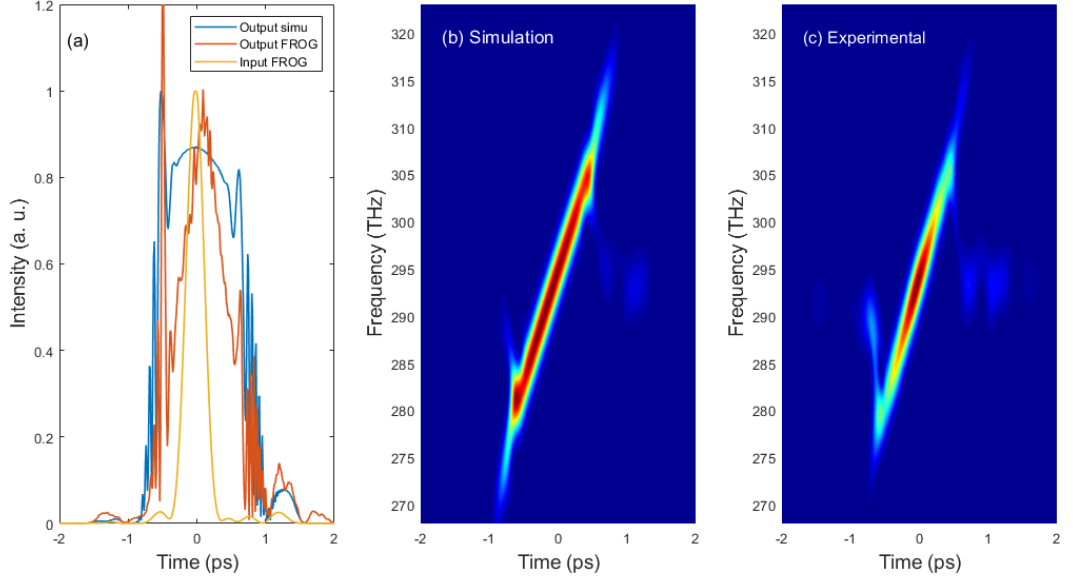


Figure II.7 – (a) FROG-retrieved temporal intensity profile of the input (yellow), experimentally obtained MPC output (red), numerically obtained MPC output (blue) pulse for $160 \mu\text{J}$ input energy ($P_{peak}/P_{crit} = 0.73$); The corresponding (b) numerically and (c) experimentally obtained spectrogram at the MPC output.

2.3 Measurement of intensity and phase spatio-spectral profiles

In this section, we investigate the spatio-spectral profiles at the output of the MPC as the non-linearity increases. First, the spatial profile as well as the spatial quality factor are measured, followed by an imaging spectrometer measurement, and a full characterization using INSIGHT measurement to assess the spatio-spectral properties.

2.3.1 Spatial and spatio-spectral characterization of the MPC output beam

At the output of the MPC, we measured the beam profile as well as the beam quality factor M^2 at different level of input energy, as shown in figure II.8. We can see that there is a very slight degradation of the beam quality with increased input energy. In addition, we observe a sort of beam asymmetry in the intensity profile but with a preservation of a Gaussian-shaped beam profile.

Measuring the M^2 factor is not enough to quantify the presence of spatio-spectral couplings since it is not spectrally resolved, meaning that it does not provide any information about the homogeneity of the spectral broadening across the beam spatial profile. A way to have access to this information is to measure the spectrum across the beam transverse profile using a small aperture optical fiber scanned across the beam profile and by introducing the overlap factor V , as proposed by [Weitenberg 17b]. This overlap factor is calculated by using the following expression:

$$V(x) = \frac{\left[\int (I(\lambda)I_0(\lambda))^{1/2} d\lambda \right]^2}{\left[\int I(\lambda)d\lambda \int I_0(\lambda)d\lambda \right]}, \quad (\text{II.2})$$

where $I(\lambda)$ is the spectral intensity of each spectrum, and $I_0(\lambda)$ is the spectral intensity at the beam axis.

This value $V(x)$ represents the resemblance in terms of spectral intensity between the spectrum measured at location x and the spectrum at the beam center. By weighting the overlap with the intensity it is possible to define a mean overlap factor that quantifies the homogeneity of the spectrum across the beam profile.

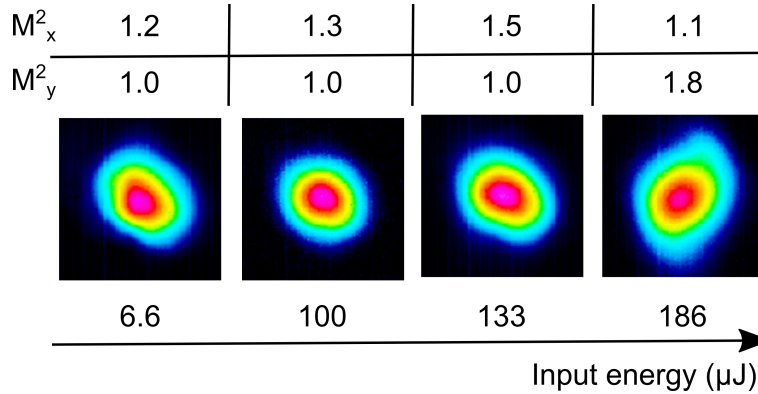


Figure II.8 – Measured spatial profile at the output of the MPC for increasing values of input energy and the measured beam quality factor M^2 .

Another similar way to measure to the different spectra across the beam is to use an imaging spectrometer setup. The experimental imaging spectrometer setup we used is composed of an 800 lines/mm grating, a 50 mm focal length cylindrical lens and an InGaAs based camera with a 30 μm pixel size. This type of InGaAs detector presents an almost constant sensitivity on a wide range from 1000 nm to 1600 nm and remains sensitive down to 850 nm wavelength. In our measurements, the camera is voluntarily saturated for the spectral components near 1030 nm in order to better observe the spatio-spectral structures of the full broadened spectrum. The results are shown in figure II.9.

From the measured spectrum across the transverse profile, no signs of spatio-spectral couplings are present for 133 μJ input energy ($P_{peak}/P_{crit} = 0.58$). However, some slight signs of couplings appear as the energy increases to 166 μJ ($P_{peak}/P_{crit} = 0.73$). At this point the beam pointing starts to be unstable, and rapidly becoming very unstable at 186 μJ pulse energy ($P_{peak}/P_{crit} = 0.81$). Even with this beam instability, the spatio-spectral profile recorded using a low integration time, as shown in bottom of figure II.9, is still not showing very clear signs of couplings in intensity. To quantify this assertion, the calculated mean spectral overlap factor is 97%, at this extreme level of nonlinearity. We do not clearly understand the mechanism behind the beam instability, but it might be due to small initial fluctuations in intensity that are transferred to changes in the beam propagation through the large amount of Kerr spatial phase. Although the spectro-imaging measurements are a very useful first attempt at characterizing space-time couplings, it is far from being complete. In particular, it reveals nothing of the spatio-spectral phase couplings that might appear. This is addressed in the next section.

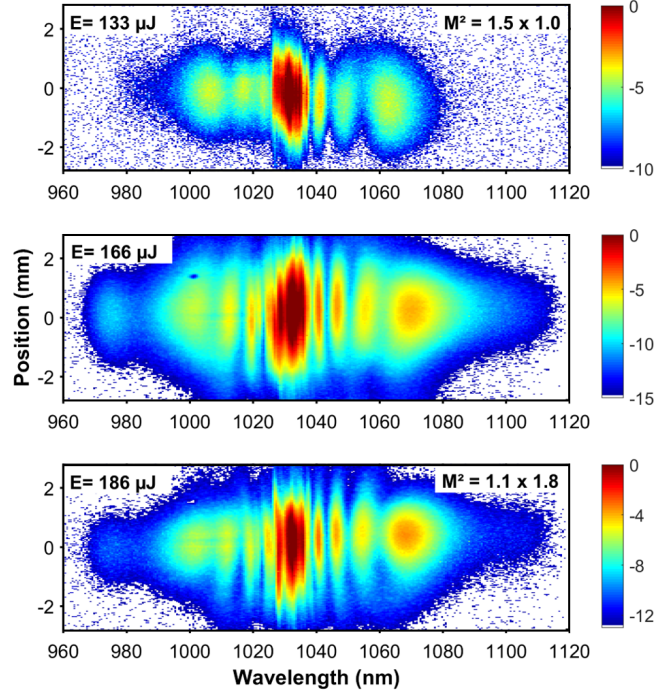


Figure II.9 – Experimental spectro-imaging measurements in logarithmic (dB) scale for increasing values of P_{peak}/P_{crit} of 0.58 (top), 0.73 (middle), and 0.81 (bottom).

2.3.2 Full 3D characterization of the electric field using INSIGHT

A better understanding of the spatio-spectral properties of the broadened laser pulses can be obtained by using a more complete spatio-spectral technique, such as INSIGHT [Borot 18]. The access to such a measurement device was made possible during a collaboration with LIDYL, CEA Saclay. Figure II.10 shows the result of an INSIGHT measurement at the output of the MPC for 133 μJ input energy. Slices of intensity (a)-(c) and phase (d)-(f) at three sample wavelengths can be obtained along with reconstructed integrated quantities (g)-(i). For higher pulse energies, the INSIGHT characterization was not possible because of the increasing shot-to-shot instability of the beam.

What is really powerful in such a complete spatio-spectral measurement is the ability to measure both the amplitude and phase at all frequencies within the laser pulses. Therefore, information on frequency-resolved aberrations, the so-called spatio-temporal or spatio-spectral couplings [Akturk 10], can be provided by the non-integrated processed data. Figure II.10 (a)-(c) shows three maps of the spatial intensity profiles at 1000 nm, 1030 nm, and 1060 nm and the corresponding spatial phase profiles, depicted in figure II.10 (d)-(f). Although at 1060 nm there is a beginning of some intensity degradation, the phase maps contain very small magnitude low-order aberrations. In fact, in this case the main aberration is a minor wavelength-independent astigmatism, which does not contribute to spatio-temporal deterioration. We do not measure any low-order spatio-temporal couplings such as pulse-front tilt or pulse-front curvature. A single number, the so-called spatio-temporal Strehl ratio [Jeandet 19] can be used to assess the severity of the chromatic phase couplings. In the case of the data shown in figure II.10,

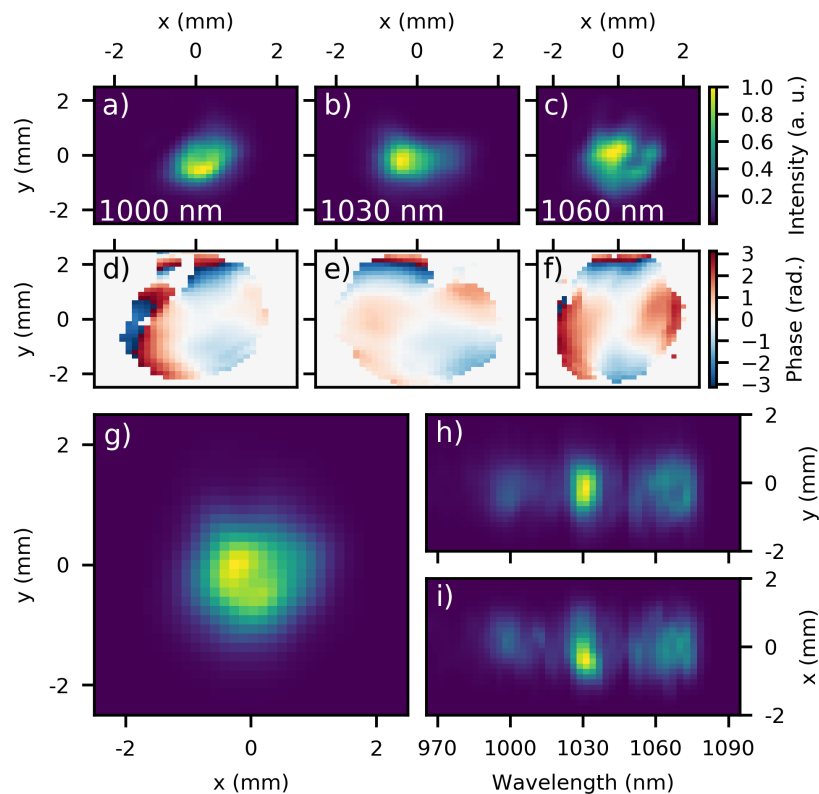


Figure II.10 – Results of the INSIGHT measurement for $P_{peak}/P_{crit} = 0.58$. The full spatio-spectral data from the INSIGHT measurement produces the 2D amplitude profiles (a-c) and phase profiles (d-f) for the three wavelengths shown of 1000, 1030, and 1060 nm. The spectrally-integrated beam profile (g) and spatio-spectral profiles (h-i) provide a comparison to standard devices. In (h) and (i) the intensity is integrated along the spatial axis that is not shown.

the spatio-temporal Strehl ratio is 0.9, meaning that the spatio-temporal couplings (i.e. the purely chromatic aberrations which would not be possible to correct via a deformable mirror) are responsible for a decrease in focused intensity by 10%.

Figure II.10 (g) shows the spectrally-integrated beam profile, and by using the data in the top panel of figure II.10, it is possible to numerically reconstruct the imaging spectrometer as shown in the integrated 2D spectrograms in figure II.10 (h)-(i). The integrated results provide a good benchmark for the INSIGHT results, in that they agree qualitatively with previous measurements. Despite the fact that fine features are not reproduced due to the limited spectral resolution of these INSIGHT measurements compared to the imaging spectrometer (related to the range of the delay scan done), the results, especially in figure II.10 (h)-(i), are comparable.

3 Conclusion

To conclude, we have seen briefly the sources of spatio-temporal/spectral couplings and their potential influence on laser sources performances. In some cases, the investigation of the complete electric field is necessary, providing the motivation for the development of several spatio-temporal/spectral techniques used to characterize the 3D electric field.

Then, we have studied the behavior of a highly nonlinear gas-filled MPC in terms of spatio-spectral couplings. The MPC used in the experiment has a near concentric geometry allowing the beam to pass 42 times in a pressurized chamber filled with 3.8 bar of xenon serving as the nonlinear medium. The normal propagation regime accompanied by the nonlinearity introduced by the nonlinear medium provided the necessary conditions to observe optical wave breaking at the output of the MPC.

The experimental results obtained at the output of the MPC are compared to the results obtained using the 1D model numerical simulation. This model was able to accurately produce the observation of wave breaking, validating the use of a simple 1D numerical model to describe pulse propagation in MPCs with Gaussian beams where the nonlinearity does not lead to major changes in the beam caustic along propagation.

Spatio-spectral measurements were performed at the output of the MPC using an imaging spectrometer and a full 3D characterization of the electric field, called INSIGHT, performed at the output of a MPC for the first time to our knowledge. Despite the high level of nonlinearity, both methods showed no severe spatio-spectral inhomogeneity at the output of the MPC.

The results obtained in this study show that gas-filled MPCs can be used at peak power levels close to the critical power without inducing significant spatio-spectral couplings in intensity or phase. Therefore, performing nonlinear optical functions usually implemented in optical fibers can be done in MPCs while scaling the pulse energy.

Since the beginning of this Ph.D thesis, a number of experiments confirmed the robustness of gas-filled MPCs with respect to spatial and spatio-temporal degradation, with experiments performed at a B-integral per roundtrip level up to 4.5 rad [Kramer 20].

Chapter III

Spectral Compression in a Multipass Cell

Objectives

This third chapter starts with a general introduction about the generation of high energy picosecond pulses. Then, a brief description of the principle of spectral compression is presented. An important part of this chapter describes the experimental demonstration of the proof of principle of spectral compression in fused silica plates inserted in a MPC. This made possible the generation of near Fourier transform-limited high peak power picosecond pulses from an Yb-doped fiber chirped pulse amplifier (FCPA). The obtained results are illustrated and discussed.

Contents

1	Introduction	58
2	Concept of SPM-induced spectral compression	60
3	Preliminary results	62
3.1	Spectral compression in 3.8 bar of xenon	62
4	Generation of high energy near FTL picosecond pulses	63
4.1	Experimental setup	63
4.2	Results and discussions	65
4.3	Control of the output spectral shape	67
4.4	Comparison between experimental and numerical simulation results	70
4.5	Spatial and spatio-spectral characterization	72
5	Conclusion	73

1 Introduction

Many scientific and industrial applications require the use of high energy high repetition rate picosecond pulses with a near FTL spectrum. In particular, they are required in developing secondary sources, where the primary infrared picosecond beam is subjected to one or multiple frequency conversion to obtain UV pulses used in electron guns in free electron laser installations [Will 11], or is used for pumping in parametric processes such as optical parametric chirped-pulse amplification systems (OPCPA) [Prinz 15]. These applications have operating points in the 1-20 ps laser pulse duration and often require a narrow spectral width. This narrow spectral width is dictated by the need to use second, third, fourth harmonic of the initial frequency of the laser source, especially in electron gun and OPCPA applications. Using FTL initial pulses can make the process of nonlinear conversion much simpler, relaxing the constraints on the spectral acceptance of the nonlinear crystals used in the process. The narrow spectral width also makes the use of such high repetition FTL ps pulses interesting for nonlinear vibrational microscopy where high spectral brightness and high spectral resolution is required such as coherent anti-stokes Raman scattering (CARS) [Cheng 04] or stimulated Raman scattering microscopy [Freudiger 08].

There are several ways to generate high energy picosecond pulses by different amplification techniques. A widely adopted solution is to use Nd-doped material-based amplifiers. By using more sophisticated architecture, energies of several hundreds of microjoules in 10 ps pulses can be obtained [Siebold 04, Heese 11]. However, shorter pulse durations cannot be obtained with such amplifier systems due to the narrow spectral emission cross section of neodymium, and average power scaling is limited by the relatively large quantum defect. Ytterbium-doped fibers amplifiers (YDFAs) can also be used to amplify picosecond pulses, with the associated benefits of large gain, beam quality, and average power scaling, but the small core dimensions restrict the pulse energy below 10 μJ . The chirped-pulse amplification technique (CPA) [Strickland 85] that is regularly used to scale the energy of femtosecond laser sources cannot be easily implemented for FTL picosecond pulses due to the narrow spectral bandwidth. This latter complexifies the introduction of the required dispersion in the pulse stretcher that becomes larger and practically harder to implement. However, divided-pulse amplification (DPA) can be used in this context providing an alternative technique [Kong 12].

Another elegant way to generate FTL ps pulses is possible through SPM-based spectral compression of negatively chirped pulses in a nonlinear medium. Spectral compression in optical fiber was firstly studied with negatively chirped pulses in 1993 [Planas 93, Oberthaler 93]. Most of spectral compression experiments have been performed in different types of single transverse mode solid-core fibers including standard fibers [Washburn 00], optical gain fibers [Limpert 02, Limpert 05, Zaouter 07], photonic crystal fibers [Andresen 05, Sidorov-Biryukov 08, Andresen 11], with lengths ranging from tens of cm to several km, and studied in silicon nitride nonlinear waveguides [Mei 16]. It is also suitable for a variety of wavelengths: Ti:sapphire wavelengths [Washburn 00, Andresen 05], the mostly used 1 μm [Limpert 05, Andresen 11], 1.55 μm [Fatome 12] windows, and the 2 μm band [Bao 16]. Using

optical fibers allows the increase of the interaction length almost arbitrarily, and fix the spatial profile. Hence, the pulse energy is limited by the damage threshold at the fiber facet and catastrophic self-focusing if the peak power exceeds the critical power in fused silica. This corresponds to energies of 1-10 μJ for pulses in the 1-10 ps duration range. Spectral compression could be performed in principle in gas-filled capillaries, but the lossy nature of such waveguides restricts their use to pulse energies above 1 mJ for picosecond pulses. However, it has never been done to our knowledge. The use of gas-filled Kagome or anti-resonant microstructured hollow-core fibers can fill the gap in the pulse energy, but no demonstration was reported. Spectral compression can sustain simultaneous amplification of the pulse in fiber amplifiers [Limpert 02, Limpert 05, Zaouter 07], thereby generating high power near-transform-limited ps pulses from a fs oscillator, and counteracting the spectral broadening usually observed after direct amplification of ps pulses. Hybrid architecture where nonlinearities are distributed over fiber and bulk amplifiers, such as in [Pouysegur 15] can also be used to amplify ps pulses. Both mentioned amplification methods are alternative techniques for energy scaling of ps pulses. For mJ energy level, spectral compression was reported in few experiments. These experiments used few mm to few cm long bulk media, such as BK7 glass [Liu 06], silica glass [Iwaszczuk 12], and barium-light-flint (BaLF) glass [Mitrofanov 18]. However, in these experiments the spectral compression factors are moderate. In such bulk media case, spatio-spectral couplings due to the complex spatio-temporal dynamics are inevitable, which limits the applicability of the method.

As we have seen in chapter I, multipass cells have been used as a platform to perform nonlinear optics at high energies while essentially retaining the one dimensional dynamics that is observed optical fibers. The use of solid-state or gas-filled MPC was mainly oriented towards temporal pulse compression in a wide range of pulse energies and durations. In the case of bulk MPCs, the peak power scaling is not limited by the critical power of self-focusing since the pulse exits the nonlinear medium before catastrophic collapse at each pass. Therefore, MPCs are a valid alternative to solid-or hollow-core fibers and capillaries to perform nonlinear optics, with some additional advantages in terms of power transmission, dispersion management, choice of nonlinear medium, and polarization maintaining properties.

In this chapter, we describe the use and implementation of a solid-state MPC to perform spectral compression at 7 μJ input energy beyond what is possible in solid core fibers, allowing the generation of near FTL ps pulses from a negatively chirped fs laser pulses generated by an Yb-doped fiber amplifier. The obtained results are discussed and compared to numerical simulations. The results obtained from this work is published in [Daher 20a]. Before diving into the core of the experiment, the following section reminds the principle of SPM-induced spectral narrowing.

2 Concept of SPM-induced spectral compression

As we have seen in chapter I section 1.3.1, SPM is often responsible for affecting the spectral shape of laser pulses propagating in a nonlinear medium, more precisely for inducing spectral broadening associated with modulated structure across the spectrum. This spectral broadening is observed in the case of an initial Fourier-transform limited (unchirped) or positively chirped pulse propagating in a normal dispersion regime. However, introducing a negative frequency chirp on the initial pulse can modify this behavior and lead to a reduction in the spectral width. The principle behind this spectral narrowing effect is described in this section.

The evolution of the spectrum of a pulse due to the effect of SPM is related to the dependence of the nonlinear refractive index on the field intensity. SPM gives rise to a chirp (frequency shift) proportional to the first derivative of the temporal (gradient) intensity profile of the pulse. Figure III.1, taken from [Boscolo 18], illustrates the spectral dynamics of the nonlinear propagation of an input Gaussian pulse in a fiber using time-frequency representations (spectrograms) which makes the understanding of the dynamics simpler and more intuitive.

Let us consider a short pulse with a broad spectrum. When applying a negative chirp to that pulse, the initial pulse is temporally broadened and the leading and the trailing edges of the pulse contain the high and the low frequencies, respectively. The variation of the instantaneous frequency induced by SPM, negative at the leading and positive at the trailing edge of the pulse, produces a shift towards the low frequencies of the leading edge and towards the high frequencies of the trailing edges of the pulse. The white arrows in figure III.1 (a1), representing the temporal gradient of the initial pulse, illustrates the rate at which the instantaneous frequency evolves along the fiber. After a certain propagation distance along the fiber, this phenomenon leads to a redistribution of the extreme frequencies towards the central frequency, concentrating the energy near the center frequency, as shown in figure III.1 (a3) and (b3). At this stage of propagation the chirp has no longer a monotonic temporal variation, as it was the case for $z=0$. Therefore, some interference between different parts of the pulse having the same frequency may occur, resulting in an oscillatory structure spectral shape (figure III.1 (b3)). As the pulse propagates even further, the chirp of the pulse becomes even more nonmonotonic with an increase of the chirp slope near the pulse center (figure III.1 (a4)). As a consequence, the spectrum broadens with a wide range of frequencies that can interfere, by that leading to more oscillations in the spectrum together with strong side lobes, as shown in figure III.1 (b4). The quality of the spectral shape obtained by SPM-based spectral narrowing depends highly on the temporal intensity profile of the pulse, since the frequency shift induced by SPM, in turn, is determined by the temporal intensity profile, which itself is related to the spectral profile since the pulses are chirped. A detailed description of the impact of the initial pulse shape on the SPM-based nonlinear spectral compression can be found in [Boscolo 18].

There are several techniques and methods to perform spectral narrowing [Toneyan 16], other than the one described just above. Spectral-width narrowing of a fundamental soliton propagating in an anomalous-dispersion-increasing fiber can occur as a result of its adiabatic

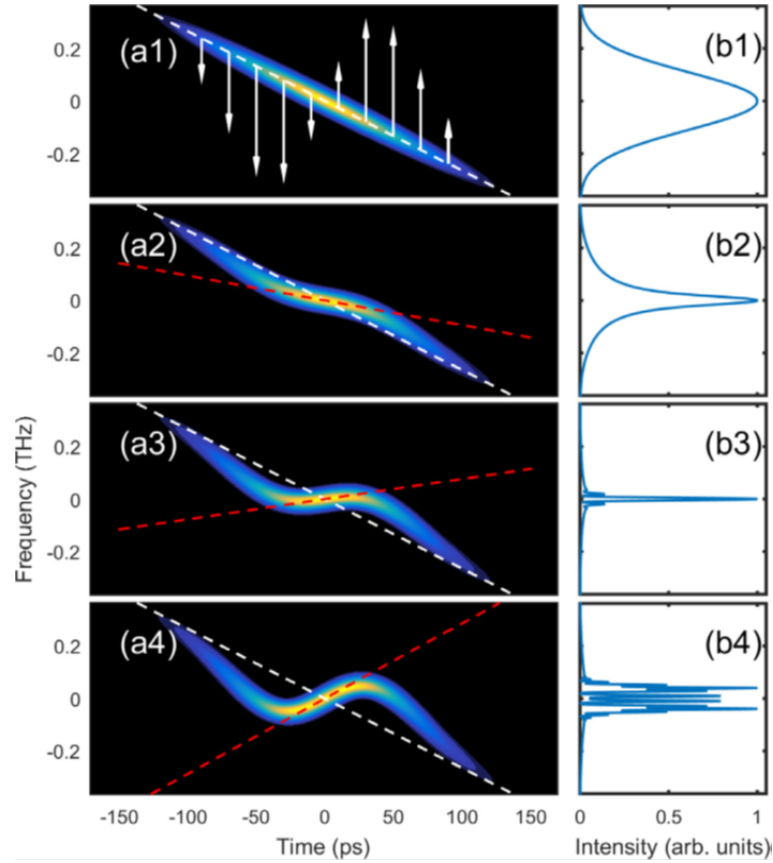


Figure III.1 – Spectro-temporal representation of a Gaussian pulse at different propagation distances in the fibre: $z = 0$, $z = 93$ m, $z = z_G$, and $z = 500$ m (panels 1-4, respectively). Subplots (a) and (b) show the spectrograms and the spectral intensity profiles, respectively. The white dashed lines represent the slope of the chirp in the central part of the pulse at the fibre input $C_G(0)$, while the slope coefficients $C_G(z)$ at the particular nonzero z are plotted with red dashed lines. The white arrows have a length proportional to the temporal gradient of the pulse intensity profile [Boscolo 18].

adaptation to the slowly varying dispersion along the fiber [Nishizawa 10]. This technique provided high spectral compression factor (> 20) on a tunable wavelength (1620 - 1850 nm). In a highly nonlinear fiber, ultrashort laser pulses can experience spectral compression in the regime of soliton self-frequency shift induced by Raman effect [Fedotov 09]. In [Mansuryan 08], spectral compression is done by a phase addition process, particularly through the sum-frequency generation (SFG) in a nonlinear crystal. For the experiments presented in this chapter, only SPM-induced spectral compression technique in a normal dispersion regime is considered.

3 Preliminary results

In this section, we expose the first experimental observation of spectral compression that we performed before discussing the final results described in section 4.

3.1 Spectral compression in 3.8 bar of xenon

Benefiting from the MPC setup filled with 3.8 bar of xenon that we have used in the previous experiment described in chapter II, we have tried to observe spectral compression at the output of the MPC. The experimental setup used is the same as the one of figure II.2 with the same geometrical configuration of the MPC. This time the laser is operating at a repetition rate of 300 kHz. As mentioned in section 2, the input pulse needs to be chirped negatively before being exposed to SPM during its propagation in the nonlinear medium, in order to observe spectral compression. Therefore, the pulse is negatively chirped. This was done by changing the distance between the gratings inside the fiber chirped pulse amplifier to obtain a pulse duration of around 2 ps at FWHM.

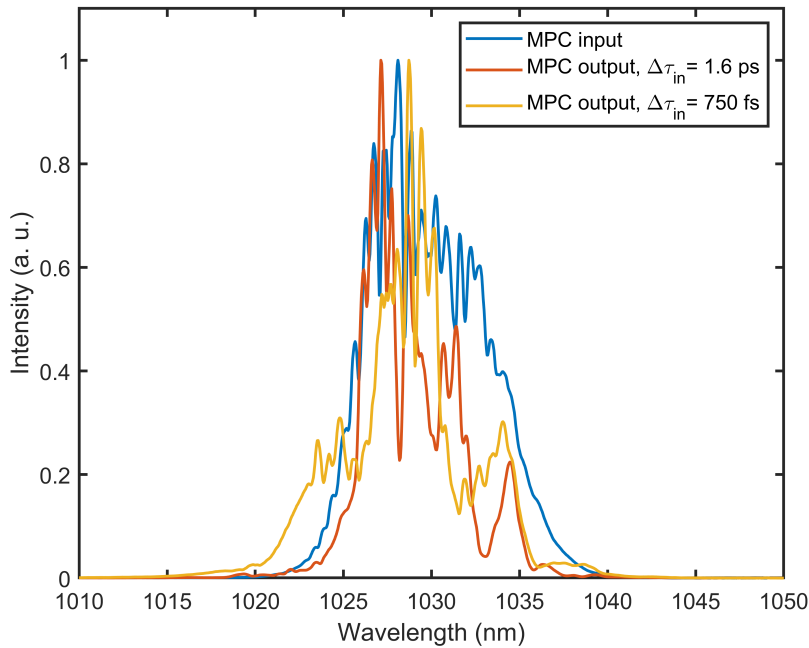


Figure III.2 – Measured spectral profile at the MPC input (blue), at the MPC output for 100 μJ input energy with 1.6 ps (red) and 750 fs (yellow) pulse duration at FWHM.

Figure III.2 illustrates the observed spectrum at the output of the MPC for 100 μJ input energy, compared to the laser input spectrum. We do observe a sort of narrowing of the spectrum at an input energy of 100 μJ with a spectral width of 5 nm at FWHM compared to that of the input pulse with 7 nm at FWHM. This can be understood by the fact that the SPM-induced chirp introduced by the nonlinearity of the xenon is not enough to compensate for the amount of the quadratic phase introduced by the compressor. Therefore, we have reduced the amount of the negative chirp to obtain a pulse with an input pulse duration of 750 fs. This time the spectrum is compressed at an input energy of 100 μJ with a 3 nm spectral width

at FWHM as shown in figure III.2. The measured output duration for this case at the MPC output is around 1 ps at FWHM, far from a FTL pulse. From this very brief observation, we deduced that we need more nonlinearity in order to obtain a FTL ps pulses, we can replace the gaseous nonlinear medium with a solid-state plate of fused silica inserted near the center of the MPC.

4 Generation of high energy near FTL picosecond pulses

In this section, we illustrate and discuss the use of a solid-state MPC to perform spectral compression of negatively chirped fs pulses, resulting in the generation of near FTL ps pulses. Fine adjustment of the spectral shape can be obtained by using phase control by means of a pulse shaper, when introducing the negative chirp to the input pulse.

4.1 Experimental setup

The experimental setup used is presented in figure III.3.

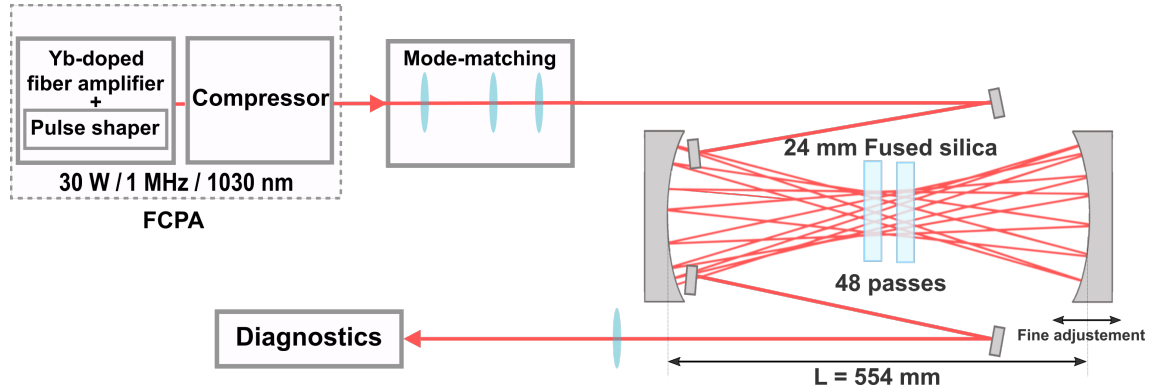


Figure III.3 – Experimental setup used to generate high energy FTL picosecond pulses.

Laser system The laser system used in this experiment is also an Yb-doped fiber chirped pulse amplifier, delivering quasi-FTL 260 fs, 30 μ J at 1 MHz repetition rate. The output spectrum of the laser exhibits a nearly Gaussian shape centered at 1030 nm with a 6 nm spectral width at FWHM. The FROG measurement of the laser pulse is shown in figure III.4. The output spatial quality of the laser beam is $M^2 = 1.1$ along both horizontal and vertical directions. A commercially available pulse shaper is inserted in the laser architecture before the main amplifier to allow control over the spectral intensity and phase at the output of this laser system which is operated in quasi-linear regime.

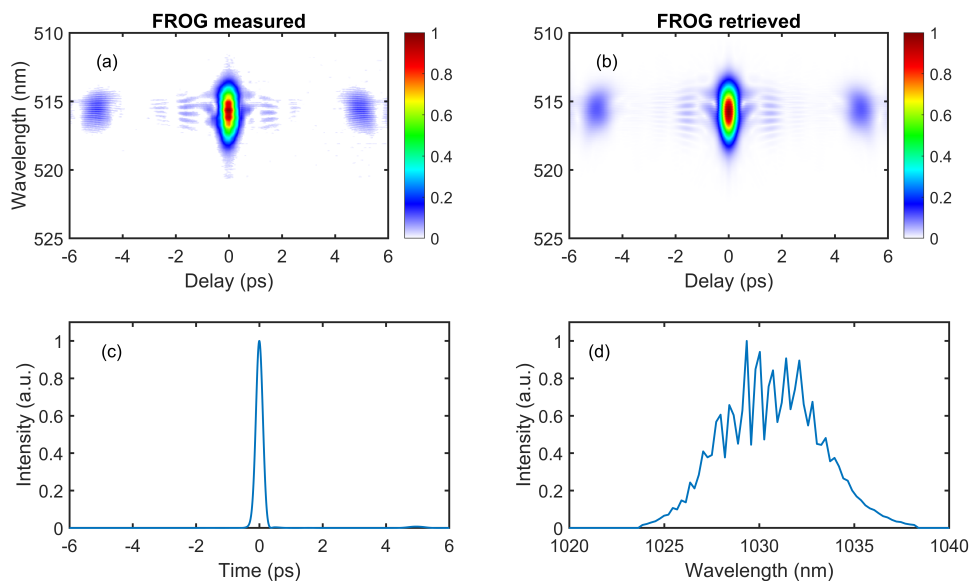


Figure III.4 – FROG measurement for the FTL pulse at the output of the laser system. The measurement is done on a grid of 512×512 points. (a) Measured FROG trace; (b) Retrieved FROG trace with an error of 0.0025, plotted in linear scale; (c) FROG-retrieved temporal intensity; (d) FROG-retrieved spectral intensity profile.

MPC configuration The MPC used in this experiment consists of two inches diameter mirrors with a radius of curvature of 300 mm coated with high reflectivity and low group delay dispersion dielectric stacks on a 980-1080 nm bandwidth. The two mirrors are separated by a distance of 554 mm. The beam is mode-matched to the stationary MPC beam using an arrangement of three lenses, resulting in a beam diameter of $370 \mu\text{m}$ at the waist, 9% larger than the stationary waist beam diameter (assuming an $M^2 = 1.1$). At the MPC mirrors, the beam diameter is 1.24 mm at which the energy density is well below the damage threshold. Two 3 mm width rectangular mirrors placed in front of one of the MPC mirrors are used for beam in/out couplings. The number of roundtrips inside the MPC is 24. The beam at the output of the MPC is collimated and sent to be characterized.

At first, we introduced one 12 mm-thick AR-coated fused silica plate near the center of the MPC to serve as the nonlinear medium. Using fused silica allows us to introduce a higher level of nonlinearity compared to gas-filled MPCs, due to a three order of magnitude higher nonlinear refractive index $n_2 = 2.2 \times 10^{-20} \text{ m}^2/\text{W}$ [Kabaciński 19]. For an input pulse negatively chirped to 1.7 ps duration using the grating pair compressor and an input energy of $27.5 \mu\text{J}$, the spectrum obtained at the output of the MPC is spectrally compressed to 2 nm at FWHM. The power transmission of the MPC, including the mode-matching optics is 70%. To even further compress the spectrum and get closer to obtain a near FTL pulse at the output of the MPC, two 12 mm-thick fused silica plates are inserted near the center of the MPC, separated by 23 mm, as shown in figure III.3. This time the power transmission of the MPC is 51%, including the mode-matching optics. This low value is mostly due to the non-optimal AR coating of the fused silica plates, with an estimated reflectance higher than 0.1% for each

interface. It could be readily increased using a single 24 mm plate and better quality AR coating [Schulte 16, Weitenberg 17a], which was not available at the time of the experiment.

4.2 Results and discussions

In this part, the necessary negative chirp is firstly introduced by changing the distance between the gratings of the compressor inside the FCPA. The pulse duration is broadened from 260 fs to 2.1 ps. The corresponding FROG measurement is shown in figure III.5, obtained by means of a home-built second harmonic generation FROG. This same FROG device is also used to measure the pulse temporal profile and spectrum at the output of the MPC.

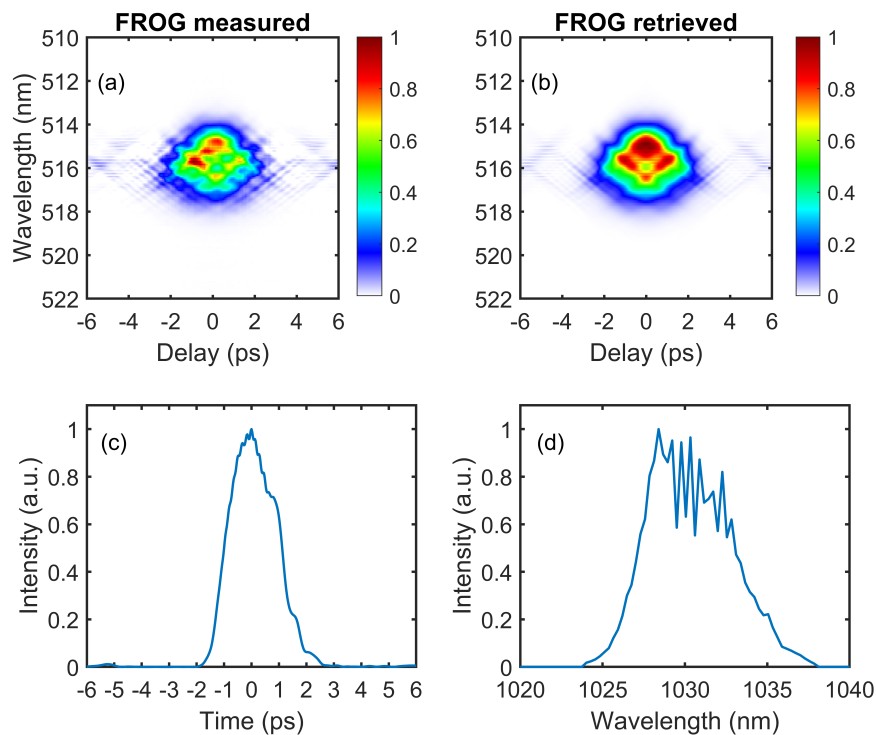


Figure III.5 – FROG measurement at the output of the laser system for the grating pair-induced negative chirp configuration. The measurement is done on a grid of 512×512 points. (a) Measured FROG trace; (b) Retrieved FROG trace with an error of 0.011, plotted in linear scale; (c) FROG-retrieved temporal intensity; (d) FROG-retrieved spectral intensity profile.

In this case, figure III.6 shows the results of an optimal spectral compression obtained at $19 \mu\text{J}$ input energy. The spectrum FWHM is compressed from 6 nm down to 1.06 nm while the temporal duration of the negatively chirped pulse remains unchanged after spectral compression. The time-bandwidth product (TBP) of the pulse at the output of the MPC is 0.66 indicating a transform-limited pulse: the TBP of a FTL pulse exhibiting the temporal profile of the output pulse in this example is 0.64. From figure III.6 (d) we can see that the obtained compressed spectrum presents an asymmetrical spectral shape with side lobes on the long wavelength side. This asymmetry is also noticeable in the corresponding FROG traces shown in figure III.6 (a)-(b).

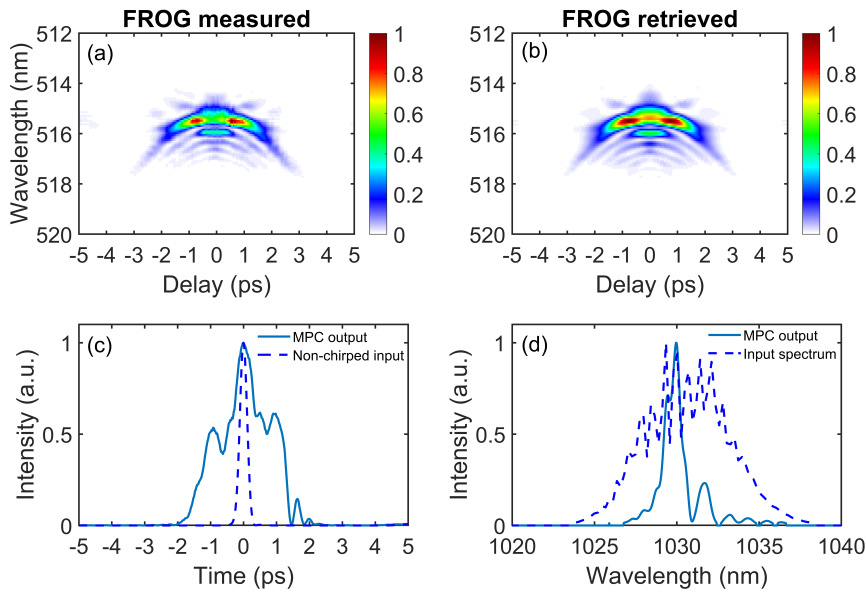


Figure III.6 – (a) Measured and (b) retrieved FROG traces plotted in linear scale at the MPC output at $19 \mu\text{J}$ input energy; (c) FROG-retrieved temporal intensity profile (solid) at the MPC output and the temporal profile of the input laser pulse before negative chirping (dashed); (d) FROG-retrieved spectral intensity profile (solid) at the MPC output and spectrum of the input laser pulse (dashed).

Figure III.7 displays the spectrograms of the negatively chirped input pulse and that of the MPC output pulse treated from the FROG retrieved data. We can clearly see that after spectral compression the energy is mostly concentrated near the central frequency with an irregular form showing a sort of slightly decreasing slope. As mentioned in section 2, the spectral compression mechanism involves an initial negative instantaneous frequency chirp and subsequent SPM-induced frequency shift. When all relevant quantities such as instantaneous frequency, spectral, and temporal intensity profiles are symmetric with respect to a center frequency, the process leads to a symmetric spectrum. However, slight asymmetry in these shapes due to e. g. the real gain profile of the amplifier, or cubic spectral phase, lead to a non-symmetric output spectrum as observed here. In order to control the spectral compression and obtain a cleaner spectral shape at the output, we use the pulse shaper embedded in the laser architecture. This is the subject of the next section.

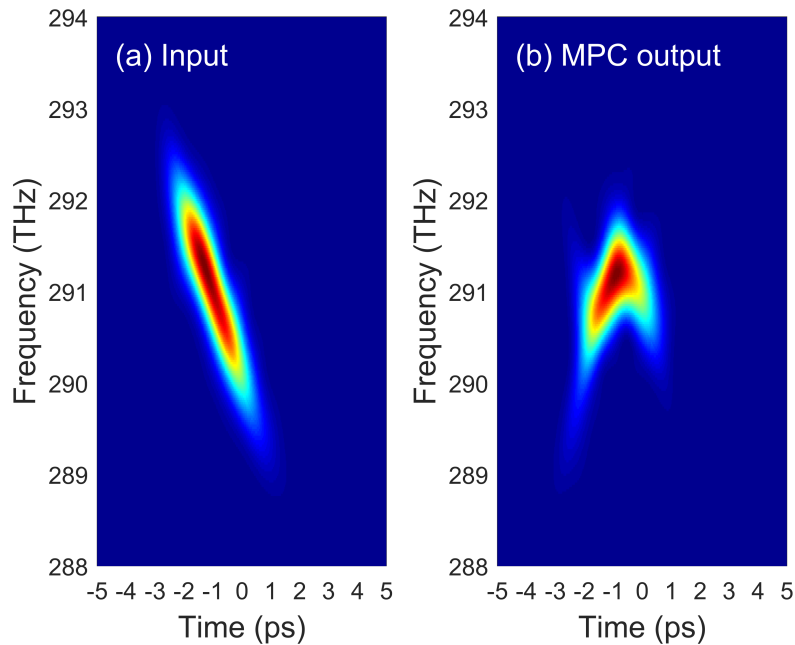


Figure III.7 – Spectrogram of the (a) negatively chirped input pulse and of the (b) pulse at the MPC output for 19 μJ input energy.

4.3 Control of the output spectral shape

In this second experiment, the negative chirp is introduced by using a pulse shaper. The pulse shaper used is based on a spatial light modulator inserted in the Fourier plane of a 4f dispersive line, with a spectral resolution of 100 pm. Using this pulse shaper, we are capable of shaping both the intensity and phase.

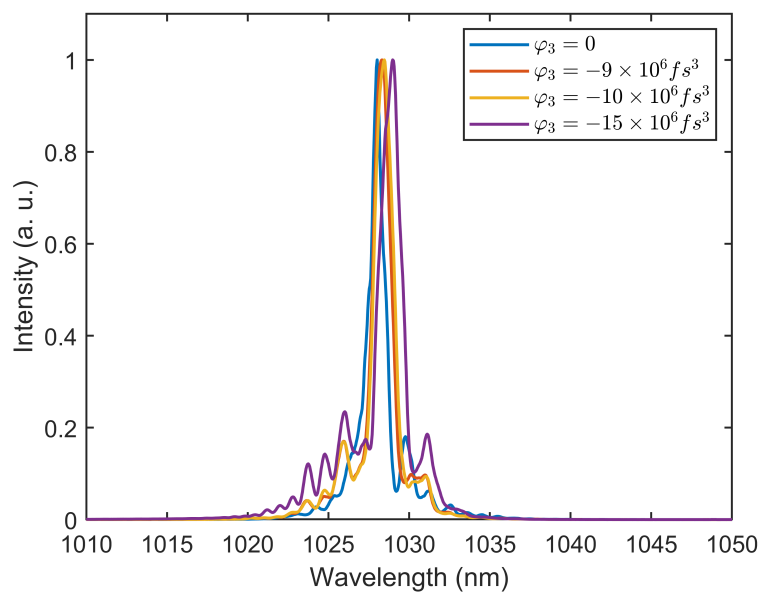


Figure III.8 – Measured spectral profiles at the output of the MPC with a negatively chirped input pulse introducing a $\varphi_2 = -190 \times 10^3 \text{ fs}^2$ and different values of φ_3 .

Starting from a situation where the compressor is aligned to optimally compress the pulse to 260 fs, we started by introducing, with the pulse shaper, a quadratic phase $\varphi_2 = -190 \times 10^3 \text{ fs}^2$ to negatively chirp the pulse to around 2 ps duration. Without introducing a cubic phase, the output compressed spectrum is obtained at $23 \mu\text{J}$ and presents an asymmetrical shape as was the case in the previous section. The corresponding measured spectrum is plotted in blue in figure III.8. By adding a cubic phase we observe some energy distribution in the side lobes of the compressed spectrum. For $\varphi_3 = -9 \times 10^6 \text{ fs}^3$ and $\varphi_3 = -10 \times 10^6 \text{ fs}^3$, the asymmetrical shape is less pronounced with more or less equally distributed intensity at both side of the central peak. If we increase even further the value of the cubic phase, an oscillatory structure at the short wavelength side is observed, leading again to an asymmetrical shape as shown in figure III.8. For the cases with an added cubic phase, the compressed spectrum is observed at $27 \mu\text{J}$ input energy.

From this observation we negatively chirped the optimally compressed pulse by introducing at the pulse shaper a quadratic phase $\varphi_2 = -190 \times 10^3 \text{ fs}^2$ and a cubic phase $\varphi_3 = -9 \times 10^6 \text{ fs}^3$ leading to the generation of 2.4 ps pulses at the output of the FCPA. The corresponding FROG measurement of the obtained chirped pulse is illustrated in figure III.9. Note that chirping with the grating compressor leads to the opposite sign of third-order spectral phase, since the φ_3/φ_2 ratio is negative for gratings pairs.

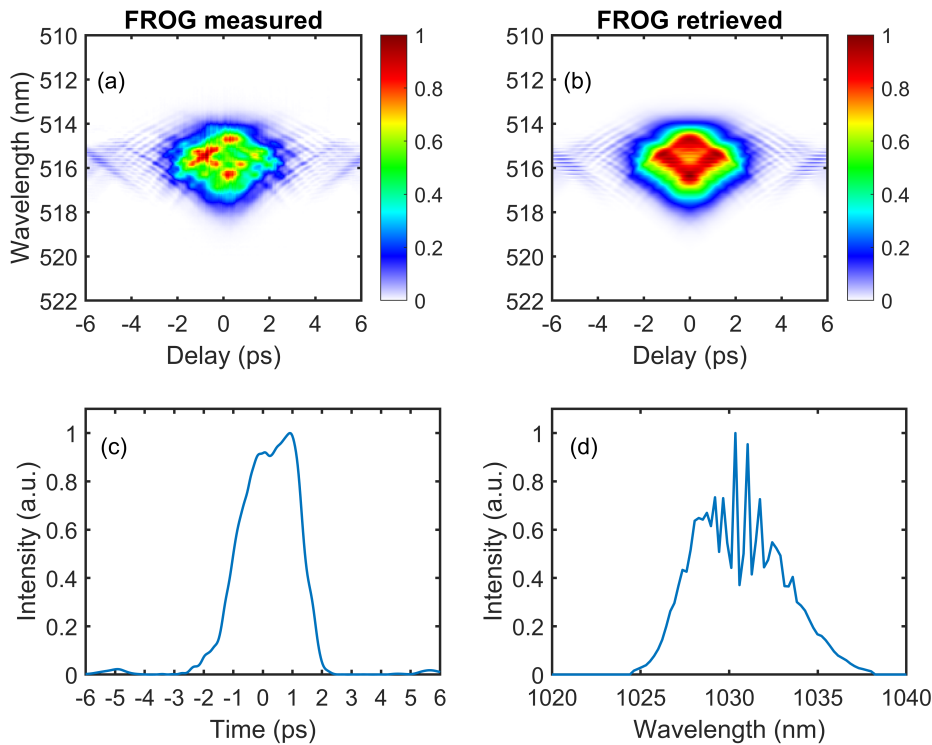


Figure III.9 – FROG measurement at the output of the laser system for the pulse shaper-induced negative chirp configuration. The measurement is done on a grid of 512×512 points. (a) Measured FROG trace; (b) Retrieved FROG trace with an error of 0.014, plotted in linear scale; (c) FROG-retrieved temporal intensity; (d) FROG-retrieved spectral intensity profile.

The results of the FROG measurement obtained after the MPC for $27 \mu\text{J}$ input energy are presented in figure III.10. The spectrum is compressed to 1.13 nm and the temporal duration is 2.1 ps at FWHM with a TBP of 0.68. Although the compressed spectral width is approximately equal to that obtained in the previous case, the spectral compression is now symmetric. This equally distributed intensity can also be seen in the FROG traces in figure III.10 (a)-(b). Further improvement in the output spectrum, in particular lower sidelobes intensity, could be obtained by using a parabolic-shaped input pulse such as in [Andresen 11, Fatome 12]. The obtained temporal pulse profile approaches a square distribution, as already suggested in [Finot 16].

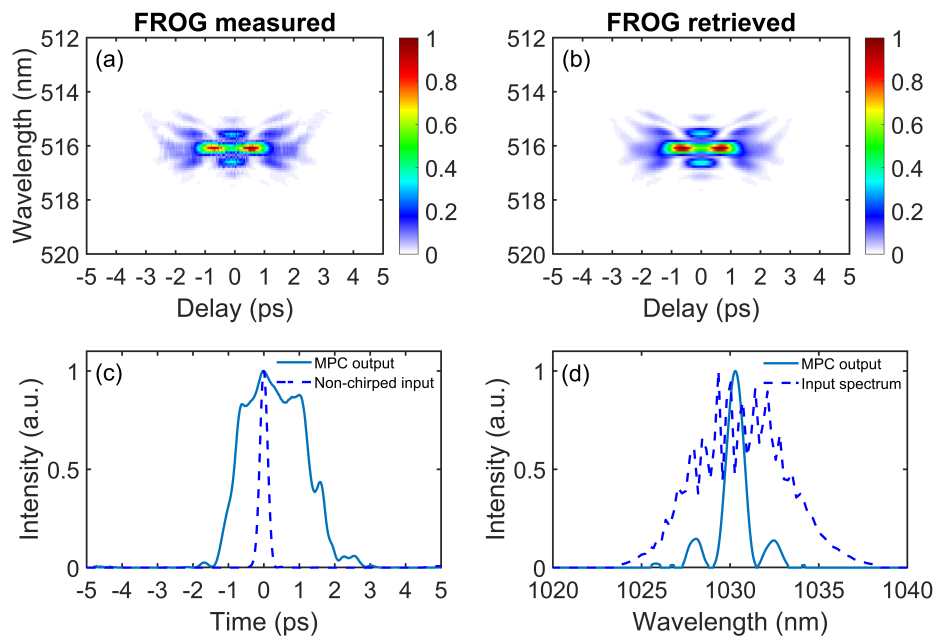


Figure III.10 – (a) Measured and (b) retrieved FROG traces plotted in linear scale at the MPC output at $27 \mu\text{J}$ input energy; (c) FROG-retrieved temporal intensity profile (solid) at the MPC output and the temporal profile of the input laser pulse before negative chirping (dashed); (d) FROG-retrieved spectral intensity profile (solid) at the MPC output and spectrum of the input laser pulse (dashed).

For this case, the spectrograms treated from the retrieved FROG data are illustrated in figure III.11, showing a concentration of the energy towards the central frequency for the output spectrum (figure III.11 (b)). The obtained spectrogram is very similar to that obtained theoretically in figure III.1.

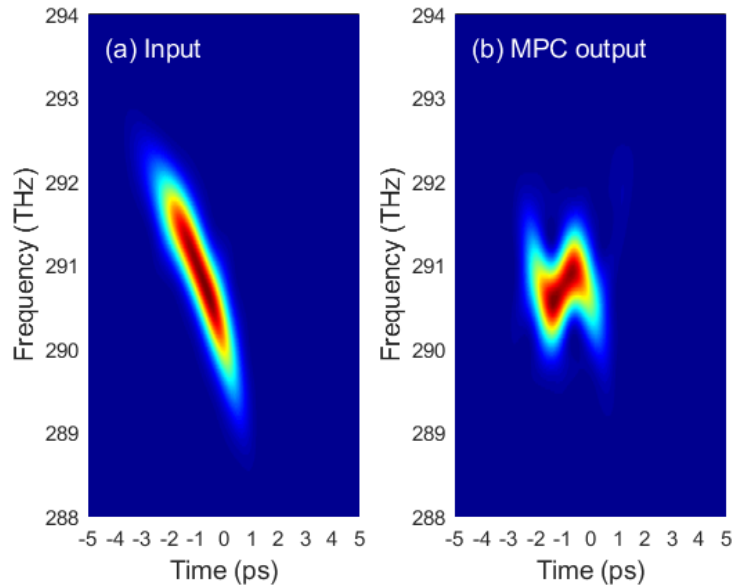


Figure III.11 – Spectrogram of the (a) negatively chirped input pulse and of the (b) pulse at the MPC output for $27 \mu\text{J}$ input energy.

4.4 Comparison between experimental and numerical simulation results

In this section, we compare the obtained experimental results of the previous two sections to numerical simulations. The numerical model used is a simplified model described in [Hanna 20]. This hybrid model uses a standard approach based on a generalized nonlinear Schrödinger equation in the time domain, coupled to a simple Gaussian beam evolution based on ABCD matrices that include the Kerr lens. In particular, it allows to describe the impact of nonlinearity on the beam caustic inside the MPC. The parameters used in the simulations are the same as in the experiment. The initial condition is taken from the measured input FROG traces in both cases: negative chirp introduced using the grating pair or using the pulse shaper.

Figure III.12 shows the temporal profiles measured at the input of the MPC along with measured and simulated spectral and temporal profiles at the output of the MPC in both experimental configurations. There is a good qualitative agreement between experimental and numerical results. In particular, we see that the change of sign for the third order spectral phase introduced by the pulse shaper leads to a change in the input intensity profile, with a steepest edge being transferred from the leading edge to the trailing edge, resulting in a more symmetric spectrally compressed spectrum.

For the gratings compressor-induced chirp case, the estimated B-integral for the first roundtrip is 0.51 rad, while it is 0.54 rad for the second experiment, leading to a total accumulated B-integral of respectively 9.0 rad and 9.5 rad after 24 roundtrips. Figure III.13 shows the beam radius evolution as a function of the propagation distance in the MPC obtained by numerical simulation for the case of the negative chirp induced using the pulse shaper. The caustic evolution shows that, due to the Kerr lens at the plates, there are amplitude oscillations of the beam radius size of the order of 10% in addition to the roundtrip modulation caused by

propagation in the MPC. Figure III.14 displays the experimental and simulated spectrograms obtained at the output of the spectral compression system in the grating pair and pulse shaper cases, showing a qualitative agreement.

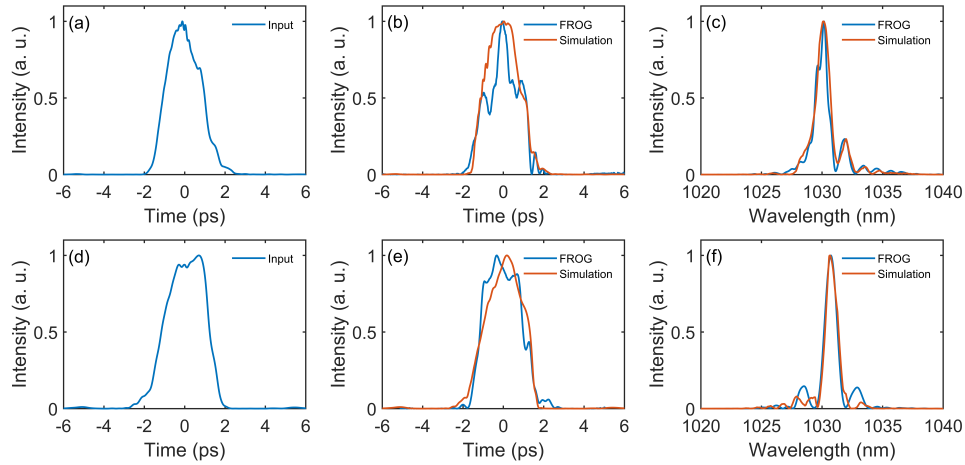


Figure III.12 – First row, grating pair-induced negative chirp configuration; second row, pulse shaper-induced negative chirp configuration. (a),(d) FROG-retrieved temporal intensity profile of the input chirped pulse; (b),(e) FROG-retrieved temporal intensity profile (blue) compared to numerically simulated temporal intensity profile (red) at the MPC output; (c),(f) FROG-retrieved spectral intensity profile at the MPC output (blue) compared to spectral intensity profile obtained by simulation (red).

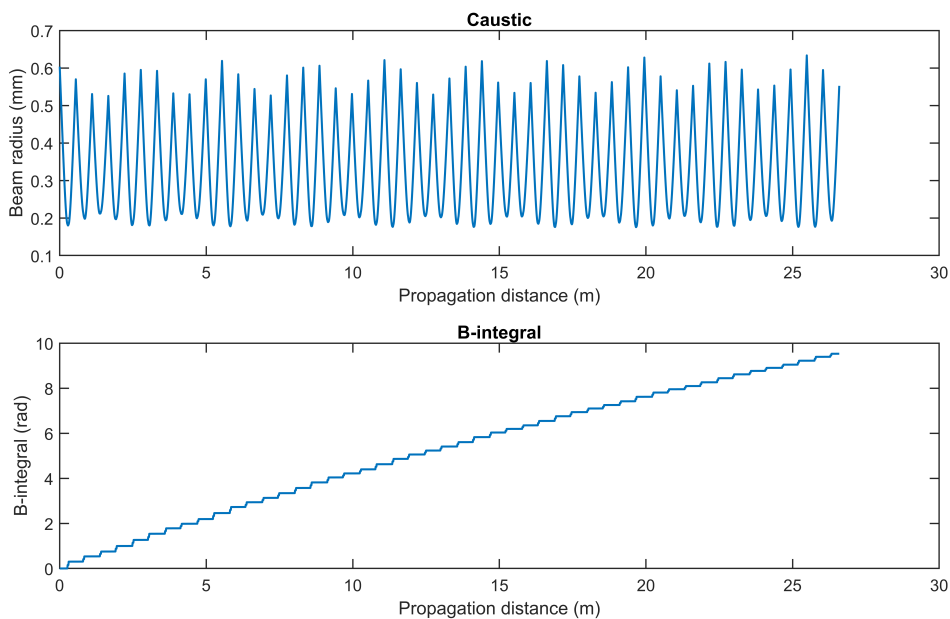


Figure III.13 – Top, numerically obtained caustic evolution as a function of the propagation distance in the MPC. Bottom, numerically obtained total B-integral as a function of the propagation distance in the MPC.

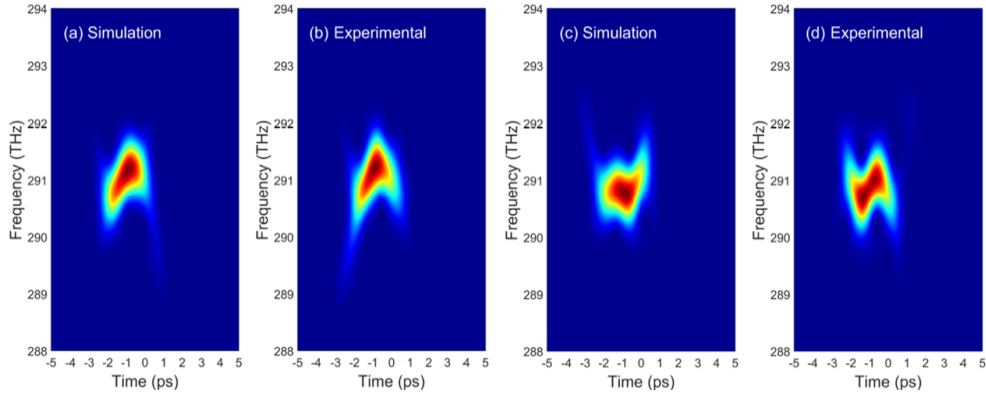


Figure III.14 – Spectrograms obtained by simulation at the output of the MPC in the (a) grating pair-induced negative chirp case and in the (c) pulse shaper-induced negative chirp case; FROG-treated spectrograms at the output of the MPC in the (b) grating pair-induced negative chirp case and in the (d) pulse shaper-induced negative chirp case.

4.5 Spatial and spatio-spectral characterization

In this section, we investigate the spatio-spectral properties at the output of the MPC. We study the spatio-spectral homogeneity of the beam after the MPC by using an imaging spectrometer setup. This setup consists of an f-f arrangement composed of an 800 lines/mm grating, a 50 mm focal length cylindrical lens and a CCD camera with a 4 μm pixel size. We also measure the beam spatial profile and M^2 quality factor at the output of the MPC.

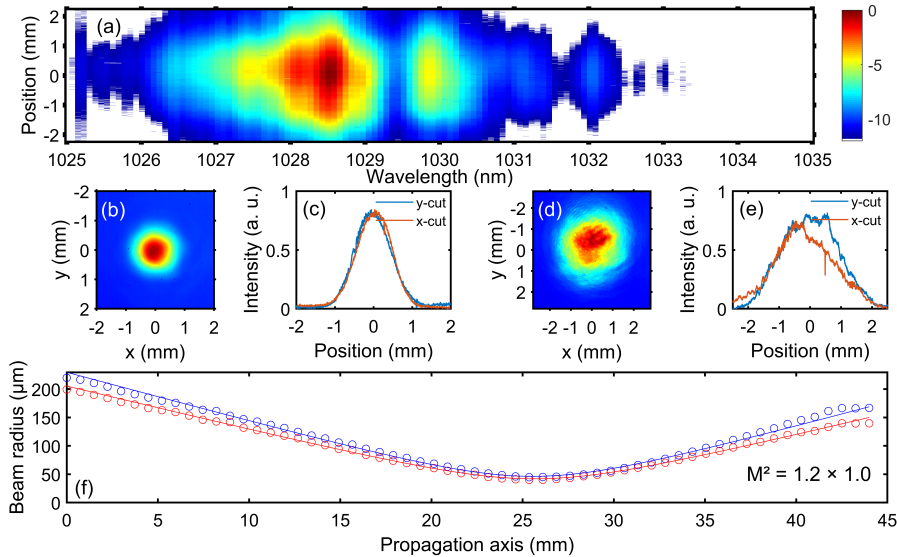


Figure III.15 – (a) Experimental spectro-imaging measurement in logarithmic (dB) scale for 19 μJ input energy; (b) measured spatial beam profile of the input laser beam, and (c) corresponding lineouts; (d) measured spatial beam profile at the MPC output at 19 μJ input energy and (e) corresponding lineouts; (f) measured beam caustics and corresponding Gaussian beam fit at the MPC output in both directions.

The results are illustrated in figure III.15. Although the intensity profile shows some degradation at the output, the measured M^2 is 1.2×1.0 along the vertical and the horizontal directions respectively, showing that the beam remains close to Gaussian. The larger beam size at the output of the MPC is due to the fact that the beam was collimated with a larger focal length than at the input. The mean spectral overlap factor V is 98%, confirming quantitatively the absence of spatio-spectral intensity inhomogeneity.

5 Conclusion

In this chapter, we have seen that a solid-state material-based MPC can be used to perform spectral compression leading to the generation of near FTL ps pulses. This allows the generation of near-transform-limited 2.1 ps pulses from a femtosecond Yb-doped laser amplifier while preserving the spatial quality of the beam.

By fine adjustments of the spectral phase at the input of the MPC using a pulse shaper, we generate a symmetric spectrum at the output. The experimentally observed temporal and spectral profiles are in good agreement with those obtained by numerical 1D simulation.

This proof of principle constitutes an additional example of the use of MPC to scale energy of nonlinear subsystems that are usually implemented using optical fibers, extending the possibilities to design multiple output femtosecond / picosecond synchronized laser sources. Bulk-based MPCs have been demonstrated with input peak-power ten times higher to the critical peak-power [Schulte 16, Weitenberg 17a]. Therefore, straightforward energy scaling of such setup to 100 μJ is possible, while the mJ energy range would be accessible using gas-filled schemes.

Chapter IV

Raman Conversion in a Multipass cell

Objectives

In this last chapter, we study the effect of stimulated Raman scattering in a solid-state MPC using positively chirped femtosecond pulses generated from an Ytterbium-doped fiber chirped pulse amplifier. First, we study the conversion efficiency at the output of the MPC for different input temporal pulse durations. Then, we characterize the spatial properties of the pump and the converted beams and compare them experimentally to a single pass scheme. The obtained results are then validated by numerical simulations confirming the observation of a spatial filtering effect in the MPC. Furthermore, temporal characterization is performed at the output of the MPC, and temporal compression of the Stokes beams is achieved.

Contents

1	Introduction	76
2	Study of stimulated Raman scattering in a MPC	77
2.1	Influence of the input temporal duration	77
2.1.1	Experimental setup	77
2.1.2	Results and discussions	79
2.2	Spatial filtering action in a MPC	82
2.2.1	Experimental setup	82
2.2.2	Conversion efficiency	83
2.2.3	Spatial characterization at the MPC output	85
2.2.4	SRS in single pass scheme	86
2.2.5	Comparison and discussion	89
2.3	Temporal characterization	90
2.3.1	Temporal measurement of stretched pulses	90
2.3.2	Compression of wavelength-shifted pulses	94
3	Conclusion	96

1 Introduction

Several applications require the use of wavelengths beyond $1 \mu\text{m}$. Some studies showed that using longer wavelength fs driving laser pulses makes it possible to generate higher photon energy attosecond X-ray pulses [Chen 10] and improve the efficiency of THz generation [Clerici 13]. Lasers operating between 1.2 and $1.8 \mu\text{m}$ are of interest for light detection and ranging (lidar) [Amann 01], gas sensing [Gibson 17], and for medical imaging applications such as optical coherence tomography [Tilma 11] and multi-photon microscopy [Kobat 09]. Obtaining intense femtosecond laser pulses in the short wavelength infrared range (SWIR) is made possible by difference frequency generation (DFG) and optical parametric chirped pulse amplification. However, the lack of a suitable broadband gain or the requirement of strict phase matching in the nonlinear crystals can make it difficult to maintain a wide gain bandwidth well above $1.1 \mu\text{m}$.

Stimulated Raman scattering is an alternative technique for pulse frequency conversion with automatic phase matching. It is a widely used method to extend the wavelength coverage of laser sources in CW [Casula 18], nanosecond [McKay 14], picosecond [Zverev 93] to femtosecond [Mackonis 20] temporal regimes. For pump pulses in the femtosecond regime, the pulse duration is shorter than the Raman mode dephasing time of the Raman material (a few ps for most Raman crystals), which is inversely proportional to the Raman gain bandwidth. In this case, SRS-induced frequency conversion is challenging due to the Raman transient regime. In this regime, the threshold pump intensity is increased compared with the steady-state case [Hilfer 90], and electronic third-order effects such as SPM, cross-phase modulation (XPM), and self-focusing can become predominant. The dominance of these intensity-dependent effects can be eased by chirping the femtosecond input pulse. The generated Stokes pulses can be compressed temporally since they partly inherit the chirp of the pump pulse [Jordan 94]. This has been shown in single pass solid-state Raman crystals such as $\text{Ba}(\text{NO}_3)_2$ [Zhavoronkov 01, Grigsby 08], YVO_4 [Trägårdh 16], $\text{KGd}(\text{WO}_4)_2$ [Grabtchikov 03, Orlovich 12], in fiber amplifiers [Zhou 10], high-pressure gas-filled cells [Jordan 94, Vicario 16], and waveguides [Carpeggiani 20]. The simplest way to perform SRS-induced wavelength conversion is by using solid-state media [Cerný 04], since it is a robust, compact setup and does not require control of gas pressure or guiding structure. A typical Raman crystal length is of several centimeters in single or double pass schemes, and power scaling can be limited by the onset of self-focusing. Furthermore, single pass schemes are often associated with some degradation of the output spatial beam quality. In these schemes, only the pump is irradiating the Raman medium while Stokes signals arise from noise [Zhavoronkov 01]. However, several demonstrations showed that it is possible to enhance the conversion efficiency and spatial quality of the generated Stokes signals by providing a spatially coherent seed beam for the SRS process, through Raman amplification of supercontinuum pulses [Mackonis 20] or multistage Raman conversion schemes [Lisinetskii 08]. Typical efficiencies obtained in Raman wavelength conversion experiments range from a few percent to few tens of percent.

As we have seen in chapter I section 4.5, the use of MPCs to perform temporal compression of femtosecond laser pulses is accompanied by homogeneous and high-quality output beams

due to the distribution of the nonlinearity over a large number of beam foci. So one could increase the number of stages in the Raman conversion medium by using a setup of a MPC while benefiting from the good spatial beam quality mentioned just above. In 1980, a MPC setup was used to increase the interaction length in the Raman active gases such as hydrogen [Trutna 80, Sußmann 92], and carbon dioxide [Saint-Loup 90, Sußmann 92] to perform frequency conversion of narrow bandwidth nanosecond pulses. In this chapter, we revisit this idea to demonstrate the possibility to transfer the energy of an input chirped femtosecond pulses to longer wavelengths through the process of stimulated Raman scattering in a solid material placed at the center of a MPC. We demonstrate Raman conversion inside a 3 mm-long potassium gadolinium tungstate (KGW) crystal inserted in a MPC, in the stretched femtosecond pulse regime. A large number of passes in the Raman medium can be achieved by using the MPC scheme, leading to a large interaction length while operating at peak powers well above the critical power for self-focusing. A first part of the study exposes the impact of the input pulse duration on the conversion efficiency obtained at the output of the MPC. In addition, co-propagation of the pump and Stokes beams inside the MPC leads to a spatial filtering effect that results in a high spatial quality of the converted beams. This property is presented in the second part, is illustrated with an experimental comparison with a single pass scheme in a 20 mm-long KGW, and backed up by numerical simulations. Finally, the output converted beams at the MPC output are spectrally and temporally characterized with an attempt to temporally recompress the converted beams. This will be the subject of the last section of this chapter.

2 Study of stimulated Raman scattering in a MPC

2.1 Influence of the input temporal duration

2.1.1 Experimental setup

The experimental setup of this study is presented in figure IV.1. In this part, we experimentally investigate how the conversion efficiencies depend on the input stretched pulsewidths. At a given energy level, as the pulse is stretched two phenomena with opposite consequences arise. First, the peak power decreases, which lowers the nonlinearity and therefore the Raman response. Second, the Raman process evolves from the purely transient regime to the CW regime, thereby increasing the overall Raman gain. We performed this study to observe which effect is predominant in our parameter ranges. Only power efficiencies measurement were done in this part.

Laser system The input pulses are generated from a high-energy femtosecond ytterbium-doped fiber chirped pulse amplifier delivering 26 W maximum average power with a 150 kHz repetition rate and a spectrum centered at 1030 nm. Although the pulses can be compressed down to 300 fs, the compressor of the laser is offset to generate positively chirped pulses with a duration of 10 to 35 ps at FWHM.

MPC configuration The input pump beam is directed to the MPC through an arrangement of three lenses in order to match the stationary beam of the MPC, resulting in a beam diameter

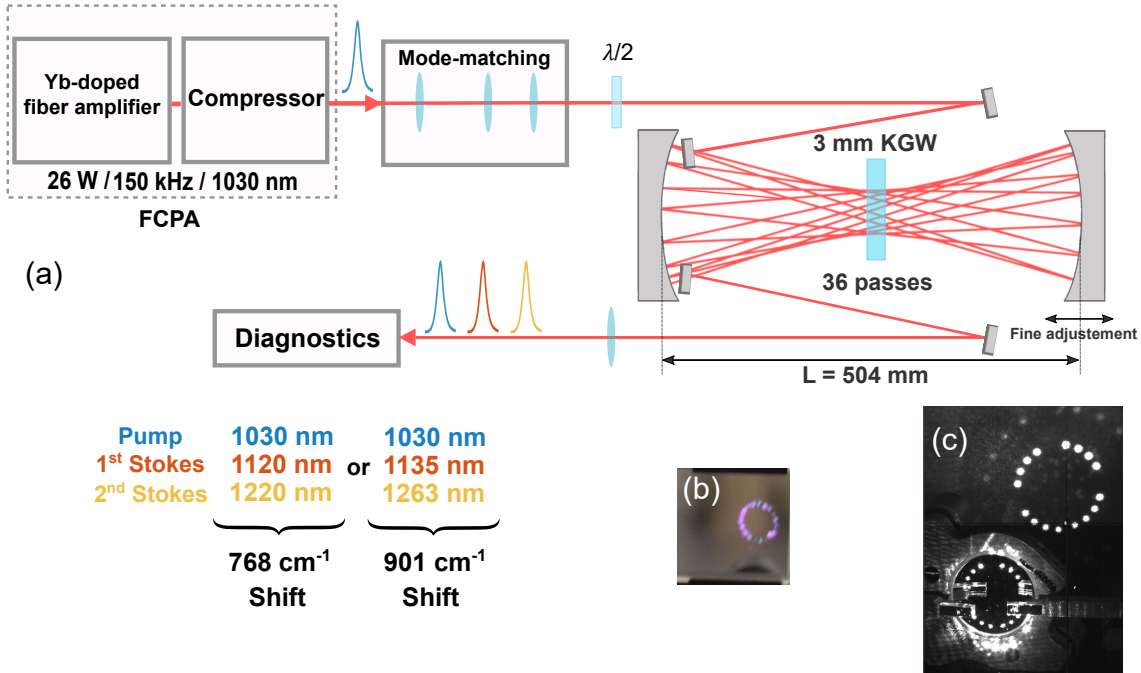


Figure IV.1 – (a) Experimental setup used to perform Raman conversion in a MPC; (b) Beam spots arrangement inside the KGW crystal; (c) Beam spots arrangement at one of the MPC mirrors. The spot structure seen on the top right corresponds to leaks through the mirror.

of $\sim 400 \mu\text{m}$ at the waist. The mirrors used in this MPC are two 1-inch diameter concave mirrors with a radius of curvature of 300 mm separated by 504 mm. The concave mirrors are coated with low group-velocity dispersion dielectric stacks on a 1000-1300 nm bandwidth, allowing a high reflectivity of $>99.95\%$ at the pump and both the first and second Stokes wavelengths. Near the center of the MPC a 3 mm-thick AR coated KGW crystal is added as a nonlinear Raman medium. With this MPC configuration, the number of roundtrips is 18, as shown in figure IV.1 (c) and (b), leading to a total propagation distance of 10.8 cm in KGW. The transmission of the MPC in linear regime is 80%.

We choose to use a KGW crystal due to its relatively common use as a Raman medium with high Raman gain, high damage threshold, and moderate thermal conductivity ($\sim 3 \text{ W m}^{-1} \text{ K}^{-1}$) [Mochalov 97]. This crystal exhibits multiple intense spontaneous Raman vibrations, as shown in table I.1, that depend on the pump polarization with respect to the crystal indicatrix axes (N_g , N_m , and N_p). It is cut normal to the N_p axis, so one can obtain Raman shifts of 768 cm^{-1} and 901 cm^{-1} with linewidths of 7.8 cm^{-1} and 5.9 cm^{-1} , respectively. Access to both Raman shifts in the experiment is allowed by using a half-wave plate placed before the MPC setup. In addition, the KGW crystal possesses a relatively short dephasing time of several picoseconds (around 2 ps according to [Kaminskii 99]) which makes it a good candidate for SRS-conversion experiments of picosecond and femtosecond pulses. At the output, the beam is collimated and sent to be characterized.

2.1.2 Results and discussions

At the output of the MPC, the 1st Stokes and 2nd Stokes beams are observed for the cases of the positively chirped input pump with pulse duration of 10 ps, 15 ps and 35 ps. For the 768 cm⁻¹ shift, the spectral profiles of the 1st and 2nd Stokes lines are observed at central wavelengths of around 1120 nm and 1220 nm, respectively. For the 901 cm⁻¹ shift, the 1st and 2nd Stokes lines are observed with spectral profiles centered at around 1135 nm and 1263 nm, respectively. More details about the spectral characterization is shown later in section 2.2 and 2.3.

In order to measure the power contained in each beam (pump, Stokes lines) at the output of the MPC, we have separated the pump and Stokes lines spatially using a transmission diffraction grating. Figure IV.2 displays the measured average output power of the pump and Stokes lines as a function of the total power at the MPC output. The maximum conversion efficiencies for each Stokes shift and line and various pulse durations are reported in table IV.1.

Duration (ps)	Conversion efficiency (%)			
	768 cm ⁻¹ shift		901 cm ⁻¹ shift	
	1 st Stokes	2 nd Stokes	1 st Stokes	2 nd Stokes
10	46	37	48	13
15	42	31	42	24
35	40	11	48	4

Table IV.1 – Maximum conversion efficiency at the output of the MPC.

With the increase in the pump pulse duration, the generation of the first and second Stokes is obtained at an increased value of input power, as shown in figure IV.3. This can be understood by the fact that the peak power is reduced with the increased pulse duration. However, the damage threshold decreases with the pulsewidth, and we did not explore the full energy range at 10 ps pulse duration. It is interesting to note that the longest pulsewidth of 35 ps allows to obtain the largest 1st order Stokes power, since conversion to the 2nd Stokes line is postponed compared to the 15 ps case. This last case allows the largest conversion to the second Stokes line.

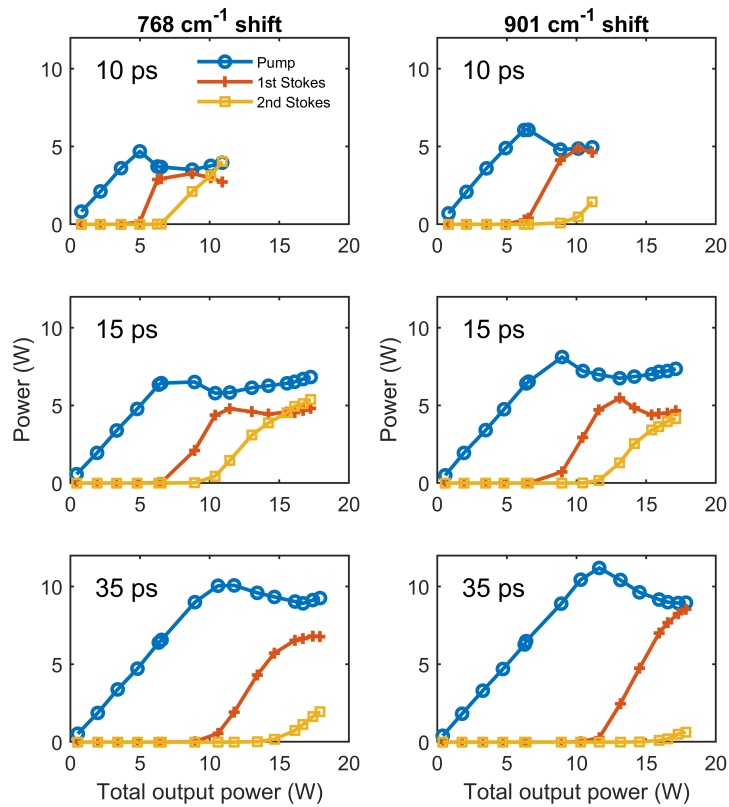


Figure IV.2 – Row 1: Average power of the pump and Stokes lines for the (left) 768 cm⁻¹ and (right) 901 cm⁻¹ shift as a function of the total output power for a pump duration of 10 ps at FWHM; Row 2: Average power of the pump and Stokes lines for the (left) 768 cm⁻¹ and (right) 901 cm⁻¹ shift as a function of the total output power for a pump duration of 15 ps at FWHM; Row 3: Average power of the pump and Stokes lines for the (left) 768 cm⁻¹ and (right) 901 cm⁻¹ shift as a function of the total output power for a pump duration of 35 ps at FWHM;

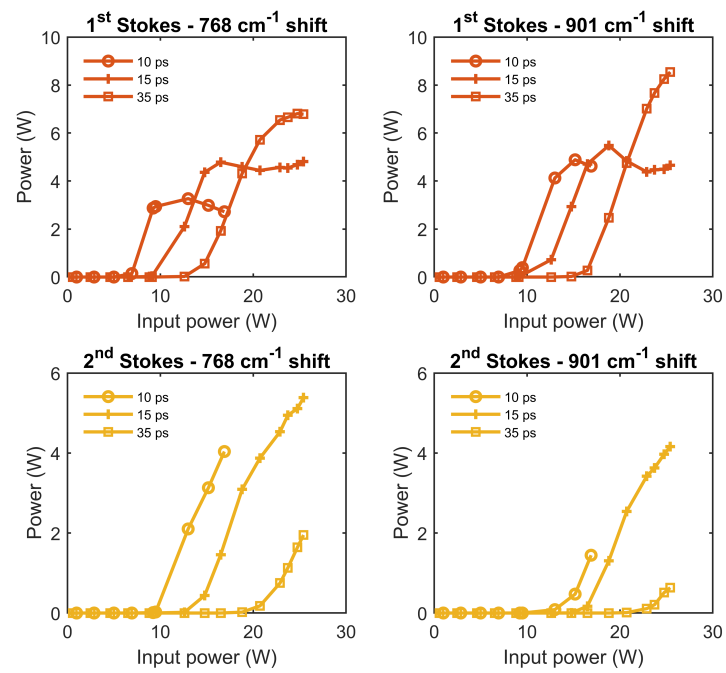


Figure IV.3 – Row 1: Average power of the 1st Stokes line for the (left) 768 cm⁻¹ and (right) 901 cm⁻¹ shift as a function of the input power for a pump duration of 10 ps, 15 ps and 35 ps at FWHM. Row 2: Average power of the 2nd Stokes line for the (left) 768 cm⁻¹ and (right) 901 cm⁻¹ shift as a function of the input power for a pump duration of 10 ps, 15 ps and 35 ps at FWHM.

2.2 Spatial filtering action in a MPC

Due to a problem in the laser system that we are using, the setup had to be re-implemented into another experimental room to continue the study with an emphasis on the spatial and temporal quality of the converted beams at the MPC output. We chose to work with a fixed stretched pulse duration that allows observation of the second Stokes line.

2.2.1 Experimental setup

For this study, the scheme is not so different from the one used in section 2 and is shown in figure IV.4. The input pulses are also generated from a high-energy ytterbium-doped fiber chirped pulse amplifier delivering a maximum average power of 19 W with a 150 kHz repetition rate, corresponding to 126 μJ pulse energy, at 1030 nm central wavelength. The input pulse is positively chirped from 320 fs to 18.7 ps at FWHM, larger than the Raman dephasing times in KGW of the order of a few ps. The corresponding FROG-retrieved measurement is shown in figure IV.5. We clearly see that the temporal profile is replicating the spectra shape, as expected for a highly chirped femtosecond pulse. The measured spatial quality factor of the laser beam is $M^2 = 1.06$ in both horizontal and vertical directions. For this study the pump beam is first directed to the MPC through the arrangement of three lenses. This MPC presents the same geometrical configuration as the one described in section 2.1.1 ($L = 504$ mm and 1-inch diameter mirrors with 300 mm radius of curvature, 18 roundtrips) with the 3 mm-long KGW inserted near the center of the MPC. At maximum input power, the estimated peak power is 6 MW, which is much higher than the critical power in the KGW of around 400 kW. The self-focusing distance in these conditions is estimated to be 6.7 cm, 20 times longer than the crystal length. The beam exiting the MPC is collimated with a 750 mm-focal length lens and sent to various devices for characterization.

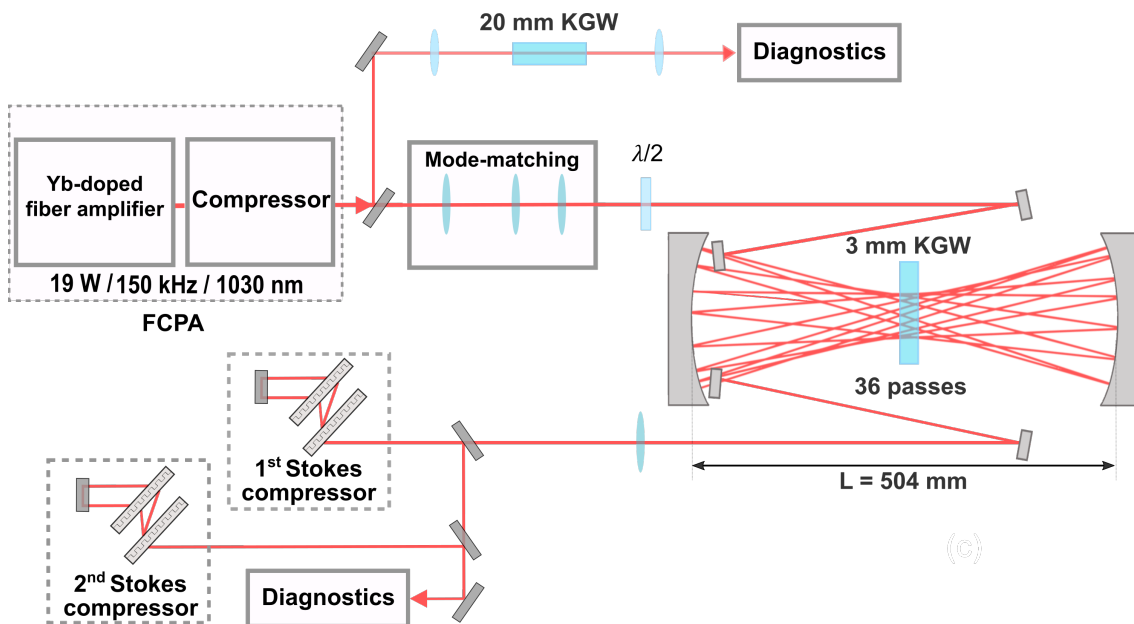


Figure IV.4 – Experimental setup for Raman conversion in a MPC and Stokes compression.

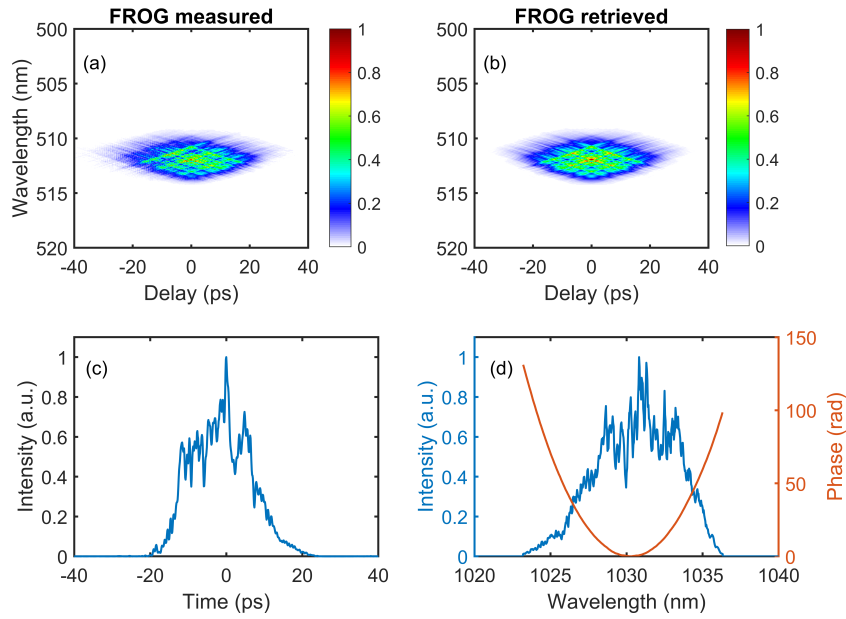


Figure IV.5 – Positively chirped input pump (a) measured and (b) retrieved FROG traces plotted in linear scale; (c) FROG-retrieved temporal intensity profile and (d) FROG-retrieved spectral intensity profile of the positively chirped input pump pulse (blue) and the retrieved spectral phase (red).

2.2.2 Conversion efficiency

Before performing spatial characterization, we have separated the pump and Stokes lines spatially at the output of the MPC using a transmission diffraction grating in order to measure the power of each beam and have an idea of the obtained conversion efficiency. Figure IV.6 displays the average output power of the pump and Stokes lines as a function of the total power at the MPC output. The corresponding spectral lines obtained at the output of the MPC at the maximum input power are also illustrated in figure IV.6. For the 768 cm^{-1} shift, a maximum conversion efficiency of 44.6% and 30% is obtained at an input energy of $93\ \mu\text{J}$ and $126\ \mu\text{J}$ for the first and second Stokes lines, respectively. As for the 901 cm^{-1} shift, the efficiency drops to 42% and 17.4%, and is obtained at an input energy of $112\ \mu\text{J}$ and $126\ \mu\text{J}$, for the first and the second Stokes lines, respectively. This drop in the conversion efficiency for the 901 cm^{-1} shift can be explained by the fact that the steady-state Raman gain coefficient is higher for the 768 cm^{-1} line ($g_R = 4.4\text{ cm/GW}$) than for the 901 cm^{-1} ($g_R = 3.3\text{ cm/GW}$).

We also performed spectral measurements at the output of the MPC using an Optical Spectrum Analyzer (OSA). Figure IV.7 displays the measured output spectral intensity profiles of the pump, Stokes lines obtained for both shifts at the output of the MPC. Figure IV.7 (a) and (d) displays the output pump spectral profile for different values of input energy. We can notice that the intensity on the short wavelength side is reduced when the input energy is increased, or in other words when there is conversion to Stokes beams. This is related to the delayed response of the Raman effect that converts more efficiently at the trailing edge of the pulse, corresponding to the short wavelength side of the pump spectrum. This is also observed in numerical simulations in section 2.3. As for the Stokes beams, the spectral shape also varies

with the input pump energy with a noticeable peak structure.

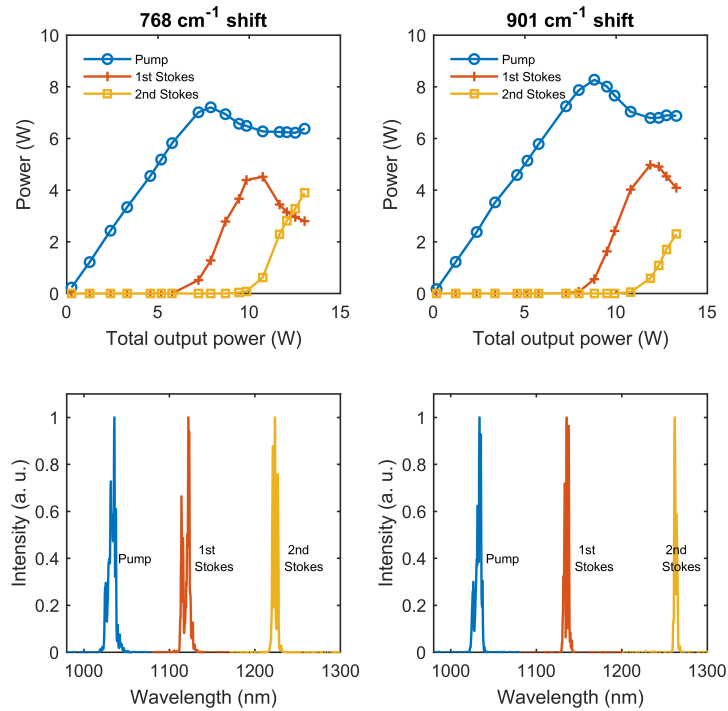


Figure IV.6 – Left column: (top) Average power of the pump and Stokes lines for the 768 cm⁻¹ shift as a function of the total output power and (bottom) corresponding measured spectra; Right column: (top) Average power of the pump and Stokes lines for the 901 cm⁻¹ shift as a function of the total output power and (bottom) corresponding measured spectra.

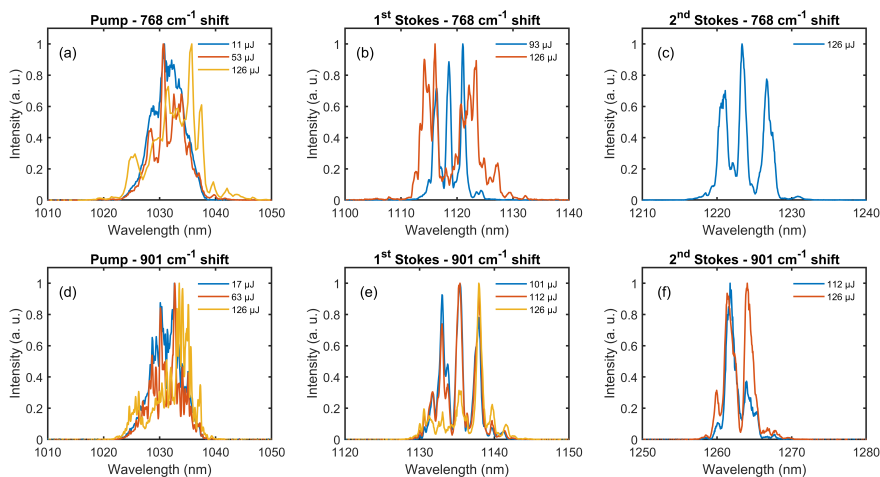


Figure IV.7 – First row, 768 cm⁻¹ shift: Measured spectral profile for the (a) pump at the MPC output at different values of input energy, (b) 1st Stokes and (c) 2nd Stokes lines at the MPC output. Second row, 901 cm⁻¹ shift: Measured spectral profile for the (d) pump at the MPC output at different values of input energy, (e) 1st Stokes and (f) 2nd Stokes lines at the MPC output.

2.2.3 Spatial characterization at the MPC output

In the following, we focus on the 768 cm^{-1} Stokes lines for further spatial characterization. The spatial profiles measured at the output of the MPC for the pump at low power and for the Stokes lines at maximum conversion efficiency are shown in figure IV.8. We use longpass filters adapted for each of the Stokes beams in order to isolate them and an InGaAs-based detector camera.

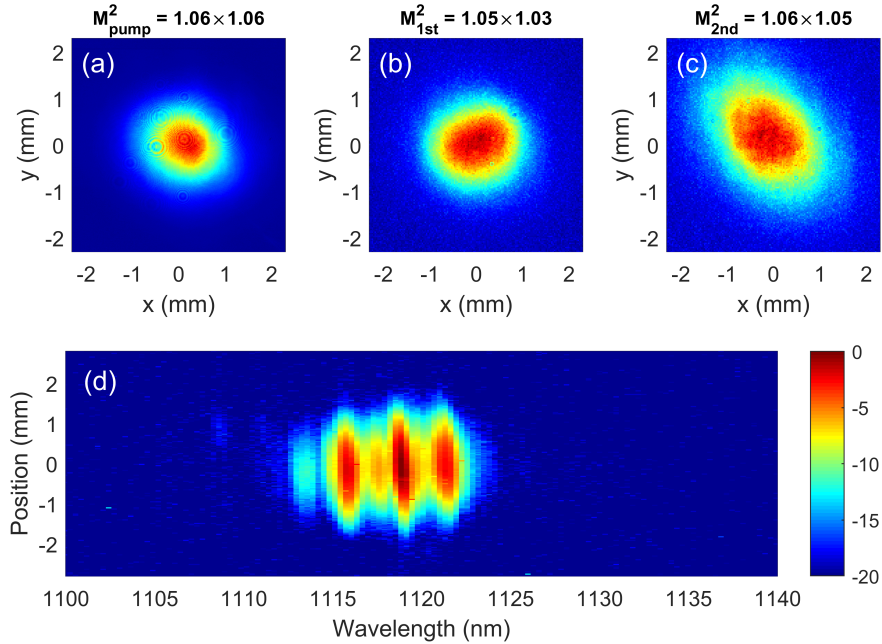


Figure IV.8 – Measured spatial beam profile of the (a) pump, (b) 1^{st} Stokes and (c) 2^{nd} Stokes lines for the 768 cm^{-1} at the MPC output; (d) Experimental spectro-imaging measurement in logarithmic (dB) scale.

A measured beam diameter of 2.3 by 2.4 mm, 2.5 by 2.6 mm, and 2.6 by 3.9 mm at $1/e^2$ is obtained at the MPC output for the pump, 1^{st} Stokes and 2^{nd} Stokes, respectively. This increase in beam size is coherent with the fact that a larger central wavelength translates into faster divergence for a given waist size. We also measured the beam quality factor of the 1^{st} Stokes and 2^{nd} Stokes lines with obtained values of $M^2 = 1.05 \times 1.03$ and $M^2 = 1.06 \times 1.05$ obtained, respectively. These results show the preservation of the beam quality of the pump beam in the generated Stokes signals with a more pronounced ellipticity observed in the 2^{nd} Stokes. The origin of this ellipticity is not clear. However, it is worthwhile to mention that no ellipticity is observed for the 2^{nd} order of the other Stokes shift of 901 cm^{-1} , as shown in figure IV.9. No M^2 measurement were performed for the output converted beams for the 901 cm^{-1} shift.

We also check the spatio-spectral properties of the 1st Stokes line by using an imaging spectrometer setup. It consists of an f-f arrangement composed of an 800 lines/mm grating, a 100 mm focal length cylindrical lens and an InGaAs camera with a 30 μm pixel size. The result, presented in figure IV.8 (d), shows no obvious spectral inhomogeneity in the beam, as expected from a MPC setup.

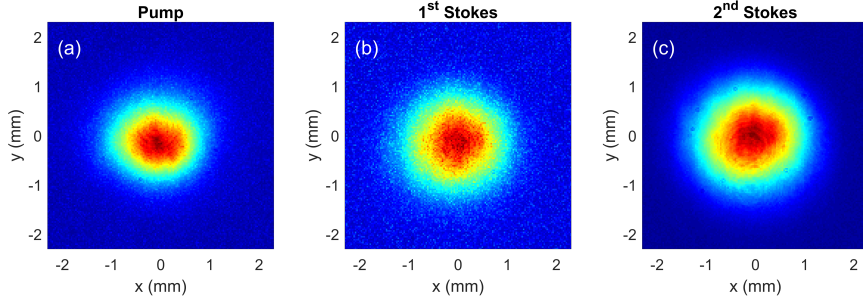


Figure IV.9 – Measured spatial beam profile of the (a) pump, (b) 1st Stokes and (c) 2nd Stokes lines for the 901 cm^{-1} shift at the MPC output.

The spatial properties of the Stokes beams are remarkable compared to previously reported single pass Raman conversion experiments [Zhavoronkov 01]. We therefore perform an experimental comparison with a single pass scheme to check this result. This is the subject of the next section.

2.2.4 SRS in single pass scheme

The same input chirped pump pulses are focused into a 20 mm-long KGW crystal with a 400 mm-focal length lens, as shown in the upper part of figure IV.4. The KGW crystal is positioned slightly after the waist at a location where the beam diameter is $\sim 400 \mu\text{m}$, to obtain a comparable intensity compared to the MPC case. The beam is then collimated and sent for characterization. The first Stokes line obtained for the 768 cm^{-1} is observed at full pump pulse energy, with a converted power of 2 W, corresponding to a conversion efficiency of 10%.

Figure IV.10 shows the measured beam profiles of the pump at low power and first Stokes at maximum power which are measured at the same position after collimation. The diameter of the obtained Stokes beam is 3.3 by 3.2 mm at $1/e^2$, much larger than the measured diameter of the pump beam, of 0.4 mm. The beam quality factor of the Stokes beam is $M^2 = 2.7 \times 2.5$ along the horizontal and vertical directions, respectively. As for the 901 cm^{-1} , the first Stokes line is observed at full pump pulse energy, with a converted power of 1 W, corresponding to a conversion efficiency of around 5%. The beam quality factor of the Stokes beam for this shift is a little better than the other one with a value of $M^2 = 1.8 \times 1.7$ along the horizontal and vertical directions, respectively.

We also performed spectral measurements at the output of the 20 mm KGW crystal using the OSA. Figure IV.12 displays the measured spectral intensity profiles of the input pump (blue curves in IV.12 (a) and (c)), and the measured spectral intensity profile at the output of the KGW crystal for maximum input energy of $126 \mu\text{J}$ (green curves in IV.12 (a) and (c)). The measured spectral profile of the first Stokes at the output of the 20 mm KGW crystal obtained for both shifts is presented in figure IV.12 (b) and (d). Nonlinear propagation and conversion to the Raman-shifted wavelength is accompanied by the appearance of highly structured spectra. This will be more commented in section 2.3.

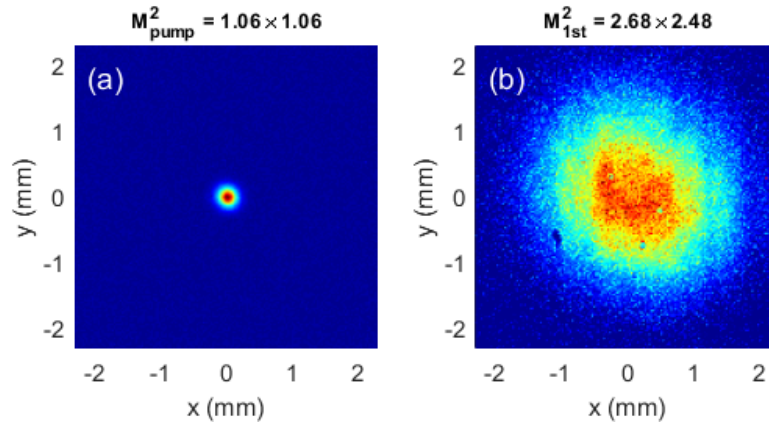


Figure IV.10 – Measured spatial profiles of the (a) pump and (b) 1^{st} Stokes line for the 768 cm^{-1} shift at the same position after collimation at the output of the 20 mm KGW crystal.

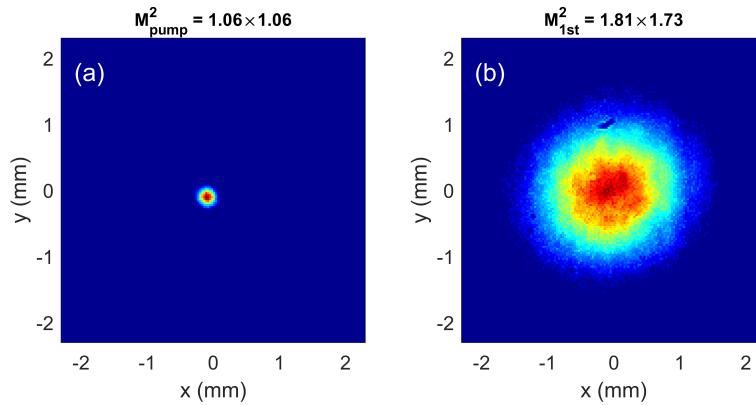


Figure IV.11 – Measured spatial profiles of the (a) pump and (b) 1^{st} Stokes line for the 901 cm^{-1} shift at the same position after collimation at the output of the 20 mm KGW crystal.

Note that for the 768 cm^{-1} shift a small signal of Anti-Stokes is observed at a central wavelength of 953 nm , as shown in figure IV.13.

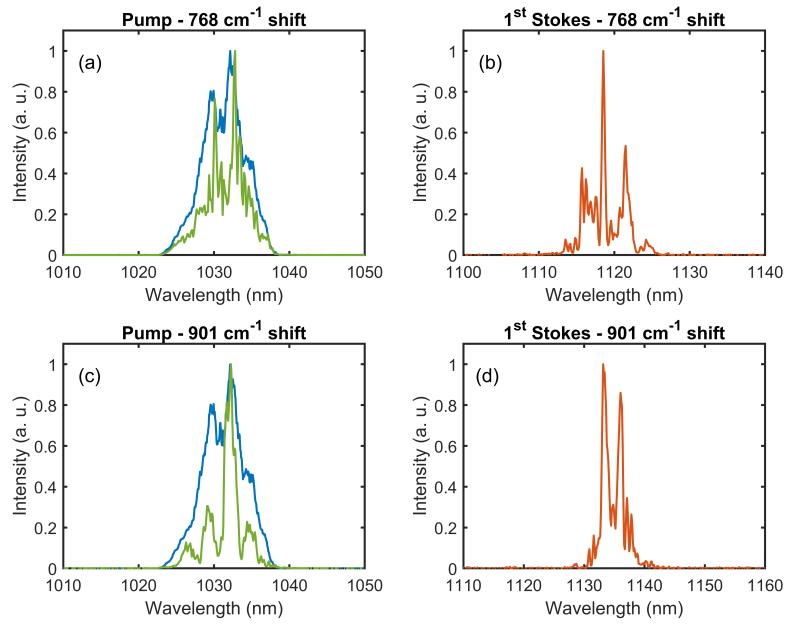


Figure IV.12 – Measured spectral intensity profile of the (a) pump at the input (blue) and at the output (green) of the 20 mm KGW at maximum input energy and (b) of the 1st Stokes line for the 768 cm⁻¹ shift at maximum input energy. Measured spectral intensity profile of the (c) pump at the input (blue) and at the output (green) of the 20 mm KGW at maximum input energy and (d) of the 1st Stokes line for the 901 cm⁻¹ shift at maximum input energy.

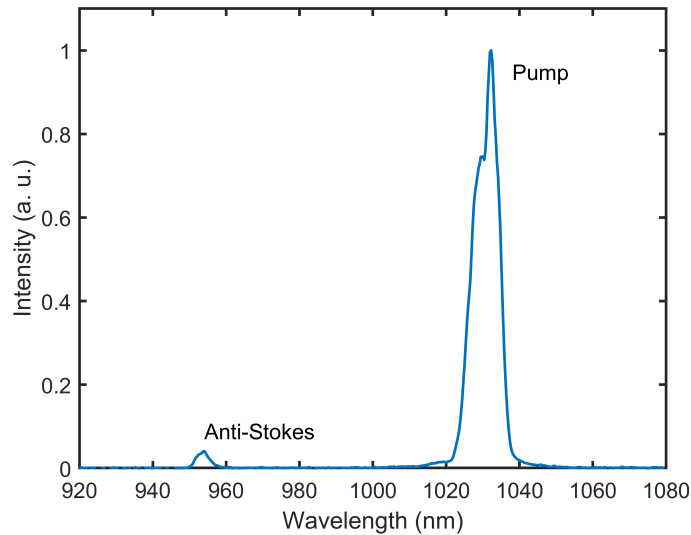


Figure IV.13 – Measured Anti-Stokes and pump spectral profiles at the output of the KGW crystal at maximum input energy for the 768 cm⁻¹ shift.

2.2.5 Comparison and discussion

The spatial features observed in the previous section can be interpreted as follows. The local Raman gain coefficient is proportional to the intensity, which leads to a much larger gain at the beam center. As a result, for small enough pump depletion, the Raman converted beam in single pass is much smaller than the pump beam, which translates to a much larger beam after diffraction and collimation. In addition, for non-seeded setups, the process starts from quantum noise, so that the spatial coherence is low, resulting in mediocre beam quality factors. In contrast, in the MPC setup, the generated Stokes beam in the first passes is then co-propagated with the pump, and spatial filtering imparted by propagation in the MPC and the Raman gain at each pass progressively induces spatial coherence and a beam size that is comparable to the pump beam. Although this process reduces the Stokes signal growth compared to a single pass setup, this is compensated by the fact that multiple passes in the cell result in a larger interaction distance with the nonlinear material.

To back up this interpretation, we perform a Hankel transform-based split-step 2D nonlinear propagation simulation including all relevant effects, described by Eq.(I.1), and seeded by the FROG-measured input pulse. The results of the numerical simulation is illustrated in figure IV.14. It shows a comparison of the energy conversion as well as the beam size evolution for the case of a single pass and MPC setup scheme. The simulation is performed for a set of parameters corresponding to the experiments performed.

The beam radius variation as a function of the propagation distance in the 20 mm KGW crystal, which starts at $z = 0.09$ m and ends at $z = 0.11$ m, shows that the 1st Stokes beam is generated much smaller than the pump beam inside the crystal which leads to more divergence at the output of the KGW crystal. However, in the case of the MPC, the beam radii of the converted beams converge to approximately the same size as the pump beam. The beam size of the second Stokes line features a larger size at the MPC mirrors, which is probably due to the difference in central wavelength and therefore in diffraction properties.

In both cases, the large values of the beam radii for the converted beams observed at the beginning of the propagation is due to the fact that these are evaluated by first filtering the spatio-temporal field over a bandwidth corresponding to the Stokes line, and then computing the radius of the beam using the second moment of the spatial field. In the absence of any converted radiation, the only light that is present in the filtered bandwidth is the "one photon per spatial and temporal mode with a random phase" noise that is added to account for quantum noise and act as the Raman seeder. These photons are distributed homogeneously in time and space, and therefore yield a beam size that is comparable to the size of the numerical window. As propagation takes place, the absorbing layer at the edges of the computation window progressively filters this noise, which causes the decreases in size observed in the simulations. In all cases, the beam radii start to have a meaning when a significant energy has been converted to the bandwidths of interest.

In the singlepass case, we clearly observe the effect of the Kerr lens on the pump, that causes a focusing of the pump beam after the KGW crystal, since its length of 20 mm starts to be comparable with the estimated self-focusing distance of 6.7 cm.

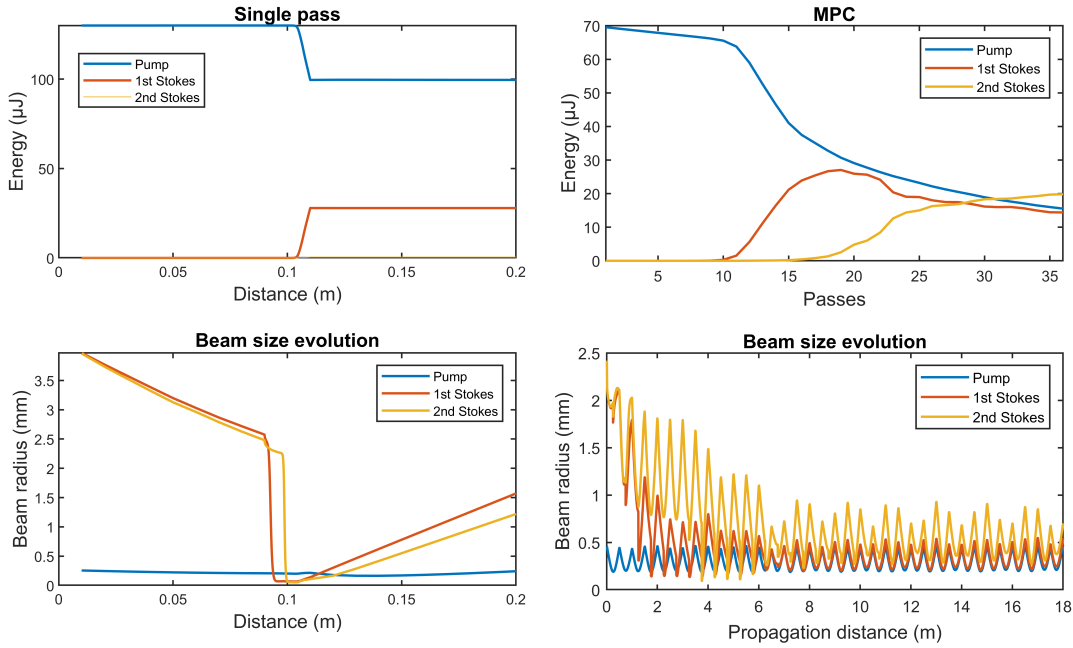


Figure IV.14 – Simulation result for a set of parameter corresponding to the performed experiment in (left) single pass and (right) MPC. The 20 mm Raman crystal starts at $z=0.09$ m and ends at $z=0.11$ m, at the $200 \mu\text{m}$ waist radius of the beam. Energy conversion as a function of the propagation distance for (top left) the single pass in a 20 mm KGW crystal and (top right) the MPC case; Beam size evolution as a function of the propagation distance for (bottom left) the single pass in a 20 mm KGW crystal and (bottom right) the MPC case.

2.3 Temporal characterization

2.3.1 Temporal measurement of stretched pulses

In this part, we will focus on the characterization of the pump and Stokes beams obtained for the 768 cm^{-1} shift at the output of the MPC. The characterization is done using a second-harmonic-generation FROG setup at maximum conversion efficiency for each of the Stokes lines of the 768 cm^{-1} shift. The pulse durations at FWHM for the first and second Stokes lines are 8.8 ps and 6.3 ps, respectively. This is due to the fact that the delayed Raman response induces more efficient conversion at the trailing edge of the input pulse resulting in shorter converted pulse widths, as shown in figure IV.15.

Temporal and spectral evolutions as a function of the propagation distance in the MPC can be obtained by using numerical simulation. This is presented in figure IV.17. On the top right of the figure, we see the numerically obtained temporal profiles at the output of the MPC using the set of corresponding parameters of the experiment and seeded by the input FROG measurement. There is a qualitative agreement with the measured temporal profiles illustrated in figure IV.15. Each Stokes line appear successfully in time, due to the delayed nature of the Raman response.

Figure IV.16 illustrates the spectrograms obtained from the FROG-retrieved fields for the pump pulse, first and second Stokes beams. The instantaneous frequency for the three cases

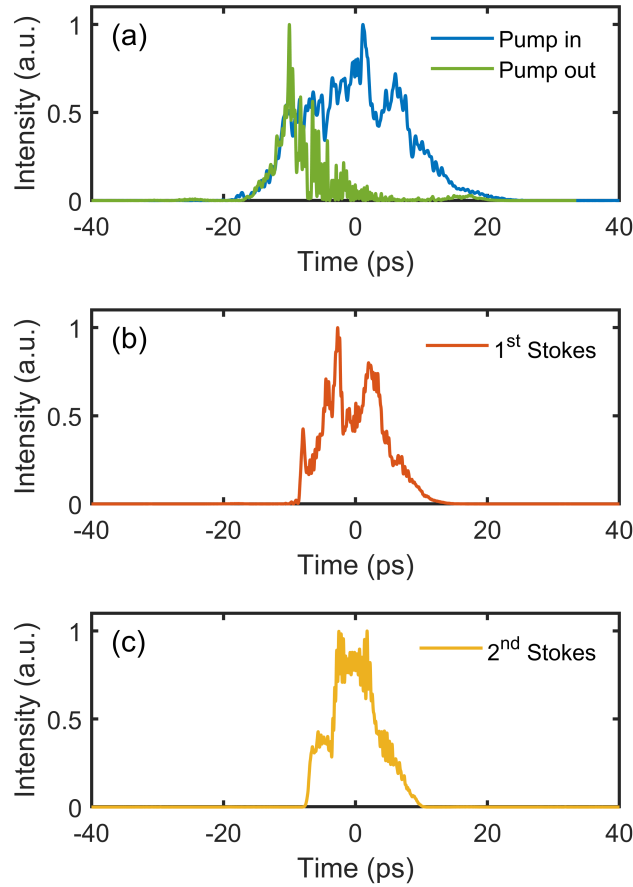


Figure IV.15 – (a) FROG-retrieved temporal intensity profile of the chirped input pump (blue) and the pump (green) at the MPC output at maximum input energy; (b) FROG-retrieved temporal intensity profile of the 1st Stokes at the MPC output at 93 μJ input energy; (d) FROG-retrieved temporal intensity profile of the 2nd Stokes at the MPC output at 126 μJ input energy.

increases over time with the same average slope, confirming that the input chirp is imprinted onto the converted pulses. However, in figure IV.16 (b) and (c) we notice a staircase-like structure in the instantaneous frequency of the first and second Stokes, which has not been reported before to our knowledge. This characteristic could be related to the fact that the input chirped pulse does not exhibit a smooth temporal intensity profile. SPM and XPM effects can then act on the spectrograms as instantaneous frequency shifters, resulting in these frequency oscillations around the main chirp slope. Using numerical simulations seeded by the FROG-measured input pulse, the oscillations around the main chirp slope in the spectrogram can indeed be reproduced at locations corresponding to intensity modulations of the input pump pulse. This is shown in figure IV.19. Note that figure IV.16 and IV.19 do not correspond to the same situations. Figure IV.16 shows the spectrogram at the maximum converted power for each Stokes line, where figure IV.19 shows the spectrogram at the output of the MPC for a single input energy, the same as figure IV.14.

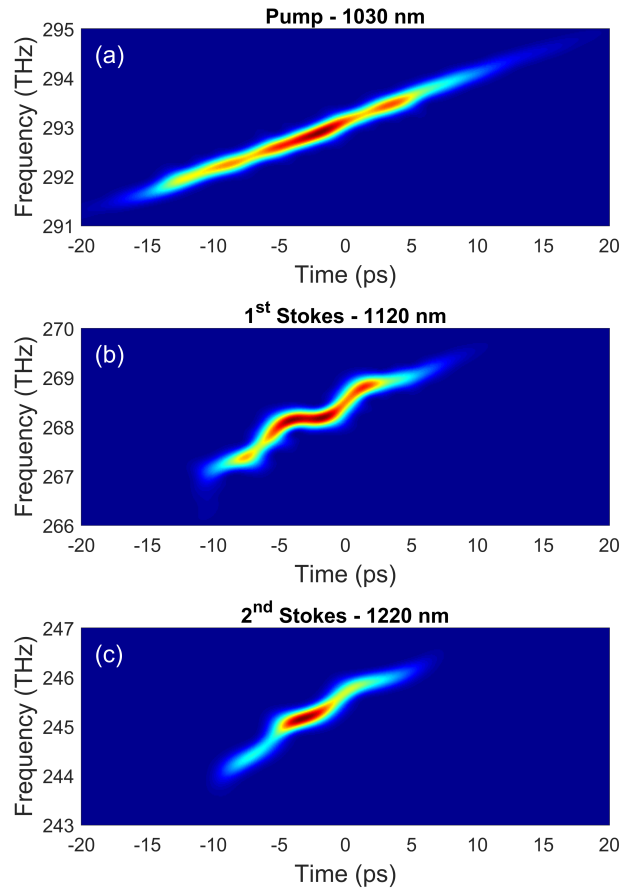


Figure IV.16 – Spectrogram of the (a) chirped input pump at the MPC input, non-compressed (b) 1st Stokes and (c) 2nd Stokes at the MPC output.

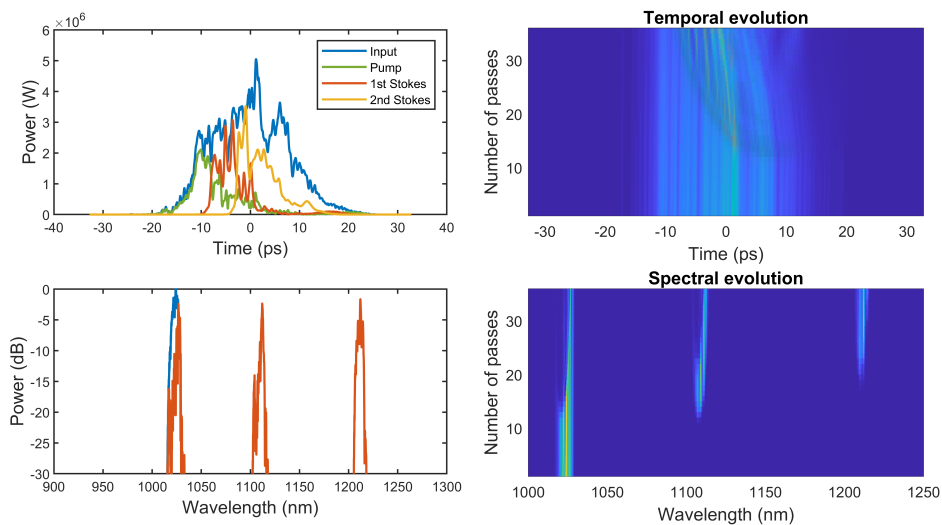


Figure IV.17 – Simulation results for a set of parameter corresponding to the performed experiment in the MPC; (Top left) Temporal intensity profile at the MPC output; (Top right) Temporal evolution as a function of the number of passes in the MPC; (Bottom left) Spectral intensity profiles at the MPC output; (Bottom right) Spectral evolution as a function of the number of passes in the MPC.

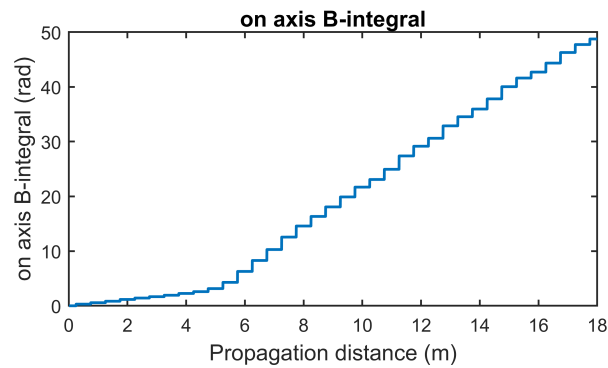


Figure IV.18 – Numerically calculated B-integral on axis as a function of the propagation distance in the MPC.

Figure IV.18 shows the on-axis B-integral as a function of distance. In this case, the B-integral is defined as the maximum phase excursion in time due to the nonlinear effect, including the delayed Raman response. The onset of stimulated Raman scattering is clear at about 6 m of propagation distance, where the Raman-induced phase becomes much larger than the electronic contribution of instantaneous self-phase modulation. This coincides with the generation of significant power at the Stokes wavelength, as depicted in figure IV.14.

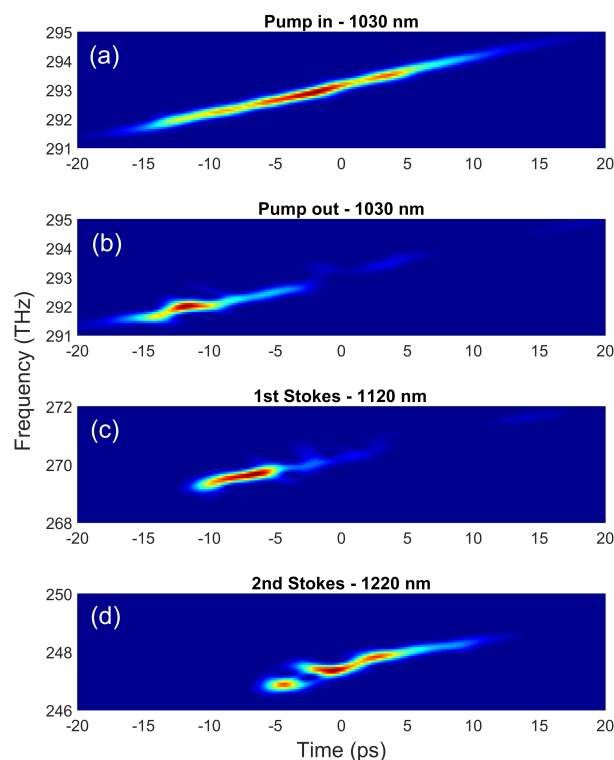


Figure IV.19 – Numerically obtained spectrogram of the (a) chirped input pump at the MPC input, (b) pump at the MPC output, non-compressed (c) 1st Stokes and (d) 2nd Stokes at the MPC output.

2.3.2 Compression of wavelength-shifted pulses

We now describe our attempts to temporally compress the Stokes beams at the output of the MPC for an input energy corresponding to maximum efficiency for each line. We used a pair of diffraction gratings in transmission with a number of lines/mm adapted for each of the Stokes lines. More specifically, they have been chosen so that the φ_3/φ_2 ratio matches the pump compressor at Littrow incidence. The optimal compression point is searched by fine adjustments of the incident angle on the gratings and of the distance separating them.

For the first Stokes (1120 nm), a pair of gratings with 1570 lines/mm is used, and the compression yields a pulse duration of 520 fs at FWHM, as shown in figure IV.20 (c). The compressor throughput is 80%. For the second Stokes beam (1220 nm), a pair of gratings with 1400 lines/mm is used, compressing the second Stokes to 800 fs pulse duration at FWHM, where the retrieved temporal profile is shown in figure IV.21 (c), with a compressor efficiency of 66%. This temporal compression is clearly not very clean, with large pedestals and side pulses. This can be traced back to the structure observed in the time-frequency domain (spectrograms), showing a non-homogeneous chirp rate, or equivalently a higher order spectral phase, that the gratings pair can not compensate. In addition, the corresponding spectrograms of the FROG measurements of the compressed 1st and 2nd Stokes shown in figure IV.22 shows a good compression at around the center of the pulse but with slight remaining chirp.

It is also noticeable, that the obtained spectra possess a peak structure for both the first and the second Stokes, as shown in figure IV.20 (d) and IV.21 (d). This spectrally observed structure is likely related to the SPM/XPM-induced spectrogram shaping observed in figure IV.16.

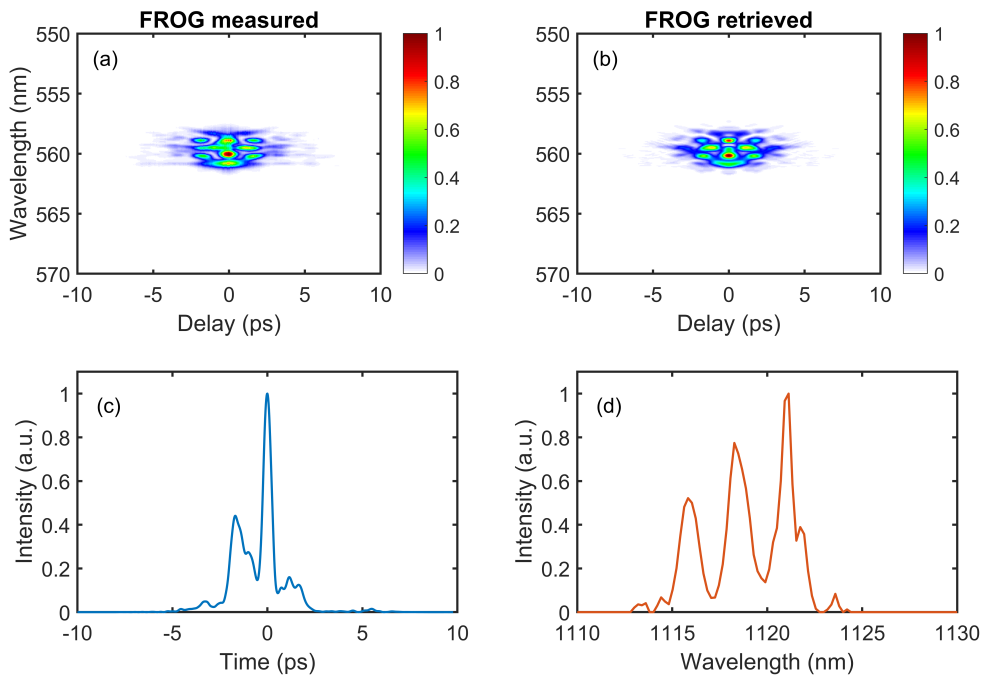


Figure IV.20 – (a) Measured and (b) retrieved FROG traces plotted in linear scale at the MPC output at 93 μJ input energy; (c) FROG-retrieved temporal intensity profile and (d) FROG-retrieved spectral intensity profile of the 1st Stokes after compression at the MPC output.

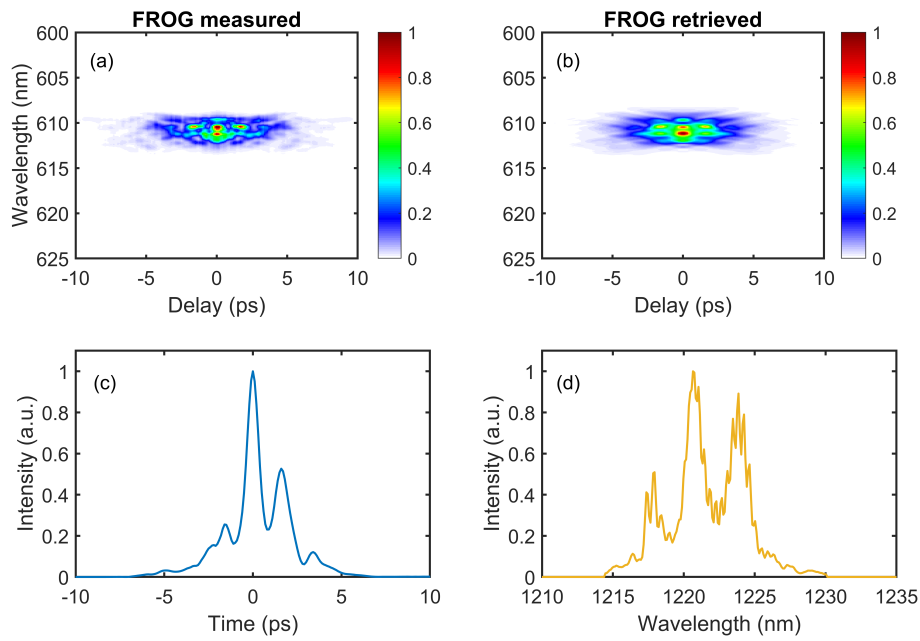


Figure IV.21 – (a) Measured and (b) retrieved FROG traces plotted in linear scale at the MPC output at $126 \mu\text{J}$ input energy; (c) FROG-retrieved temporal intensity profile and (d) FROG-retrieved spectral intensity profile of the 2^{nd} Stokes after compression at the MPC output.

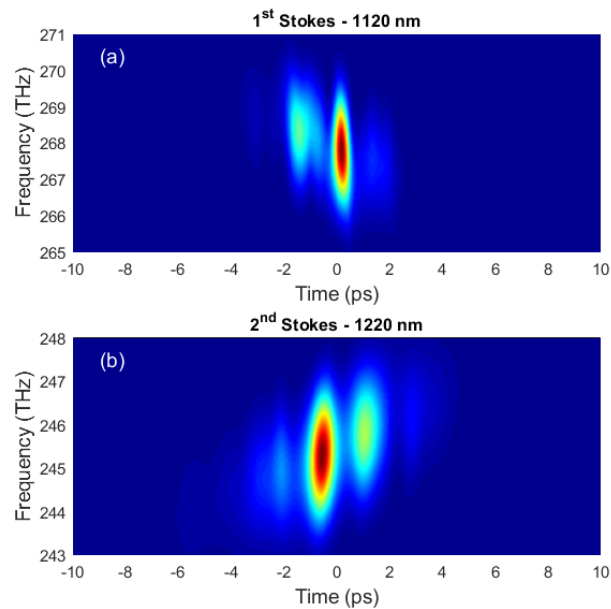


Figure IV.22 – Spectrogram of the temporally compressed (a) 1^{st} Stokes and (b) 2^{nd} Stokes.

3 Conclusion

Nonlinear Raman frequency shifting is a widely used method to extend the wavelength coverage of laser sources in temporal regimes ranging from CW to femtosecond pulses. To do so, a number of architectures have been reported, using a single or several stages of Raman generation / amplification, that can be seeded or not.

In this chapter, it is shown that co-propagation of the pump and Stokes beam inside a solid-state MPC imparts a spatial filtering action, resulting in high quality converted beams, with efficiencies that are comparable to the state of the art. This architecture also allows the use of peak powers much higher than the critical power in the material over long overall interaction lengths. Spatial characterization at the MPC output is performed and compared to a single pass scheme illustrating the spatial filtering action which is also backed-up and observed in Hankel transform-based numerical simulations.

Temporal characterization at the output of the MPC is performed for the pump and the Stokes beams. Stokes lines for the 768 cm^{-1} shift are then temporally compressed at the output of the MPC. The temporal compression obtained is not very clean due to the non-homogeneous chirp rate, or equivalently a higher order spectral phase acquired during propagation, that cannot be compensated for by the gratings pair. A peak structure is observed in the spectral profiles of the 1st and 2nd Stokes which is likely related to effect of SPM and XPM. This was a proof-of-principle experiment, and a first attempt at conversion. It is probably possible to optimize the conversion towards a given Stokes line and the compressibility by adjusting parameters such as input pulse chirp, MPC mirrors, Raman material length, etc.

Extending the possibilities in terms of target wavelength and input pulse energy could be done by using other efficient Raman materials such as diamond or even molecular gases such as hydrogen. Furthermore, the MPC could allow control of the Raman cascade by using mirrors with engineered coatings to stop the cascade at a given Stokes line.

Finally, since Raman scattering is an inelastic process, scaling the average power can be limited by thermal effects [McKay 14, Heinzig 21]. In this MPC scheme, the thermal load is distributed to distinct spots at each pass through the Raman material, which could be advantageous. We therefore believe that Raman conversion is an interesting application of nonlinear MPCs.

General Conclusion

Nonlinear optics is a major component of the technological toolkit in ultrafast optics. Its implementation in multipass cells has been a trend for the past few years, especially in the field of post-compression of laser sources. MPCs allows distribution of the nonlinear interaction over large distances and multiple beam foci, maintaining spatio-temporal couplings under control. These platforms provide numerous engineering possibilities to control the nonlinear interactions, through the choice of MPC geometry, nonlinear media, and design of the cell mirrors. In addition, they offer remarkable properties in terms of their energy throughput, their energy and power scalability, and their robustness to beam pointing and position fluctuations due to their extended free aperture. However, the main challenge for this technique is mirror coating technology. It is difficult to combine the different requirements on the MPC mirrors, since they should support the require bandwidth, possess a high reflectivity to keep a high throughput, and exhibit a very high laser-induced damage threshold, to keep the size of the beam at the MPC mirrors reasonable. At one point a tradeoff must be made. Numerous work based on multipass cells have been performed since 2016, with a variety of laser sources and nonlinear media, where the majority lies within the context of temporal compression by self-phase modulation. It was demonstrated to be a very reliable post-compression technique that nowadays exists as a commercially available product called *Compress*, manufactured by Amplitude.

One of the main advantage of MPCs over single or multi-plate setups is the accumulation of a large B-integral in the time domain while keeping the spatial and spatio-temporal properties under control. Although simulations and experiments have established the robustness of MPCs against spatio-temporal degradations, it was not fully established how far we can push the nonlinearity in MPC setups while retaining spatio-spectral couplings-free output beams, although a clear upper bound is the critical power in the gas medium.

Therefore, the first part of this thesis was dedicated to the study of spatio-spectral properties of the output beam propagating in a highly nonlinear xenon-filled MPC. We observed the effect of wave breaking in this highly nonlinear normal dispersion propagation regime. Spatio-spectral measurements were performed using an imaging spectrometer and a full 3D characterization technique to characterize the output beam. The work showed that gas-filled MPCs can be used at peak power levels close to the critical power without introducing severe spatio-temporal couplings in intensity or phase.

An interesting feature of self-phase modulation is its dependency on the sign of the input chirp of the incident pulse. Although SPM results at the output of the nonlinear medium in

spectral broadening for FTL or positively chirped pulses, spectral compression is the consequence of incident pulses with a negative chirp. Mainly it is due to the fact that the nonlinear phase accumulated during propagation shifts extreme spectral components towards the center of the spectrum, canceling the initial chirp and generating almost FTL pulses with an unchanged duration. The optical fiber community has been using SPM-induced spectral compression in optical fiber as a tool to turn a femtosecond laser source into a close to FTL picosecond source. However, the pulse energies are limited by self-focusing to the μJ range. Bulk material-based MPC can be an alternative way to perform spectral compression while allowing peak powers in excess to the critical power, thereby scaling the energy of spectrally compressed pulses. We have demonstrated the generation of near FTL high peak power picosecond pulses through the use of a solid-state MPC where the beam recirculates in 24 mm-long fused silica inserted near the center of the cell. The input 260 fs pulses originating from an Yb-doped fiber amplifier are negatively chirped to 2.4 ps and then are spectrally compressed at the output of the MPC from 6 nm to 1.1 nm with an output energy of 13.5 μJ and a near FTL pulses of 2.1 ps. Using a pulse shaper included in the FCPA, the spectral shape at the output of the MPC was symmetrized. The spatial quality and spatio-spectral homogeneity are conserved in this process.

Stimulated Raman scattering used to perform wavelength conversion of available laser sources is an interesting effect to investigate in multipass cells. It has been implemented since 1980 to extend the interaction length in Raman active gases to perform wavelength conversion of narrow bandwidth nanosecond pulses. Therefore, a part of the work done in this thesis focused on the re-implementation of Raman conversion in a MPC, but this time using a solid-state MPC to perform wavelength conversion of positively chirped femtosecond pulses generated from an Yb-doped fiber amplifier. A 3 mm-long KGW crystal is inserted near the center of the cell to serve as the Raman material. The input 1030 nm pulses can be shifted to around 1120 nm or 1130 nm (1st Stokes) and 1220 nm or 1260 nm (2nd Stokes) depending on the input laser polarization. High conversion efficiencies $> 40\%$ and good spatial beam quality ($M^2 < 1.2$) for the generated Stokes beams have been obtained. Propagation of the pump and the Stokes signals inside the MPC resulted in a spatial filtering action, which is not observed in the case of a single pass scheme. We then compressed the converted pulses at the output of the MPC to sub-picosecond duration by compensating the positive chirp that the Stokes beams inherit from the input pump pulse. These Raman conversion MPC could be used in other temporal regimes, e.g., with picosecond or nanosecond pulses and with other nonlinear materials. Scaling the average power could be advantageous in such MPC schemes since the thermal load is distributed to distinct spots at each pass through the Raman material.

Although it is not described in this manuscript, in the course of this thesis, a work in collaboration with Laboratoire d'Optique Appliquée (LOA) and LIDYL (CEA) was done in order to reach the few-cycle temporal regime of mJ energy Ti:Sa laser sources. It consisted on a single-stage multipass-cell-based compressor filled with argon. The MPC is composed of two 50.8 mm enhanced silver-coated mirrors of 1.5 m radius of curvature separated by ~ 3 m, yielding a nearly concentric configuration. The pulses are compressed from 30 fs down to

5.3 fs, corresponding to two optical cycles at 800 nm with 67% overall efficiency. The output post-compressed beam exhibits very good spatial quality and homogeneity. During this experimental work, the spectral broadening capability was explored at different gas pressures, in order to determine the optimum configuration that leads to the shortest accessible compressed pulse. The obtained results provide some guidelines for optimizing the compressed pulse quality and further scaling multipass-cell-based post-compression down to the single-cycle regime. The obtained results were published recently in [Daniault 21], attached at the end of this document.

During the course of this thesis, a number of papers on MPC used in nonlinear optics have been published. A first example deals with supercontinuum generation. Although it has not been implemented experimentally, numerical simulations show that localized compressed blue-shifted spatio-temporal wavepackets with extremely short durations can be obtained upon propagation in a MPC including a plate of nonlinear bulk material [Mei 21]. This phenomenon is shown to be more efficient when distributing the nonlinearity into a large number of passes in the MPC. Although experimental observations of such effects will most likely be difficult due to technological limitations with mirror coating design, this research shows that complicated nonlinear spatio-temporal phenomena could be conducted and researched more effectively in MPCs.

Another example is the compression of beams that are more complex than the fundamental Gaussian beam, either in terms of intensity and phase profiles or in terms of polarization state. Using numerical simulations, it has been shown in [Cao 19] that it is possible to compress radially or azimuthally polarized beams, that can be described as combinations of orthogonally linearly polarized Hermite-Gaussian beams. It is shown that up to a certain level of nonlinearity, the spatio-temporal homogeneity at the output is satisfactory, similarly to the case of standard beams. The same team investigated the possibility to compress Laguerre-Gaussian beams that carry an orbital angular momentum [Cao 20]. Such beams were experimentally used in nonlinear MPCs [Kaumanns 21] because their peak intensity is reduced compared to a conventional beam carrying the same pulse energy. These works show that it is possible to exploit the spatially multimode degree of freedom in multipass cells.

A recent numerical work focused on the use of nonlinear ellipse rotation to enhance the temporal contrast of ultrashort pulses [Pajer 21]. When an elliptically polarized pulse propagates in a Kerr medium, an intensity-dependent rotation of the axes of the polarization ellipse occurs due to cross-phase modulation. This phenomenon can be used to enhance the temporal contrast defined as the ratio of the peak power to the power of pre- or post-pulses, or to the power of a broad temporal pedestal. A nonlinear filtering action results from the nonlinear ellipse rotation used in capillaries for contrast enhancement. The same can be done in MPCs in addition to temporal compression.

Several experimental works reported the generation of spectral content on the short-wavelength side of the pulses that went through self-phase modulation in gas-filled MPCs

in order to be temporally compressed [Russbueldt 19, Kaumanns 18]. This short-wavelength spectral content, that occurs at high nonlinearity level, was interpreted as a four-wave-mixing process that satisfies a quasi-phase matching relationship [Hanna 20]. The periodic nature of the nonlinearity in MPCs can offer phase matching opportunities. Therefore, these parasitic effects observed in pulse compression experiment can be eventually implemented intentionally in order to perform wavelength conversion through four-wave mixing, as reported in gas-filled capillaries [Belli 19].

In the near future, the range of applications of MPCs as a platform for nonlinear optics will undoubtedly expand. The robustness of these setups with respect to spatio-temporal couplings at reasonable nonlinearity levels makes MPCs a sort of extension of optical fibers, a privileged geometry to study and use nonlinear optics in science and engineering.

Bibliography

- [Agrawal 13] G. P. Agrawal. *Nonlinear fiber optics Academic*. New York, vol. 19892, page 44, 2013.
- [Akturk 10] S. Akturk, X. Gu, P. Bowlan, et R. Trebino. *Spatio-temporal couplings in ultrashort laser pulses*. *Journal of Optics*, vol. 12, no. 9, page 093001, 2010.
- [Alonso 10] B. Alonso, Í. J. Sola, Ó. Varela, J. Hernández-Toro, C. Méndez, J. San Román, A. Zair, et L. Roso. *Spatiotemporal amplitude-and-phase reconstruction by Fourier-transform of interference spectra of high-complex-beams*. *JOSA B*, vol. 27, no. 5, pages 933–940, 2010.
- [Amann 01] M.-C. Amann, T. M. Bosch, M. Lescure, R. A. Myllylae, et M. Rioux. *Laser ranging: a critical review of unusual techniques for distance measurement*. *Optical engineering*, vol. 40, pages 10–19, 2001.
- [Anderson 92] D. Anderson, M. Desaix, M. Lisak, et M. L. Quiroga-Teixeiro. *Wave breaking in nonlinear-optical fibers*. *JOSA B*, vol. 9, no. 8, pages 1358–1361, 1992.
- [Andresen 05] E. R. Andresen, J. Thøgersen, et S. R. Keiding. *Spectral compression of femtosecond pulses in photonic crystal fibers*. *Optics letters*, vol. 30, no. 15, pages 2025–2027, 2005.
- [Andresen 11] E. R. Andresen, J. M. Dudley, D. Oron, C. Finot, et H. Rigneault. *Transform-limited spectral compression by self-phase modulation of amplitude-shaped pulses with negative chirp*. *Optics letters*, vol. 36, no. 5, pages 707–709, 2011.
- [Arisholm 04] G. Arisholm, J. Biegert, P. Schlup, C. P. Hauri, et U. Keller. *Ultra-broadband chirped-pulse optical parametric amplifier with angularly dispersed beams*. *Optics express*, vol. 12, no. 3, pages 518–530, 2004.
- [Balla 20] P. Balla, A. B. Wahid, I. Sytceвич, C. Guo, A.-L. Viotti, L. Silletti, A. Cartella, S. Alisauskas, H. Tavakol, U. Grosse-Wortmann, et al. *Postcompression of picosecond pulses into the few-cycle regime*. *Optics letters*, vol. 45, no. 9, pages 2572–2575, 2020.

- [Bao 16] C. Bao, X. Xiao, et C. Yang. *Spectral Compression of a Dispersion-Managed Mode-Locked Tm:Fiber Laser at 1.9 μm* . IEEE Photonics Technology Letters, vol. 28, no. 4, pages 497–500, 2016.
- [Basiev 99] T. T. Basiev, A. A. Sobol, P. G. Zverev, V. V. Osiko, et R. C. Powell. *Comparative spontaneous Raman spectroscopy of crystals for Raman lasers*. Applied Optics, vol. 38, no. 3, pages 594–598, 1999.
- [Belli 19] F. Belli, A. Abdolvand, J. C. Travers, et P. S. J. Russell. *Highly efficient deep UV generation by four-wave mixing in gas-filled hollow-core photonic crystal fiber*. Optics letters, vol. 44, no. 22, pages 5509–5512, 2019.
- [Borot 18] A. Borot et F. Quéré. *Spatio-spectral metrology at focus of ultrashort lasers: a phase-retrieval approach*. Optics express, vol. 26, no. 20, pages 26444–26461, 2018.
- [Boscolo 18] S. Boscolo, F. Chaussard, E. Andresen, H. Rigneault, et C. Finot. *Impact of initial pulse shape on the nonlinear spectral compression in optical fibre*. Optics & Laser Technology, vol. 99, pages 301–309, 2018.
- [Bowlan 06] P. Bowlan, P. Gabolde, A. Shreenath, K. McGresham, R. Trebino, et S. Akturk. *Crossed-beam spectral interferometry: a simple, high-spectral-resolution method for completely characterizing complex ultrashort pulses in real time*. Optics Express, vol. 14, no. 24, pages 11892–11900, 2006.
- [Brabec 97] T. Brabec et F. Krausz. *Nonlinear optical pulse propagation in the single-cycle regime*. Physical Review Letters, vol. 78, no. 17, page 3282, 1997.
- [Cao 19] H. Cao, R. S. Nagymihaly, V. Chvykov, N. Khodakovskiy, et M. Kalashnikov. *Multipass-cell-based post-compression of radially and azimuthally polarized pulses to the sub-two-cycle regime*. JOSA B, vol. 36, no. 9, pages 2517–2525, 2019.
- [Cao 20] H. Cao, R. S. Nagymihaly, et M. Kalashnikov. *Relativistic near-single-cycle optical vortex pulses from noble gas-filled multipass cells*. Optics Letters, vol. 45, no. 12, pages 3240–3243, 2020.
- [Carpeggiani 20] P. Carpeggiani, G. Coccia, G. Fan, E. Kaksis, A. Pugžlys, A. Baltuška, R. Piccoli, Y.-G. Jeong, A. Rovere, R. Morandotti, et al. *Extreme Raman red shift: ultrafast multimode nonlinear space-time dynamics, pulse compression, and broadly tunable frequency conversion*. Optica, vol. 7, no. 10, pages 1349–1354, 2020.
- [Casula 18] R. Casula, J.-P. Penttinen, M. Guina, A. J. Kemp, et J. E. Hastie. *Cascaded crystalline Raman lasers for extended wavelength coverage:*

-
- continuous-wave, third-Stokes operation*. *Optica*, vol. 5, no. 11, pages 1406–1413, 2018.
- [Chen 10] M.-C. Chen, P. Arpin, T. Popmintchev, M. Gerrity, B. Zhang, M. Seaberg, D. Popmintchev, M. Murnane, et H. Kapteyn. *Bright, coherent, ultrafast soft x-ray harmonics spanning the water window from a tabletop light source*. *Physical review letters*, vol. 105, no. 17, page 173901, 2010.
- [Cheng 04] J.-X. Cheng et X. S. Xie. *Coherent anti-Stokes Raman scattering microscopy: instrumentation, theory, and applications*. *The Journal of Physical Chemistry B*, vol. 108, no. 3, pages 827–840, 2004.
- [Cheng 16] Y.-C. Cheng, C.-H. Lu, Y.-Y. Lin, et A. Kung. *Supercontinuum generation in a multi-plate medium*. *Optics express*, vol. 24, no. 7, pages 7224–7231, 2016.
- [Clerici 13] M. Clerici, M. Peccianti, B. E. Schmidt, L. Caspani, M. Shalaby, M. Giguere, A. Lotti, A. Couairon, F. Légaré, T. Ozaki, et al. *Wavelength scaling of terahertz generation by gas ionization*. *Physical Review Letters*, vol. 110, no. 25, page 253901, 2013.
- [Cousin 12] S. L. Cousin, J. M. Bueno, N. Forget, D. R. Austin, et J. Biegert. *Three-dimensional spatiotemporal pulse characterization with an acousto-optic pulse shaper and a Hartmann–Shack wavefront sensor*. *Optics letters*, vol. 37, no. 15, pages 3291–3293, 2012.
- [Daher 20a] N. Daher, F. Guichard, X. Délen, Y. Zaouter, M. Hanna, et P. Georges. *Spectral compression in a multipass cell*. *Optics Express*, vol. 28, no. 15, pages 21571–21577, 2020.
- [Daher 20b] N. Daher, F. Guichard, S. W. Jolly, X. Delen, F. Quere, M. Hanna, et P. Georges. *Multipass cells: 1D numerical model and investigation of spatio-spectral couplings at high nonlinearity*. *JOSA B*, vol. 37, no. 4, pages 993–999, 2020.
- [Daniault 21] L. Daniault, Z. Cheng, J. Kaur, J.-F. Hergott, F. Réau, O. Tcherbakoff, N. Daher, X. Délen, M. Hanna, et R. Lopez-Martens. *Single-stage few-cycle nonlinear compression of milliJoule energy Ti:Sa femtosecond pulses in a multipass cell*. *Opt. Lett.*, vol. 46, no. 20, pages 5264–5267, Oct 2021.
- [Emaury 13] F. Emaury, C. F. Dutin, C. J. Saraceno, M. Trant, O. H. Heckl, Y. Y. Wang, C. Schriber, F. Gerome, T. Südmeyer, F. Benabid, et al. *Beam delivery and pulse compression to sub-50 fs of a modelocked thin-disk laser in a gas-filled Kagome-type HC-PCF fiber*. *Optics express*, vol. 21, no. 4, pages 4986–4994, 2013.

- [Fan 21] G. Fan, P. Carpeggiani, Z. Tao, G. Coccia, R. Safaei, E. Kaksis, A. Pugzlys, F. Légaré, B. Schmidt, et A. Baltuška. *70 mJ nonlinear compression and scaling route for an Yb amplifier using large-core hollow fibers*. Optics Letters, vol. 46, no. 4, pages 896–899, 2021.
- [Fatome 12] J. Fatome, B. Kibler, E. R. Andresen, H. Rigneault, et C. Finot. *All-fiber spectral compression of picosecond pulses at telecommunication wavelength enhanced by amplitude shaping*. Applied optics, vol. 51, no. 19, pages 4547–4553, 2012.
- [Faure 01] J. Faure. *Etude expérimentale de l'interaction d'un laser Terawatt avec un plasma sous-dense: production d'une source brillante et courte d'électrons relativistes*. PhD thesis, Ecole Polytechnique X, 2001.
- [Fedotov 09] A. Fedotov, A. Voronin, I. Fedotov, A. Ivanov, et A. Zheltikov. *Spectral compression of frequency-shifting solitons in a photonic-crystal fiber*. Optics letters, vol. 34, no. 5, pages 662–664, 2009.
- [Finot 16] C. Finot et S. Boscolo. *Design rules for nonlinear spectral compression in optical fibers*. JOSA B, vol. 33, no. 4, pages 760–767, 2016.
- [Fisher 69] R. A. Fisher, P. Kelley, et T. Gustafson. *Subpicosecond pulse generation using the optical Kerr effect*. Applied Physics Letters, vol. 14, no. 4, pages 140–143, 1969.
- [Franken 61] e. P. Franken, A. E. Hill, C. Peters, et G. Weinreich. *Generation of optical harmonics*. Physical Review Letters, vol. 7, no. 4, page 118, 1961.
- [Freudiger 08] C. W. Freudiger, W. Min, B. G. Saar, S. Lu, G. R. Holtom, C. He, J. C. Tsai, J. X. Kang, et X. S. Xie. *Label-free biomedical imaging with high sensitivity by stimulated Raman scattering microscopy*. Science, vol. 322, no. 5909, pages 1857–1861, 2008.
- [Fritsch 18] K. Fritsch, M. Poetzlberger, V. Pervak, J. Brons, et O. Pronin. *All-solid-state multipass spectral broadening to sub-20 fs*. Optics letters, vol. 43, no. 19, pages 4643–4646, 2018.
- [Gabolde 06] P. Gabolde et R. Trebino. *Single-shot measurement of the full spatio-temporal field of ultrashort pulses with multi-spectral digital holography*. Optics express, vol. 14, no. 23, pages 11460–11467, 2006.
- [Gallet 14] V. Gallet, S. Kahaly, O. Gobert, et F. Quéré. *Dual spectral-band interferometry for spatio-temporal characterization of high-power femtosecond lasers*. Optics letters, vol. 39, no. 16, pages 4687–4690, 2014.
- [Gibson 17] G. M. Gibson, B. Sun, M. P. Edgar, D. B. Phillips, N. Hempler, G. T. Maker, G. P. Malcolm, et M. J. Padgett. *Real-time imaging of methane*

-
- gas leaks using a single-pixel camera.* Optics express, vol. 25, no. 4, pages 2998–3005, 2017.
- [Grabtchikov 03] A. Grabtchikov, R. Chulkov, V. Orlovich, M. Schmitt, R. Maksimenko, et W. Kiefer. *Observation of Raman conversion for 70-fs pulses in KGd (WO₄)₂ crystal in the regime of impulsive stimulated Raman scattering.* Optics letters, vol. 28, no. 11, pages 926–928, 2003.
- [Grebing 20] C. Grebing, M. Müller, J. Buldt, H. Stark, et J. Limpert. *Kilowatt-average-power compression of millijoule pulses in a gas-filled multi-pass cell.* Optics Letters, vol. 45, no. 22, pages 6250–6253, 2020.
- [Grigsby 08] F. B. Grigsby, P. Dong, et M. C. Downer. *Chirped-pulse Raman amplification for two-color, high-intensity laser experiments.* JOSA B, vol. 25, no. 3, pages 346–350, 2008.
- [Gröbmeyer 20] S. Gröbmeyer, K. Fritsch, B. Schneider, M. Poetzlberger, V. Pervak, J. Brons, et O. Pronin. *Self-compression at 1 μ m wavelength in all-bulk multi-pass geometry.* Applied Physics B, vol. 126, no. 10, pages 1–6, 2020.
- [Guichard 15] F. Guichard, A. Giree, Y. Zaouter, M. Hanna, G. Machinet, B. Debord, F. Jérôme, P. Dupriez, F. Druon, C. Hönniger, et al. *Nonlinear compression of high energy fiber amplifier pulses in air-filled hypocycloid-core Kagome fiber.* Optics express, vol. 23, no. 6, pages 7416–7423, 2015.
- [Guizar-Sicairos 04] M. Guizar-Sicairos et J. C. Gutiérrez-Vega. *Computation of quasi-discrete Hankel transforms of integer order for propagating optical wave fields.* JOSA A, vol. 21, no. 1, pages 53–58, 2004.
- [Hanna 17] M. Hanna, X. Délen, L. Lavenu, F. Guichard, Y. Zaouter, F. Druon, et P. Georges. *Nonlinear temporal compression in multipass cells: theory.* JOSA B, vol. 34, no. 7, pages 1340–1347, 2017.
- [Hanna 20] M. Hanna, N. Daher, F. Guichard, X. Délen, et P. Georges. *Hybrid pulse propagation model and quasi-phase-matched four-wave mixing in multipass cells.* JOSA B, vol. 37, no. 10, pages 2982–2988, 2020.
- [He 17] P. He, Y. Liu, K. Zhao, H. Teng, X. He, P. Huang, H. Huang, S. Zhong, Y. Jiang, S. Fang, et al. *High-efficiency supercontinuum generation in solid thin plates at 0.1 TW level.* Optics Letters, vol. 42, no. 3, pages 474–477, 2017.
- [Heese 11] C. Heese, A. Oehler, L. Gallmann, et U. Keller. *High-energy picosecond Nd: YVO₄ slab amplifier for OPCPA pumping.* Applied Physics B, vol. 103, no. 1, pages 5–8, 2011.

- [Heinzig 21] M. Heinzig, G. Palma-Vega, B. Yildiz, T. Walbaum, T. Schreiber, et A. Tünnermann. *Continuous-wave cascaded second Stokes diamond Raman laser at 1477 nm*. Optics Letters, vol. 46, no. 5, pages 1133–1136, 2021.
- [Herriott 64] D. Herriott, H. Kogelnik, et R. Kompfner. *Off-axis paths in spherical mirror interferometers*. Applied Optics, vol. 3, no. 4, pages 523–526, 1964.
- [Hilfer 90] G. Hilfer et C. R. Menyuk. *Stimulated Raman scattering in the transient limit*. JOSA B, vol. 7, no. 5, pages 739–749, 1990.
- [Iaconis 98] C. Iaconis et I. A. Walmsley. *Spectral phase interferometry for direct electric-field reconstruction of ultrashort optical pulses*. Optics letters, vol. 23, no. 10, pages 792–794, 1998.
- [Iwaszczuk 12] K. Iwaszczuk, B. Zhou, M. Bache, et P. U. Jepsen. *Spectral compression of intense femtosecond pulses by self phase modulation in silica glass*. In CLEO: Science and Innovations, pages JW4A–61. Optical Society of America, 2012.
- [Jargot 18] G. Jargot, N. Daher, L. Lavenue, X. Delen, N. Forget, M. Hanna, et P. Georges. *Self-compression in a multipass cell*. Optics letters, vol. 43, no. 22, pages 5643–5646, 2018.
- [Jeandet 19] A. Jeandet, A. Borot, K. Nakamura, S. W. Jolly, A. J. Gonsalves, C. Tóth, H.-S. Mao, W. P. Leemans, et F. Quéré. *Spatio-temporal structure of a petawatt femtosecond laser beam*. Journal of Physics: Photonics, vol. 1, no. 3, page 035001, 2019.
- [Jocher 12] C. Jocher, T. Eidam, S. Hädrich, J. Limpert, et A. Tünnermann. *Sub 25 fs pulses from solid-core nonlinear compression stage at 250 W of average power*. Optics letters, vol. 37, no. 21, pages 4407–4409, 2012.
- [Jolly 20] S. W. Jolly, O. Gobert, et F. Quéré. *Spatio-temporal characterization of ultrashort laser beams: a tutorial*. Journal of Optics, vol. 22, no. 10, page 103501, 2020.
- [Jordan 94] C. Jordan, K. Stankov, G. Marowsky, et E. Canto-Said. *Efficient compression of femtosecond pulses by stimulated Raman scattering*. Applied Physics B, vol. 59, no. 4, pages 471–473, 1994.
- [Kabaciński 19] P. Kabaciński, T. M. Kardaś, Y. Stepanenko, et C. Radzewicz. *Non-linear refractive index measurement by SPM-induced phase regression*. Optics express, vol. 27, no. 8, pages 11018–11028, 2019.
- [Kaminskii 99] A. A. Kaminskii, H. J. Eichler, K.-i. Ueda, N. V. Klassen, B. S. Redkin, L. E. Li, J. Findeisen, D. Jaque, J. Garcia-Sole, J. Fernández, et al.

-
- Properties of Nd³⁺-doped and undoped tetragonal PbWO₄, NaY (WO₄)₂, CaWO₄, and undoped monoclinic ZnWO₄ and CdWO₄ as laser-active and stimulated Raman scattering-active crystals.* Applied optics, vol. 38, no. 21, pages 4533–4547, 1999.
- [Kane 93] D. J. Kane et R. Trebino. *Single-shot measurement of the intensity and phase of an arbitrary ultrashort pulse by using frequency-resolved optical gating.* Optics letters, vol. 18, no. 10, pages 823–825, 1993.
- [Kaumanns 18] M. Kaumanns, V. Pervak, D. Kormin, V. Leshchenko, A. Kessel, M. Ueffing, Y. Chen, et T. Nubbemeyer. *Multipass spectral broadening of 18 mJ pulses compressible from 1.3 ps to 41 fs.* Optics letters, vol. 43, no. 23, pages 5877–5880, 2018.
- [Kaumanns 20] R. M. Kaumanns. *Generation of energetic femtosecond pulses at high average power.* PhD thesis, lmu, 2020.
- [Kaumanns 21] M. Kaumanns, D. Kormin, T. Nubbemeyer, V. Pervak, et S. Karsch. *Spectral broadening of 112 mJ, 1.3 ps pulses at 5 kHz in a LG 10 multipass cell with compressibility to 37 fs.* Optics Letters, vol. 46, no. 5, pages 929–932, 2021.
- [Kobat 09] D. Kobat, M. E. Durst, N. Nishimura, A. W. Wong, C. B. Schaffer, et C. Xu. *Deep tissue multiphoton microscopy using longer wavelength excitation.* Optics express, vol. 17, no. 16, pages 13354–13364, 2009.
- [Kong 12] L. Kong, L. Zhao, S. Lefrancois, D. Ouzounov, C. Yang, et F. Wise. *Generation of megawatt peak power picosecond pulses from a divided-pulse fiber amplifier.* Optics letters, vol. 37, no. 2, pages 253–255, 2012.
- [Köttig 20] F. Köttig, D. Schade, J. Koehler, P. S. J. Russell, et F. Tani. *Efficient single-cycle pulse compression of an ytterbium fiber laser at 10 MHz repetition rate.* Optics express, vol. 28, no. 7, pages 9099–9110, 2020.
- [Kramer 20] P. L. Kramer, M. K. Windeler, K. Mecseki, E. G. Champenois, M. C. Hoffmann, et F. Tavella. *Enabling high repetition rate nonlinear THz science with a kilowatt-class sub-100 fs laser source.* Optics express, vol. 28, no. 11, pages 16951–16967, 2020.
- [Krausz 09] F. Krausz et M. Ivanov. *Attosecond physics.* Reviews of modern physics, vol. 81, no. 1, page 163, 2009.
- [Lavenu 18] L. Lavenu, M. Natile, F. Guichard, Y. Zaouter, X. Delen, M. Hanna, E. Mottay, et P. Georges. *Nonlinear pulse compression based on a gas-filled multipass cell.* Optics letters, vol. 43, no. 10, pages 2252–2255, 2018.

- [Lavenu 19a] L. Lavenu, M. Natile, F. Guichard, X. Délen, M. Hanna, Y. Zaouter, et P. Georges. *High-power two-cycle ultrafast source based on hybrid nonlinear compression*. Optics express, vol. 27, no. 3, pages 1958–1967, 2019.
- [Lavenu 19b] L. Lavenu. *Source laser à fibre dopée Yb de haute énergie délivrant des impulsions de quelques cycles optiques*. PhD thesis, Université Paris-Saclay (ComUE), 2019.
- [Limpert 02] J. Limpert, T. Gabler, A. Liem, H. Zellmer, et A. Tünnermann. *SPM-induced spectral compression of picosecond pulses in a single-mode Yb-doped fiber amplifier*. Applied Physics B, vol. 74, no. 2, pages 191–195, 2002.
- [Limpert 05] J. Limpert, N. Deguil-Robin, I. Manek-Hönninger, F. Salin, T. Schreiber, A. Liem, F. Röser, H. Zellmer, A. Tünnermann, A. Courjaud, et al. *High-power picosecond fiber amplifier based on nonlinear spectral compression*. Optics letters, vol. 30, no. 7, pages 714–716, 2005.
- [Lisinetkii 08] V. Lisinetkii, V. Orlovich, H. Rhee, X. Wang, et H. Eichler. *Efficient Raman amplification of low divergent radiation in barium nitrate crystal*. Applied Physics B, vol. 91, no. 2, pages 299–303, 2008.
- [Liu 06] J. Liu, X. Chen, J. Liu, Y. Zhu, Y. Leng, J. Dai, R. Li, et Z. Xu. *Spectrum reshaping and pulse self-compression in normally dispersive media with negatively chirped femtosecond pulses*. Optics express, vol. 14, no. 2, pages 979–987, 2006.
- [Loriot 13] V. Loriot, G. Gitzinger, et N. Forget. *Self-referenced characterization of femtosecond laser pulses by chirp scan*. Optics express, vol. 21, no. 21, pages 24879–24893, 2013.
- [Lu 14] C.-H. Lu, Y.-J. Tsou, H.-Y. Chen, B.-H. Chen, Y.-C. Cheng, S.-D. Yang, M.-C. Chen, C.-C. Hsu, et A. H. Kung. *Generation of intense supercontinuum in condensed media*. Optica, vol. 1, no. 6, pages 400–406, 2014.
- [Lu 18] C.-H. Lu, T. Witting, A. Husakou, M. J. Vrakking, A. Kung, et F. J. Furch. *Sub-4 fs laser pulses at high average power and high repetition rate from an all-solid-state setup*. Optics express, vol. 26, no. 7, pages 8941–8956, 2018.
- [Lu 19] C.-H. Lu, W.-H. Wu, S.-H. Kuo, J.-Y. Guo, M.-C. Chen, S.-D. Yang, et A. Kung. *Greater than 50 times compression of 1030 nm Yb: KGW laser pulses to single-cycle duration*. Optics express, vol. 27, no. 11, pages 15638–15648, 2019.

-
- [Mackonis 20] P. Mackonis, A. Petrukenas, A. M. Rodin, V. Girdauskas, et A. Michailovas. *Two-stage transient stimulated Raman chirped-pulse amplification in KGd (WO₄)₂ with compression to 145 fs*. Optics Letters, vol. 45, no. 24, pages 6627–6630, 2020.
- [Mansuryan 08] T. Mansuryan, A. Zeytunyan, M. Kalashyan, G. Yesayan, L. Mouradian, F. Louradour, et A. Barthélémy. *Parabolic temporal lensing and spectrotemporal imaging: a femtosecond optical oscilloscope*. JOSA B, vol. 25, no. 6, pages A101–A110, 2008.
- [Marcuse 82] D. Marcuse. *Light transmission optics*. New York, 1982.
- [Maxwell 65] J. C. Maxwell. *VIII. A dynamical theory of the electromagnetic field*. Philosophical transactions of the Royal Society of London, no. 155, pages 459–512, 1865.
- [McKay 14] A. McKay, O. Kitzler, et R. P. Mildren. *High power tungstate-crystal Raman laser operating in the strong thermal lensing regime*. Optics express, vol. 22, no. 1, pages 707–715, 2014.
- [Mei 16] C. Mei, J. Yuan, K. Wang, X. Sang, et C. Yu. *Chirp-free spectral compression of parabolic pulses in silicon nitride channel waveguides*. In 2016 21st OptoElectronics and Communications Conference (OECC) held jointly with 2016 International Conference on Photonics in Switching (PS), pages 1–3. IEEE, 2016.
- [Mei 21] C. Mei et G. Steinmeyer. *Space-time focusing and coherence properties of supercontinua in multipass cells*. Physical Review Research, vol. 3, no. 1, page 013259, 2021.
- [Meyer 19] F. Meyer, N. Hekmat, T. Vogel, A. Omar, S. Mansourzadeh, F. Fobbe, M. Hoffmann, Y. Wang, et C. Saraceno. *Milliwatt-class broadband THz source driven by a 112 W, sub-100 fs thin-disk laser*. Optics express, vol. 27, no. 21, pages 30340–30349, 2019.
- [Meyer 20] F. Meyer, T. Vogel, S. Ahmed, et C. J. Saraceno. *Single-cycle, MHz repetition rate THz source with 66 mW of average power*. Optics letters, vol. 45, no. 9, pages 2494–2497, 2020.
- [Milosevic 00] N. Milosevic, G. Tempea, et T. Brabec. *Optical pulse compression: bulk media versus hollow waveguides*. Optics letters, vol. 25, no. 9, pages 672–674, 2000.
- [Miranda 12] M. Miranda, T. Fordell, C. Arnold, A. L’Huillier, et H. Crespo. *Simultaneous compression and characterization of ultrashort laser pulses using chirped mirrors and glass wedges*. Optics express, vol. 20, no. 1, pages 688–697, 2012.

- [Mitrofanov 18] A. V. Mitrofanov, M. M. Nazarov, A. A. Voronin, D. A. Sidorov-Biryukov, V. Y. Panchenko, et A. M. Zheltikov. *Free-beam spectral self-compression at supercritical peak powers*. Optics letters, vol. 43, no. 22, pages 5693–5696, 2018.
- [Mochalov 97] I. V. Mochalov. *Laser and nonlinear properties of the potassium gadolinium tungstate laser crystal KGd (WO₄)₂: Nd³⁺-(KGW: Nd)*. Optical Engineering, vol. 36, pages 1660–1669, 1997.
- [Morin 10] F. Morin. *Conception d'une source à impulsions courtes à 1600 nm à fibres dopées erbium: application à la greffe de cornée*. PhD thesis, Paris 11, 2010.
- [Müller 21] M. Müller, J. Buldt, H. Stark, C. Grebing, et J. Limpert. *Multipass cell for high-power few-cycle compression*. Optics Letters, vol. 46, no. 11, pages 2678–2681, 2021.
- [Nagy 21] T. Nagy, P. Simon, et L. Veisz. *High-energy few-cycle pulses: post-compression techniques*. Advances in Physics: X, vol. 6, no. 1, page 1845795, 2021.
- [Natile 19] M. Natile, A. Golinelli, L. Lavenu, F. Guichard, M. Hanna, Y. Zaouter, R. Chiche, X. Chen, J. Hergott, W. Boutu, et al. *CEP-stable high-energy ytterbium-doped fiber amplifier*. Optics letters, vol. 44, no. 16, pages 3909–3912, 2019.
- [Nishizawa 10] N. Nishizawa, K. Takahashi, Y. Ozeki, et K. Itoh. *Wideband spectral compression of wavelength-tunable ultrashort soliton pulse using comb-profile fiber*. Optics express, vol. 18, no. 11, pages 11700–11706, 2010.
- [Nisoli 97] M. Nisoli, S. De Silvestri, O. Svelto, R. Szipöcs, K. Ferencz, C. Spielmann, S. Sartania, et F. Krausz. *Compression of high-energy laser pulses below 5 fs*. Optics letters, vol. 22, no. 8, pages 522–524, 1997.
- [Oberthaler 93] M. Oberthaler et R. Höpfel. *Special narrowing of ultrashort laser pulses by self-phase modulation in optical fibers*. Applied physics letters, vol. 63, no. 8, pages 1017–1019, 1993.
- [Oksenhendler 10] T. Oksenhendler, S. Coudreau, N. Forget, V. Crozatier, S. Grabielle, R. Herzog, O. Gobert, et D. Kaplan. *Self-referenced spectral interferometry*. Applied Physics B, vol. 99, no. 1, pages 7–12, 2010.
- [Orlovich 12] V. Orlovich, Y. I. Malakhov, Y. M. Popov, D. Busko, M. Danailov, A. Demidovich, P. Apanasevich, et R. Chulkov. *Raman conversion of femtosecond laser pulses in crystals*. Laser Physics Letters, vol. 9, no. 11, page 770, 2012.

-
- [Pajer 21] V. Pajer et M. Kalashnikov. *High temporal contrast ultrashort pulses generated by nonlinear ellipse rotation in multipass cells*. Laser Physics Letters, vol. 18, no. 6, page 065401, 2021.
- [Pariante 16] G. Pariante, V. Gallet, A. Borot, O. Gobert, et F. Quéré. *Space-time characterization of ultra-intense femtosecond laser beams*. Nature Photonics, vol. 10, no. 8, pages 547–553, 2016.
- [Park 09] J. Park, J.-h. Lee, et C. H. Nam. *Generation of 1.5 cycle 0.3 TW laser pulses using a hollow-fiber pulse compressor*. Optics letters, vol. 34, no. 15, pages 2342–2344, 2009.
- [Planas 93] S. Planas, N. P. Mansur, C. B. Cruz, et H. Fragnito. *Spectral narrowing in the propagation of chirped pulses in single-mode fibers*. Optics letters, vol. 18, no. 9, pages 699–701, 1993.
- [Pouysegur 15] J. Pouysegur, F. Guichard, Y. Zaouter, M. Hanna, F. Druon, C. Höninger, E. Mottay, et P. Georges. *Hybrid high-energy high-power pulsewidth-tunable picosecond source*. Optics letters, vol. 40, no. 22, pages 5184–5187, 2015.
- [Prinz 15] S. Prinz, M. Haefner, C. Y. Teisset, R. Bessing, K. Michel, Y. Lee, X. T. Geng, S. Kim, D. E. Kim, T. Metzger, et al. *CEP-stable, sub-6 fs, 300-kHz OPCPA system with more than 15 W of average power*. Optics express, vol. 23, no. 2, pages 1388–1394, 2015.
- [Raman 28] C. V. Raman. *A new radiation*. Indian Journal of physics, vol. 2, pages 387–398, 1928.
- [Rolland 88] C. Rolland et P. B. Corkum. *Compression of high-power optical pulses*. JOSA B, vol. 5, no. 3, pages 641–647, 1988.
- [Russbueldt 19] P. Russbueldt, J. Weitenberg, J. Schulte, R. Meyer, C. Meinhardt, H. Hoffmann, et R. Poprawe. *Scalable 30 fs laser source with 530 W average power*. Optics letters, vol. 44, no. 21, pages 5222–5225, 2019.
- [Sabella 11] A. Sabella, J. A. Piper, et R. P. Mildren. *Efficient conversion of a 1.064 μm Nd: YAG laser to the eye-safe region using a diamond Raman laser*. Optics Express, vol. 19, no. 23, pages 23554–23560, 2011.
- [Saint-Loup 90] R. Saint-Loup, B. Lavorel, G. Millot, C. Wenger, et H. Berger. *Enhancement of sensitivity in high-resolution stimulated Raman spectroscopy of gases: Application to the $2\nu_2$ (1285 cm^{-1}) band of CO_2* . Journal of Raman spectroscopy, vol. 21, no. 2, pages 77–83, 1990.
- [Sainte-Marie 17] A. Sainte-Marie, O. Gobert, et F. Quere. *Controlling the velocity of ultrashort light pulses in vacuum through spatio-temporal couplings*. Optica, vol. 4, no. 10, pages 1298–1304, 2017.

- [Saleh 19] B. E. Saleh et M. C. Teich. *Fundamentals of photonics*. John Wiley & sons, 2019.
- [Schulte 16] J. Schulte, T. Sartorius, J. Weitenberg, A. Vernaleken, et P. Russbuedt. *Nonlinear pulse compression in a multi-pass cell*. *Optics Letters*, vol. 41, no. 19, pages 4511–4514, 2016.
- [Shimizu 67] F. Shimizu. *Frequency broadening in liquids by a short light pulse*. *Physical Review Letters*, vol. 19, no. 19, page 1097, 1967.
- [Sidorov-Biryukov 08] D. Sidorov-Biryukov, A. Fernandez, L. Zhu, A. Pugžlys, E. Serebryanikov, A. Baltuška, et A. Zheltikov. *Spectral narrowing of chirp-free light pulses in anomalously dispersive, highly nonlinear photonic-crystal fibers*. *Optics express*, vol. 16, no. 4, pages 2502–2507, 2008.
- [Siebold 04] M. Siebold, M. Hornung, J. Hein, G. Paunescu, R. Sauerbrey, T. Bergmann, et G. Hollemann. *A high-average-power diode-pumped Nd: YVO 4 regenerative laser amplifier for picosecond-pulses*. *Applied Physics B*, vol. 78, no. 3, pages 287–290, 2004.
- [Song 21] J. Song, Z. Wang, R. Lv, X. Wang, H. Teng, J. Zhu, et Z. Wei. *Generation of 172 fs pulse from a Nd: YVO 4 picosecond laser by using multi-pass-cell technique*. *Applied Physics B*, vol. 127, no. 4, pages 1–6, 2021.
- [Strickland 85] D. Strickland et G. Mourou. *Compression of amplified chirped optical pulses*. *Optics communications*, vol. 55, no. 6, pages 447–449, 1985.
- [Sußmann 92] R. Sußmann, T. Weber, E. Riedle, et H. Neusser. *Frequency shifting of pulsed narrow-band laser light in a multipass Raman cell*. *Optics communications*, vol. 88, no. 4-6, pages 408–414, 1992.
- [Südmeyer 03] T. Südmeyer, F. Brunner, E. Innerhofer, R. Paschotta, K. Furusawa, J. Baggett, T. Monro, D. Richardson, et U. Keller. *Nonlinear femtosecond pulse compression at high average power levels by use of a large-mode-area holey fiber*. *Optics letters*, vol. 28, no. 20, pages 1951–1953, 2003.
- [Tilma 11] B. W. Tilma, Y. Jiao, J. Kotani, B. Smalbrugge, H. P. Ambrosius, P. J. Thijs, X. J. Leijtsens, R. Ntzel, M. K. Smit, et E. A. Bente. *Integrated Tunable Quantum-Dot Laser for Optical Coherence Tomography in the 1.7 μ m Wavelength Region*. *IEEE Journal of Quantum Electronics*, vol. 48, no. 2, pages 87–98, 2011.
- [Tomlinson 85] W. Tomlinson, R. H. Stolen, et A. M. Johnson. *Optical wave breaking of pulses in nonlinear optical fibers*. *Optics letters*, vol. 10, no. 9, pages 457–459, 1985.

-
- [Toneyan 16] H. Toneyan, A. Zeytunyan, R. Zadoyan, et L. Mouradian. *Classic, all-fiber, and similaritonic techniques of spectral compression*. In Journal of Physics: Conference Series, volume 672, page 012016. IOP Publishing, 2016.
- [Trägårdh 16] J. Trägårdh, J. Schniete, M. Parsons, et G. McConnell. *A femtosecond Raman generator for long wavelength two-photon and third harmonic generation imaging*. APL Photonics, vol. 1, no. 9, page 091303, 2016.
- [Trebino 97] R. Trebino, K. W. DeLong, D. N. Fittinghoff, J. N. Sweetser, M. A. Krumbügel, B. A. Richman, et D. J. Kane. *Measuring ultrashort laser pulses in the time-frequency domain using frequency-resolved optical gating*. Review of Scientific Instruments, vol. 68, no. 9, pages 3277–3295, 1997.
- [Trutna 80] W. Trutna et R. Byer. *Multiple-pass Raman gain cell*. Applied optics, vol. 19, no. 2, pages 301–312, 1980.
- [Tsai 19] C.-L. Tsai, F. Meyer, A. Omar, Y. Wang, A.-Y. Liang, C.-H. Lu, M. Hoffmann, S.-D. Yang, et C. J. Saraceno. *Efficient nonlinear compression of a mode-locked thin-disk oscillator to 27 fs at 98 W average power*. Optics letters, vol. 44, no. 17, pages 4115–4118, 2019.
- [Ueffing 18a] M. Ueffing. *Direct amplification of femtosecond pulses*. PhD thesis, LMU München, 2018.
- [Ueffing 18b] M. Ueffing, S. Reiger, M. Kaumanns, V. Pervak, M. Trubetskov, T. Nubbemeyer, et F. Krausz. *Nonlinear pulse compression in a gas-filled multipass cell*. Optics letters, vol. 43, no. 9, pages 2070–2073, 2018.
- [Vicario 16] C. Vicario, M. Shalaby, A. Konyashchenko, L. Losev, et C. P. Hauri. *High-power femtosecond Raman frequency shifter*. Optics letters, vol. 41, no. 20, pages 4719–4722, 2016.
- [Vicentini 20] E. Vicentini, Y. Wang, D. Gatti, A. Gambetta, P. Laporta, G. Galzerano, K. Curtis, K. McEwan, C. R. Howle, et N. Coluccelli. *Nonlinear pulse compression to 22 fs at 15.6 μ J by an all-solid-state multipass approach*. Optics express, vol. 28, no. 4, pages 4541–4549, 2020.
- [Vincenti 12] H. Vincenti et F. Quéré. *Attosecond lighthouses: how to use spatiotemporally coupled light fields to generate isolated attosecond pulses*. Physical review letters, vol. 108, no. 11, page 113904, 2012.
- [Viotti 21] A.-L. Viotti, S. Alisauskas, A. Bin Wahid, P. Balla, N. Schirmel, B. Manschwetus, I. Hartl, et C. M. Heyl. *60 fs, 1030 nm FEL pump-probe laser based on a multi-pass post-compressed Yb: YAG source*. Journal of synchrotron radiation, vol. 28, no. 1, 2021.

- [Wahlstrand 12] J. Wahlstrand, Y.-H. Cheng, et H. Milchberg. *High field optical non-linearity and the Kramers-Kronig relations*. Physical review letters, vol. 109, no. 11, page 113904, 2012.
- [Walmsley 09] I. A. Walmsley et C. Dorrer. *Characterization of ultrashort electromagnetic pulses*. Advances in Optics and Photonics, vol. 1, no. 2, pages 308–437, 2009.
- [Washburn 00] B. R. Washburn, J. A. Buck, et S. E. Ralph. *Transform-limited spectral compression due to self-phase modulation in fibers*. Optics Letters, vol. 25, no. 7, pages 445–447, 2000.
- [Weitenberg 17a] J. Weitenberg, T. Saule, J. Schulte, et P. Rußbüldt. *Nonlinear Pulse Compression to Sub-40 fs at 4.5 μ J Pulse Energy by Multi-Pass-Cell Spectral Broadening*. IEEE Journal of Quantum Electronics, vol. 53, no. 6, pages 1–4, 2017.
- [Weitenberg 17b] J. Weitenberg, A. Vernaleken, J. Schulte, A. Ozawa, T. Sartorius, V. Pervak, H.-D. Hoffmann, T. Udem, P. Russbüldt, et T. W. Hänsch. *Multi-pass-cell-based nonlinear pulse compression to 115 fs at 7.5 μ J pulse energy and 300 W average power*. Optics express, vol. 25, no. 17, pages 20502–20510, 2017.
- [Will 11] I. Will, H. I. Templin, S. Schreiber, et W. Sandner. *Photoinjector drive laser of the FLASH FEL*. Optics Express, vol. 19, no. 24, pages 23770–23781, 2011.
- [Zaouter 07] Y. Zaouter, E. Cormier, P. Rigail, C. Hönninger, et E. Mottay. *30 W, 10 μ J, 10-ps SPM-induced spectrally compressed pulse generation in a low non-linearity ytterbium-doped rod-type fibre amplifier*. In Fiber Lasers IV: Technology, Systems, and Applications, volume 6453, page 64530O. International Society for Optics and Photonics, 2007.
- [Zhavoronkov 01] N. Zhavoronkov, F. Noack, V. Petrov, V. Kalosha, et J. Herrmann. *Chirped-pulse stimulated Raman scattering in barium nitrate with subsequent recompression*. Optics letters, vol. 26, no. 1, pages 47–49, 2001.
- [Zhou 10] S. Zhou, T. Takamido, S. Imai, et F. Wise. *Exploitation of stimulated Raman scattering in short-pulse fiber amplifiers*. Optics letters, vol. 35, no. 14, pages 2397–2399, 2010.
- [Zverev 93] P. G. Zverev, J. T. Murray, R. C. Powell, R. J. Reeves, et T. T. Basiev. *Stimulated Raman scattering of picosecond pulses in barium nitrate crystals*. Optics communications, vol. 97, no. 1-2, pages 59–64, 1993.
- [Cerný 04] P. Cerný, H. Jelínková, P. G. Zverev, et T. T. Basiev. *Solid state lasers with Raman frequency conversion*. Progress in Quantum Electronics, vol. 28, no. 2, pages 113–143, 2004.

List of Publications

Peer Reviewed Journal Articles

- 1. Multipass cells: 1D numerical model and investigation of spatio-spectral couplings at high nonlinearity**
Nour Daher, Florent Guichard, Spencer W. Jolly, Xavier Délen, Fabien Quéré, Marc Hanna, and Patrick Georges
Journal of the Optical Society of America B, Volume 37, Issue 4, pages 993-999 (2020)
- 2. Hybrid pulse propagation model and quasi-phase-matched four-wave mixing in multipass cells**
Marc Hanna, Nour Daher, Florent Guichard, Xavier Délen, and Patrick Georges
Journal of the Optical Society of America B, Volume 37, Issue 10, pages 2982-2988 (2020)
- 3. Spectral compression in a multipass cell**
Nour Daher, Florent Guichard, Xavier Délen, Yoann Zaouter, Marc Hanna, and Patrick Georges
Optics Express, Volume 28, Issue 15, pages 21571-21577 (2020)
- 4. Nonlinear beam matching to gas-filled multipass cells**
Marc Hanna, Louis Daniault, Florent Guichard, Nour Daher, Xavier Délen, Rodrigo Lopez-Martens, and Patrick Georges
OSA Continuum, Volume 4, Issue 2, pages 732-738 (2021)
- 5. Raman wavelength conversion in a multipass cell**
Nour Daher, Xavier Délen, Florent Guichard, Marc Hanna, and Patrick Georges
Optics Letters, Volume 46, Issue 14, pages 3380-3383 (2021)
- 6. Single-stage few-cycle nonlinear compression of milliJoule energy Ti:Sa femtosecond pulses in a multipass cell**
Louis Daniault, Zhao Cheng, Jaismeen Kaur, Jean-françois Hergott, Fabrice Réau, Olivier Tcherbakoff, Nour Daher, Xavier Délen, Marc Hanna, and Rodrigo Lopez-martens
Optics Letters, Volume 46, Issue 20, pages 5264-5267 (2021)
- 7. Nonlinear optics in multipass cells**
Marc Hanna, Florent Guichard, Nour Daher, Quentin Bournet, Xavier Délen, and Patrick Georges
Laser & Photonics Reviews, Volume 15, Issue 12, 2100220 (2021)

Conferences

Presenting author in **bold** font.

1. **Nonlinear spectral compression in a multipass cell**
Nour Daher, Florent Guichard, Xavier Délen, Yoann Zaouter, Marc Hanna and Patrick Georges
Europhoton, 2020, virtual, paper Fr-M2.6, Oral presentation
2. **Raman conversion in a multipass cell**
Nour Daher, Xavier Délen, Florent Guichard, Marc Hanna, and Patrick Georges
European Conference on Lasers and Electro-Optics and European Quantum Electronics Conference (CLEO Europe), 2021, virtual, paper CF-3.3, Oral presentation
3. **Raman frequency shifting of stretched femtosecond pulses in a multipass cell**
Nour Daher, Xavier Délen, Florent Guichard, Marc Hanna, and Patrick Georges
Optique Dijon, France, 2021, Poster
4. **Single-stage few-cycle nonlinear compression of Ti:Sa femtosecond pulses in a multipass cell**
Louis Daniault, Zhao Cheng, Jaismeen Kaur, Jean-françois Hergott, Fabrice Réau, Olivier Tcherbakoff, Nour Daher, Xavier Délen, Marc Hanna, and Rodrigo Lopez-Martens
The European Optical Society Annual meeting (EOSAM), 2021, Rome, Italy, paper TOM13 S10:2



Multipass cells: 1D numerical model and investigation of spatio-spectral couplings at high nonlinearity

NOUR DAHER,^{1,*} FLORENT GUICHARD,² SPENCER W. JOLLY,³  XAVIER DÉLEN,¹
FABIEN QUÉRÉ,³ MARC HANNA,¹  AND PATRICK GEORGES¹

¹Laboratoire Charles Fabry, UMR 8501, Institut d'Optique, CNRS, Université Paris Saclay, 2 Avenue Augustin Fresnel, 91127 Palaiseau, France

²Amplitude Laser, 11 Avenue de Canteranne, Cité de la Photonique, 33600 Pessac, France

³LIDYL, CEA, CNRS, Université Paris-Saclay, CEA Saclay, 91191 Gif-sur-Yvette, France

*Corresponding author: nour.daher@institutoptique.fr

Received 16 December 2019; revised 31 January 2020; accepted 11 February 2020; posted 11 February 2020 (Doc. ID 386049); published 9 March 2020

Multipass cells (MPCs) are used nowadays as nonlinear tools to perform spectral broadening and temporal manipulation of laser pulses while maintaining a good spatial quality and spatio-spectral homogeneity. However, intensive 3D nonlinear spatio-temporal simulations are required to fully capture the physics associated with pulse propagation inside these systems. In addition, the limitations of such a scheme are still under investigation. In this study, we first establish a 1D model as a useful design tool to predict the temporal and spectral properties of the output pulse for nearly Gaussian beams, in a wide range of cavity configurations and nonlinearity levels. This model allows us to drastically reduce the computation time associated with MPC design. The validity of the 1D model is first checked by comparing it to 3D simulations. The results of the 1D model are then compared with experimental data collected from a near-concentric gas-filled multipass cell presenting a high level of nonlinearity, enabling the observation of wave breaking. In a second part, we experimentally characterize the spatio-spectral profile at the output of this experimental setup, both with an imaging spectrometer and with a complete 3D characterization method known as INSIGHT. The results show that gas-filled multipass cells can be used at peak power levels close to the critical power without inducing significant spatio-spectral couplings in intensity or phase. © 2020 Optical Society of America

<https://doi.org/10.1364/JOSAB.386049>

1. INTRODUCTION

Nonlinear optics in single-mode fibers is a research area that has bloomed continuously since the 1980s until today [1]. It has allowed both the observation and understanding of fundamental phenomena in nonlinear physics, as well as enabled a plethora of applications, for instance, in telecommunications and coherent light sources. One of the reasons for the success of this field is the one-dimensional nature of light propagation along the fiber. This simplifies the dynamics considerably and makes it easier to grasp nonlinear phenomena that can still be of great complexity. One of the salient examples is supercontinuum generation, which is much easier to describe and predict in optical fibers [2] than in bulk media [3].

In terms of applications, one of the weaknesses of single-mode optical fibers is that the energy or peak power of pulses that can be manipulated using nonlinear optics phenomena is limited by the small transverse dimensions of the fiber core. In silica-core fibers, self-focusing limits the peak power to values

in the range 1–10 MW. Hollow-core fibers allow an increase of this value [4], but in all cases there is a small but nonzero overlap between the guiding material and the optical field, which makes energy scaling difficult in practice. The most robust solution to scale the energy while retaining a guided propagation is to use hollow capillaries [5]. These structures are lossy and multimode by nature but can approximate a low-loss single-mode waveguide by proper excitation of the fundamental mode and by selecting a large enough core diameter.

Recently, multipass cells (MPCs) either including a bulk medium [6] or filled with a rare gas [7–9] have been used to perform nonlinear temporal compression of femtosecond pulses in various regimes (normal dispersion [6–9], soliton compression in anomalous dispersion [10]), in a large range of pulse energies (from microjoules [6,11] to millijoules [7,9]) and output pulse durations (from > 100 fs [6] to few cycles [10,12]). In all these demonstrations, it was observed that the MPC essentially acts like a 1D nonlinear object, with negligible impact of the

nonlinearity on the spatial properties of the beams. MPCs can therefore be seen as a vehicle to perform 1D nonlinear functions or experiments with energetic pulses. They provide a large number of design degrees of freedom in terms of nonlinearity (bulk plates or gas with adjustable pressures) and dispersion engineering (through the mirror coatings). They can also provide long propagation distances in the nonlinear medium with a compact setup.

In this article we address two questions. First, we aim at assessing to which degree a MPC can be thought of as a simple 1D nonlinear waveguide. We first introduce the notion of “equivalent waveguide” for different types of MPCs and compare numerically a full 3D propagation model to the simplified 1D model obtained using this notion. The developed 1D model is shown to quantitatively predict the observed temporal and spectral properties of the output pulse when the nonlinearity level is low enough to essentially preserve the beam Gaussian shape and caustic evolution. The 1D model is then compared with an experiment in a near-concentric MPC at increasing nonlinearity level and is shown to remain valid at peak power values above half the critical power. In particular, it is able to reproduce the observation of wave breaking, a well-known phenomenon in the context of nonlinear fiber optics in the normal dispersion regime.

In a second part, we experimentally study the spatio-spectral profile at the output of MPCs as the peak power approaches the critical power. This is done using both an imaging spectrometer and a complete 3D characterization technique known as INSIGHT [13]. The results show that the output pulses are essentially free of spatio-temporal couplings even at peak power levels close to the critical power.

2. EQUIVALENT WAVEGUIDE AND 1D MODEL

We start by defining the equivalent 1D model for different MPC geometries. We assume a Gaussian beam shape and propagation in order to establish this model. Since linear effects such as dispersion or attenuation are not affected by the changes in beam size, they can be directly transposed from the 3D situation to the 1D situation. We therefore focus on the nonlinear effects.

In the case of an MPC including a thin plate of bulk medium, as shown in Fig. 1(a), the simplest approach is to neglect the nonlinearity introduced by propagation outside of the medium.

The beam size inside the material can be considered constant if its thickness is much less than the Rayleigh range. In this case, the equivalent waveguide is simply a waveguide with an effective area equal to πw_{NL}^2 , where w_{NL} is the beam waist in the nonlinear medium, a length given by $2 N_{rt} z_{NL}$, where N_{rt} is the number of round trips and z_{NL} is the thickness of the medium, and the nonlinear index n_2 is the same as the bulk material. The dispersive properties of the MPC mirrors can be either accounted for as discrete elements inserted after each propagation length z_{NL} to mimic the real implementation or distributed over the propagation inside the medium. The use of such a “bulk” MPC allows peak powers in excess of the critical power, and equivalent propagation in a piece of bulk material longer than the self-focusing distance. Given that the nonlinearity of gas is typically 3 orders of magnitude less than that of bulk media, this equivalent 1D approach is reasonable, as an example, for cells of lengths in the few tens of centimeters range, and nonlinear media lengths in the few millimeters range, in which case the nonlinearity accumulated in the medium accounts for approximately 90% of the total.

Let us now consider the case of a symmetric two-mirror Herriot cell [14], with mirror radius of curvature R and distance between the mirrors L , filled with a gas with nonlinear index n_2 and dispersion β_2 , as depicted in Fig. 1(b). By identifying the nonlinearity accumulated over one pass [15] and the nonlinearity accumulated in a waveguide with a constant beam size, the equivalent waveguide is found to have the following properties: same overall length $2 N_{rt} L$, same nonlinear index n_2 , same dispersion β_2 if the mirror dispersion is added as an additional discrete contribution at each propagation length L , and an effective area given by

$$A_{eff} = M^2 \frac{\lambda L}{2 \operatorname{atan} \left(\sqrt{\frac{L}{2R-L}} \right)}, \quad (1)$$

where λ is the central wavelength, and M^2 is the beam quality parameter of the input beam.

Finally, we consider the case of a MPC in a $4f$ configuration, shown in Fig. 1(c), as used in [7]. This geometry allows an additional degree of freedom in the design, since the smallest beam waist size in the gas is now unrelated to the mirror radius of curvature and cell length. In this case, using the same approach

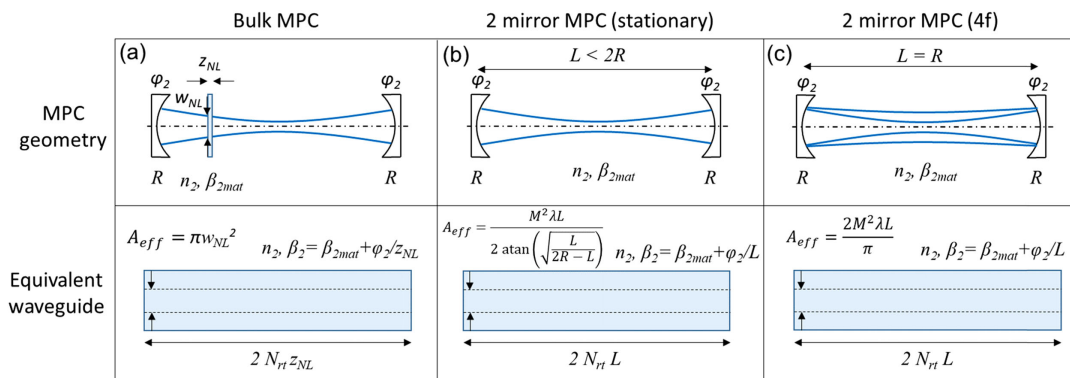


Fig. 1. Summary of equivalent waveguide parameters for three MPC geometries: (a) bulk medium, (b) stationary gas-filled MPC, and (c) $4f$ gas-filled MPC.

as in Ref. [15], the B -integral (averaged over the beam transverse profile) accumulated over one round trip is found to be given by

$$B = \frac{P_{\text{peak}}}{M^2 P_{\text{crit}}} \frac{\pi^2}{4}, \quad (2)$$

where P_{peak} is the pulse peak power and $P_{\text{crit}} = \lambda^2/8n_2$ is the critical power for self-focusing in the gas medium. One remarkable result is that this B -integral does not depend on the chosen small waist, because the large waist size is inversely proportional to the small one. As a consequence, the equivalent waveguide effective area is given by

$$A_{\text{eff}} = M^2 \frac{2\lambda L}{\pi}. \quad (3)$$

Figure 1 summarizes the equivalent waveguide characteristics in these three MPC geometries. We now compare numerical results obtained with a full 3D model of the propagation to this simplified 1D approach, to investigate its validity range.

The 3D model is described in Ref. [15] and is based on an envelope equation [16] solved using the split-step method. This model includes self-steepening in addition to diffraction, dispersion to all orders, and instantaneous Kerr effect. The 1D model is a standard split-step algorithm typically used to model propagation in single-mode fibers and includes the exact same effects, excepting diffraction.

We first compare the 3D and 1D models for a set of parameters resembling the experimental configuration reported in Ref. [8]. The MPC is close to confocal with a mirror radius of curvature of 300 mm, and a cell length of 290 mm filled with xenon at a pressure of 1 bar. The dispersion data is extrapolated from the Sellmeier coefficients reported in Ref. [17], and the nonlinear index is given by $n_2 = 5.2 \times 10^{-23} \text{ m}^2/\text{W}$ [18]. The input pulses have a Gaussian profile in time and space with a 300 fs pulse duration and 150 μJ energy, and propagate along 35 round trips in the MPC. The input spatial profile is chosen to match the stationary condition in the MPC. These parameters correspond to a $P_{\text{peak}}/P_{\text{crit}}$ ratio of 0.18. The 3D model is implemented on a grid size of $64 \times 64 \times 256$ in the space/time domain with steps $dx = dy = 30 \mu\text{m}$, $dt = 10 \text{ fs}$, and $dz = 12 \text{ mm}$ in the propagation direction. For the 1D model, the equivalent effective area is $A_{\text{eff}} = 0.19 \text{ mm}^2$. Figure 2 shows the results of both models, clearly illustrating the fact that at this nonlinearity level, the 1D model quantitatively reproduces the results of the 3D model at a much-reduced computational cost. This makes it a very useful design tool. The small discrepancy shows that the 1D model tends to slightly underestimate the spectral broadening, which is further explored in the following.

For the second comparison, we choose a xenon-filled cell with the following geometry: mirror radius of curvature 300 mm, cell length 551 mm, close to the concentric configuration. These dimensions were chosen to match the experimental parameters used in the next sections, and because the concentric configuration allows the use of relatively compact setups while keeping the beam size at the mirror large, which is important to avoid optical damage.

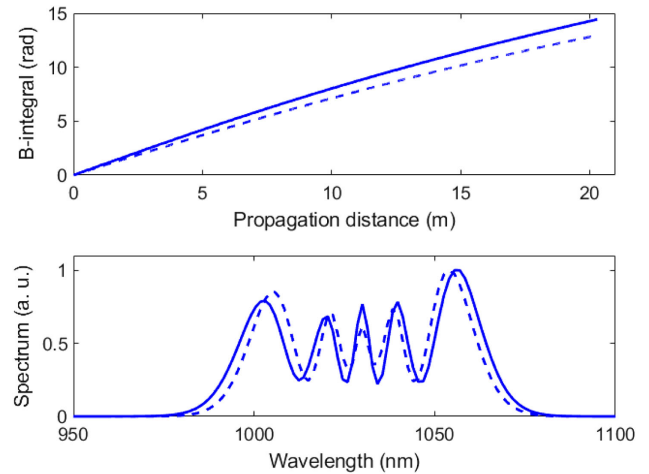


Fig. 2. Top: B -integral as a function of distance in the near-confocal MPC for a xenon pressure of 1 bar. Bottom: spectrum at the output of the MPC. The solid lines correspond to the 3D simulation and the dashed lines to the 1D simulation.

The input pulses have a Gaussian profile in time and space with a 350 fs pulse duration and 200 μJ energy, and propagate along five round trips in the MPC. This number of round trips is chosen to easily illustrate the comparison between the 3D and 1D models in terms of caustic evolution. Two xenon pressures are considered: 0.5 bar, corresponding to a low level of nonlinearity ($P_{\text{peak}}/P_{\text{crit}} = 0.1$), and 3 bars, corresponding to a very high level of nonlinearity ($P_{\text{peak}}/P_{\text{crit}} = 0.6$). The 3D model is implemented on a grid size of $128 \times 128 \times 256$ in the space/time domain with steps $dx = dy = 50 \mu\text{m}$, $dt = 10 \text{ fs}$, and $dz = 5.6 \text{ mm}$ in the propagation direction. For the 1D model, the equivalent effective area is $A_{\text{eff}} = 0.22 \text{ mm}^2$. Figure 3 shows the comparison results. At low nonlinearity, the 1D model still follows closely the 3D model. The main reason is that the caustic evolution during propagation is essentially unmodified by the spatial Kerr effect, as shown in Fig. 3 (top). However, at high nonlinearity, the Kerr lens clearly modifies the beam caustic from the stationary situation. In particular, the first pass shows a beam waist smaller than in the linear case, and an oscillation of the beam size with respect to the unperturbed evolution is observed. This results in a higher level of nonlinearity than the 1D model predicts, as shown in Fig. 2 (middle). The output spectrum is therefore broader for the 3D model than for the 1D model. Note that these discrepancies appear at levels of nonlinearity that are higher than most experimental reports, making the 1D approximation still very useful as a design tool.

Although the beam sizes are modified by the spatial Kerr effect at high nonlinearity level, the 3D simulation shows no spatio-spectral intensity couplings at 3 bars of xenon pressure, corresponding to $P_{\text{peak}}/P_{\text{crit}} = 0.6$. In this case the B -integral per round trip calculated assuming an unperturbed caustic and perfect homogenization is 2.5 rad, and the B -integral of the first round trip from the 3D simulation is 4.3 rad. This 3D B -integral is calculated by taking the on-axis value divided by 2, which should be equal to the average value of the 1D model in the case of perfect Gaussian beam and homogenization. Although it might be surprising that this very large nonlinearity does not induce significant spatio-spectral couplings [19], it has

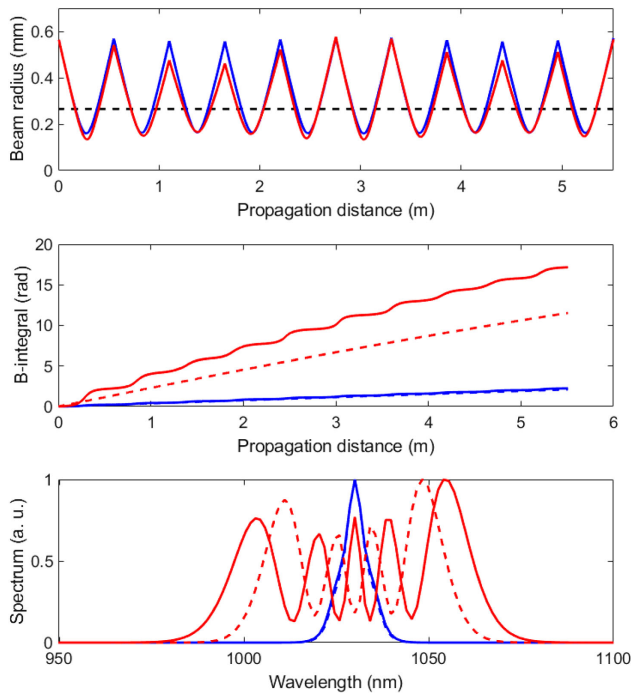


Fig. 3. Top: beam radius as a function of distance in the near-concentric MPC for a xenon pressure of 0.5 bar (blue) and 3 bars (red). The black dashed line corresponds to the equivalent waveguide beam radius. Middle: B -integral as a function of distance in the MPC for a xenon pressure of 0.5 bar (blue) and 3 bars (red). The solid line is the 3D simulation and the dashed line is the 1D simulation. Bottom: spectrum at the output of the MPC for a xenon pressure of 0.5 bar (blue) and 3 bars (red). The solid line is the 3D simulation and the dashed line is the 1D simulation.

also been observed experimentally that a B -integral per round trip of 2.4 rad does not result in the onset of spatio-spectral couplings in intensity, as revealed by an imaging spectrometer characterization [9]. We would like to point out that this is in contradiction with the result reported at the end of our earlier report [15] that showed a rapid increase of the spatio-spectral coupling for the concentric configuration as the nonlinearity is increased. After re-examination of the corresponding simulation data we believe this was the result of insufficient sampling density, a problem that is increasingly challenging as we approach the concentric configuration. Indeed, the beam divergence and size that must be accommodated by the sampling grid both increase. This leaves the question open of how much nonlinearity can be tolerated in a MPC before spatio-spectral couplings appear. We investigate this question experimentally in Section 4.

3. EXPERIMENTAL VALIDATION OF THE 1D MODEL

We start by comparing the 1D model described above with an experiment designed to be able to observe wave breaking. It is a phenomenon that is well known in optical fibers [20], has been recently observed in MPCs [7], and requires a high level of nonlinearity, thereby providing an appropriate physical testbed for the 1D model described here. The experimental setup used

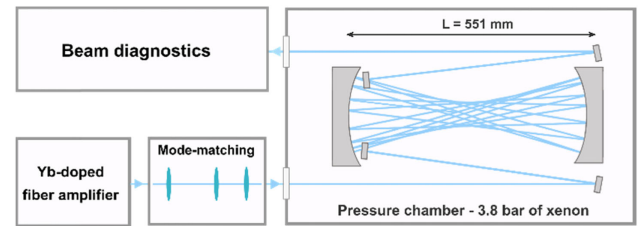


Fig. 4. Experimental setup.

in this study, shown in Fig. 4, includes a MPC that consists of two concave mirrors with a radius of curvature of 300 mm placed in a 3.8-bar xenon-filled gas chamber. The input laser pulse sent into the multipass cell originates from an Yb-doped fiber amplifier delivering a maximum input pulse of 200 μ J energy at a central wavelength of 1030 nm at 150 kHz repetition rate, corresponding to a maximum average power of 30 W. The measured values of the spatial beam quality M^2 are 1.2×1.2 along two orthogonal axes.

Xenon was chosen as the nonlinear medium due to its high nonlinear index among noble gases. At our gas pressure of 3.8 bars the nonlinear index is given by $n_2 = 2.0 \times 10^{-22} \text{ m}^2/\text{W}$, corresponding to a critical power for self-focusing of 0.67 GW, and the group velocity dispersion is 296 fs^2/m . This critical power is higher than yet very close to the maximum input peak power that can be reached by our laser source of $P_{\text{peak}} = 0.59 \text{ GW}$, allowing us to investigate highly nonlinear regimes in this MPC. Two rectangular $3 \times 10 \text{ mm}^2$ mirrors located in front of one of the MPC mirrors were used for in-out coupling of the laser beam. The concave MPC mirrors are chosen to present a high reflection coefficient ($>99.9\%$) on a 980–1080 nm bandwidth and are coated with a dispersive HR coating with a group delay dispersion ($\text{GDD} = -25 \pm 10 \text{ fs}^2$) that partially compensates the normal dispersion introduced by the nonlinear gas medium. The distance separating the two mirrors is chosen to be 551 mm, near a concentric geometrical configuration. By finely adjusting the length between the two mirrors and the input coupling into the cell, we obtain 21 round trips resulting in a total propagation length of 24.5 m including the path before and after the MPC in the gas-filled enclosure. The beam is mode-matched using an arrangement of three lenses, in order to provide beam radii close to theoretical values of 154 μm at the center of the cell expanding to 624 μm on the concave MPC mirrors. This kind of MPC geometry is advantageous, as mentioned earlier, for inducing spectral broadening at relatively high input pulse energy while mitigating any damage of the MPC mirrors since the beam size becomes large on the mirrors allowing us to maintain a fluence on the mirrors well below the damage threshold. However, with a relatively small waist at the center of the cell, one should pay attention to gas ionization. In our case, the maximum intensity at the center of the MPC is $7.9 \times 10^{11} \text{ W}/\text{cm}^2$, well below the ionization threshold for xenon.

The power transmission of the experimental setup is 86%, including the mode-matching optics. This reduced value compared to previous reports might be due to aging of the optical coatings. The beam exiting the MPC is collimated and sent to the diagnostics. The temporal characterization of the output

pulse was made by means of a home-built second-harmonic-generation frequency-resolved optical gating setup allowing us to investigate the occurrence of wave breaking for different values of input energies. This nonlinear effect is observed in nonlinear optical fibers when the combination of self-phase modulation and group-velocity dispersion makes a pulse broaden and change its shape toward an almost rectangular form. This pulse evolution then features the appearance of fast temporal oscillations on both sides of the pulse [20]: the redshifted light near the leading edge travels faster for $\beta_2 > 0$ and overtakes the unshifted light in the tail of the pulse, while the opposite takes place at the trailing edge of the pulse. This gives birth to temporal interference oscillations and subsequent generation of new frequencies at the spectrum edge.

Figure 5 shows the pulse temporal and spectral profiles measured at different levels of input energy compared with the results obtained by the 1D numerical model described above, taking into account the measured spectrum and spectral phase of the input pulse. The temporal profile changes from a Gaussian-shaped pulse to a rectangular-shaped pulse with oscillations appearing on both temporal edges of the pulse as the energy is increased. These oscillations are accompanied by the appearance of broad sidelobes on the pulse spectrum. Wave breaking is experimentally observed, in our case, at input energies $> 60 \mu\text{J}$. At $60 \mu\text{J}$ input energy, the estimated B -integral at which wave breaking occurs is 11.2 rad [20], and the accumulated B -integral obtained from the 1D model corresponding to the experimental parameters is 12 rad , in

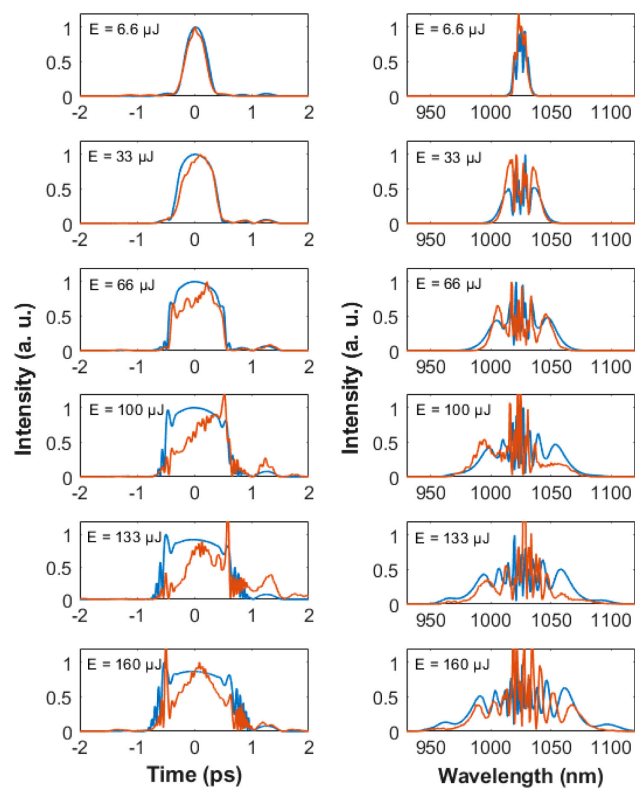


Fig. 5. Left column, FROG-retrieved temporal intensity profile (red) compared to numerically simulated temporal intensity profile (blue) obtained for different levels of input energy at the output of the MPC filled with 3.8 bars of xenon. Right column, measured spectrum (red) compared to spectrum obtained by simulation (blue).

quantitative agreement. There is a good agreement between the experimental results and the model, at $P_{\text{peak}}/P_{\text{crit}}$ ratios up to 0.73 (160 μJ pulse energy), illustrating the value of this simple 1D picture. While it might be surprising at first that the 1D model is still valid at such a high nonlinearity level, we believe that this is due to the fact that it is straightforward to account for an imperfect beam through the M^2 value, as shown in Section 2. It is more difficult to do so with 3D models, since an exact shape of intensity and phase imperfections must be assumed or measured.

4. MEASUREMENT OF INTENSITY AND PHASE SPATIO-SPECTRAL PROFILES

In this section, we investigate the spatio-spectral profiles at the output of the MPC as the nonlinearity increases. Indeed, although energy scaling limitations are well defined regarding gas ionization and mirror damage, the limitation in terms of nonlinearity (either in terms of B -integral per pass or peak power to critical power ratio) is not clear to our knowledge. In particular, it is not yet fully understood how far the nonlinearity level can be pushed in MPCs while still retaining a spatio-spectral coupling-free output beam, although a clear upper bound is the critical power in the gas medium. To study the spatio-spectral couplings in the beam after the multipass cell, we first use an imaging spectrometer setup. This setup is an f-f arrangement composed of an 800 lines/mm grating, a 50 mm focal length cylindrical lens, and an InGaAs CCD camera with a $30 \mu\text{m}$ pixel size. The camera is voluntarily saturated for the spectral components near 1030 nm in order to better observe the spatio-spectral structures of the full broadened spectrum. The results are plotted in Fig. 6.

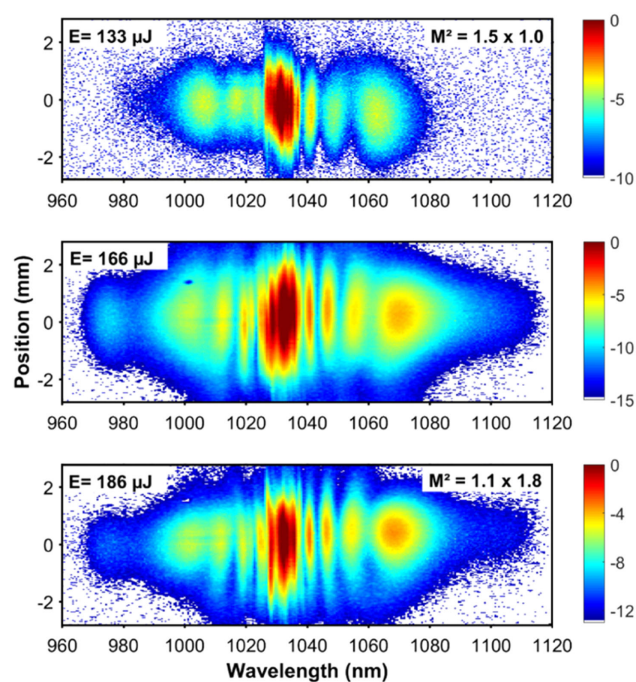


Fig. 6. Experimental spectro-imaging measurements in logarithmic (dB) scale for increasing energies of 133 μJ (top), 166 μJ (middle), and 186 μJ (bottom).

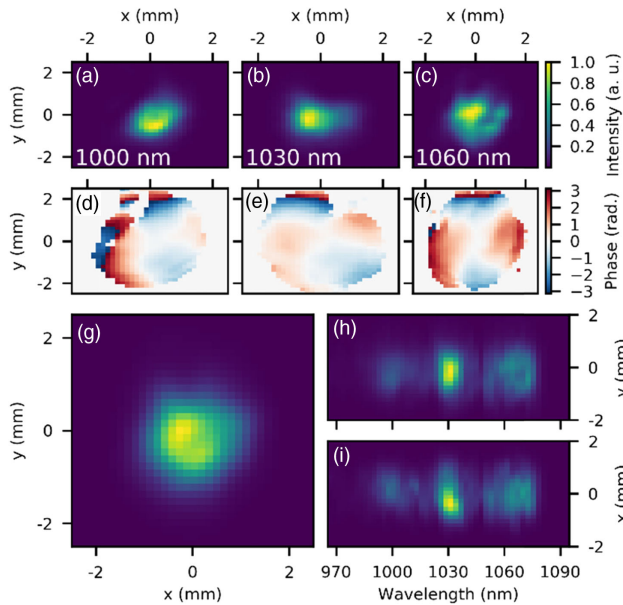


Fig. 7. Results of the INSIGHT measurement. The full spatio-spectral data from the INSIGHT measurement produces the (a)–(c) 2D amplitude profiles and (d)–(f) phase profiles for the three wavelengths shown of 1000, 1030, and 1060 nm. (g) The spectrally integrated beam profile and (h)–(i) spatio-spectral profiles provide a comparison to standard devices. In (h) and (i) the intensity is integrated along the spatial axis that is not shown.

For 133 μJ input energy, corresponding to a $P_{\text{peak}}/P_{\text{crit}}$ ratio of 0.58, the measured spectrum across the transverse profile does not show signs of spatio-spectral couplings. As the energy is increased to 166 μJ ($P_{\text{peak}}/P_{\text{crit}} = 0.73$), some slight signs of couplings appear. At this point the beam pointing starts to be unstable. At 186 μJ pulse energy ($P_{\text{peak}}/P_{\text{crit}} = 0.81$) the beam is very unstable. However, when the spatio-spectral profile is recorded using a low integration time, as shown at the bottom of Fig. 5, it is still not showing very clear signs of couplings in intensity. To quantify this assertion, the mean spectral overlap factor V [21] is 97% even at this extreme nonlinearity level. The mechanism for the observed beam instability is not clearly understood but might be due to the fact that small initial fluctuations in intensity are transferred to changes in the beam propagation through the large amount of Kerr spatial phase.

In order to further assess the spatio-spectral properties of the broadened laser pulses, we use the INSIGHT technique [13], which involves spatially resolved Fourier-transform interferometry at three positions around the focus. Using a phase retrieval algorithm this allows for reconstruction of the spatio-spectral phase in addition to the spectral amplitude already afforded by the Fourier-transform spectroscopy. The results of an INSIGHT measurement at 133 μJ can be seen in Fig. 7, showing both slices of intensity (a)–(c) and phase (d)–(f) at three sample wavelengths, and reconstructed integrated quantities (g)–(i). INSIGHT characterization at higher energy levels was not possible because of the increasing shot-to-shot instability of the beam.

The power of the complete spatio-spectral measurement is the ability to measure both the amplitude and phase at all frequencies within the laser pulses. Therefore, the nonintegrated

processed data can provide information on frequency-resolved aberrations, the so-called spatio-temporal or spatio-spectral couplings [22]. Three maps of the spatial intensity and phase profiles at 1000, 1030, and 1060 nm are shown in Figs. 6(a)–6(c) (intensity) and Figs. 6(d)–6(f) (phase). Although especially at 1060 nm the intensity profile begins to degrade, the phase maps contain very small magnitude low-order aberrations. In fact, in this case the main aberration is a minor wavelength-independent astigmatism, which does not contribute to spatio-temporal deterioration. We do not measure any low-order spatio-temporal couplings such as pulse-front tilt or pulse-front curvature. A single number, the so-called spatio-temporal Strehl ratio [23] can be used to assess the severity of the chromatic phase couplings. In the case of the data shown in Fig. 7, the spatio-temporal Strehl ratio is 0.9, meaning that the spatio-temporal couplings (i.e., the purely chromatic aberrations which would not be possible to correct via a deformable mirror) are responsible for a decrease in focused intensity by 10%.

Figure 7(g) shows the spectrally integrated beam profile, along with integrated 2D spectrograms in Figs. 7(h)–7(i) that numerically reconstruct the imaging spectrometer used to produce the data in the top panel of Fig. 6. The integrated results provide a good benchmark for the INSIGHT results, in that they agree qualitatively with previous measurements. Despite the fact that fine features are not reproduced due to the limited spectral resolution of these INSIGHT measurements compared to the imaging spectrometer (related to the range of the delay scan done), the results, especially in Figs. 7(h)–7(i), are comparable.

5. CONCLUSION

To conclude, we have proposed a simple 1D numerical model that can be used to describe pulse propagation in MPCs with Gaussian beams and is valid when the nonlinearity does not lead to major changes in the beam caustic along propagation. This model is tested experimentally in a near-concentric xenon-filled MPC and allows us to accurately reproduce the observation of wave breaking. We also perform a full 3D characterization of the electric field at the output of a MPC for the first time to our knowledge using the INSIGHT method. Despite the very high level of nonlinearity introduced, no severe spatio-spectral inhomogeneity at the output of the multipass cell has been observed, whether in intensity or phase. Our results show that MPCs can be used to perform nonlinear optical functions usually implemented in optical fibers while scaling the pulse energy.

Funding. Agence Nationale de la Recherche (ANR-10-LABX-0039-PALM, ANR-16-CE30-0027-01-HELLIX).

REFERENCES

- G. P. Agrawal, *Nonlinear Fiber Optics*, 5th ed. (Academic, 2012).
- J. M. Dudley, G. Genty, and S. Cohen, "Supercontinuum generation in photonic crystal fiber," *Rev. Mod. Phys.* **78**, 1135 (2006).
- A. Dubietis and A. Couairon, *Ultrafast Supercontinuum Generation in Transparent Solid-State Media* (Springer, 2019).
- T. Balciunas, C. Fourcade-Dutin, G. Fan, T. Witting, A. A. Voronin, A. M. Zheltikov, F. Gerome, G. G. Paulus, A. Baltuska, and F. Benabid,

- "A strong-field driver in the single-cycle regime based on self-compression in a kagome fibre," *Nat. Commun.* **6**, 6117 (2015).
5. M. Nisoli, S. De Silvestri, O. Svelto, R. Szipöcs, K. Ferencz, Ch. Spielmann, S. Sartania, and F. Krausz, "Compression of high-energy laser pulses below 5 fs," *Opt. Lett.* **22**, 522–524 (1997).
 6. J. Schulte, T. Sartorius, J. Weitenberg, A. Vernaleken, and P. Russbuedt, "Nonlinear pulse compression in a multi-pass cell," *Opt. Lett.* **41**, 4511–4514 (2016).
 7. M. Ueffing, S. Reiger, M. Kaumanns, V. Pervak, M. Trubetskov, T. Nubbemeyer, and F. Krausz, "Nonlinear pulse compression in a gas-filled multipass cell," *Opt. Lett.* **43**, 2070–2073 (2018).
 8. L. Lavenu, M. Natile, F. Guichard, Y. Zaouter, X. Delen, M. Hanna, E. Mottay, and P. Georges, "Nonlinear pulse compression based on a gas-filled multipass cell," *Opt. Lett.* **43**, 2252–2255 (2018).
 9. M. Kaumanns, V. Pervak, D. Kormin, V. Leshchenko, A. Kessel, M. Ueffing, Y. Chen, and T. Nubbemeyer, "Multipass spectral broadening of 18 mJ pulses compressible from 1.3 ps to 41 fs," *Opt. Lett.* **43**, 5877–5880 (2018).
 10. G. Jargot, N. Daher, L. Lavenu, X. Delen, N. Forget, M. Hanna, and P. Georges, "Self-compression in a multipass cell," *Opt. Lett.* **43**, 5643–5646 (2018).
 11. J. Weitenberg, T. Saule, J. Schulte, and P. Rußbüldt, "Nonlinear pulse compression to sub-40 fs at 4.5 μ J pulse energy by multi-pass-cell spectral broadening," *IEEE J. Quantum Electron.* **53**, 1–4 (2017).
 12. L. Lavenu, M. Natile, F. Guichard, X. Délen, M. Hanna, Y. Zaouter, and P. Georges, "High-power two-cycle ultrafast source based on hybrid nonlinear compression," *Opt. Express* **27**, 1958–1967 (2019).
 13. A. Borot and F. Quéré, "Spatio-spectral metrology at focus of ultrashort lasers: a phase-retrieval approach," *Opt. Express* **26**, 26444–26461 (2018).
 14. D. Herriott, H. Kogelnick, and R. Kompfner, "Off-axis paths in spherical mirror interferometers," *Appl. Opt.* **3**, 523–526 (1964).
 15. M. Hanna, X. Délen, L. Lavenu, F. Guichard, Y. Zaouter, F. Druon, and P. Georges, "Nonlinear temporal compression in multipass cells: theory," *J. Opt. Soc. Am. B* **34**, 1340–1347 (2017).
 16. T. Brabec and F. Krausz, "Nonlinear optical pulse propagation in the single-cycle regime," *Phys. Rev. Lett.* **78**, 3282 (1997).
 17. A. Bideau-Mehu, Y. Guern, R. Abjean, and A. Johannin-Gilles, "Measurement of refractive indices of neon, argon, krypton, and xenon in the 253.7–140.4 nm wavelength range. Dispersion relations and estimated oscillator strengths of the resonance lines," *J. Quant. Spectrosc. Radiat. Transfer* **25**, 395–402 (1981).
 18. J. K. Wahlstrand, Y.-H. Cheng, and H. M. Milchberg, "High field optical nonlinearity and the Kramers-Kronig relations," *Phys. Rev. Lett.* **109**, 113904 (2012).
 19. N. Milosevic, G. Tempea, and T. Brabec, "Optical pulse compression: bulk media versus hollow waveguides," *Opt. Lett.* **25**, 672–674 (2000).
 20. D. Anderson, M. Desaix, M. Lisak, and M. L. Quiroga-Teixeiro, "Wave breaking in nonlinear-optical fibers," *J. Opt. Soc. Am. B* **9**, 1358–1361 (1992).
 21. J. Weitenberg, A. Vernaleken, J. Schulte, A. Ozawa, T. Sartorius, V. Pervak, H. Hoffmann, T. Udem, P. Russbüldt, and T. W. Hänsch, "Multi-pass-cell-based nonlinear pulse compression to 115 fs at 7.5 μ J pulse energy and 300 W average power," *Opt. Express* **25**, 20502–20510 (2017).
 22. S. Akturk, X. Gu, P. Bowlan, and R. Trebino, "Spatio-temporal couplings in ultrashort laser pulses," *J. Opt.* **12**, 093001 (2010).
 23. A. Jeandet, A. Borot, K. Nakamura, S. W. Jolly, A. J. Gonsalves, C. Tóth, H.-S. Mao, W. P. Leemans, and F. Quéré, "Spatio-temporal structure of a petawatt femtosecond laser beam," *J. Phys.* **1**, 035001 (2019).



Hybrid pulse propagation model and quasi-phase-matched four-wave mixing in multipass cells

MARC HANNA,^{1,*}  NOUR DAHER,¹ FLORENT GUICHARD,² XAVIER DÉLEN,¹ AND PATRICK GEORGES¹

¹Université Paris-Saclay, Institut d'Optique Graduate School, CNRS, Laboratoire Charles Fabry, 91127 Palaiseau, France

²Amplitude Laser, 11 Avenue de Canteranne, Cité de la Photonique, 33600 Pessac, France

*Corresponding author: marc.hanna@institutoptique.fr

Received 20 April 2020; revised 15 July 2020; accepted 17 August 2020; posted 17 August 2020 (Doc. ID 395789); published 15 September 2020

We describe a nonlinear propagation model based on a generalized Schrödinger equation in the time domain coupled to Gaussian beam evolution through ABCD matrices that account for Kerr lensing in the spatial domain. This model is well suited to simulate propagation in mildly nonlinear systems such as multipass cells for temporal compression. It is validated against both a full (x, y, z, t) numerical model and recently reported experimental results in multipass cells, with excellent agreement. It also allows us to identify the physical mechanism for the recently reported parasitic appearance of spectral content in the 700–950 nm range in argon-filled multipass cells that are used to compress pulses at 1030 nm. We think this is due to a quasi-phase-matched degenerate four-wave mixing process. This process could be used in the future to perform wavelength conversion as is already done in fibers and capillaries. © 2020 Optical Society of America

<https://doi.org/10.1364/JOSAB.395789>

1. INTRODUCTION

Pulse propagation models have been routinely used for decades both to design experiments and interpret their results in the field of ultrafast photonics [1,2]. They can include physical phenomena such as dispersion, diffraction, loss, gain, and nonlinearity, with models spanning a wide range of complexity and taking into account a number of dimensions going from 2D (t, z) or (x, z) to 4D (x, y, z, t) . The value of these models is given by their ability to predict or reproduce the experimental observations in a qualitative or quantitative manner and to do so in a reasonable computing time. This requires adapting the model complexity to the physics at hand.

As an example, nonlinear propagation in single transverse mode fibers can be very well described with (t, z) models, assuming that the transverse field distribution is the fundamental mode of the fiber. Although this is an approximation at high nonlinearity level, when the spatial Kerr effect starts modifying the transverse index distribution locally and instantaneously, a very large number of studies have successfully relied on these models to interpret the obtained data and design experiments [3].

Modeling highly nonlinear ultrafast phenomena in free space, such as filamentation [4] or supercontinuum generation [5], on the other hand, requires at least an additional space dimension

if a cylindrical symmetry is assumed, or a full 4D model. This allows an accurate description of space-time couplings that are almost always observed in experiments. In addition, strong field light–matter interaction effects such as ionization and its impact on propagation, or higher-order nonlinearity, must be accounted for since they play a central role in this physics. These models are complex and require a much larger computing effort than the (t, z) models used for single-mode fiber, which somehow restricts their use and value.

In this paper, we describe a nonlinear propagation model in free space that is adapted to situations where (i) the impact of nonlinearity on the spatial profile is reduced to a change in size and radius of curvature, which allows us to describe it as a Gaussian beam and (ii) negligible space–time couplings are introduced on the propagating field. It is based on a split-step method that propagates the field in time using a generalized nonlinear Schrödinger equation and in space using an ABCD matrix model that accounts for diffraction and a Kerr lens. The time and space parts are coupled through the evolution of peak intensity and beam size. The model presented here is particularly well suited to describe propagation in nonlinear regenerative amplifiers [6], or multipass cells (MPCs) [7–10], where it was shown that an injected Gaussian beam essentially retains its character upon propagation and that space–time

couplings are only observed at extreme levels of nonlinearity [11,12]. Compared to the model presented in Ref. [11], that is, purely (t, z) without a description of spatial effects, the model presented here allows to take into account Kerr lensing that can have nonnegligible impact on the beam caustic, as will be discussed hereunder. Compared to full 4D dimensional models [13], it is much faster in terms of computing time and allows us to account for the impact of beam imperfections on the level of nonlinearity easily through an M^2 beam quality factor. Although several models using the Gaussian ansatz in both space and time have already been proposed [14,15], they fail to predict the complex temporal behavior induced by nonlinear propagation, leading to pulses that cannot be described by a Gaussian ansatz in the time domain and are therefore not appropriate in the MPC context.

The paper is organized as follows. In the first part, we first describe the temporal and spatial parts of the model and how they are coupled. We compare the results both to a full 4D model and to the very simple 2D model described in Ref. [11], showing that the level of physical description adopted is ideal for the particular problem of propagation in MPCs. In a second part, we apply the model to reproduce the experimental data obtained in high-energy gas-filled MPC experiments that use near-concentric configurations [16,17]. In this case, the small beam size and large divergence at the MPC waist makes 4D simulations particularly computationally intensive, underlining the usefulness of our model. The experimental data is quantitatively reproduced, and the numerical results allow us to interpret an observation reported in both cases: the generation of spectral content in the 700–950 nm range. We believe it is due to quasi-phase-matched (QPM) four-wave mixing (FWM) in the normal dispersion regime, and we provide the corresponding phase-matching curve to back this interpretation.

The model can easily describe propagation in both gas-filled MPCs and MPCs including plates of nonlinear material, as well as include dispersion imparted by both material and mirror coatings and all third-order nonlinear effects such as self-phase modulation, self-steepening, and Raman scattering. It provides an efficient tool for the design and data analysis of these nonlinear subsystems that are currently being developed at a fast pace.

2. MODEL DESCRIPTION AND VALIDATION

A. Description

Propagation in the time domain is modeled using the following generalized Schrödinger equation [1]:

$$\frac{\partial A}{\partial z} = - \left(i \frac{\beta_2}{2} \frac{\partial^2}{\partial t^2} - \frac{\beta_3}{6} \frac{\partial^3}{\partial t^3} + \dots \right) A + i\gamma \left(1 + \frac{i}{\omega_0} \frac{\partial}{\partial t} \right) A \times \int_0^\infty R(t') |A(z, t - t')|^2 dt', \tag{1}$$

where $A(z, t)$ is the field normalized so that $|A(z, t)|^2$ is the optical power, z is the propagation distance, t is time, β_n is the n th-order Taylor coefficient of the propagation constant in the material $\beta(\omega) = \omega n(\omega)/c$, ω_0 is the central angular

frequency, c is the speed of light in a vacuum, and $R(t)$ is the normalized third-order nonlinear response of the material, which includes the instantaneous electronic contribution and delayed molecular contributions. Since the dispersive part of this propagation equation is implemented in the frequency domain using a split-step method [1], the full spectral dependence of the local index of refraction $n(\omega)$ is taken into account using an appropriate Sellmeier equation. Quantum noise can be added using a one-photon-per-mode approach [3]. This temporal equation is coupled to the spatial evolution through the nonlinear coefficient $\gamma = n_2 \omega_0 / c A_{\text{eff}}$, where n_2 is the nonlinear index of the material and $A_{\text{eff}} = \pi w(z)^2$ is the effective area of the beam. The beam radius w evolves according to the spatial part of the propagation model described below.

The linear and nonlinear material properties are changed as a function distance to account for propagation in the various materials of the MPC, and discrete transfer functions can be added to account for the spectral reflectivity and dispersion of the coatings on mirrors or bulk plates.

The spatial part of the model consists in propagating the reduced complex Gaussian parameter \hat{q} using the same step dz as in the split-step algorithm used to solve the temporal propagation equation. This parameter is defined as

$$\frac{1}{\hat{q}} = \frac{1}{\hat{R}} + i \frac{\lambda_0}{\pi w^2}, \tag{2}$$

where $1/\hat{R} = n/R$ is the reduced radius of curvature and λ_0 is the central wavelength in a vacuum. This parameter completely determines the Gaussian spatial profile and is propagated according to the usual ABCD matrix formalism [18] according to

$$\hat{q}_{z+dz} = \frac{A\hat{q}_z + B}{C\hat{q}_z + D}. \tag{3}$$

The ABCD matrix that describes propagation over a length dz of material is given by

$$M = \begin{pmatrix} 1 - \frac{dz}{2n f_{\text{Kerr}}} & \frac{dz}{n} \left(1 - \frac{dz}{4f_{\text{Kerr}}} \right) \\ -\frac{1}{f_{\text{Kerr}}} & 1 - \frac{dz}{2n f_{\text{Kerr}}} \end{pmatrix}. \tag{4}$$

It corresponds to propagation in free space in a material with index of refraction n over a length dz , in which a lens with focal length f_{Kerr} is introduced at half distance. Because of the dependence of the ABCD matrix on the beam size, the model must be implemented by incrementing the distance by small steps dz over which the beam size and radius of curvature change only infinitesimally. The definition of the nonlinear focal length is not trivial, and it leads to different results depending on the model used for propagation [19]. The approach we take to evaluate a physically meaningful value is as follows. We start from the precise expression established for the critical power for a Gaussian beam [2,20] $P_{\text{crit}} = 3.77 \frac{\lambda_0^2}{8\pi n n_2}$. This expression corresponds to exact compensation between diffraction and self-focusing, although it is an unstable physical situation. Nonlinear propagation of a time-independent Gaussian beam of power P_{peak} using the model described above is then simulated, with a Kerr focal length equal to

$$f_{\text{Kerr}} = K \frac{\pi w^4}{P_{\text{peak}} n_2 dz}, \quad (5)$$

where K is a constant that can be adjusted. Apart from the constant, this expression corresponds to the expression of the Kerr focal length obtained by using a parabolic approximation for the Gaussian beam intensity profile [21]. The value of K is then adjusted to obtain catastrophic self-focusing for $P_{\text{peak}} > P_{\text{crit}}$ and diffraction for $P_{\text{peak}} < P_{\text{crit}}$ upon free-space propagation in the nonlinear material. We find that this corresponds to $K = 0.47$. When coupled to the time-domain model, the value of the Kerr focal length is defined using the peak power, although one could argue that this focal length varies instantaneously. The nature of our model imposes the absence of space–time couplings, and the peak power is therefore used since it corresponds to the maximum energy density in the time domain.

Imperfections in the beam can easily be taken into account in a first approximation by using an M^2 factor. In this case, an equivalent beam size of $w \times M$ must be used when evaluating the nonlinear parameter γ and the nonlinear focal length f_{Kerr} . In addition, by keeping track of two different \hat{q} parameters for both transverse dimensions, the propagation of elliptical and/or astigmatic Gaussian beams can easily be accounted for.

Possible ionization of the medium is not taken into account in this model. This phenomenon is very threshold-like, and its onset quickly leads to drastic modifications of the beam shape. We therefore considered that it was not relevant in a model that assumes a Gaussian beam shape. The maximum intensity must therefore be monitored to ensure that the ionization rate is negligible.

The overall model is implemented using a propagation step dz small enough to guarantee small changes in beam size, radius of curvature, and temporal and spectral profiles. The temporal model is coupled to the spatial part through the value of peak power, which is coupled back to the time domain through the value of the beam size that defines the level of nonlinearity γ . Note that although this model is valid for spatial profiles close to a Gaussian beam, it is quite general in terms of temporal/spectral intensity and phase profiles. We now examine the validity of this model by comparing it to other approaches to compute the propagation of pulses in a test case.

B. Validation

The test case we choose is the same as in our previous work [11], to allow direct comparison between three numerical models. The first model is a 4D model described in Ref. [13], which fully accounts for diffraction, dispersion, and third-order nonlinearity by solving an envelope equation [22] using the split-step method in space and time. The second model is a purely 2D model that assumes a constant beam size. This beam size is calculated by averaging the nonlinearity accumulated by the linear stationary beam in the MPC over one round-trip as described in Ref. [11]. The third model is the one described in this paper.

We model propagation in a near-concentric MPC composed of two mirrors with radius of curvature 300 mm separated by 551 mm, filled with 3 bars of xenon. The input pulses are Gaussian in space and time with a full width at half-maximum

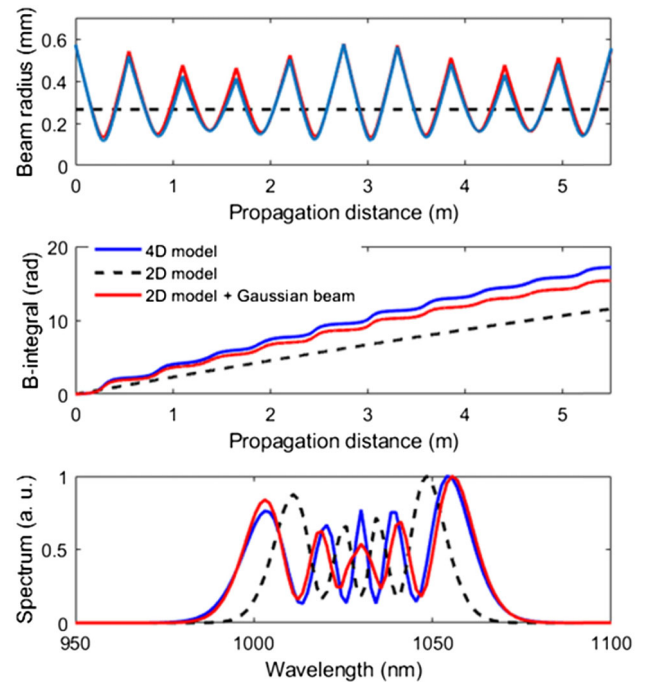


Fig. 1. Comparison of the three numerical models. Top: evolution of the beam caustic. Middle: accumulated B-integral as a function of distance. Bottom: output spectrum. The blue solid lines correspond to the 4D model, the black dashed line to a constant beam size 2D model, and the red line to the hybrid model presented in this paper.

(FWHM) pulse duration of 350 fs, an energy of 200 μJ , and a central wavelength of 1030 nm. The corresponding spectral FWHM is 4.5 nm. They are injected in the cell with a spatial Gaussian parameter that corresponds to the linear stationary beam and are propagated over five round-trips. The numerical simulation parameters are the following. For the 4D model, the grid steps are $dx = dy = 60 \mu\text{m}$, $dz = 5 \text{ mm}$, $dt = 20 \text{ fs}$, and the grid size is $6 \text{ mm} \times 6 \text{ mm}$ in the transverse plane and 2 ps in the time domain. For the constant beam size model and the hybrid model, the temporal grid is the same, and the longitudinal step size is $dz = 1 \text{ mm}$. The results are plotted in Fig. 1.

As already described in Ref. [11], these parameters correspond to a high level of nonlinearity ($P_{\text{peak}}/P_{\text{crit}} = 0.6$), for which the simplified spatially averaged approach significantly underestimates the level of nonlinearity, resulting in a lower amount of spectral broadening. The reason for this is that nonlinearity in the space domain leads to significant changes in the beam size upon propagation, as can be observed in Fig. 1 (top), which is not taken into account by the simple constant beam size approach of the 2D model.

In contrast, by coupling nonlinear beam size evolution to the 2D model as described in this article, we are able to faithfully reproduce the caustic evolution, B-integral accumulation, and output spectrum as clearly observed in Fig. 1. There remains a small underestimation of the nonlinearity, but it has no significant impact on the output spectrum. This could be caused by a slight spatial intensity profile deviation from a purely Gaussian beam. To conclude this part, the simple model presented here allows us to describe highly nonlinear propagation in MPCs

better than the longitudinally invariant model, and it is relevant as long as no significant space–time couplings or deviation from the Gaussian beam shape are induced. These hypotheses have been observed to hold for MPCs in almost all experimental reports. The added computational cost compared to a purely 2D model is negligible, with the benefit that the caustic evolution can be predicted. As shown above, this allows a more precise evaluation of the nonlinearity level, but it is also very useful to design experiments. Indeed, since nonlinear caustic evolution deviates significantly from the linear stationary beam, the maximum fluence on the mirrors or intensity in the gas is also changed, and this model allows for a more realistic prediction of mirror damage and gas ionization thresholds. We now use this model to compare its results to previous experimental reports.

3. APPLICATION TO NEAR-CONCENTRIC GAS-FILLED MPCs

A. Benchmarking Against Experimental Reports

We have chosen two reports that implement near concentric gas-filled MPC configurations, for which the computation effort of a 4D approach requires more than a common laptop computer. In contrast, the modified 2D model proposed here typically takes a few tens of seconds to run on such a machine. The experiments are described in Refs. [16,17]. The model is implemented without any adjustable parameters based on the information provided in these references. The most significant difference between the experiments and the data used in the model is that we have assumed an ideal Gaussian temporal profile at the input.

The first experiment that we numerically reproduce is described in Ref. [16], and it corresponds to the current record in terms of pulse energy compressed using an MPC. Input pulses of 18 mJ at 5 kHz repetition rate are compressed from 1.3 ps down to 40 fs in a 2.985 m long MPC with 1.5 m radius of curvature mirrors, filled with argon at 0.6 bar. The hybrid 2D model is implemented with a temporal step $dt = 2$ fs on a temporal window of 10 ps, with a longitudinal spatial step $dz = 5$ mm. The results of the simulation are shown in Fig. 2 and are in quantitative agreement with the reported experimental results. The amount of group delay dispersion (GDD) used to compress the pulses (by maximizing the peak power) in the simulation is -7600 fs² as opposed to -9400 fs² reported in Ref. [16]. This discrepancy might be due to dispersion of the MPC mirrors or other elements such as windows in the experiment, or possibly slight quadratic phase in the input beam. The simulated output pulse duration is 38 fs, in excellent agreement with the experiment, as well as the obtained output spectrum, which accurately reproduces the experimentally observed broadening and peak structure. The caustic evolution depicted in Fig. 2 (top) shows that the nonlinearity induces slow and relatively low-amplitude oscillations on the beam size in addition to the round-trip modulation caused by propagation in the MPC.

The second experiment we use to benchmark the model is reported in Ref. [17], and it corresponds to the highest average power ever reported in an MPC-based nonlinear compression setup. Input pulses of 1.1 mJ at 500 kHz repetition rate are

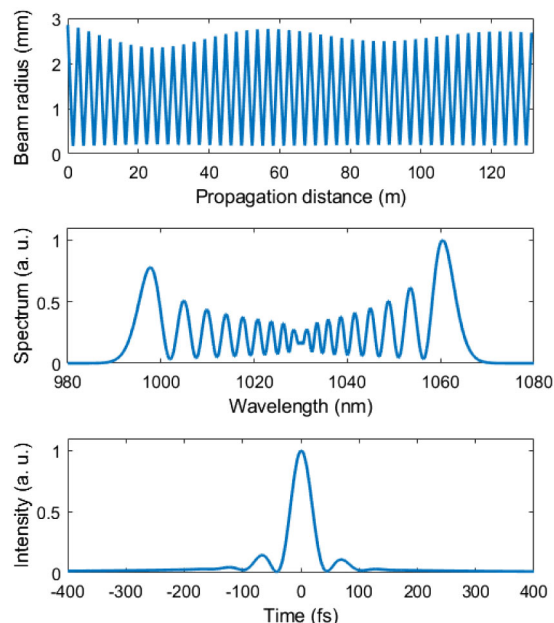


Fig. 2. Numerical results corresponding to the experiment reported in Ref. [16]. Top: beam caustic evolution. Middle: Output spectrum. Bottom: output temporal profile of the compressed pulse.

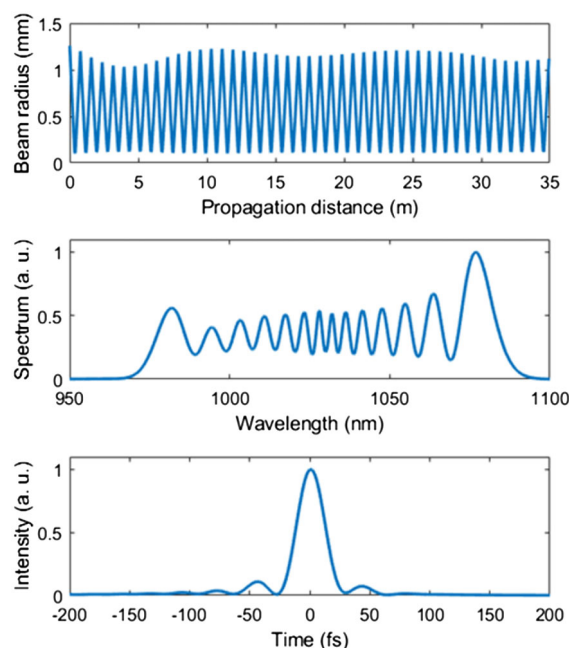


Fig. 3. Numerical results corresponding to the experiment reported in Ref. [17]. Top: beam caustic evolution. Middle: output spectrum. Bottom: output temporal profile of the compressed pulse.

compressed from 590 fs down to 30 fs in a 794 mm long MPC made of 400 mm radius of curvature mirrors filled with argon at 4 bar. The hybrid model is implemented with a temporal step $dt = 2$ fs on a temporal window of 10 ps, with a longitudinal spatial step $dz = 5$ mm. The simulation results are plotted in Fig. 3. The output pulses are compressed with a pure GDD of

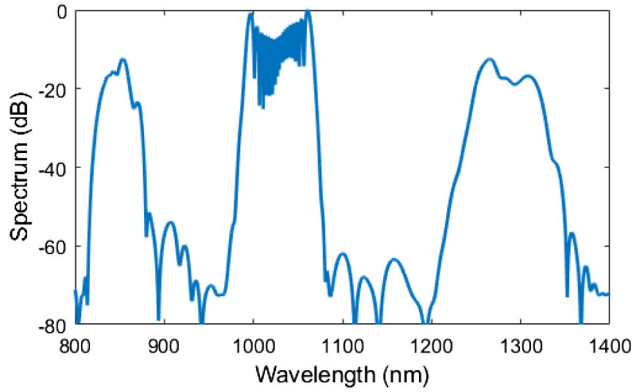


Fig. 4. Numerical output spectrum corresponding to Ref. [16] in logarithmic scale.

-4400 fs^2 as opposed to -5300 fs^2 in the experiment. The output pulse duration is 27 fs, in agreement with the experiment. One noticeable difference is the absence of a spectral peak at 1030 nm in the simulation, which is easily explained by the fact that a pure Gaussian input pulse in the time domain was used as the initial condition. The experimentally observed spectral peak is typically due to a residual pedestal of the input pulse in the time domain that is not spectrally broadened. Apart from this central peak at 1030 nm, the simulated output spectrum reproduces well both the overall broadening and the peak structure observed in the experimental report. We now examine a feature reported by both reports in light of the numerical model.

B. Quasi-Phase-Matched Four-Wave Mixing in MPCs

Both experimental demonstrations mentioned in the previous section report the generation of spectral content in the frequency range 700–950 nm at maximum power/nonlinearity. To investigate this observation, Fig. 4 shows the numerical output spectrum corresponding to Ref. [16] in the broad spectral range 800–1400 nm using a logarithmic scale, generated using the hybrid 2D model. We observe the appearance of spectral content around 860 nm and 1280 nm, which is reminiscent of the signature of phase-matched degenerate FWM that can be observed, e.g., in fibers [23,24]. In this phenomenon, two photons are annihilated at the pump wavelength, while one signal and one idler photon is created on each spectral side. This process satisfies conservation of energy and momentum, and it can be efficient if phase matching is satisfied. In the absence of contributions from waveguide dispersion, this requires that the pump wavelength lies in the anomalous dispersion region of the medium [1]. However, it has been shown that phase matching can be achieved in fibers in the normal dispersion regime by exploiting waveguide dispersion [25,26].

Since propagation in MPCs is in free space, and because 1030 nm is located in the normal dispersion region for argon, there is no obvious possibility to attribute the reported observation to a phase-matched FWM process. However, both these observations were made in concentric MPCs, where the nonlinearity is highly located at the cell waist. The nonlinearity $\gamma(z)$ is therefore a periodic function with period L_{MPC} , defined as the distance between the mirror cells. This opens the possibility of a

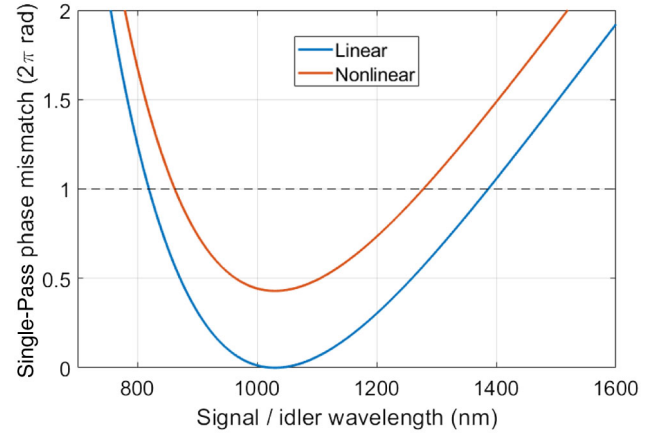


Fig. 5. Linear ($B_{\text{roundtrip}} = 0$) and nonlinear QPM curves for FWM corresponding to [16].

QPM process [27]: energy transfer to the sidebands occurs upon propagation through the waist (over the Rayleigh range in a first approximation), and quasi-linear propagation in the remainder of the cell resynchronizes the relative idler, signal, and pump phases for the energy transfer at the next waist.

To further investigate if the observation is compatible with this physical origin, we evaluate the corresponding phase-matching condition in MPCs. The pump, signal, and idler angular frequencies must satisfy energy conservation $2\omega_p = \omega_s + \omega_i$. Considering only the linear contribution to phase matching as a first simple approximation, the QPM condition can be written as

$$\Delta\beta_L = \beta(\omega_s) + \beta(\omega_i) - 2\beta(\omega_p) = \frac{2m\pi}{L_{\text{MPC}}}, \quad (6)$$

where m is an integer. The propagation constants in Eq. (6) are simply determined by the gas nature and pressure, neglecting contributions from other sources such as mirror coatings. The QPM process can be more efficient if the region where nonlinearity occurs is shorter than half the coherence length $L_{\text{coh}} = 2\pi/|\Delta\beta_L|$, so the energy always transfers from the pump to the signal and idler. In the nondepleted pump and weak signal/idler approximation, the nonlinear contribution to phase matching can be readily included as $\Delta\beta_{\text{NL}}(z) = 2\gamma(z)P_{\text{peak}}$ [1]. In this case, the QPM condition becomes

$$\int_0^{L_{\text{MPC}}} (\Delta\beta_L + \Delta\beta_{\text{NL}}) dz = \Delta\beta_L L_{\text{MPC}} + B_{\text{roundtrip}} = 2m\pi, \quad (7)$$

where $B_{\text{roundtrip}}$ is the B-integral per round-trip that can be evaluated for a given gas-filled MPC configuration using [13]

$$B_{\text{roundtrip}} = \frac{8\pi n_2 P_{\text{peak}}}{\lambda_p^2} \arctan\left(\sqrt{\frac{L}{2R-L}}\right). \quad (8)$$

The linear [corresponding to Eq. (6)] and nonlinear [Eq. (7)] FWM QPM curves for the experiment reported in Ref. [16] are plotted in Fig. 5.

We first notice on the linear curve that, due to the normal dispersion regime, perfect phase matching is not possible elsewhere

than at the pump wavelength, which corresponds to simple self-phase modulation (SPM). In the linear approximation, the first-order QPM sidebands are located at 820 nm and 1385 nm. The nonlinear contribution to phase matching shifts the curve upwards, resulting in phase-matched sidebands closer to the pump wavelength. Note that in the nonlinear QPM condition described in Eq. (7), it is assumed that SPM at the signal/idler wavelength is negligible, so the curve is meaningless at wavelengths that overlap with the pump spectrum. In this region the interaction is always phase matched since it corresponds to pure SPM.

We observe that nonlinear QPM of the first order ($m = 1$) occurs at signal and idler wavelengths around 860 nm and 1280 nm, which further backs our hypothesis that QPM FWM is at the origin of the observed spectral content. The Rayleigh range in Ref. [16] is 10 cm, while the average coherence length is greater than 1 m, which verifies the condition for an efficient QPM process. The generated wavelengths in the simulation shown in Fig. 4 match very well those predicted by the nonlinear phase-matching condition. We have verified that this holds true when changing the parameters such as peak power, MPC length, etc. The experimentally reported value of around 930 nm differs quite a bit, but this might possibly be due to uncertainties in the actual peak power and the exact dispersion of argon. It could also be due to additional dispersion introduced at the mirror coatings that is not accounted for here.

The experiment described in Ref. [17] can be interpreted similarly with a quasi-phase-matching that is satisfied at 895 nm and 1235 nm, while the numerical simulation shows the initial appearance of sidebands at these wavelengths, with a progressive shift towards a greater wavelength separation from the pump upon propagation. We believe this shift to be due to the decrease of peak power caused by the nonnegligible group-velocity dispersion of argon at a pressure of 4 bar.

It should be noted that the gain provided by this process is very high, since what is observed is essentially optical parametric generation. Although a parasitic effect in the reported compression experiment, this process could be used, e.g., to amplify ultrashort pulses, as is already the case in optical fibers [26] or gas-filled capillaries [28,29]. This FWM phenomenon bears a lot of resemblance to modulation instability in dispersion oscillating fibers [30], for which a similar QPM condition exists and therefore can be observed in the normal dispersion regime as well. The main difference is that the oscillating quantity along the propagation distance in our case is the nonlinearity.

4. CONCLUSION

We have presented a hybrid nonlinear pulse propagation model that is based on a rather complete approach in the time domain and includes a basic description of Gaussian beam size and radius of curvature in the spatial domain. It is well suited to describe propagation in nonlinear MPCs, for which the spatial nonlinearity is often low enough to consider that the spatial profile remains Gaussian and negligible space-time couplings are introduced. This approach allows us to include the influence of the caustic evolution on the nonlinearity. The model is validated against a more complete but computation-intensive numerical approach, as well as two recent experiments that are at

the state of the art in terms of performance. Finally, it allows us to identify the origin of a parasitic process in these experiments, which we believe is due to QPM FWM. Although the model is only applied to rare gas-filled near-concentric MPCs in this work, it is straightforward to apply it in the case of molecular gases or MPCs including solid plates of medium, in arbitrary geometries, to describe a large panel of possible nonlinear interactions.

Funding. Agence Nationale de la Recherche (ANR-10-LABX-0039-PALM, ANR-16-CE30-0027-01-HELLIX, ANR-19-CE30-0001-02-MIRTHYX).

Disclosures. The authors declare no conflicts of interest.

REFERENCES

- G. P. Agrawal, *Nonlinear Fiber Optics*, 5th ed. (Academic, 2012).
- A. Couairon, E. Brambilla, T. Corti, D. Majus, O. de J. Ramirez-Gongora, and M. Kolesik, "Practitioner's guide to laser pulse propagation models and simulation," *Eur. Phys. J. Spec. Top.* **199**, 5–76 (2011).
- J. M. Dudley, G. Genty, and S. Coen, "Supercontinuum generation in photonic crystal fiber," *Rev. Mod. Phys.* **78**, 1135–1184 (2006).
- A. Couairon and A. Mysyrowicz, "Femtosecond filamentation in transparent media," *Phys. Rep.* **441**, 47–189 (2007).
- A. Dubietis and A. Couairon, *Ultrafast Supercontinuum Generation in Transparent Solid-state Media* (Springer, 2019).
- J. Pouysegur, M. Delaigue, Y. Zaouter, C. Hönninger, E. Mottay, A. Jaffrès, P. Loiseau, B. Viana, P. Georges, and F. Druon, "Sub-100-fs Yb:CALGO nonlinear regenerative amplifier," *Opt. Lett.* **38**, 5180–5183 (2013).
- J. Schulte, T. Sartorius, J. Weitenberg, A. Vernaleken, and P. Russbueltdt, "Nonlinear pulse compression in a multi-pass cell," *Opt. Lett.* **41**, 4511–4514 (2016).
- M. Ueffing, S. Reiger, M. Kaumanns, V. Pervak, M. Trubetskov, T. Nubbemeyer, and F. Krausz, "Nonlinear pulse compression in a gas-filled multipass cell," *Opt. Lett.* **43**, 2070–2073 (2018).
- L. Lavenu, M. Natile, F. Guichard, Y. Zaouter, X. Delen, M. Hanna, E. Mottay, and P. Georges, "Nonlinear pulse compression based on a gas-filled multipass cell," *Opt. Lett.* **43**, 2252–2255 (2018).
- L. Lavenu, M. Natile, F. Guichard, X. Délen, M. Hanna, Y. Zaouter, and P. Georges, "High-power two-cycle ultrafast source based on hybrid nonlinear compression," *Opt. Express* **27**, 1958–1967 (2019).
- N. Daher, F. Guichard, S. W. Jolly, X. Délen, F. Quéré, M. Hanna, and P. Georges, "Multipass cells: 1D numerical model and investigation of spatio-spectral couplings at high nonlinearity," *J. Opt. Soc. Am. B* **37**, 993–999 (2020).
- P. L. Kramer, M. K. R. Windeler, K. Mecseki, E. G. Champenois, M. C. Hoffmann, and F. Tavella, "Enabling high repetition rate nonlinear THz science with a kilowatt-class sub-100 fs laser source," *Opt. Express* **28**, 16951–16967 (2020).
- M. Hanna, X. Délen, L. Lavenu, F. Guichard, Y. Zaouter, F. Druon, and P. Georges, "Nonlinear temporal compression in multipass cells: theory," *J. Opt. Soc. Am. B* **34**, 1340–1347 (2017).
- A. G. Kostenbauder, "Ray-pulse matrices: a rational treatment for dispersive optical systems," *IEEE J. Quantum Electron.* **26**, 1148–1157 (1990).
- C. Jirauschek and F. X. Kärtner, "Gaussian pulse dynamics in gain media with Kerr nonlinearity," *J. Opt. Soc. Am. B* **23**, 1776–1784 (2006).
- M. Kaumanns, V. Pervak, D. Kormin, V. Leshchenko, A. Kessel, M. Ueffing, Y. Chen, and T. Nubbemeyer, "Multipass spectral broadening of 18 mJ pulses compressible from 1.3 ps to 41 fs," *Opt. Lett.* **43**, 5877–5880 (2018).
- P. Russbueltdt, J. Weitenberg, J. Schulte, R. Meyer, C. Meinhardt, H. D. Hoffmann, and R. Poprawe, "Scalable 30 fs laser source with 530 W average power," *Opt. Lett.* **44**, 5222–5225 (2019).

18. A. E. Siegman, *Lasers* (University Science Books, 1986).
19. S. Leghmizi, A. Hasnaoui, B. Boubaha, A. Aissani, and K. Ait-Ameur, "On the different ways for defining the effective focal length of a Kerr lens effect," *Laser Phys.* **27**, 106201 (2017).
20. G. Fibich and A. L. Gaeta, "Critical power for self-focusing in bulk media and in hollow waveguides," *Opt. Lett.* **25**, 335–337 (2000).
21. W. Koechner, *Solid-state Laser Engineering*, 6th ed. (Springer, 2006).
22. T. Brabec and F. Krausz, "Nonlinear optical pulse propagation in the single-cycle regime," *Phys. Rev. Lett.* **78**, 3282–3285 (1997).
23. M. E. Marhic, P. A. Andrekson, P. Petropoulos, S. Radic, C. Peucheret, and M. Jazayerifar, "Fiber optical parametric amplifiers in optical communication systems," *Laser Photon. Rev.* **9**, 50–74 (2015).
24. M. Hanna, F. Druon, and P. Georges, "Fiber optical parametric chirped-pulse amplification in the femtosecond regime," *Opt. Express* **14**, 2783–2790 (2006).
25. C. Jauregui, A. Steinmetz, J. Limpert, and A. Tünnermann, "High-power efficient generation of visible and mid-infrared radiation exploiting four-wave-mixing in optical fibers," *Opt. Express* **20**, 24957–24965 (2012).
26. W. Fu and F. W. Wise, "Normal-dispersion fiber optical parametric chirped-pulse amplification," *Opt. Lett.* **43**, 5331–5334 (2018).
27. J. A. Armstrong, N. Bloembergen, J. Ducuing, and S. Pershan, "Interactions between light waves in a nonlinear dielectric," *Phys. Rev.* **127**, 1918–1939 (1962).
28. C. G. Durfee, S. Backus, H. C. Kapteyn, and M. M. Murnane, "Intense 8-fs pulse generation in the deep ultraviolet," *Opt. Lett.* **24**, 697–699 (1999).
29. F. Belli, A. Abdolvand, J. C. Travers, and P. St.J. Russell, "Highly efficient deep UV generation by four-wave mixing in gas-filled hollow-core photonic crystal fiber," *Opt. Lett.* **44**, 5509–5512 (2019).
30. A. Mussot, M. Conforti, S. Trillo, F. Copie, and A. Kudlinski, "Modulation instability in dispersion oscillating fibers," *Adv. Opt. Photon.* **10**, 1–42 (2018).



Spectral compression in a multipass cell

NOUR DAHER,^{1,*} FLORENT GUICHARD,² XAVIER DÉLEN,¹ YOANN ZAOUTER,² MARC HANNA,¹  AND PATRICK GEORGES¹

¹Université Paris-Saclay, Institut d'Optique Graduate School, CNRS, Laboratoire Charles Fabry, 91127 Palaiseau, France

²Amplitude Laser, 11 Avenue de Canteranne, Cité de la Photonique, 33600 Pessac, France

*nour.daher@institutoptique.fr

Abstract: Starting from a femtosecond ytterbium-doped fiber amplifier, we demonstrate the generation of near Fourier transform-limited high peak power picosecond pulses through spectral compression in a nonlinear solid-state-based multipass cell. Input 260 fs pulses negatively chirped to 2.4 ps are spectrally compressed from 6 nm down to 1.1 nm, with an output energy of 13.5 μ J and near transform-limited pulses of 2.1 ps. A pulse shaper included in the femtosecond source provides some control over the output spectral shape, in particular its symmetry. The spatial quality and spatio-spectral homogeneity are conserved in this process. These results show that the use of multipass cells allows energy scaling of spectral compression setups while maintaining the spatial properties of the laser beam.

© 2020 Optical Society of America under the terms of the [OSA Open Access Publishing Agreement](#)

1. Introduction

Spectral compression of negatively chirped pulses in a nonlinear medium is an elegant way to turn a femtosecond laser source into a close to Fourier transform-limited (FTL) picosecond source [1]. This allows the design of synchronized sources with widely different durations, of particular importance for a variety of nonlinear spectroscopy experiments such as stimulated Raman scattering microscopy [2]. Powerful laser sources delivering few picosecond UV pulses are also required in free electron laser installations to trigger the photocathode [3], and can be obtained by frequency converting FTL ps pulses in the near infrared. Starting from a femtosecond laser, self-phase modulation can be used to generate both picosecond sources through spectral compression [4] and a few-cycle beam through temporal compression [5]. Spectral compression can be intuitively understood as follows: an initial negative frequency chirp is compensated by the frequency shift induced by self-phase modulation. This frequency shift, in turn, is determined by the temporal intensity profile, which itself is related to the spectral profile since the pulses are chirped.

Most spectral compression experiments have been performed in single transverse mode solid-core optical fibers [1,4,6–9], that allow to increase the interaction length almost arbitrarily, and fix the spatial profile. As a consequence, the pulse energy is limited by the damage threshold at the fiber facet and catastrophic self-focusing if the peak power exceeds the critical power in fused silica. This corresponds to energies of 1–10 μ J for pulses in the 1–10 ps duration range. Although it has never been done to our knowledge, gas-filled capillaries could in principle be used to perform spectral compression, but their losses typically restricts their use to pulse energies above 1 mJ for picosecond pulses. This gap in pulse energy could in principle be filled by use of gas-filled Kagome or anti-resonant microstructured hollow-core fibers, but no demonstration was reported. An alternative technique for energy scaling is possible using hybrid architectures, where nonlinearities are distributed over fiber and bulk amplifiers [10]. A few experiments [11,12] have also reported the observation of spectral compression in bulk media for pulses with much higher energies (mJ level), with moderate spectral compression factors. In this case, the complex

spatio-temporal dynamics induces spatio-spectral couplings, which limits the applicability of the method.

Recently, multipass cells (MPC) have been proposed and used as a platform to perform nonlinear optics at high pulse energies while essentially retaining the one dimensional dynamics that is observed in optical fibers. A solid or gas nonlinear medium is inserted inside the cell, allowing easy tuning of the nonlinearity level through the gas pressure or bulk medium thickness, while dispersion properties may be easily tailored through appropriate mirrors coatings. This concept has been used mostly to implement temporal compression in a wide range of pulse energies and durations [13–17]. In the case of experiments that make use of a bulk medium inserted in the MPC the peak power scaling is not limited by the critical power because the pulses exit the nonlinear medium before catastrophic collapse at each pass. MPCs are therefore a valid alternative to solid- or hollow-core fibers and capillaries as a platform for nonlinear optics, and can be advantageous in terms of transmission, possibilities in dispersion and nonlinearity engineering, and polarization-maintaining properties.

In this article, we report the use of a MPC to perform spectral compression at $\sim 27 \mu\text{J}$ input energy, beyond what is possible in solid core fibers. Negatively chirped pulses generated from a high-energy ytterbium-doped fiber chirped pulse amplifier (FCPA) are spectrally compressed, starting from a spectral full width at half maximum (FWHM) of 6 nm down to 1.1 nm. In the time domain, this corresponds to the generation of FTL 2.1 ps pulses. The MPC nonlinearity is provided by plates of fused silica inserted in the cell. A pulse shaper included in the fiber amplifier architecture allows us to finely adjust the negative frequency chirp and control the process in order to obtain a symmetrical spectral compression. The measured output beam quality factor is $M^2 = 1.2 \times 1.0$ with high spectral homogeneity. This proof of principle constitutes an additional example of the use of MPC to scale the energy of nonlinear subsystems that are usually implemented using optical fibers.

2. Experiment

Spectral compression is performed with the experimental setup shown in Fig. 1. The input pulses originate from a FCPA operating at a central wavelength of 1030 nm, delivering quasi-FTL 260 fs 30 μJ pulses at a repetition rate of 1 MHz. The output spectrum exhibits a nearly Gaussian shape with a FWHM of 6 nm. A commercially available pulse shaper is inserted in the laser architecture before the main amplifier to allow control over the spectral intensity and phase in this quasi-linear amplifier system, similarly to the system described in [18]. This pulse shaper is based on a spatial light modulator inserted in the Fourier plane of a 4f dispersive line, with a spectral resolution of 100 pm, and provides both intensity and phase shaping capabilities. The measured spatial quality factor of the laser beam is $M^2 = 1.1$ along both horizontal and vertical directions.

The multipass cell is a Herriot-type [19] cell and consists of two concave mirrors with 2 inches diameter facing each other with a radius of curvature of 300 mm and coated with high reflectivity, low group delay dispersion dielectric stacks on a 980-1080 nm bandwidth. Two 12 mm-thick AR-coated fused silica plates, spaced by 23 mm, are added near the center of the MPC to serve as nonlinear media. Using fused silica as a nonlinear medium allows us to introduce a higher level of nonlinearity compared to gas-filled MPCs, due to a three order of magnitude higher nonlinear refractive index $n_2 = 2.2 \times 10^{-20} \text{ m}^2/\text{W}$ [20]. This does not prevent operation at peak powers well above the critical power of self-focusing of 5 MW if the self-focusing distance is greater than the plate thickness [13]. The distance between the MPC mirrors is adjusted to 554 mm. Mode-matching to the stationary MPC beam is achieved by an arrangement of three lenses, resulting in a beam diameter of 370 μm at the waist, 9% larger than the resonant waist beam diameter (assuming an $M^2=1.1$). The beam diameter on mirrors is 1.24 mm, leading to an energy density well below the damage threshold, thus allowing straightforward energy scaling of this

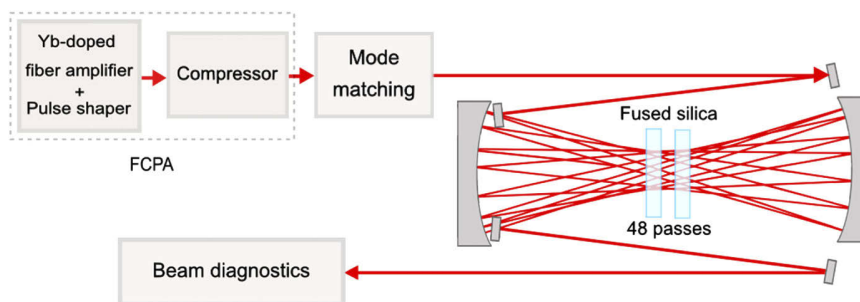


Fig. 1. Experimental setup. The high energy FCPA system includes a pulse shaper that allows modification of the output spectral phase, and the compressor can also be adjusted to modify the output pulse chirp. Mode matching is achieved by an arrangement of three lenses. After propagation in the MPC, the beam is analyzed using a FROG setup, beam profiler, M^2 measurement setup, and imaging spectrometer.

scheme. Two 3 mm width rectangular mirrors located in front of one of the MPC mirrors are used to couple the beam into and out of the cell. The number of roundtrips (reflections on each MPC mirror) in the MPC is 24.

The power transmission of the MPC is 51%, including the mode-matching optics. This low value is mostly due to the non-optimal AR coating of the fused silica plates, with an estimated reflectance higher than 0.1% for each interface. It could be readily increased using a single 24 mm plate and better quality AR coating [13,14]. The beam at the output of the MPC is collimated and characterized. The pulse temporal profile and spectrum at the output of the MPC are measured by means of a home-built second harmonic-generation frequency resolved optical gating (FROG) setup.

We start by introducing the necessary negative chirp for spectral compression by changing the distance between the gratings inside the FCPA. The pulse duration is broadened from 260 fs to 2.1 ps. In this case, Fig. 2 shows the results of an optimal spectral compression obtained at 19 μJ input energy. The spectrum FWHM is compressed from 6 nm down to 1.06 nm while the temporal duration of the negatively chirped pulse remains unchanged after spectral compression. The time-bandwidth product (TBP) of the pulse at the output of the MPC is 0.66 indicating a transform-limited pulse: the TBP of a FTL pulse exhibiting the temporal profile of the output pulse in this example is 0.64. An asymmetrical spectral shape with side lobes on the long wavelength side is observed after compression as shown in Fig. 2(d). This is also noticeable in the associated FROG traces shown in Figs. 2(a)–2(b).

As stated in the introduction, the spectral compression mechanism involves an initial negative instantaneous frequency chirp and subsequent SPM-induced frequency shift. When all relevant quantities such as instantaneous frequency, spectral, and temporal intensity profiles are symmetric with respect to a center frequency, the process leads to a symmetric spectrum. However, slight asymmetry in these shapes due to e. g. the real gain profile of the amplifier, or cubic spectral phase, lead to a non-symmetric output spectrum as observed here. In order to control the spectral compression and obtain a cleaner spectral shape at the output, we use the pulse shaper embedded in the laser architecture.

In this second experiment, starting from an optimally compressed pulse with a duration of 260 fs, the chirp is now introduced at the pulse shaper with a quadratic phase $\varphi_2 = -190 \times 10^3 \text{ fs}^2$ and a cubic phase $\varphi_3 = -9 \times 10^6 \text{ fs}^3$ leading to the generation of 2.4 ps pulses at the output of the FCPA. Note that chirping with the grating compressor lead to the opposite sign of third-order spectral phase, since the φ_3/φ_2 ratio is negative for gratings pairs. The results of the FROG measurement obtained after the MPC for 27 μJ input energy are presented in Fig. 3. The spectrum

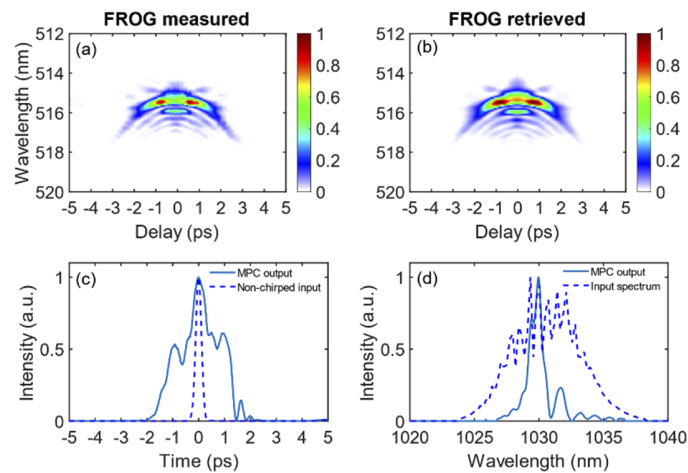


Fig. 2. (a) Measured and (b) retrieved FROG traces plotted in linear scale at the MPC output at 19 μJ input energy; (c) FROG-retrieved temporal intensity profile (solid) at the MPC output and the temporal profile of the input laser pulse before negative chirping (dashed); (d) FROG-retrieved spectral intensity profile (solid) at the MPC output and spectrum of the input laser pulse (dashed).

is compressed to 1.13 nm and the temporal duration is 2.1 ps at FWHM with a TBP of 0.68. Although the compressed spectral width is approximately equal to that obtained in the previous case, the spectral compression is now symmetric. This equally distributed intensity can also be seen in the FROG traces in Figs. 3(a)–3(b). Further improvement in the output spectrum, in particular lower sidelobes intensity, could be obtained by using a parabolic-shaped input pulse such as in [1,21]. The obtained temporal pulse profile approaches a square distribution, as already suggested in [22].

We now compare these experimental results to numerical simulations using a simplified model as described in [23]. This hybrid model uses a standard approach based on a generalized nonlinear Schrödinger equation in the time domain, coupled to a simple Gaussian beam evolution based on ABCD matrices that include the Kerr lens. In particular, it allows to describe the impact of nonlinearity on the beam caustic inside the MPC. The parameters used in the simulations are the same as in the experiment. The initial condition is taken from the measured input FROG traces in both cases: negative chirp introduced using the grating pair or using the pulse shaper. Figure 4 shows the temporal profiles measured at the input of the MPC along with measured and simulated spectral and temporal profiles at the output of the MPC in both experimental configurations. For the gratings compressor-induced chirp case, the estimated B-integral for the first roundtrip is 0.51 rad, while it is 0.54 rad for the second experiment, leading to a total accumulated B-integral of respectively 9.0 rad and 9.5 rad after 24 roundtrips. There is a good qualitative agreement between experimental and numerical results. In particular, we see that the change of sign for the third order spectral phase introduced by the pulse shaper leads to a change in the input intensity profile, with a steepest edge being transferred from the leading edge to the trailing edge, resulting in a more symmetric spectrally compressed spectrum.

Another critical aspect to investigate at the output of MPCs is the spatio-spectral properties. We study the spatio-spectral homogeneity of the beam after the multipass cell by using an imaging spectrometer setup. It consists of an f-f arrangement composed of an 800 lines/mm grating, a 50 mm focal length cylindrical lens and a CCD camera with a 4 μm pixel size. We also measure the beam spatial profile and M^2 quality factor at the output of the MPC. The results are presented

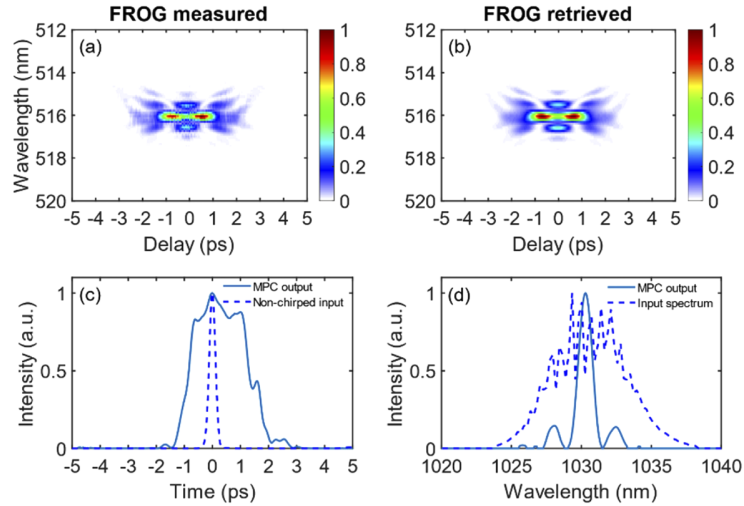


Fig. 3. (a) Measured and (b) retrieved FROG traces plotted in linear scale at the MPC output at 27 μJ input energy; (c) FROG-retrieved temporal intensity profile (solid) at the MPC output and the temporal profile of the input laser pulse before negative chirping (dashed); (d) FROG-retrieved spectral intensity profile (solid) at the MPC output and spectrum of the input laser pulse (dashed).

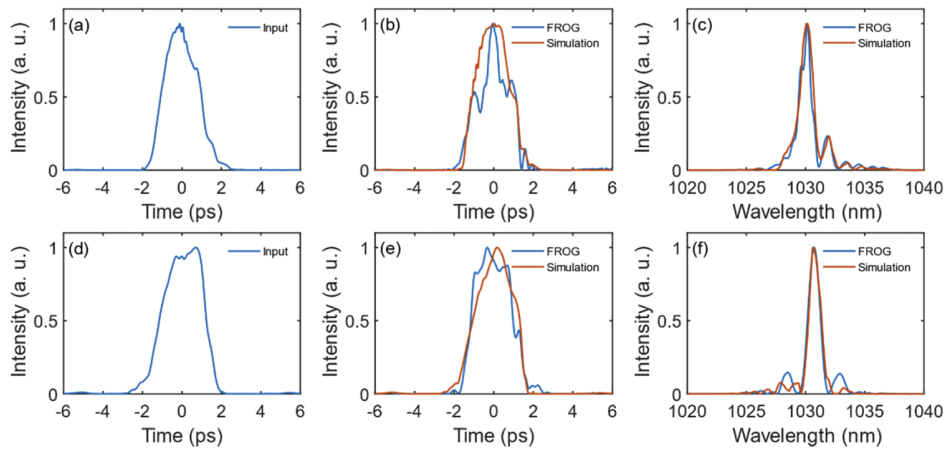


Fig. 4. First row, grating pair-induced negative chirp configuration; second row, pulse shaper-induced negative chirp configuration. (a),(d) FROG-retrieved temporal intensity profile of the input chirped pulse; (b),(e) FROG-retrieved temporal intensity profile (blue) compared to numerically simulated temporal intensity profile (red) at the MPC output; (c),(f) FROG-retrieved spectral intensity profile at the MPC output (blue) compared to spectral intensity profile obtained by simulation (red).

in Fig. 5. Although the intensity profile shows some degradation at the output, the measured M^2 is 1.2×1.0 along the vertical and the horizontal directions respectively, showing that the beam remains close to Gaussian. The larger beam size at the output of the MPC is due to the fact that the beam was collimated with a larger focal length than at the input. The mean spectral overlap factor V [24] is 98%, confirming quantitatively the absence of spatio-spectral intensity inhomogeneity.

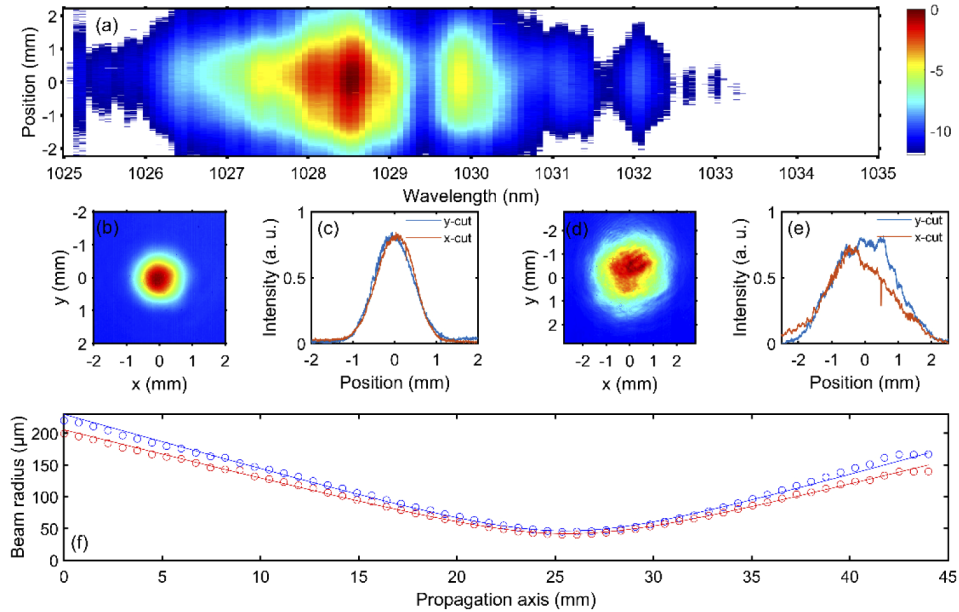


Fig. 5. (a) Experimental spectro-imaging measurement in logarithmic (dB) scale for $19 \mu\text{J}$ input energy; (b) measured spatial beam profile of the input laser beam, and (c) corresponding lineouts; (d) measured spatial beam profile at the MPC output at $19 \mu\text{J}$ input energy and (e) corresponding lineouts; (f) measured beam caustics and corresponding Gaussian beam fit at the MPC output in both directions.

3. Conclusion

To conclude, we report the use of a solid-state material-based MPC to implement spectral compression. This allows the generation of near-transform-limited 2.1 ps pulses from a femtosecond Yb-doped laser amplifier while preserving the spatial quality of the beam. By fine adjustments of the spectral phase at the input of the MPC using a pulse shaper, we generate a symmetric spectrum at the output. The experimentally observed temporal and spectral profiles are in good agreement with those obtained by numerical 1D simulation. We therefore demonstrate the ability to use multipass cells to perform spectral compression at energy levels beyond what is possible in fibers, extending the possibilities to design multiple output femtosecond / picosecond synchronized laser sources. Bulk-based MPCs have been demonstrated with input peak-power ten times higher to the critical peak-power [13,14]. Thus, straightforward energy scaling of such setup to $100 \mu\text{J}$ is possible, while the mJ energy range would be accessible using gas-filled schemes.

Funding

Agence Nationale de la Recherche (ANR-10-LABX-0039-PALM, ANR-16-CE30-0027-01-HELLIX).

Disclosures

The authors declare no conflicts of interest.

References

1. E. R. Andresen, J. M. Dudley, D. Oron, C. Finot, and H. Rigneault, "Transform-limited spectral compression by self-phase modulation of amplitude-shaped pulses with negative chirp," *Opt. Lett.* **36**(5), 707–709 (2011).
2. C. W. Freudiger, W. Min, B. G. Saar, S. Lu, G. R. Holtom, C. He, J. C. Tsai, J. X. Kang, and X. Sunney Xie, "Label-Free Biomedical Imaging with High Sensitivity by Stimulated Raman Scattering Microscopy," *Science* **322**(5909), 1857–1861 (2008).
3. I. Will, H. I. Templin, S. Schreiber, and W. Sandner, "Photoinjector drive laser of the FLASH FEL," *Opt. Express* **19**(24), 23770–23781 (2011).
4. B. R. Washburn, J. A. Buck, and S. E. Ralph, "Transform-limited spectral compression due to self-phase modulation in fibers," *Opt. Lett.* **25**(7), 445–447 (2000).
5. L. Lavenu, M. Natile, F. Guichard, X. Délen, M. Hanna, Y. Zaouter, and P. Georges, "High-power two-cycle ultrafast source based on hybrid nonlinear compression," *Opt. Express* **27**(3), 1958–1967 (2019).
6. S. A. Planas, N. L. Pires Mansur, C. H. Brito Cruz, and H. L. Fragnito, "Spectral narrowing in the propagation of chirped pulses in single-mode fibers," *Opt. Lett.* **18**(9), 699–701 (1993).
7. Y. Zaouter, E. Cormier, P. Rigail, C. Hönninger, and E. Mottay, "30W, 10 μ J, 10-ps SPM-induced spectrally compressed pulse generation in a low non-linearity ytterbium-doped rod-type fibre amplifier," *Proc. SPIE* **6453**, 64530O (2007).
8. J. Limpert, T. Gabler, A. Liem, H. Zellmer, and A. Tünnermann, "SPM-induced spectral compression of picosecond pulses in a single-mode Yb-doped fiber amplifier," *Appl. Phys. B* **74**(2), 191–195 (2002).
9. E. R. Andresen, J. Thøgersen, and S. R. Keiding, "Spectral compression of femtosecond pulses in photonic crystal fibers," *Opt. Lett.* **30**(15), 2025–2027 (2005).
10. J. Pouysegur, F. Guichard, Y. Zaouter, M. Hanna, F. Druon, C. Hönninger, E. Mottay, and P. Georges, "Hybrid high-energy high-power pulsewidth-tunable picosecond source," *Opt. Lett.* **40**(22), 5184–5187 (2015).
11. A. V. Mitrofanov, M. M. Nazarov, A. A. Voronin, D. A. Sidorov-Biryukov, V. Y. Panchenko, and A. M. Zheltikov, "Free-beam spectral self-compression at supercritical peak powers," *Opt. Lett.* **43**(22), 5693–5696 (2018).
12. J. Liu, X. Chen, J. Liu, Y. Zhu, Y. Leng, J. Dai, R. Li, and Z. Xu, "Spectrum reshaping and pulse self-compression in normally dispersive media with negatively chirped femtosecond pulses," *Opt. Express* **14**(2), 979–987 (2006).
13. J. Schulte, T. Sartorius, J. Weitenberg, A. Vernaleken, and P. Russbüldt, "Nonlinear pulse compression in a multi-pass cell," *Opt. Lett.* **41**(19), 4511–4514 (2016).
14. J. Weitenberg, T. Saule, J. Schulte, and P. Rußbüldt, "Nonlinear Pulse Compression to Sub-40 fs at 4.5 μ J Pulse Energy by Multi-Pass-Cell Spectral Broadening," *IEEE J. Quantum Electron.* **53**(6), 1–4 (2017).
15. M. Ueffing, S. Reiger, M. Kaumanns, V. Pervak, M. Trubetskov, T. Nubbemeyer, and F. Krausz, "Nonlinear pulse compression in a gas-filled multipass cell," *Opt. Lett.* **43**(9), 2070–2073 (2018).
16. L. Lavenu, M. Natile, F. Guichard, Y. Zaouter, X. Delen, M. Hanna, E. Mottay, and P. Georges, "Nonlinear pulse compression based on a gas-filled multipass cell," *Opt. Lett.* **43**(10), 2252–2255 (2018).
17. M. Kaumanns, V. Pervak, D. Kormin, V. Leshchenko, A. Kessel, M. Ueffing, Y. Chen, and T. Nubbemeyer, "Multipass spectral broadening of 18 mJ pulses compressible from 1.3 ps to 41 fs," *Opt. Lett.* **43**(23), 5877–5880 (2018).
18. L. Lavenu, M. Natile, F. Guichard, Y. Zaouter, M. Hanna, E. Mottay, and P. Georges, "High-energy few-cycle Yb-doped fiber amplifier source based on a single nonlinear compression stage," *Opt. Express* **25**(7), 7530–7537 (2017).
19. D. Herriott, H. Kogelnick, and R. Kompfner, "Off-axis paths in spherical mirror interferometers," *Appl. Opt.* **3**(4), 523–526 (1964).
20. P. Kabaciński, T. M. Kardaś, Y. Stepanenko, and C. Radzewicz, "Nonlinear refractive index measurement by SPM-induced phase regression," *Opt. Express* **27**(8), 11018–11028 (2019).
21. J. Fatome, B. Kibler, E. R. Andresen, H. Rigneault, and C. Finot, "All-fiber spectral compression of picosecond pulses at telecommunication wavelength enhanced by amplitude shaping," *Appl. Opt.* **51**(19), 4547–4553 (2012).
22. C. Finot and S. Boscolo, "Design rules for nonlinear spectral compression in optical fibers," *J. Opt. Soc. Am. B* **33**(4), 760–767 (2016).
23. M. Hanna, N. Daher, F. Guichard, X. Delen, and P. Georges, "Hybrid pulse propagation model and quasi-phase matched four-wave mixing in multipass cells," submitted for publication.
24. J. Weitenberg, A. Vernaleken, J. Schulte, A. Ozawa, T. Sartorius, V. Pervak, H. Hoffmann, T. Udem, P. Russbüldt, and T. W. Hänsch, "Multi-pass-cell-based nonlinear pulse compression to 115 fs at 7.5 μ J pulse energy and 300 W average power," *Opt. Express* **25**(17), 20502–20510 (2017).

Nonlinear beam matching to gas-filled multipass cells

MARC HANNA,^{1,*}  LOUIS DANIAULT,² FLORENT GUICHARD,³ NOUR DAHER,¹ XAVIER DÉLEN,¹ RODRIGO LOPEZ-MARTENS,² AND PATRICK GEORGES¹

¹Université Paris-Saclay, Institut d'Optique Graduate School, CNRS, Laboratoire Charles Fabry, 91127, Palaiseau, France

²Laboratoire d'Optique Appliquée, CNRS, Ecole Polytechnique, ENSTA Paris, Institut Polytechnique de Paris, 181 chemin de la Humière et des Joncherettes, 91120, Palaiseau, France

³Amplitude Laser, 11 Avenue de Canteranne, Cité de la Photonique, 33600 Pessac, France

*marc.hanna@institutoptique.fr

Abstract: Gas-filled multipass cells are an appealing alternative to capillaries to implement nonlinear temporal compression of high energy femtosecond lasers. Here, we provide an analytic expression for stationary beam coupling to multipass cells that takes into account nonlinear propagation. This allows a constant beam size on the mirrors and at the cell waist, thereby making the optical design more accurate, for example to avoid optical damage or significant ionization. The analysis is validated using spatio-temporal numerical simulations of the propagation in a near-concentric configuration. This is particularly important for multipass cells that are operated in a highly nonlinear regime, which is the current trend since it allows a lower number of roundtrips, relaxing the constraint on mirror coatings performance.

© 2021 Optical Society of America under the terms of the [OSA Open Access Publishing Agreement](#)

1. Introduction

Nonlinear temporal compression [1] is an important technique that allows a lot of flexibility in ultrafast laser design. As an example, it can be used to turn efficient and robust ytterbium-doped materials-based lasers that typically emit pulses of a few hundred of femtosecond into few-cycle sources [2]. When the energy of the pulses to be compressed is above approximately 100 μJ , the nonlinear media of choice used in compression setups are rare gases. Glass capillaries filled with noble gases have been used for 25 years for that purpose, since they allow both beam confinement and large interaction lengths. An alternative solution is to use a gas-filled multipass cell (MPC). These systems have been proposed recently [3,4], and since then a number of experiments have shown excellent performances in a wide variety of input pulse duration, energy, and average power [5–11], particularly in terms of energy transmission.

One of the limits of energy scaling in gas-filled MPCs is that the peak power must be maintained below the critical power of the gas to avoid beam collapse. For any input pulse characteristics, this condition defines a maximum pressure for the particular gas used to fill the MPC, therefore limiting the B-integral per roundtrip. Experimental demonstrations tend to approach this limit, since it was observed that the spatio-spectral homogeneity remains satisfactory even for peak powers above half the critical power [12]. Operating MPCs at high nonlinearity level allows a lower number of roundtrips for a given compression ratio, thereby relaxing constraints on the mirror coatings both in terms of reflectivity and dispersion.

Input beam coupling in gas-filled MPCs is typically matched to the stationary Gaussian beam [13], to ensure a constant beam size evolution from one roundtrip to the next. This is particularly important to avoid damage on the mirrors or excess ionization at the MPC waist. Up to now, the stationary Gaussian beam target used for beam matching has been obtained ignoring the contribution of nonlinear refraction in the gas, which causes oscillations of the beam size over

the roundtrips upon nonlinear propagation [14]. These oscillations are more pronounced at high nonlinearity, calling for an improved input beam coupling analysis. Although beam matching can be fine-tuned during experiments, starting from the linear stationary beam, to obtain better homogeneity of the beam sizes at the mirrors, an improved understanding of the impact of nonlinearity on the caustic would help to guide this delicate procedure. Here we show that, in the aberrationless approximation, there exists a stationary Gaussian beam even in the presence of the distributed nonlinear refraction of the gas. We provide an analytical formula for optimized nonlinear beam matching to MPCs. We verify with spatio-temporal numerical simulations of the propagation that this nonlinear beam matching indeed results in stationary propagation in a highly nonlinear configuration. In particular, a near concentric MPC is considered, since it typically allows the most compact design at any given input energy level. Finally, a procedure to achieve this nonlinear beam matching experimentally is outlined. We believe that improved understanding and description of the spatial aspects of nonlinear propagation in these MPCs will allow the expansion of their use, in particular for high energy ultrafast laser systems.

2. Properties of the nonlinearly matched beam

Propagation of a continuous wave (CW) Gaussian beam in a homogeneous nonlinear medium with linear refractive index n_0 and nonlinear refractive index n_2 was shown to satisfy modified laws with respect to the linear case [15]:

$$w(z) = w_0 \sqrt{1 + \sigma \left(\frac{z}{z_R} \right)^2} \quad (1)$$

$$R(z) = z \left(1 + \frac{1}{\sigma} \left(\frac{z_R}{z} \right)^2 \right), \quad (2)$$

where w is the beam radius at l/e , R is the radius of curvature of the wavefront, z is the propagation distance, w_0 is the beam radius at its waist, $z_R = \pi w_0^2 / \lambda$ is the linear Rayleigh range, λ and λ_0 are the central wavelength in the medium and in vacuum respectively, and $\sigma = 1 - P/P_{crit}$ is a nonlinear correction factor that depends on the ratio of the beam power P to the critical power for self-focusing $P_{crit} = 3.77 \lambda_0^2 / 8 \pi n_0 n_2$ [16]. We consider propagation of such a beam in a nonlinear MPC as depicted in Fig. 1. To obtain the waist w_0 of the stationary beam in the nonlinear regime, we fix the radius of curvature of the nonlinear beam to be equal to the mirror radius of curvature at the mirror location. This yields

$$w_0 = \sqrt{\frac{\lambda L}{2\pi} \sqrt{\sigma \left(\frac{2R_M}{L} - 1 \right)}}, \quad (3)$$

where R_M is the radius of curvature of the mirrors, and L is the MPC length. As a result of this modified size and propagation characteristics, and following the same reasoning as in [4], the beam-averaged B-integral accumulated over a roundtrip is

$$B = \frac{8\pi n_0 n_2 P_{peak}}{\lambda_0^2 \sqrt{\sigma}} \arctan \left(\sqrt{\frac{L}{2R_M - L}} \right). \quad (4)$$

Because the stationary nonlinear beam is both smaller and has a lower divergence than its linear counterpart, we note that the B-integral per pass increases by a factor $1/\sqrt{\sigma}$ compared to the linear propagation approximation. These expressions are valid for a CW beam, and must be adapted to the case of optical pulses.

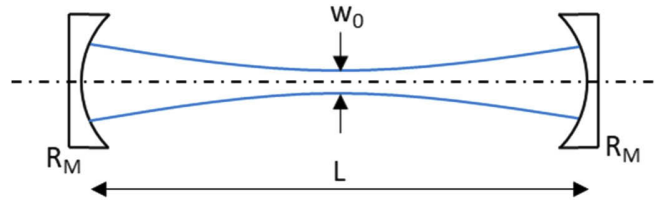


Fig. 1. MPC geometry.

To do this, we use an approach that is equivalent to the concept of effective area in guided-wave nonlinear optics [17]. For a given temporal pulse shape $P(t)$ and energy $E = \int P(t)dt$, we look for the rectangular-shaped pulse that accumulates the same average nonlinear phase $d\varphi_{NL}$ in the time domain over a distance dz :

$$\overline{d\varphi_{NL}} = \frac{\int P(t)d\varphi_{NL}(t)dt}{\int P(t)dt}, \quad (5)$$

where $d\varphi_{NL}(t) = \gamma P(t)dz$ is the nonlinear phase accumulated at time t , and γ is the local nonlinear coefficient. This results in the following definition for the effective pulsewidth:

$$\Delta t_{eff} = \frac{(\int P(t)dt)^2}{\int P^2(t)dt}, \quad (6)$$

with a corresponding effective peak power $P_{eff} = E/\Delta t_{eff}$. For a Gaussian pulse with full width at half maximum in power Δt_{FWHM} and peak power P_{peak} , the effective pulsewidth and power are given by

$$\Delta t_{eff} = \sqrt{\frac{\pi}{2 \ln(2)}} \Delta t_{FWHM} \quad P_{eff} = \frac{P_{peak}}{\sqrt{2}}. \quad (7)$$

Just like the effective area allows to take into account spatially averaged nonlinear effects in the time domain, the effective power defined in Eq. (7) allows us to take into account time-averaged nonlinear effects in the spatial domain. Note that these definitions of the effective duration and power are valid for third-order nonlinear effects that can be described as an intensity-dependent index. If we make the assumption that the temporal profile does not change upon propagation, which is verified if dispersion has negligible impact, then beam propagation can be accurately described using the modified Gaussian beam defined by Eqs. (1) and (2), with a nonlinear correction term given by $\sigma = 1 - P_{eff}/P_{crit}$. This time-averaged correction term must also be used in Eqs. (3) and (4) to yield the stationary beam waist and B-integral in the MPC. Note that in Eq. (4), the effective power must be used to compute σ , but the actual peak power must be used in the rest of the expression.

3. Validation with numerical simulations

We now use these results in numerical simulations to assess their validity. Nonlinear propagation is modelled by solving the spatio-temporal nonlinear envelope equation [18], taking into account diffraction, dispersion, and Kerr effects including self-phase modulation, self-focusing, and self-steepening. It is implemented using a split-step Fourier approach [17]. The pulsed beam at a given longitudinal position is described by a two-dimensional field which is a function of time and the radial coordinate, assuming cylindrical symmetry. Transition from the direct space to the Fourier space is achieved using the fast Fourier transform in time and the quasi-discrete Hankel transform [19] in space. The space-time grid for the simulations presented in next sections is as follows: 4 ps time window with 512 points, 7 mm maximum radius for the transverse dimension with 512 points, and a longitudinal step of 2.5 mm.

We choose to test the validity of the stationary nonlinear beam matching using simulation parameters approximately matching those of the experimental implementation described in [11], done in a highly nonlinear regime. Perfect Gaussian pulses with a central wavelength of 1030 nm, duration 700 fs, and energy 7 mJ are launched in a MPC filled with 1 bar of argon, corresponding to a nonlinear parameter σ of 0.6. The dispersion and nonlinear index of argon ($n_2=0.97\times 10^{-23}$ m²/W at 1 bar) are taken from [20,21]. The MPC mirrors have a radius of curvature of 1 m, a reflection coefficient of 99.5%, and are separated by a length of 1.995 m, slightly detuned from the concentric arrangement into the stability zone. In the linear propagation approximation, this results in a MPC waist of 131 μ m, and a beam radius of 2.5 mm on the mirrors. The nonlinear waist given by Eq. (3) is 115 μ m.

The evolution of the time-averaged RMS beam radius is plotted in Fig. 2 as a function of the number of passes through the MPC, both on the mirrors and at the MPC waist. Three situations are considered: purely linear propagation as a reference, nonlinear propagation if the beam is launched using linear beam matching, and nonlinear propagation using the nonlinear beam matching procedure described above. When linear beam matching is used, we can clearly observe that nonlinear refraction focuses the beam to a smaller waist, and that the caustic's periodicity is perturbed, causing a progressive decrease of the beam size on the mirrors and an increase at the MPC waist. For this particular case, the decrease in beam size from 2.5 to 1.9 mm corresponds to a fluence multiplied by 1.7, which could cause mirror damage depending on the experimental safety margin. At the waist, the beam radius varies in the range 103–133 μ m, which again corresponds to a variation of intensity of a factor 1.7. In contrast, using the nonlinear beam matching condition leads to a stable beam size both at the mirrors and at the focus, with values of 2.18 ± 0.02 mm and 117 ± 1 μ m respectively.

Looking in more details, Fig. 3 shows the peak intensity at the MPC waist obtained numerically, which is the quantity that ultimately matters for the ionization limit. Although the beam radius shown in Fig. 2 for the nonlinear beam matching case is almost constant upon propagation, we observe that the peak intensity varies in the range 43 - 64 TW/cm², indicating that aberrations lead to beam reshaping away from the perfect Gaussian beam. Still, this intensity variation is much smaller than in the linearly beam matched case, where the intensity is changed by more than a factor 2, over the range 36 - 81 TW/cm².

The numerically calculated on-axis B-integral for the first roundtrip is shown in Fig. 4 in the linear and nonlinear beam matching cases. The beam matching does not change the B-integral significantly. This can be understood as follows: it is easy to show that the B-integral accumulated by a Gaussian beam over propagation from minus infinity to plus infinity does not depend on the beam waist [4]. This remains approximately true if the B-integral is computed over a path that includes the beam waist and is much greater than the Rayleigh range, which is the case in a near concentric MPC. This also remains true for the modified nonlinear Gaussian beams used in this paper, which explains that the B-integral per roundtrip is hardly modified, even when the beam sizes at the waist and on the mirrors evolve from one roundtrip to the next.

After a roundtrip, the accumulated B-integral reaches a value of 11.2 rad, corresponding to a beam-averaged value of 5.6 rad for a Gaussian beam, to be compared to the analytical value predicted by Eq. (4) of 4.3 rad, and to the linear propagation approximation ($\sigma=1$) value of 3.3 rad. The reason for the discrepancy between the numerically obtained result and the analytical estimate can be traced back to the higher-order spatial phase (aberrations) imparted by the Kerr lens, that leads to a smaller effective area in the vicinity of the beam waist. This is in line with the observations made on the evolution of peak intensity.

Note that the present analysis entirely neglects ionization and plasma-related effects, which are typically avoided in gas-filled MPCs. Indeed, since these phenomena are much more nonlinear than the Kerr effect, their effect result in complete beam breakdown above a threshold that

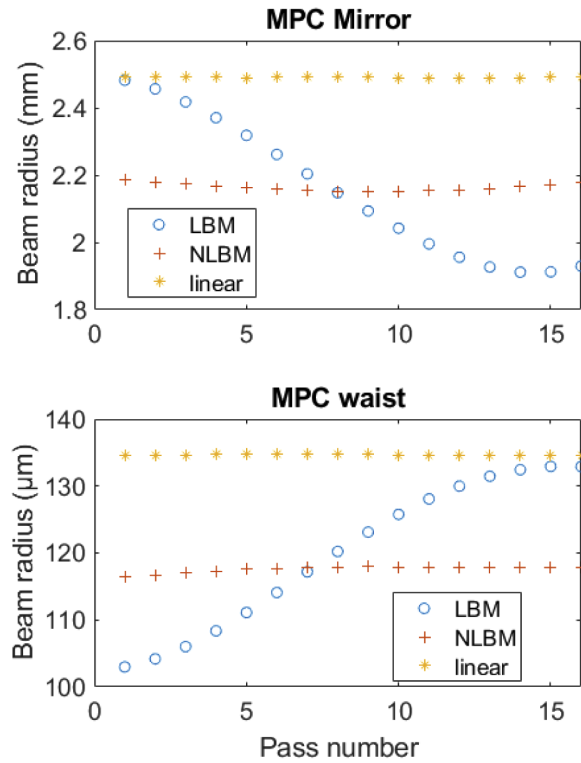


Fig. 2. Time-averaged RMS beam radius sampled at the MPC mirrors (top) and at the MPC center (bottom) as a function of pass number in the MPC in three different cases: linear refers to purely linear beam matching and propagation, LBM refers to linear beam matching and nonlinear propagation, NLBM to nonlinear beam matching and propagation.

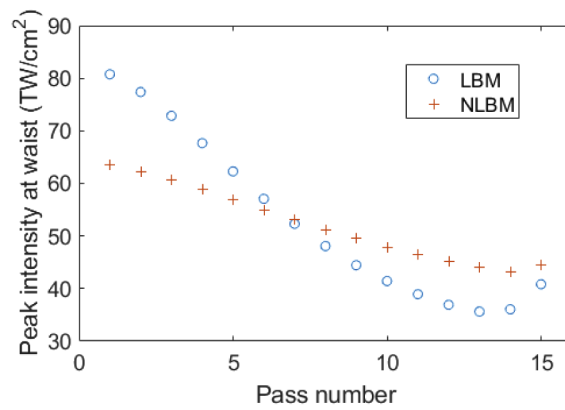


Fig. 3. Peak intensity at the MPC center as a function of pass number in two cases: LBM refers to linear beam matching and nonlinear propagation, NLBM to nonlinear beam matching and propagation.

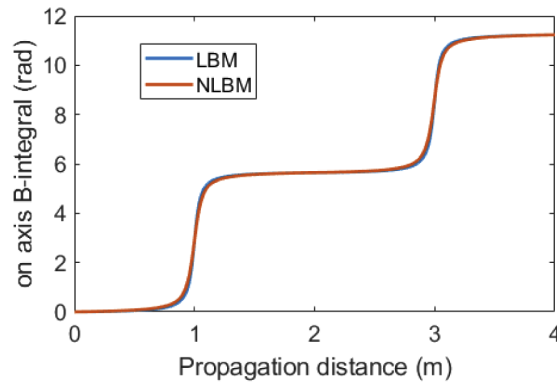


Fig. 4. On-axis B-integral accumulated over the first roundtrip in the MPC. LBM refers to linear beam matching, NLBM to nonlinear beam matching.

corresponds to the onset of significant ionization rate [7], depending on the ionization potential for the considered rare gas.

4. Experimental beam matching procedure

We now discuss how to use this result in practice. Propagation in a gas-filled MPC is modified by nonlinear refraction in the gas as soon as the beam goes through the window that is used to seal the cell. However, mode matching to the cell is often achieved at atmospheric air pressure and at reduced power to facilitate experimental adjustments and diagnostics, resulting in an essentially linear propagation. This can be taken into account using the following procedure. One of the result concerning the nonlinear Gaussian beam described in Eqs. (1) and (2) is that its propagation through an optical system can be easily computed using the standard ABCD matrix method, applied to a modified generalized reduced radius of curvature [15] defined as

$$\frac{1}{\widetilde{q}_{NL}} = \frac{n_0}{R} + i\sqrt{\sigma} \frac{\lambda_0}{\pi w^2}. \quad (8)$$

In order to determine what the optimal beam waist and location are in the absence of nonlinear gas, one should therefore start from the MPC center with the optimal nonlinear beam size given by Eq. (3), and propagate the beam back through the optical system to the entrance window using the nonlinear \widetilde{q}_{NL} parameter corresponding to the expected peak power and gas nature and pressure. From the entrance window, the beam can then be linearly propagated ($\sigma = 1$) towards the MPC center to reveal the target beam waist and position to be used during the beam matching procedure.

As an example, let us consider the case of the MPC described in section 3. If we assume that, from the input window, the beam first propagates over 1 m, then is focused into the MPC waist by a $f=1$ m lens or mirror, the waist radius that should be aimed for in the absence of gas is 150 μm , in order to reach the optimal waist size of 115 μm in the presence of gas. In this configuration, the waist position is unchanged by nonlinear refraction, but it is not always the case. This illustrates the practical importance of the present study for experimental implementations of highly nonlinear MPCs.

5. Conclusion

As a conclusion, we derive the stationary condition for a symmetric MPC in the nonlinear aberrationless Gaussian beam approximation. The notion of effective power allows to easily

account for the pulsed nature of beams. This analysis is checked using spatio-temporal numerical simulations, validating the fact that nonlinear refraction should be taken into account to optimize coupling in highly nonlinear MPCs.

Although we have restricted the analysis to gas-filled cells, nonlinear propagation using ABCD matrices and the \widehat{q}_{NL} parameter could be used to perform the same analysis in MPCs that include plates of bulk material. This formalism can also be used to guide experimental design of optical systems for input and output coupling of gas-filled capillary setups. Overall, we believe that these results will be helpful in designing future high energy MPCs for temporal compression of high energy laser sources.

Funding. Agence Nationale de la Recherche (ANR-10-LABX-0039-PALM, ANR-16-CE30-0027-01-HELLIX, ANR-19-CE30-0001-02-MIRTHYX).

Disclosures. The authors declare no conflicts of interest.

References

1. M. Nisoli, S. De Silvestri, O. Svelto, R. Szipöcs, K. Ferencz, C. Spielmann, S. Sartania, and F. Krausz, "Compression of high-energy laser pulses below 5 fs," *Opt. Lett.* **22**(8), 522–524 (1997).
2. L. Lavenu, M. Natile, F. Guichard, X. Délen, M. Hanna, Y. Zaouter, and P. Georges, "High-power two-cycle ultrafast source based on hybrid nonlinear compression," *Opt. Express* **27**(3), 1958–1967 (2019).
3. J. Schulte, T. Sartorius, J. Weitenberg, A. Vernaleken, and P. Russbuehdt, "Nonlinear pulse compression in a multi-pass cell," *Opt. Lett.* **41**(19), 4511–4514 (2016).
4. M. Hanna, X. Délen, L. Lavenu, F. Guichard, Y. Zaouter, F. Druon, and P. Georges, "Nonlinear temporal compression in multipass cells: theory," *J. Opt. Soc. Am. B* **34**(7), 1340–1347 (2017).
5. M. Ueffing, S. Reiger, M. Kaumanns, V. Pervak, M. Trubetskov, T. Nubbemeyer, and F. Krausz, "Nonlinear pulse compression in a gas-filled multipass cell," *Opt. Lett.* **43**(9), 2070–2073 (2018).
6. L. Lavenu, M. Natile, F. Guichard, Y. Zaouter, X. Delen, M. Hanna, E. Mottay, and P. Georges, "Nonlinear pulse compression based on a gas-filled multipass cell," *Opt. Lett.* **43**(10), 2252–2255 (2018).
7. M. Kaumanns, V. Pervak, D. Kormin, V. Leshchenko, A. Kessel, M. Ueffing, Y. Chen, and T. Nubbemeyer, "Multipass spectral broadening of 18 mJ pulses compressible from 1.3 ps to 41 fs," *Opt. Lett.* **43**(23), 5877–5880 (2018).
8. P. Russbuehdt, J. Weitenberg, J. Schulte, R. Meyer, C. Meinhardt, H. D. Hoffmann, and R. Poprawe, "Scalable 30 fs laser source with 530 W average power," *Opt. Lett.* **44**(21), 5222–5225 (2019).
9. C. Grebing, M. Müller, J. Buldt, H. Stark, and J. Limpert, "Kilowatt-average-power compression of millijoule pulses in a gas-filled multi-pass cell," *Opt. Lett.* **45**(22), 6250–6253 (2020).
10. P. Balla, A. Bin Wahid, I. Sytceovich, C. Guo, A.-L. Viotti, L. Silletti, A. Cartella, S. Alisaukas, H. Tavakol, U. Grosse-Wortmann, A. Schönberg, M. Seidel, A. Trabattoni, B. Manschwetus, T. Lang, F. Calegari, A. Couairon, A. L'Huillier, C. L. Arnold, I. Hartl, and C. M. Heyl, "Postcompression of picosecond pulses into the few-cycle regime," *Opt. Lett.* **45**(9), 2572–2575 (2020).
11. P. L. Kramer, M. K. R. Windeler, K. Mecseki, E. G. Champenois, M. C. Hoffmann, and F. Tavella, "Enabling high repetition rate nonlinear THz science with a kilowatt-class sub-100 fs laser source," *Opt. Express* **28**(11), 16951–16967 (2020).
12. N. Daher, F. Guichard, S. W. Jolly, X. Délen, F. Quéré, M. Hanna, and P. Georges, "Multipass cells: 1D numerical model and investigation of spatio-spectral couplings at high nonlinearity," *J. Opt. Soc. Am. B* **37**(4), 993–999 (2020).
13. A. E. Siegman, "Lasers," (University Science Books, 1986).
14. M. Hanna, N. Daher, F. Guichard, X. Délen, and P. Georges, "Hybrid pulse propagation model and quasi-phase-matched four-wave mixing in multipass cells," *J. Opt. Soc. Am. B* **37**(10), 2982–2988 (2020).
15. P.-A. Belanger and C. Pare, "Self-focusing of Gaussian beams: an alternate derivation," *Appl. Opt.* **22**(9), 1293–1295 (1983).
16. A. Couairon, E. Brambilla, T. Corti, D. Majus, O. de J. Ramirez-Gongora, and M. Kolesik, "Practitioner's guide to laser pulse propagation models and simulation," *Eur. Phys. J. Spec. Top.* **199**(1), 5–76 (2011).
17. G. P. Agrawal, "Nonlinear fiber optics," 5th edition, (Academic Press, 2012).
18. T. Brabec and F. Krausz, "Nonlinear optical pulse propagation in the single-cycle regime," *Phys. Rev. Lett.* **78**(17), 3282–3285 (1997).
19. M. Guizar-Sicairos and J. C. Gutiérrez-Vega, "Computation of quasi-discrete Hankel transforms of integer order for propagating optical wave fields," *J. Opt. Soc. Am. A* **21**(1), 53–58 (2004).
20. A. Bideau-Mehu, Y. Guern, R. Abjean, and A. Johannin-Gilles, "Measurement of refractive indices of neon, argon, krypton, and xenon in the 253.7–140.4 nm wavelength range. Dispersion relations and estimated oscillator strengths of the resonance lines," *J. Quant. Spectrosc. Radiat. Transfer* **25**(5), 395–402 (1981).
21. J. K. Wahlstrand, Y.-H. Cheng, and H. M. Milchberg, "High Field Optical Nonlinearity and the Kramers-Kronig Relations," *Phys. Rev. Lett.* **109**(11), 113904 (2012).



Optics Letters

Raman wavelength conversion in a multipass cell

NOUR DAHER,^{1,*} XAVIER DÉLEN,¹ FLORENT GUICHARD,² MARC HANNA,¹  AND PATRICK GEORGES¹

¹Université Paris-Saclay, Institut d'Optique Graduate School, CNRS, Laboratoire Charles Fabry, 91127 Palaiseau, France

²Amplitude, 11 Avenue de Canteranne, Cité de la Photonique, 33600 Pessac, France

*Corresponding author: nour.daher@institutoptique.fr

Received 18 May 2021; revised 17 June 2021; accepted 18 June 2021; posted 18 June 2021 (Doc. ID 431675); published 9 July 2021

Positively chirped femtosecond pulses at 1030 nm are wavelength-converted using spontaneous and stimulated Raman scattering in a potassium gadolinium tungstate crystal inserted inside a multipass cell. Recirculation in the cell and the Raman material allows both a high conversion efficiency and good spatial beam quality for the generated Stokes beams. The converted pulses can be compressed to sub-picosecond duration. Multipass cells could be an appealing alternative to other Raman shifter implementations in terms of thermal effects, control of the Raman cascade, and overall output beam quality. © 2021 Optical Society of America

<https://doi.org/10.1364/OL.431675>

Nonlinear Raman frequency shifting is a widely used method to extend the wavelength coverage of laser sources in temporal regimes ranging from CW [1] to femtosecond pulses [2]. However, when the pump pulse duration is shorter than the Raman mode dephasing time, which is inversely proportional to the Raman gain bandwidth, stimulated Raman scattering (SRS)-induced frequency conversion is challenging due to the Raman transient regime, especially with femtosecond pump pulses. In this regime, the threshold pump intensity is increased compared with the steady-state case [3], and electronic third-order effects such as self-phase modulation (SPM), cross-phase modulation (XPM), and self-focusing can become predominant. These intensity-dependent effects can be alleviated by chirping the femtosecond input pump pulse. In this case, the generated Stokes pulses can be compressed since they partly inherit the chirp of the pump pulse [4]. This has been shown in single pass solid-state Raman crystals [2,5,6], fiber amplifiers [7], and high-pressure gas-filled cells [4,8] and waveguides [9].

Performing SRS in solid-state media [10] is a robust, compact, and simple method to implement wavelength conversion since there is no controlled gas pressure or guiding structure. Several-centimeters-long rods of Raman material are typically used in single or double pass, and power scaling can be limited by the onset of self-focusing effects [6]. Moreover, the converted output spatial beam quality is often degraded especially in single pass schemes where only a pump beam is irradiating the Raman medium while Stokes signals arise from noise [5]. However, it is possible to enhance the conversion efficiency and spatial quality of the generated Stokes signals by providing a spatially coherent

seed beam for the SRS process, through Raman amplification of supercontinuum pulses [2] or multistage Raman conversion schemes [11].

Recently, multipass cells (MPCs) have been used to perform temporal compression of femtosecond laser pulses through the accumulation of SPM, with either solid [12,13] or gaseous [14,15] media as the nonlinear material. The distribution of nonlinearity over a large number of beam foci was shown to result in homogeneous and high-quality output beams. When a solid material is used, the pulse peak power is not limited to the critical power of the material due to the recirculation in a bulk medium with a thickness well below the self-focusing distance [12,13].

In this work, we demonstrate the first Raman wavelength conversion inside a 3-mm-long potassium gadolinium tungstate (KGW) crystal inserted in a MPC, in the stretched femtosecond pulse regime. Due to the large number of passes in the Raman medium provided by the MPC scheme, a large interaction length is achievable while operating at peak powers well above the critical power for self-focusing. In addition, co-propagation of the pump and Stokes beams inside the MPC leads to a spatial filtering effect that results in high spatial quality of the converted beams. This property is illustrated with an experimental comparison with a single pass scheme in a 20-mm-long KGW. The output beams in the MPC scheme are spatially and temporally characterized, demonstrating beam quality factors $M^2 < 1.2$, compressibility down to sub-picosecond durations, and conversion efficiencies of 44% and 30% for the first and second Stokes lines, respectively, for a linear polarization along the KGW N_g axis.

The scheme of our experimental setup is shown in Fig. 1. The input pulses are generated from a high-energy ytterbium-doped fiber chirped pulse amplifier (FCPA) delivering a maximum average power of 19 W with a 150 kHz repetition rate, corresponding to 126 μ J pulse energy, at 1030 nm central wavelength. The compressor of the FCPA is offset to positively chirp the 320 fs pulses to obtain a duration of 18.7 ps, larger than the Raman dephasing times in KGW, of the order of a few picoseconds [2]. The measured spatial quality factor of the laser beam is $M^2 = 1.06$ in both horizontal and vertical directions. The pump beam is first directed to the MPC through an arrangement of three lenses to match the stationary beam of the MPC, resulting in a beam diameter of ~ 400 μ m at the waist.

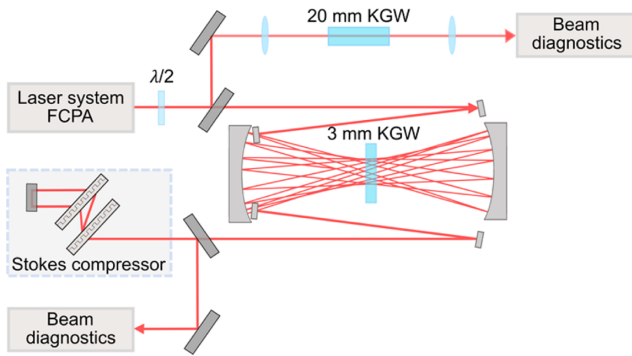


Fig. 1. Experimental setup.

The MPC is a Herriot cell [16] and consists of two concave mirrors with a radius of curvature of 300 mm separated by 504 mm and coated with a low group velocity dispersion dielectric stack on a 1000–1300 nm bandwidth, allowing a high reflectivity of $>99.95\%$ at the pump and both the first and second Stokes wavelengths. A 3-mm-thick anti-reflection coated KGW crystal with an aperture of $25\text{ mm} \times 25\text{ mm}$ is added near the center of the MPC as a nonlinear Raman medium. The number of round trips in the MPC is 18, leading to a total propagation distance of 10.8 cm in KGW. The transmission of the MPC in the linear regime, including the KGW crystal, is 80%. The KGW crystal is chosen due to its high Raman gain, high damage threshold, and moderate thermal conductivity. It is cut normal to the N_p axis, so one can obtain Raman shifts of 768 cm^{-1} and 901 cm^{-1} when the input laser polarization is aligned with the N_g and N_m axes, respectively [2]. Access to both Raman shifts in the experiment is allowed by using a half-wave plate placed before the MPC setup. At maximum input power, the estimated peak power is 6 MW, which is much higher than the critical power in the KGW of around 400 kW. The self-focusing distance in these conditions is estimated to be 6.7 cm, 20 times longer than the crystal length. The beam exiting the MPC is collimated with a 750 mm focal length lens and sent to various devices for characterization.

Figure 2 displays the average output power of the pump and Stokes lines as a function of the total power at the MPC output as well as the obtained spectra at maximum input power. For the 768 cm^{-1} shift, a maximum conversion efficiency of 44.6% and 30% is obtained at an input energy of $93\text{ }\mu\text{J}$ and $126\text{ }\mu\text{J}$ with spectra centered at 1120 nm and 1220 nm for the first and second Stokes lines, respectively. The maximum conversion efficiency drops to 42% and 17.4% for the 901 cm^{-1} shift, corresponding to an input energy of $112\text{ }\mu\text{J}$ and $126\text{ }\mu\text{J}$, with spectra centered at 1135 nm and 1263 nm for the first and second Stokes lines, respectively. This difference in conversion efficiencies is explained by the fact that the steady-state Raman gain coefficient is higher for the 768 cm^{-1} line than for the 901 cm^{-1} line.

In the following, we focus on the 768 cm^{-1} Stokes lines for further spatial and temporal characterizations. The spatial profiles measured at the output of the MPC for the pump at low power and for the Stokes lines at maximum conversion efficiency are shown in Fig. 3. A measured beam diameter of $2.3 \times 2.4\text{ mm}$, $2.5 \times 2.6\text{ mm}$, and $2.6 \times 3.9\text{ mm}$ at $1/e^2$ is obtained at the MPC output for the pump, first Stokes and second Stokes, respectively. This increase in beam size is coherent with the fact that a larger central wavelength translates into

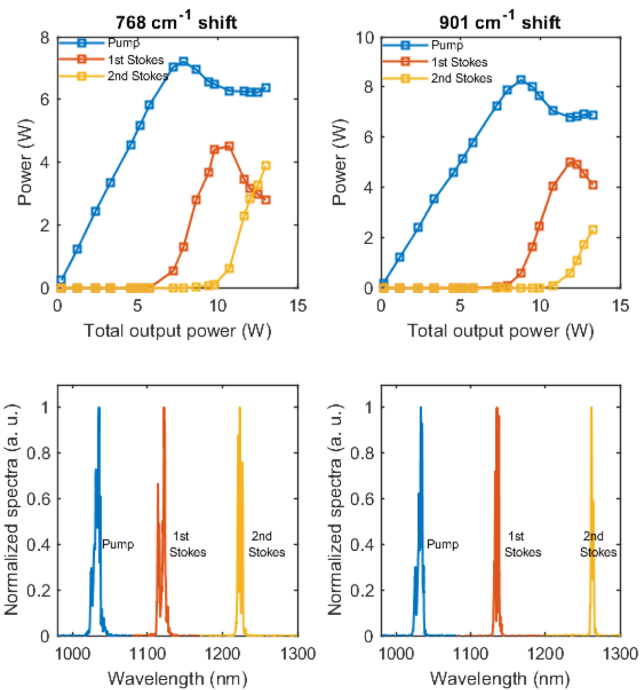


Fig. 2. Left column: (top) average power of the pump and Stokes lines for the 768 cm^{-1} shift as a function of total output power and (bottom) corresponding measured spectra. Right column: (top) average power of the pump and Stokes lines for the 901 cm^{-1} shift as a function of total output power and (bottom) corresponding measured spectra.

faster divergence for a given waist size. The reason for the larger ellipticity of the second Stokes beam is unclear, and it is not observed for the second Stokes beam of the 901 cm^{-1} shift. The M^2 beam quality factors are measured by acquiring the beam profiles using an InGaAs camera translated through a focus. The measured beam quality factors of the first Stokes and second Stokes lines are $M^2 = 1.05 \times 1.03$ and $M^2 = 1.06 \times 1.05$, respectively. This shows the preservation of the beam quality of the pump beam in the generated Stokes signals with a more pronounced ellipticity observed in the second Stokes. A spatio-spectral measurement is performed for the first Stokes line by using an imaging spectrometer setup. It consists of an $f-f$ arrangement composed of an 800 lines/mm grating, a 100 mm focal length cylindrical lens, and an InGaAs camera with a $30\text{ }\mu\text{m}$ pixel size. The result, presented in Fig. 3(d), shows no spectral inhomogeneity in the beam.

The spatial properties of the Stokes beams are remarkable compared to previously reported single pass Raman conversion experiments; we therefore perform an experimental comparison to check this result. The same input chirped pump pulses are focused into a 20-mm-long KGW crystal with a 400 mm focal length lens (upper part of Fig. 1). The KGW crystal is positioned slightly after the waist at a location where the beam diameter is $\sim 400\text{ }\mu\text{m}$, to obtain intensity comparable to the MPC case. The beam is then collimated and sent for characterization.

Only the first Stokes line is observed at full pump pulse energy, with a converted power of 2 W, corresponding to a conversion efficiency of 10%. The measured beam profiles of the pump at low power and first Stokes at maximum power are measured at the same position after collimation, and shown in Fig. 4. The diameter of the obtained Stokes beam is $3.3 \times 3.2\text{ mm}$ at

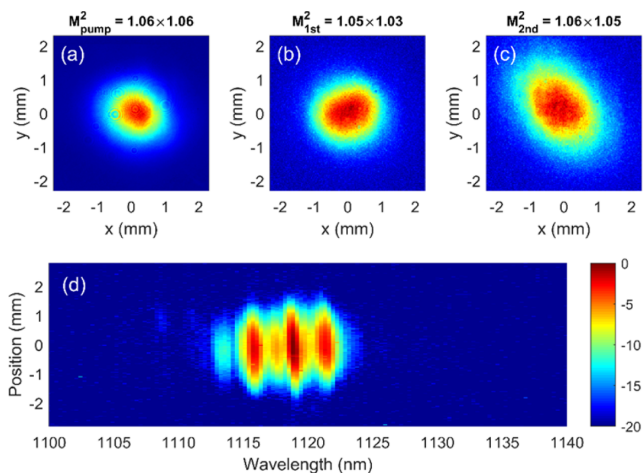


Fig. 3. Measured spatial beam profile of the (a) pump, (b) first Stokes, and (c) second Stokes lines at the MPC output. (d) Experimental spectro-imaging measurement in logarithmic (dB) scale.

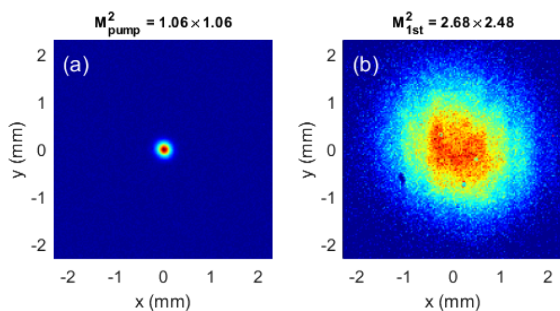


Fig. 4. Measured spatial profiles of the (a) pump and (b) first Stokes line at the same position after collimation at the output of the 20 mm KGW crystal.

$1/e^2$, much larger than the measured diameter of the pump beam of 0.4 mm. The beam quality factor of the Stokes beam is $M^2 = 2.7 \times 2.5$ along the horizontal and vertical directions. These spatial features can be interpreted as follows. The local Raman gain coefficient is proportional to intensity, which leads to a much larger gain at the beam center. As a result, for small enough pump depletion, the Raman converted beam in single pass is much smaller than the pump beam, which translates to a much larger beam after diffraction and collimation. In addition, for non-seeded setups, the process starts from quantum noise, so that the spatial coherence is low, resulting in mediocre beam quality factors. In contrast, in the MPC setup, the generated Stokes beam in the first pass is then co-propagated with the pump, and spatial filtering imparted by the Raman gain at each pass progressively induces spatial coherence and a beam size comparable to the pump beam. Although this process reduces the Stokes signal growth compared to a single pass setup, this is compensated for by the fact that multiple passes in the cell result in a larger interaction distance with the nonlinear material.

We now examine the temporal and spectral properties of the wavelength-converted beams at the output of the MPC setup. The pulses are characterized with a home-built second-harmonic-generation frequency resolved optical gating (FROG) setup, at maximum conversion efficiency for each of

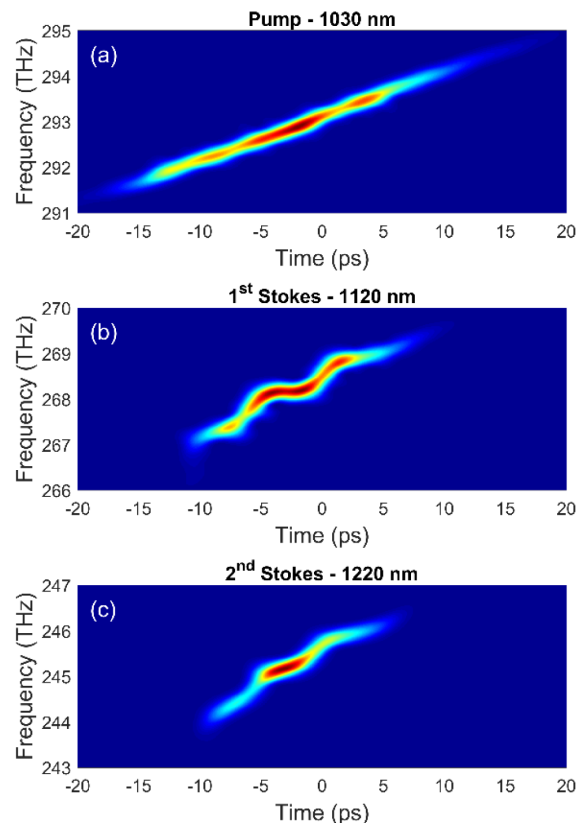


Fig. 5. Spectrogram of the (a) chirped input pump, non-compressed, (b) first Stokes, and (c) second Stokes at the MPC output.

the Stokes lines. The obtained pulse durations at FWHM are 8.8 ps and 6.3 ps for the first and second Stokes lines, respectively. This is because the delayed Raman response induces more efficient conversion at the trailing edge of the input pulse, which results in shorter converted pulse widths. Spectrograms obtained from the FROG-retrieved fields are plotted in Fig. 5 for the initial pump pulse, first Stokes beam, and second Stokes beam. In the three cases, the instantaneous frequency increases over time with the same average slope, confirming that the input chirp is imprinted onto the converted pulses. However, we notice a staircase-like structure in the instantaneous frequency of the generated first and second Stokes, which has not been reported before, to our knowledge. Although we do not have a definite explanation at this time, this characteristic could be related to the fact that the input chirped pump pulse does not exhibit a smooth temporal intensity profile. SPM and XPM effects can then act on the spectrograms as instantaneous frequency shifters, imparting these frequency oscillations around the main chirp slope.

Finally, the Stokes beams at the MPC output are temporally compressed using a pair of diffraction gratings in transmission, at an input energy corresponding to maximum efficiency for each line. The optimal compression point is searched by fine adjustment of the incident angle on the gratings and of the distance separating them. Compression of the first Stokes beam is carried out using a pair of gratings with 1570 lines/mm and yields a pulse duration of 520 fs at FWHM, as shown in Fig. 6(a). The compressor throughput is 80%. For the second Stokes beam, a pair of gratings with 1400 lines/mm is

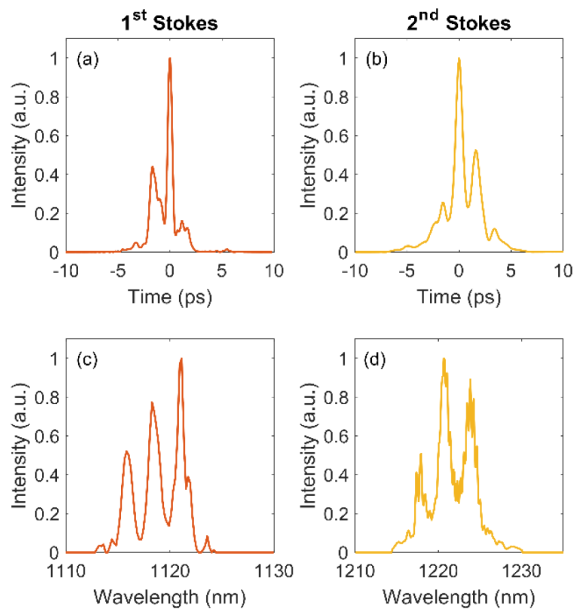


Fig. 6. Left column: (a) FROG-retrieved temporal intensity profile and (c) FROG-retrieved spectral intensity profile of the compressed first Stokes at 93 μJ input energy. Right column: (b) FROG-retrieved temporal intensity profile and (d) FROG-retrieved spectral intensity profile of the compressed second Stokes at 126 μJ input energy.

used, resulting in a duration of 800 fs at FWHM, as shown in Fig. 6(b), with a compressor efficiency of 66%. The obtained temporal pulse quality is mediocre, with large pedestals and side pulses. This can be traced back to the time–frequency structure evidenced by the spectrogram, showing a non-homogeneous chirp rate, or equivalently a higher order spectral phase, that cannot be compensated for by the gratings pair. We also notice that the obtained spectra for both first and second Stokes possess a peak structure, as shown in Figs. 6(c) and 6(d), in agreement with the independently measured spatially resolved spectrum shown in Fig. 3(d). This structure is likely related to the SPM/XPM-induced spectrogram shaping observed in Fig. 5.

In conclusion, we report the use of a solid-state material-based MPC to perform Raman frequency conversion. This allows efficient generation of the Stokes lines while preserving the beam quality due to the spatial filtering action provided by propagation inside the MPC. These setups could be used in other temporal regimes, e.g., with picosecond or nanosecond pulses. Other efficient Raman materials such as diamond or molecular gases such as hydrogen could also be used to extend the possibilities in terms of target wavelength and input pulse energy. MPCs could also provide interesting capabilities: by

carefully designing the MPC mirror coatings, it might be possible to stop the Raman cascade at a given Stokes line, thereby optimizing the energy transfer towards this line. Finally, since Raman scattering is an inelastic process, scaling the average power can be limited by thermal effects [17,18]. In this MPC scheme, the thermal load is distributed to distinct spots at each pass through the Raman material, which could be advantageous. We therefore believe that Raman conversion is an interesting application of nonlinear MPCs.

Funding. Agence Nationale de la Recherche (ANR-10-LABX-0039-PALM).

Disclosures. The authors declare no conflicts of interest.

Data Availability. Data underlying the results presented in this paper are not publicly available at this time but may be obtained from the authors upon reasonable request.

REFERENCES

1. R. Casula, J. Penttinen, M. Guina, A. J. Kemp, and J. E. Hastie, *Optica* **5**, 1406 (2018).
2. P. Mackonis, A. Petruenas, A. M. Rodin, V. Girdauskas, and A. Michailovas, *Opt. Lett.* **45**, 6627 (2020).
3. G. Hilfer and C. R. Menyuk, *J. Opt. Soc. Am. B* **7**, 739 (1990).
4. C. Jordan, K. A. Stankov, G. Marowsky, and E. J. Canto-Said, *Appl. Phys. B* **59**, 471 (1994).
5. N. Zhavoronkov, F. Noack, V. Petrov, V. P. Kalosha, and J. Herrmann, *Opt. Lett.* **26**, 47 (2001).
6. F. B. Grigsby, P. Dong, and M. C. Downer, *J. Opt. Soc. Am. B* **25**, 346 (2008).
7. S. Zhou, T. Takamido, S. Imai, and F. Wise, *Opt. Lett.* **35**, 2397 (2010).
8. C. Vicario, M. Shalaby, A. Konyashchenko, L. Losev, and C. P. Hauri, *Opt. Lett.* **41**, 4719 (2016).
9. P. A. Carpegiani, G. Coccia, G. Fan, E. Kaksis, A. Pugžlys, A. Baltuška, R. Piccoli, Y.-G. Jeong, A. Rovere, R. Morandotti, L. Razzari, B. E. Schmidt, A. A. Voronin, and A. M. Zheltikov, *Optica* **7**, 1349 (2020).
10. P. Cerny, H. Jelinkova, P. G. Zverev, and T. T. Basiev, *Prog. Quantum Electron.* **28**, 113 (2004).
11. V. A. Lisinetskii, V. A. Orlovich, H. Rhee, X. Wang, and H. J. Eichler, *Appl. Phys. B* **91**, 299 (2008).
12. J. Schulte, T. Sartorius, J. Weitenberg, A. Vernaleken, and P. Russbuehler, *Opt. Lett.* **41**, 4511 (2016).
13. G. Jargot, N. Daher, L. Lavenue, X. Delen, N. Forget, M. Hanna, and P. Georges, *Opt. Lett.* **43**, 5643 (2018).
14. M. Ueffing, S. Reiger, M. Kaumanns, V. Pervak, M. Trubetskov, T. Nubbemeyer, and F. Krausz, *Opt. Lett.* **43**, 2070 (2018).
15. L. Lavenue, M. Natile, F. Guichard, Y. Zaouter, X. Delen, M. Hanna, E. Mottay, and P. Georges, *Opt. Lett.* **43**, 2252 (2018).
16. D. Herriott, H. Kogelnick, and R. Kompfner, *Appl. Opt.* **3**, 523 (1964).
17. A. McKay, O. Kitzler, and R. P. Mildren, *Opt. Express* **22**, 707 (2014).
18. M. Heinzig, G. Palma-Vega, B. Yildiz, T. Walbaum, T. Schreiber, and A. Tünnermann, *Opt. Lett.* **46**, 1133 (2021).

Optics Letters

Single-stage few-cycle nonlinear compression of millijoule energy Ti:Sa femtosecond pulses in a multipass cell

LOUIS DANIAULT,^{1,*}  ZHAO CHENG,¹ JAISMEEN KAUR,¹ JEAN-FRANÇOIS HERGOTT,² FABRICE RÉAU,² OLIVIER TCHERBAKOFF,² NOUR DAHER,³ XAVIER DÉLEN,³ MARC HANNA,³  AND RODRIGO LOPEZ-MARTENS¹

¹Laboratoire d'Optique Appliquée, CNRS, Ecole Polytechnique, ENSTA Paris, Institut Polytechnique de Paris, 181 chemin de la Hunière et des Joncherettes, 91120 Palaiseau, France

²Université Paris-Saclay, CEA, CNRS, LIDYL, 91191 Gif-sur-Yvette, France

³Université Paris-Saclay, Institut d'Optique Graduate School, CNRS, Laboratoire Charles Fabry, 91127 Palaiseau, France

*Corresponding author: louis.daniault@ensta-paris.fr

Received 8 September 2021; revised 29 September 2021; accepted 29 September 2021; posted 29 September 2021 (Doc. ID 442707); published 15 October 2021

We report on the nonlinear temporal compression of mJ energy pulses from a Ti:Sa chirped pulse amplifier system in a multipass cell filled with argon. The pulses are compressed from 30 fs down to 5.3 fs, corresponding to two optical cycles. The post-compressed beam exhibits excellent spatial quality and homogeneity. These results provide guidelines for optimizing the compressed pulse quality and further scaling of multipass-cell-based post-compression down to the single-cycle regime. © 2021 Optical Society of America

<https://doi.org/10.1364/OL.442707>

Nonlinear spectral broadening in gas-filled hollow-core fibers (HCFs) through self-phase modulation (SPM) followed by dispersion compensation is now commonly used to temporally compress multi-mJ energy pulses down to few-cycle duration [1–3]. The HCF approach has the distinct advantage of providing spatially homogeneous spectral broadening over extended nonlinear propagation lengths (dispersion-free spectral broadening), but is limited by ionization that arises due to the high propagation intensities inside the waveguide. Recent experiments performed with multi-mJ energy pulses from Ti:Sa lasers have shown that ionization can partially compensate for pulse break-up due to self-steepening (SS), under specific conditions, to reach post-compressed pulse durations close to the single cycle [2,3]. Further scaling of this technique requires the use of increasingly large fiber core diameters and lengths, which can quickly become impractical for table-top use.

For the past few years, multipass cells (MPCs) have been employed for compressing ultrashort pulses as a promising alternative to HCFs [4,5]. The nonlinear interaction that takes place in free-space propagation, is distributed over much larger path lengths than in capillaries and provides a large spectral broadening with reduced spatiotemporal couplings. Recent experiments report compression factors comparable to those obtained with HCFs along with excellent efficiency [5–10].

To date, MPCs have been almost exclusively dedicated to Yb-based laser nonlinear compression experiments, which often require a double-stage compression scheme to reach the few-cycle regime. From pulses ranging from several 100 fs up to 1 ps duration, a first stage involves dielectric mirrors with high damage thresholds and high reflectivity but moderate bandwidths, leading to post-compressed pulses of a few tens of fs and transmission efficiencies well above 95%. The second stage requires large bandwidth optics at the expense of lower reflectivity and damage threshold, yielding few-cycle pulses with efficiencies around 80%. Some experiments also report hybrid nonlinear experiments involving a MPC as the first stage and a HCF for the second one [10]. Very recently, 290 μ J pulses from a Ti:Sa laser were post-compressed down to three optical cycles in a single-stage MPC with 45% efficiency [11]. This experiment is driven by sub-50 fs input pulses readily available from commercial Ti:Sa-based laser systems, thereby avoiding the first MPC compression stage mentioned above.

In this Letter, we report the post-compression of mJ-level, 30 fs Ti:Sa laser pulses down to 5.3 fs (~ 2 optical cycles) with 67% overall efficiency. We spatially filter the input pulses to study MPC-based compression using near-perfect Ti:Sa beam properties. The spectral broadening capability is first explored at different gas pressures. The optimum configuration is then determined, and the shortest accessible compressed pulse is characterized using single-shot second harmonic frequency-resolved optical gating (SHG-FROG). The intrinsic limitations and scalability of MPC-based compression of Ti:Sa pulses are discussed, providing reliable guidelines for further compression down to single-cycle duration.

The experimental setup is schematically shown in Fig. 1. It starts with a Ti:Sa-based femtosecond laser system (Femtopower Pro-HE) delivering 30 fs compressed pulses of 1.2 mJ energy at 1 kHz repetition rate. An acousto-optic programmable dispersive filter (Dazzler from Fastlite) in the main amplifier allows to finely tune the pulse spectral phase. The amplified beam is

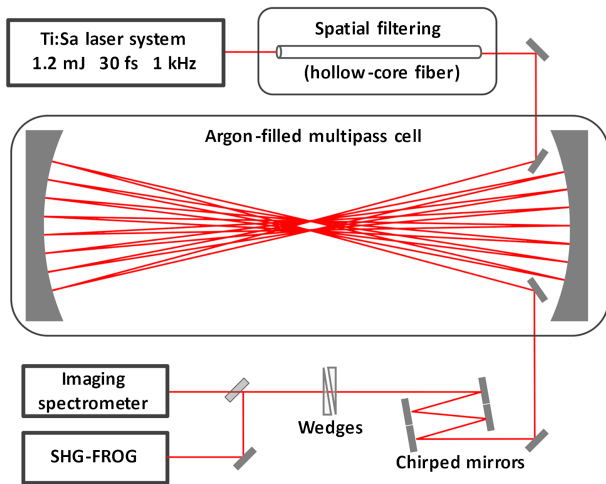


Fig. 1. Experimental setup.

then spatially filtered under vacuum by a 21 cm long HCF of 250 μm inner diameter, which fixes the beam waist position and dimensions at its output. Its throughput of about 80% leads to pulses of 1 mJ energy.

This HCF-based filtering stage is followed by a MPC made of two 50.8 mm enhanced silver-coated mirrors of 1.5 m radius of curvature separated by ~ 3 m, yielding a nearly concentric cavity. A couple of focusing/diverging optics are used after the spatial filtering stage to seed the MPC while fulfilling its stability condition, which corresponds to beam diameters of 480 μm and 3.1 mm at the waist and on the mirrors, respectively. This geometry is chosen such that the beam fluence on the mirrors stays well below their damage threshold, roughly estimated at 100 mJ/cm². The number of passes through the MPC can be set up to 18, and two small rectangular silver mirrors allow to inject/pick up the beam. The MPC is operated inside an airtight chamber filled with argon gas at different pressures.

The Dazzler in the Ti:Sa amplification chain is tuned to compensate for dispersion (lenses, windows, air) such that the pulses are Fourier-transform limited (FTL) at the input of the MPC. The output beam is then collimated to approximately 10 mm diameter using a spherical mirror and temporally compressed by a set of double-angle chirped mirrors (PC 42 from Ultrafast Innovations) combined with two fused silica wedges to finely tune the pulse spectral phase. The beam is then characterized spatially and temporally with the use of a single shot SHG-FROG and an imaging spectrometer (both devices from FemtoEasy).

The output spectrum is first studied at different gas pressures and for 18 passes through the MPC. At the highest pressure investigated, the input pulse peak power remains below 30% of the self-focusing critical power. In addition, as detailed in the following, the onset of dispersion rapidly reduces the pulse peak power throughout the passes, such that overall self-focusing effects can be neglected in all cases. Figure 2 shows the spectral shapes obtained for pressures ranging from 0 to 700 mbar, and their respective RMS widths and FTL pulse durations are plotted in Fig. 3.

It demonstrates that the spectral broadening increases linearly with the gas pressure up to about 150 mbar but saturates at higher pressures. Indeed, the gas dispersion is also pressure dependent and plays a crucial role in the broadening process. At

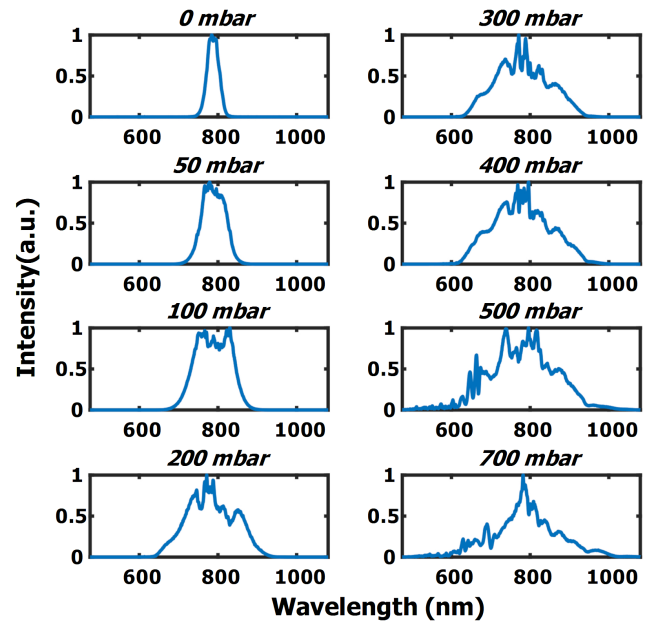


Fig. 2. Evolution of the normalized spectral shapes with increasing gas pressure.

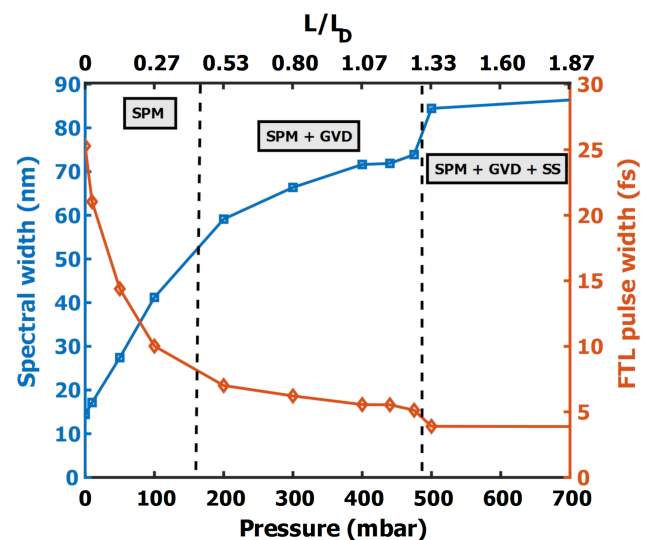


Fig. 3. Evolution of the RMS spectral widths and FTL pulse widths for different compression regimes.

lower pressures, the propagation can be considered as dispersion free. Here, all 18 passes are subject to pure SPM with a constant temporal pulse profile. The output spectra grow linearly with gas pressure and maintain a nice symmetry.

When reaching 150 mbar, the increasing spectral width along with the increasing dispersion coefficient of the gas starts to temporally spread the pulses for the last MPC passes, thereby decreasing their peak power and limiting spectral broadening. However, SPM along with dispersion leads to much smoother spectral profiles compared to dispersion-less spectral broadening, as in, e.g., HCF, where strong modulations appear with pure SPM.

At higher pressures, this effect is aggravated: although SPM becomes stronger, the pulse spreading arises earlier, at earlier

passes, such that the next ones have little contribution to the spectral broadening. Also, SPM accumulated by chirped pulses favors the onset of nonlinear spectral phase at high orders that can degrade the pulse compressibility. Thus, many passes at high pressure do not necessarily lead to shorter post-compressed pulses.

In addition, starting from 475 mbar, the spectral profile exhibits noticeable distortions and a modulated pedestal towards shorter wavelengths. The onset of such distortions is very steep when increasing the gas pressure and shows a tipping point in the pulse spectral quality. However, this specific point does not correspond to the critical power above which the beam experiences catastrophic collapse, and the ionization rate of the gas remains sufficiently low to have a noticeable impact under these conditions.

Numerical simulations based on these experimental conditions show the exact same behavior and highlight an excessive impact of SS that arises during the first pass. This leads to an optical shock exhibiting a highly distorted pulse profile. The on-axis pulse temporal profile after the first pass is simulated and plotted in Fig. 4 for different gas pressures around the tipping point mentioned above. The optical shock of the pulse and the fast ripples at its trailing edge arise quite rapidly at this nonlinearity level. The whole on-axis pulse propagation over the first pass simulated for these specific gas pressures is presented in Visualization 1, Visualization 2 and Visualization 3.

The interplay among SPM, SS, and the gas dispersion in the following passes induces strong temporal and spectral modulation in the short-wavelength region, which highly impacts the output spectral quality and pulse compressibility. It is worth noting that this effect cannot be avoided by, e.g., limiting the number of passes since the first one is the most critical in terms of pulse degradation. Moreover, even for higher pressures, the spectral bandwidth remains almost constant. This tipping point fixes the fundamental limit of spectral broadening in the MPC regardless of the number of passes and directly depends on the dimensionless parameter s characterizing the SS process ($s = 1/t_0\omega_0$, with ω_0 the central pulsation and t_0 the RMS FTL input pulse width) and the beam-averaged B-integral accumulated in the first pass. In our experimental conditions, they correspond to $s = 0.02$ and $B = 5$ rad.

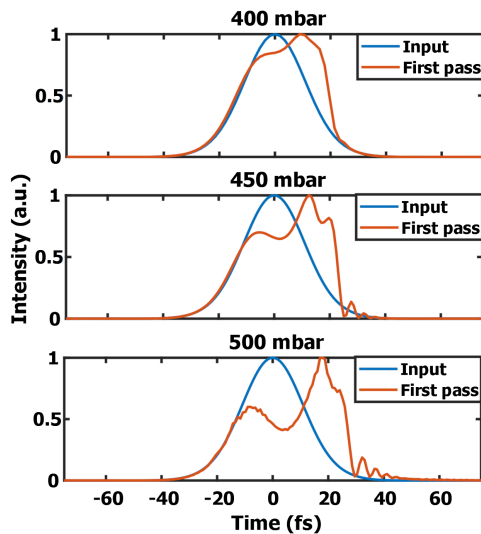


Fig. 4. Simulated on-axis pulse temporal profile for increasing gas pressure ranging from 400 mbar to 500 mbar.

This behavior is specific to short input pulses of few tens of fs duration, where SS can arise quite rapidly with increasing SPM. Conversely, in the range of 100 fs–1 ps, the B-integral per pass in the MPC is usually limited to avoid strong spatio-spectral couplings, but SS and gas dispersion have little or no impact. Also, in HCF experiments for post-compressing pulses down to the single-cycle regime, SS arises rapidly at low B-integrals, but can be partially compensated for by ionization, which has the opposite effect for moderate ionization rates [3]. However, this situation relies on very specific experimental conditions and is usually avoided in MPCs due to plasma defocusing that disturbs the beam caustic stability throughout the passes.

This study demonstrates that single-stage MPC-based post-compression is limited in B-integral in the first pass by SS, and in a number of efficient passes by dispersion. The gas pressure and the number of passes need to be chosen carefully, depending on the input pulse energy and duration. In the following, the number of passes is set to 16 and the gas pressure to 450 mbar, as a trade-off among spectral broadening, pulse compressibility, and MPC transmission efficiency.

In this configuration, the output energy of the MPC is 0.77 mJ compared to 0.98 mJ at its input, yielding a transmission of about 79%. This efficiency can be compared to the numbers of bounces on the silver mirrors, leading to a reflectivity of 98.5% for each pass over the whole spectral bandwidth. Out of the MPC, nine pairs of chirped mirrors introducing a negative group-delay dispersion of -378 fs², followed by two wedges, allow to compensate for the accumulated nonlinear spectral phase and gas dispersion. The compressed energy is measured to be 0.66 mJ, including the beam transport losses, yielding 67% overall efficiency for the full post-compression system.

The output spectrum measured by a spectrometer is shown in Fig. 5 along with the one retrieved from the SHG-FROG measurement (error of 11.10^{-3} on a 256×256 grid). The corresponding compressed pulse profile is presented in Fig. 3 and exhibits a duration of 5.3 fs FWHM, to be compared to its FTL duration of 4.7 fs. This yields a compression factor of about 5.7 and output pulses of two optical cycles. The beam-averaged B-integral accumulated over the 16 passes is about 10 rad according to our simulations. This value is notably higher

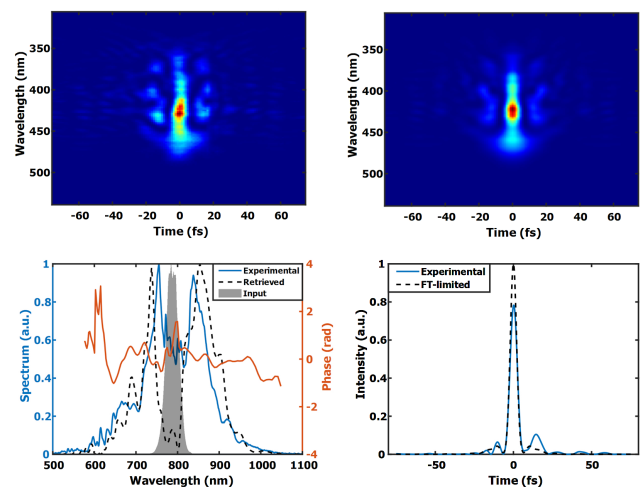


Fig. 5. Top: measured (left) and retrieved (right) SHG-FROG traces. Bottom: input, measured, and FROG-retrieved output spectra (left) and pulse temporal profile along with its FTL profile (right).

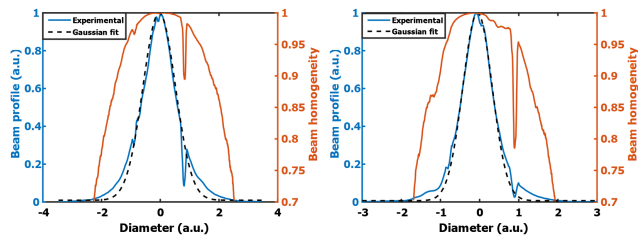


Fig. 6. Output beam profile in arbitrary units in the horizontal (left) and vertical (right) dimensions along with their spectral homogeneity. The dip in the measurements is due to unremovable dust on the spectrometer's slit.

than the compression ratio since chirped pulses experience less spectral broadening for a given B-integral, which occurs during the last passes.

This configuration is located close to the tipping point described above. Higher gas pressures and/or a higher number of passes lead to worse pulse compressibility and longer output pulse duration.

The spectral homogeneity of the beam is characterized using an imaging spectrometer. The V parameter, as defined in [5], is plotted in Fig. 6 along with the beam profile along the horizontal and vertical dimensions. Note that the hole in the beam profile is caused by unremovable dust on the spectrometer's slit. The output beam exhibits a nearly Gaussian profile with very little degradation and nice spectral homogeneity, above 99% at the beam FWHM and above 95% at $1/e^2$ in both directions.

We demonstrated the generation of 5.3 fs pulses at 0.66 mJ output energy with excellent beam quality and homogeneity using single-stage nonlinear post-compression of 30 fs Ti:Sa pulses in an argon-filled MPC. This pulse duration corresponds to two optical cycles within the pulse FWHM. The transmission efficiency is measured to be 79% for the MPC itself and 67% for the overall compression experiment.

The spectral evolution of the pulses with respect to gas pressure was studied and highlighted two main limitations. The first one comes from the gas dispersion that progressively reduces the accumulated B-integral per pass in the MPC. However, it helps to maintain a nice spectral shape without significant modulations typically obtained in dispersion-less compression experiments. Nevertheless, the number of passes needs to be restricted to generate the largest spectrum with best temporal compressibility and limited MPC losses. On the other hand, the B-integral accumulated in the first pass needs to be carefully controlled to avoid dramatic temporal pulse distortions arising through SS. This situation cannot be exploited, as the output pulse quality and compressibility are strongly deteriorated.

In our experimental conditions, these limitations restrict the compressed pulse to two optical cycles. Thus, the single-cycle

regime would require careful dispersion management within the cavity to partially (but not fully) compensate for the gas dispersion. Indeed, a completely dispersion-less post-compression scheme would lead to a significant SS and highly unbalanced output spectral shapes. Tailored dispersion throughout the propagation would limit this effect while preserving smooth and weakly modulated spectral shapes.

Furthermore, spatial filtering of the input beam prior to the MPC, although implemented for practical reasons, in particular for beam matching inside the cavity, is not an absolute necessity for achieving compression. Our next experiments will involve direct output beams at higher energies and adapted cavity designs compared to regular HCF post-compression experiments in terms of spectral and temporal pulse quality, overall post-compression efficiency, and footprint in the single-cycle regime.

Funding. Horizon 2020 Framework Programme (Advanced Grant ExCoMet 694596); Laserlab-Europe (871124); Agence Nationale de la Recherche (ANR-10-LABX-0039-PALM).

Disclosures. The authors declare no conflicts of interest.

Data availability. Data underlying the results presented in this Letter are not publicly available at this time but may be obtained from the authors upon reasonable request.

REFERENCES

1. T. Nagy, P. Simon, and L. Veisz, *Adv. Phys. X* **6**, 1845795 (2021).
2. T. Nagy, M. Kretschmar, M. J. J. Vrakking, and A. Rouzée, *Opt. Lett.* **45**, 3313 (2020).
3. M. Ouillé, A. Vernier, F. Böhle, F. M. Bocoum, A. Jullien, M. Lozano, J. P. Rousseau, Z. Cheng, D. Gustas, A. Blumenstein, P. Simon, S. Haessler, J. Faure, T. Nagy, and R. Lopez-Martens, *Light Sci. Appl.* **9**, 47 (2020).
4. M. Hanna, X. Délen, L. Lavenue, F. Guichard, Y. Zaouter, F. Druon, and P. Georges, *J. Opt. Soc. Am. B* **34**, 1340 (2017).
5. J. Weitenberg, T. Saule, J. Schulte, and P. Russbüldt, *IEEE J. Quantum Electron.* **53**, 1 (2017).
6. L. Lavenue, M. Natile, F. Guichard, Y. Zaouter, X. Delen, M. Hanna, E. Mottay, and P. Georges, *Opt. Lett.* **43**, 2252 (2018).
7. M. Kaumanns, V. Pervak, D. Kormin, V. Leshchenko, A. Kessel, M. Ueffing, Y. Chen, and T. Nubbemeyer, *Opt. Lett.* **43**, 5877 (2018).
8. P. Balla, A. Bin Wahid, I. Sytcevic, C. Guo, A.-L. Viotti, L. Silletti, A. Cartella, S. Alisauskas, H. Tavakol, U. Grosse-Wortmann, A. Schönberg, M. Seidel, A. Trabattori, B. Manschwetus, T. Lang, F. Calegari, A. Couairon, A. L'Huillier, C. L. Arnold, I. Hartl, and C. M. Heyl, *Opt. Lett.* **45**, 2572 (2020).
9. M. Müller, J. Buldt, H. Stark, C. Grebing, and J. Limpert, *Opt. Lett.* **46**, 2678 (2021).
10. L. Lavenue, M. Natile, F. Guichard, X. Délen, M. Hanna, Y. Zaouter, and P. Georges, *Opt. Express* **27**, 1958 (2019).
11. P. Rueda, F. Videla, T. Witting, G. A. Torchia, and F. J. Furch, *Opt. Express* **29**, 27004 (2021).

Résumé de la thèse en Français

Nous étudions dans ce travail la possibilité de réaliser des effets non-linéaires optiques en espace libre dans des cellules multipassages. Ceci permet de distribuer la non-linéarité en plusieurs étapes dans le milieu non-linéaire. Les cellules utilisées sont de type Herriott, constituées de deux miroirs courbes qui forment un système optique périodique stable, dans lequel les faisceaux peuvent se propager sur de nombreux allers-retours dans un milieu non-linéaire solide ou gazeux. L'objectif de la thèse consiste à étudier de manière approfondie la robustesse des cellules remplies de gaz aux couplages spatio-temporels. En outre, ces dispositifs ont presque exclusivement été utilisés dans le cadre de systèmes de compression temporelle exploitant l'automodulation de phase. Par conséquent, nous réalisons des expériences montrant la possibilité d'utiliser des cellules multipassages pour réaliser une autre fonction, la compression spectrale, ou un autre effet non-linéaire, l'effet Raman. Le manuscrit commence par une introduction générale introduisant le contexte, suivie de quatre chapitres décrivant la théorie ainsi que les travaux expérimentaux, et finit par une conclusion générale.

Le **chapitre 1** couvre les notions de bases utiles à la compréhension des différents phénomènes physiques impliqués dans la propagation des impulsions laser ultra-courtes considérées dans les expériences décrites dans les chapitres suivants. Une partie de ce chapitre se concentre sur la description du concept de cellule multipassage. Le principe de la compression non-linéaire temporelle des impulsions est décrit tout en citant les différentes techniques utilisées de nos jours, en particulier les cellules multipassages et l'état de l'art des travaux réalisés.

Le **chapitre 2** décrit la première expérience qui consiste à étudier la limite des hautes non-linéarités dans une cellule remplie de gaz. Nous étudions ensuite les propriétés des impulsions en sortie de la cellule pour des valeurs de puissance crête approchant la puissance critique du gaz utilisé. En sortie de la cellule, l'effet de "wave breaking" est observé expérimentalement. Enfin, nous montrons que le faisceau de sortie reste essentiellement homogène spectralement, notamment en utilisant des mesures spatio-spectrales ainsi qu'une méthode de caractérisation complète du champ optique (amplitude et phase) en trois dimensions.

Le **chapitre 3** présente une expérience de compression spectrale dans une cellule multipassage incluant des lames de silice. Nous utilisons l'effet d'automodulation de phase pour transformer des impulsions d'entrée femtoseconde étirées négativement en impulsions limitées par transformée de Fourier. En ajustant finement la phase spectrale à l'entrée de la cellule à l'aide d'un composant de mise en forme d'impulsions, nous générons un spectre comprimé

symétrique à la sortie de la cellule. La qualité spatiale ainsi que l'homogénéité spatio-spectrale sont conservées dans cette expérience.

Le **chapitre 4** aborde l'étude de la conversion de longueur d'onde dans un milieu solide possédant des transitions Raman inséré dans une cellule multipassage. Nous montrons qu'il est possible de convertir de manière efficace la longueur d'onde pompe à des longueurs d'onde supérieures pour des impulsions laser femtosecondes étirées positivement. Nous observons que la propagation quasi-périodique du faisceau de pompe dans la cellule engendre un effet de filtrage qui confère une bonne qualité spatiale aux faisceaux convertis. Enfin, nous caractérisons temporellement les faisceaux pompe et Stokes à la sortie de la cellule et nous réalisons la compression temporelle des faisceaux Stokes.

Les résultats obtenus montrent que les cellules multipassages sont des plateformes efficaces et utiles pour l'utilisation et l'étude des effets non-linéaires conventionnellement réalisés dans les fibres optiques et les guides d'onde.

Titre : Optique non-linéaire ultra-brève dans des cellules multipassages

Mots clés : Laser femtoseconde, Optique ultra-brève, Optique non-linéaire, Cellule multipassage

Résumé : Ce manuscrit concerne l'étude de phénomènes d'optique non-linéaire dans des cellules multipassages. Une cellule d'Herriott est constituée de deux miroirs courbes qui forment un système optique périodique stable, dans lequel les faisceaux peuvent se propager sur de nombreux allers-retours. Nous étudions la propagation d'impulsions ultra-brèves dans un tel système, dans lequel un matériau non-linéaire (solide ou gaz) a été ajouté. Ainsi, la non-linéarité optique est distribuée le long de la propagation sur de multiples trajets et foyers. Une des propriétés remarquables de ces systèmes est l'absence de couplages spatio-spectraux des impulsions en sortie. Dans ce cadre, nous avons réalisé des expériences autour de trois problématiques. Une première expérience consiste à étudier la limite des hautes non-linéarités dans une cellule remplie de gaz. Nous étudions les propriétés des impulsions de sortie pour des valeurs de puissance crête approchant la puissance critique du gaz utilisé. Nous montrons que le faisceau de sortie reste essentiellement homogène spectralement, notamment en utilisant une méthode de caractérisation complète du

champ optique (amplitude et phase) en trois dimensions. Dans un deuxième temps, nous réalisons une expérience de compression spectrale dans une cellule multipassage incluant des lames de silice fondue. Nous utilisons l'automodulation de phase dans le milieu solide pour transformer des impulsions d'entrée femtoseconde étirées négativement en impulsions picoseconde limitées par transformée de Fourier. Ceci permet une montée en énergie par rapport aux systèmes similaires réalisés à base de fibres optiques. Enfin, nous montrons qu'en insérant dans une cellule un milieu solide possédant des transitions Raman, il est possible de convertir de façon efficace des impulsions femtoseconde étirées positivement à des longueurs d'onde supérieures. La propagation quasi-périodique du faisceau de pompe dans la cellule engendre un effet de filtrage qui confère une bonne qualité spatiale aux faisceaux convertis. Ces résultats contribuent à établir le fait que les cellules multipassages constituent une plateforme efficace et utile pour l'étude et l'utilisation des effets non-linéaires en optique.

Title : Nonlinear Ultrafast Optics in Multipass Cells

Keywords : Femtosecond laser, Ultrafast optics, Nonlinear optics, Multipass cell

Abstract : This work deals with the study of nonlinear optics phenomena inside multipass cells. A Herriott cell is made of two curved mirrors that result in a stable periodic optical system, in which beams can propagate over many roundtrips. We investigate the propagation of ultrashort pulses in such a system, in which a nonlinear material (solid or gas) has been added. As a result, the optical nonlinearity is distributed over a large number of roundtrips and foci. A remarkable feature of these systems is that the output pulses do not exhibit significant spatio-spectral couplings. In this general framework, we have more specifically studied experimentally three situations. A first experiment was done to study the high nonlinearity limit in a gas-filled multipass cell. We study the output pulses properties for peak power values approaching the critical power of the gas used. We show that the output beam is essentially spectrally homogeneous, notably using a full three-dimensional

optical field (amplitude and phase) characterization technique. Second, we implement a spectral compression experiment in a multipass cell including fused silica plates. By using self-phase modulation in the solid medium, we turn negatively chirped femtosecond input pulses into Fourier transform-limited picosecond pulses. This allows energy scaling compared to previous implementations of the same functionality in optical fibers. Finally, we show that, by inserting a Raman-active solid material inside a multipass cell, it is possible to convert efficiently positively chirped femtosecond pulses towards larger wavelengths. The quasi-periodic propagation of pump pulses in the cell imparts a spatial filtering effect that results in high spatial quality output Stokes beams. Taken as a whole, these experiments contribute to establishing multipass cells as an efficient and useful platform to study and use nonlinear optical phenomena.